

Characterization and modelling of SFRC elements

Doctoral Thesis by:
Ana Blanco Álvarez

Directed by:
Antonio Aguado de Cea
Albert de la Fuente Antequera

Barcelona, March 2013

Universitat Politècnica de Catalunya
Departament d'Enginyeria de la Construcció

DOCTORAL THESIS



Curso académico: 2012-2013

Acta de calificación de tesis doctoral

Nombre y apellidos	ANA BLANCO ÁLVAREZ
DNI / NIE / Pasaporte	36517748G
Programa de doctorado	ENGINYERIA DE LA CONSTRUCCIÓ
Unidad estructural responsable del programa	DEPARTAMENT D'ENGINYERIA DE LA CONSTRUCCIÓ

Resolución del Tribunal

Reunido el Tribunal designado a tal efecto, el doctorando / la doctoranda expone el tema de la su tesis doctoral titulada "*Characterization and modelling of SFRC elements*".

Acabada la lectura y después de dar respuesta a las cuestiones formuladas por los miembros titulares del tribunal, éste otorga la calificación:

APTA/O NO APTA/O

(Nombre, apellidos y firma)		(Nombre, apellidos y firma)	
Presidente/a		Secretario/a	
(Nombre, apellidos y firma)	(Nombre, apellidos y firma)	(Nombre, apellidos y firma)	(Nombre, apellidos y firma)
Vocal	Vocal	Vocal	Vocal

_____, ____ de _____ de _____

El resultado del escrutinio de los votos emitidos por los miembros titulares del tribunal, efectuado por la Escuela de Doctorado, a instancia de la Comisión de Doctorado de la UPC, otorga la MENCIÓN CUM LAUDE:

SÍ NO

(Nombre, apellidos y firma)	(Nombre, apellidos y firma)
Presidenta de la Comisión de Doctorado	Secretaria de la Comisión de Doctorado

Barcelona a _____ de _____ de _____

*“Every great and deep difficulty bears in itself its own solution.
It forces us to change our way of thinking in order to find it.”*

Niels Bohr (1885-1962)

Nobel Prize for Physics in 1922

A toda mi familia por su apoyo,
en especial a mi abuelo Maximino,
a mis padres José Luis y Salvita
y a mi hermano Luis.

ACKNOWLEDGEMENTS - AGRADECIMIENTOS

En primer lugar quisiera agradecer a mis tutores, Antonio Aguado y Albert de la Fuente, por su inestimable apoyo y dedicación durante estos cuatro años. A Antonio por iniciarme en el ámbito de la investigación durante la carrera, por su confianza para continuar trabajando con él desarrollando esta tesis doctoral y por las oportunidades de futuro que me ha brindado. A Albert por animarme hace cuatro años a descubrir la experiencia del doctorado y guiarme a lo largo de la misma. Mi agradecimiento a ambos va más allá de lo que puedo expresar en estas líneas.

En el Departamento de Ingeniería de la Construcción he tenido la oportunidad de colaborar con profesores que han contribuido a mejorar el trabajo realizado. Me gustaría recordar a Luis Agulló Fité por su disposición a ayudar y por sus reflexiones sobre aspectos de la tesis. Sobre todo, le estaré siempre agradecida por su cercanía y por generar un entorno familiar en el grupo de investigación. Agradezco también de forma especial a Sergio H. Pialarissi Cavalaro por sus enseñanzas, por su apoyo y paciencia durante las fases de simulación numérica y por proponer uno de los estudios que conforman la tesis. Del mismo modo, quiero mostrar mi gratitud a Marc Vandewalle por su colaboración e interés en los estudios realizados.

El desarrollo de esta tesis doctoral no habría sido posible sin el apoyo económico del Comissionat per a Universitats del DIUE de la Generalitat de Catalunya por medio de la beca FI-DGR 2010 y de la beca para la estancia de investigación en el extranjero BE-DGR 2010. Asimismo, quisiera reconocer el apoyo brindado por el Col·legi d'Enginyers de Camins, Canals i Ports de Catalunya durante los tres últimos años. También agradezco a mis tutores por proporcionarme los medios económicos durante el primer año de investigación.

Quiero agradecer a las empresas BEKAERT, en particular a Ann Lambrechts, Gerhard Vitt y Thomas Bonamie, y ESCOFET, especialmente a Gerard Faneca, por su colaboración en el diseño de las campañas experimentales. Mi más sincero agradecimiento a los miembros del Laboratorio de Tecnología de Estructuras Luis Agulló (Tomàs García, Camilo Bernad, Jordi Cabrerizo, Robert Mc-Aloon, Carlos Hurtado y Jordi Lafuente) por su ayuda en la realización de los ensayos y por los momentos divertidos. Agradezco también a Carles Puig su colaboración durante la fase experimental.

Me tomaré la libertad de escribir unas líneas en inglés para que aquellos a quienes van dirigidas estas palabras puedan comprenderlas. *I would like to thank Professor Joost Walraven, Dr. Steffen Grünwald and Dr. Kees Blom for giving me the opportunity to work at Delft University of Technology for six months. They were kind enough to share their knowledge and experience with me. I am grateful to the colleagues from the Department of Structural Engineering and to the friends in Delft who made my stay in the Netherlands a great experience.*

Los momentos vividos con mis compañeros de departamento son inolvidables. Por ello, quiero agradecer con especial cariño a André Campos, Bernat Viñolas, Betty de los Ríos, Edison Osorio, Filipe Laranjeira, Francisco Mena, Isaac Galobardes, Izelman Oliveira, Jordi Cañas, Júlia Gómez, Juliana Claudino, Jussara Limeira, Liao Lin, Luca Pelà, Luis Segura, Martha Alejandra González, Nacho Segura, Nayara Klein, Ricardo Pieralisi, Sandra Manso y Yohei Endo. Quiero agradecer especialmente a Cris, Francesc, Ignasi, Joan y Víctor por su amistad durante hace más de diez años y a María, Mireia y Pati porque han sido un apoyo constante, confidentes y motivo de tantos momentos divertidos.

Por último, quiero agradecer a mis padres, mi hermano, mis abuelos, mis tíos y mi primo por su cariño, por su apoyo incondicional y por animarme a cumplir mis sueños. Mis padres siempre han puesto todos los recursos a su alcance para que pudiera conseguir mis propósitos y de ellos he aprendido el esfuerzo y la constancia en el trabajo. Mi hermano me ha enseñado a no rendirme ante la adversidad y a trabajar para dar lo máximo de uno mismo. Mis abuelos, aunque a veces en la distancia, me han motivado y han disfrutado de cada pequeño logro. Mi tía Nati y mi tío Luis me han animado siempre a disfrutar del trabajo y de la vida. En especial quiero agradecer a Pau, mi primo y mi amigo, que ha compartido la experiencia del doctorado conmigo. Después de cuatro años de momentos de alegría y éxitos pero también de dudas y momentos difíciles, puedo decir que ha sido un privilegio haber sido compañeros durante esta etapa tan decisiva.

SUMMARY

The use of fibre reinforced concrete (FRC) as a construction material has expanded beyond the traditional applications since the publication of design codes and guidelines. In fact, the industry is demanding FRC with increasing structural responsibilities and, in some cases, with the fibres as the only reinforcement.

Despite the remarkable advances in the fibre reinforcement technology and the publication of design guidelines, questions continue to arise regarding the performance, the characterization and the modelling of the material. The definition of the constitutive model of FRC and the development of methods for the characterization have been extensively studied. However, their adequacy for certain applications still remains an issue. Moreover, properties such as the fibre orientation and the creep behaviour are not minor concerns and need to be properly considered. These subjects require further research in order to work towards an accurate and efficient design procedure.

In this context, the great interest of the industry to understand better FRC behaviour has created the opportunity of performing small-scale and real-scale tests that are a valuable source of information. Therefore, a rather generalist doctoral thesis covering several subjects about the characterization and modelling of steel fibre reinforced concrete (SFRC) elements is proposed. The subjects addressed in this research refer to the flexural behaviour and modelling of RC-SFRC beams (beams with combined reinforcement of steel fibres and rebars); the flexural behaviour, fibre orientation and modelling of SFRC slabs with changing dimensions; the prediction of the tensile behaviour of SFRC and the post-cracking creep behaviour of SFRC.

The first subject concerns the adequacy of the constitutive models proposed in the current European codes and guidelines to model the flexural response of RC-SFRC beams. For that, real-scale elements with different steel fibres and fibre contents were tested. The results of the numerical modelling show that, in general, these constitutive models reproduce satisfactorily the experimental data.

In the second subject, based on the flexural behaviour of real-scale SFRC slabs, geometry factors are proposed to compensate for the inaccuracies of the current constitutive models to reproduce the response of such elements. The study conducted on the modelling of the flexural behaviour of the slabs allowed identifying a favourable effect of the fibre orientation (fibre network effect) as the width of the slabs increased.

The third subject covers a proposal of an analytical formulation to estimate the tensile stress-strain diagram of FRC from the results of the Barcelona test. The validation performed indicates the applicability of the new model to concrete reinforced with either steel fibres or plastic fibres.

The last subject focuses on the post-cracking creep behaviour of SFRC, which is assessed by performing flexural tests under sustained load on pre-cracked small-scale

beams. Based on the results, a simple model to predict the evolution of the creep coefficient with time is proposed.

RESUMEN

El uso de hormigón reforzado con fibras (HRF) como material de construcción se ha expandido más allá de las aplicaciones tradicionales desde la publicación de códigos y recomendaciones de diseño. De hecho, la industria está demandando HRF con creciente responsabilidad estructural y, en algunos casos, con las fibras como único material de refuerzo.

A pesar de los notables avances en la tecnología de refuerzo con fibras y la publicación de recomendaciones de diseño, continúan surgiendo preguntas con respecto al comportamiento, la caracterización y el diseño del material. La definición del modelo constitutivo del HRF y el desarrollo de métodos de caracterización han sido ampliamente estudiados, sin embargo, su idoneidad para ciertas aplicaciones estructurales sigue suscitando debate. Asimismo, propiedades tales como la orientación de las fibras y las deformaciones por fluencia no son aspectos menores y necesitan ser considerados adecuadamente. Con el fin de trabajar hacia un procedimiento de diseño preciso y eficiente, los citados temas deben ser ampliamente estudiados.

En este contexto, el interés de la industria por comprender mejor el comportamiento del HRF ha generado la posibilidad de realizar ensayos a pequeña escala y a escala real que son una valiosa fuente de información. Por este motivo, se plantea una tesis doctoral generalista que abarca varios temas referentes a la caracterización y diseño del hormigón reforzado con fibras de acero (HRFA). Los temas tratados en esta investigación son: el comportamiento a flexión y el diseño de vigas con refuerzo combinado de fibras y barras de acero; el comportamiento a flexión, la orientación de fibras y el diseño de losas de HRFA con diferentes dimensiones; la predicción del comportamiento a tracción del HRFA y el comportamiento y la fluencia del HRFA en estado fisurado.

El primer tema analiza la idoneidad de los actuales modelos constitutivos propuestos en los códigos y recomendaciones europeos para simular el comportamiento a flexión de vigas con refuerzo combinado. Para ello, se han ensayado elementos a escala real con diferentes tipos y contenidos de fibras de acero. Los resultados de la modelización numérica demostraron que, en general, dichos modelos constitutivos reproducen satisfactoriamente los datos experimentales.

En el segundo tema, con base en el comportamiento a flexión de losas de HRFA a escala real, se proponen factores geométricos con el fin de compensar las inexactitudes de los actuales modelos constitutivos para reproducir la respuesta de este tipo de elementos. El estudio relativo a la modelización del comportamiento a flexión de las losas permitió identificar un efecto favorable de la orientación de las fibras (efecto de la red de las fibras) que se acentúa con el ancho de las losas.

El tercer tema se centra en la propuesta de una formulación analítica para estimar la curva tensión-deformación a tracción del HRF a partir de los resultados del ensayo Barcelona. La validación realizada indica la aplicabilidad del modelo tanto para hormigones con fibras de acero como con fibras plásticas.

El último tema trata la deformación por fluencia del HRFA en estado fisurado, evaluadas mediante la realización ensayos a flexión bajo carga sostenida en vigas a pequeña escala pre-fisuradas. Con base en los resultados, se propone un modelo simple para predecir la evolución del coeficiente de fluencia en el tiempo.

TABLE OF CONTENTS

1.	INTRODUCTION.....	1
1.1.	SCOPE OF THE RESEARCH.....	1
1.2.	MOTIVATIONS	5
1.3.	OBJECTIVES.....	5
1.4.	METHODOLOGY	6

PART I: MOTIVATIONS

2.	STATE OF THE ART	9
2.1.	INTRODUCTION	9
2.2.	CONSTITUTIVE MODELS FOR FRC IN CODES AND GUIDELINES.....	10
2.2.1.	Brief overview	10
2.2.2.	German guidelines: DBV-Merkblatt Stahlfaserbeton (1992/2001).....	12
2.2.3.	RILEM TC 162-TDF Recommendations (2003).....	13
2.2.4.	Italian guidelines: CNR-DT 204 (2006).....	13
2.2.5.	Spanish code: EHE-08 (2008).....	14
2.2.6.	fib Model Code (2010)	15
2.3.	TEST METHODS TO CHARACTERIZE THE TENSILE BEHAVIOUR OF FRC.....	17
2.3.1.	Brief overview	17
2.3.2.	Barcelona test (UNE 83515:2010)	20
2.4.	ORIENTATION.....	21
2.4.1.	Factors influencing fibre orientation	21
2.4.2.	Fibre orientation in specimens with different sizes.....	23
2.4.3.	Methods to determine fibre orientation.....	24
2.5.	LONG-TERM BEHAVIOUR OF SFRC.....	25
2.5.1.	Basic concepts	25
2.5.2.	Creep of SFRC.....	28
2.6.	CONCLUDING REMARKS.....	30

PART II: RC-SFRC BEAMS

3.	FLEXURAL BEHAVIOUR AND MODELLING OF RC-SFRC BEAMS	31
3.1.	INTRODUCTION	31

3.1.1.	Objectives	32
3.1.2.	Outline of the chapter.....	32
3.2.	EXPERIMENTAL PROGRAM.....	32
3.2.1.	Specimens.....	32
3.2.2.	Materials and concrete mix	33
3.2.3.	Test setup	35
3.3.	RESULTS.....	37
3.3.1.	Crack pattern.....	37
3.3.2.	Crack width.....	40
3.3.3.	Load-deflection curves	44
3.4.	NUMERICAL MODEL	47
3.4.1.	Numerical modelling of the sectional behaviour	47
3.4.2.	Simulation of the tests	48
3.5.	CONSTITUTIVE MODELS IN EUROPEAN CODES AND GUIDELINES	50
3.5.1.	Assumptions in the numerical simulation	50
3.5.2.	Constitutive models	53
3.5.3.	Results.....	54
3.6.	CONCLUDING REMARKS.....	57

PART III: SFRC SLABS

4.	FLEXURAL BEHAVIOUR OF SFRC SLABS	59
4.1.	INTRODUCTION	59
4.1.1.	Objectives	61
4.1.2.	Outline of the chapter.....	61
4.2.	EXPERIMENTAL PROGRAM.....	61
4.2.1.	Specimens.....	61
4.2.2.	Materials and concrete mix	62
4.2.3.	Test setup	65
4.3.	RESULTS.....	67
4.3.1.	Crack patterns	67
4.3.2.	Load-deflection curves	71
4.3.3.	Load-rotation angle curves.....	76
4.3.4.	Energy absorption capacity.....	76
4.4.	CONCLUDING REMARKS.....	79
5.	FIBRE ORIENTATION IN SFRC SLABS.....	81

5.1.	INTRODUCTION	81
5.1.1.	Objectives	82
5.1.2.	Outline of the chapter.....	82
5.2.	EXPERIMENTAL PROGRAM.....	82
5.2.1.	Core drilling.....	83
5.2.2.	Preparation of the cubic specimens.....	84
5.2.3.	Inductive method for assessing the amount and orientation of steel fibres	85
5.2.4.	Method for the multidirectional characterization of SFRC.....	85
5.3.	INDUCTIVE METHOD RESULTS.....	86
5.3.1.	Fibre content.....	86
5.3.2.	Fibre orientation	87
5.4.	MULTIDIRECTIONAL METHOD RESULTS.....	98
5.4.1.	General methodology	98
5.4.2.	Small slab.....	100
5.4.3.	Medium slabs	100
5.4.4.	Large slabs.....	101
5.5.	CONCLUDING REMARKS.....	102
6.	MODELLING THE FLEXURAL BEHAVIOUR OF SFRC SLABS	105
6.1.	INTRODUCTION	105
6.1.1.	Objectives	106
6.1.2.	Outline of the chapter.....	106
6.2.	FINITE ELEMENT MODEL	107
6.2.1.	Model type.....	107
6.2.2.	Geometry and boundary conditions	107
6.2.3.	Material properties	109
6.2.4.	Study on the influence of the mesh size	111
6.3.	COMPARISON BETWEEN EXPERIMENTAL AND NUMERICAL RESULTS	112
6.3.1.	Crack patterns	112
6.3.2.	Load-deflection curves	113
6.4.	PARAMETRIC STUDY.....	115
6.4.1.	Preliminary analysis	115
6.4.2.	Variables considered	117
6.4.3.	Analysis of the influence of σ_2	117
6.4.4.	Analysis of the influence of σ_3	122
6.4.5.	Analysis of the influence of ε_2	126
6.5.	NUMERICAL FIT OF THE PARAMETERS.....	130

6.6.	FIBRE NETWORK EFFECT AND PROPOSAL OF GEOMETRY FACTORS	132
6.6.1.	Introduction.....	132
6.6.2.	Fibre network effect.....	133
6.6.3.	Proposal of geometry factors.....	136
6.7.	CONCLUDING REMARKS.....	138

PART IV: PREDICTING THE TENSILE BEHAVIOUR OF SFRC

7.	CONSTITUTIVE MODEL BASED ON THE BARCELONA TEST	141
7.1.	INTRODUCTION	141
7.1.1.	Objectives	142
7.1.2.	Outline of the chapter.....	142
7.2.	ANALYTICAL EXPRESSIONS FOR THE TENSILE STRENGTH	143
7.3.	FORMULATION TO PREDICT THE TENSILE BEHAVIOUR OF FRC.....	145
7.3.1.	Failure mechanism of the Barcelona test.....	145
7.3.2.	Formulation to estimate the stress (σ).....	145
7.3.3.	Formulation to estimate the strain (ϵ)	148
7.3.4.	Values of failure angle (β) and friction coefficient (μ).....	150
7.4.	PREDICTION OF THE TENSILE STRENGTH.....	151
7.5.	SIMPLIFIED MODEL	153
7.6.	EXPERIMENTAL PROGRAM.....	156
7.6.1.	Specimens.....	156
7.6.2.	Materials and concrete mix	156
7.6.3.	Results.....	158
7.7.	FIT BETWEEN SIMPLIFIED AND COMPLETE MODELS.....	159
7.8.	NUMERICAL VALIDATION	160
7.8.1.	Model type.....	160
7.8.2.	Geometry and boundary conditions	161
7.8.3.	Material properties	162
7.8.4.	Results.....	163
7.9.	COMPARATIVE ANALYSIS WITH THE MODELS IN EUROPEAN CODES	166
7.9.1.	Steel fibres.....	166
7.9.2.	Plastic fibres	168
7.10.	CONCLUDING REMARKS.....	170

PART V: LONG-TERM BEHAVIOUR OF SFRC

8. POST-CRACKING CREEP BEHAVIOUR OF SFRC.....	173
8.1. INTRODUCTION	173
8.1.1. Objectives	174
8.1.2. Outline of the chapter.....	174
8.2. EXPERIMENTAL PROGRAM.....	174
8.2.1. Specimens and research parameters	174
8.2.2. Materials and concrete mix	175
8.2.3. Preparation and pre-cracking of the beams.....	177
8.2.4. Long-term test	179
8.2.5. Failure test and loading history.....	187
8.3. RESULTS OF THE LONG-TERM TEST	187
8.3.1. Evolution of the crack width	187
8.3.2. Evolution of the deflection.....	193
8.3.3. Evolution of the creep coefficient	194
8.4. RESULTS OF THE FAILURE TEST.....	197
8.5. PREDICTION OF THE CREEP COEFFICIENT.....	198
8.5.1. Formulation in the EHE-08.....	198
8.5.2. Formulation in the Model Code 2010	199
8.5.3. Results.....	200
8.6. CREEP MODEL	202
8.7. CONCLUDING REMARKS.....	205

PART VI: CONCLUDING REMARKS

9. CONCLUSIONS AND FUTURE PERSPECTIVES	207
9.1. GENERAL CONCLUSIONS.....	207
9.2. SPECIFIC CONCLUSIONS	208
9.3. FUTURE PERSPECTIVES.....	213
REFERENCES.....	215
ANNEX 1. MULTIDIRECTIONAL TEST.....	229
APPENDIX 1. NEOPRENE COMPRESSION TEST.....	239
PUBLICATIONS.....	241

LIST OF FIGURES

Figure 1.1 Traditional applications of SFRC: industrial pavements (BEKAERT), roads and other pavements, sprayed concrete (Serna et al. 2009) and precast segments.	2
Figure 1.2 Subjects covered in the doctoral thesis and other subjects that require further study.....	3
Figure 1.3 Outline of the thesis.....	6
Figure 1.4 Outline of Part III of the thesis.....	7
Figure 2.1 Constitutive models proposed by the DBV.....	12
Figure 2.2 a) σ - ϵ distribution in cross section and σ - ϵ diagram and b) size factors in DBV and RILEM.....	13
Figure 2.3 Linear post-cracking model and rigid-plastic model in CNR-DT 204 (CNR 2006).	14
Figure 2.4 Simplified σ - w diagrams: a) rigid-plastic and b) linear post-cracking.....	15
Figure 2.5 Definition of the parameter γ for a) RC section and b) plain concrete section.....	16
Figure 2.6 Coefficient of variation in the bending tests and panel tests (Parmentier et al. 2008).	19
Figure 2.7 a) Barcelona test setup and b) top surface of a specimen after the test.....	20
Figure 2.8 Main stages of the production process that affect fibre orientation.....	21
Figure 2.9 Influence of boundary conditions in fibre orientation.....	21
Figure 2.10 Mechanisms of flow-induced in a) a free surface flow and b) a confined flow.	22
Figure 2.11 Types of water in the hydrated cement paste (Mehta and Monteiro 2006).	25
Figure 2.12 a) Total strain of concrete with time and b) general form of ϵ - t curve for materials subjected to creep (Neville et al. 1983).....	26
Figure 3.1 Traditional reinforcement of the beams.	33
Figure 3.2 Details of a) the loading system and b) the joints in the supports.....	35
Figure 3.3 Isostatic setup of the test and dimensions.	36
Figure 3.4 Location of the fix points in both sides of the beam.....	36
Figure 3.5 a) Detail of the fixed points and b) Digital extensometer.....	37
Figure 3.6 Crack patterns.....	38
Figure 3.7 Load-crack width curves up to 0.40 mm.....	40
Figure 3.8 Load-crack width for fibre contents of a) 0.25% and b) 0.50% in volume.	42
Figure 3.9 Load increase [%]-crack width curve.....	43
Figure 3.10 Stress profile of a SFRC section at different stages: a) linear-elastic behaviour; b), c) and d) post-cracking behaviour at different stress levels.....	43
Figure 3.11 Load-deflection curves up to 5 mm for a) 0.25% and b) 0.50% in volume.....	44
Figure 3.12 Load-deflection curves for a) 0.25% and b) 0.50% in volume.....	45
Figure 3.13 a) Sectional discretization and b) constitutive equations to simulate the stress-strain behaviour of the FRC (de la Fuente 2012b).....	47

Figure 3.14 a) Discretization of the element and b) generic M- χ diagram (Blanco et al. 2013).....	49
Figure 3.15 Failure mechanism of a) 4-point bending test (unnotched specimen) and b) 3-point bending test (notched specimen).....	50
Figure 3.16 a) MC2010 and b) assumption made for this study for the case of SF2 0.25 % _A	52
Figure 3.17 a) Variations in the concrete cover for the element SF2 0.50% _B and b) decrease of the bending moment due to the variation of the concrete cover.....	52
Figure 3.18 a) Multilinear model and b) bilinear model.....	53
Figure 3.19 a) Experimental and prediction P- δ curves for slab RC_ _A and b) load values for deflections of 6 mm, 15 mm and 45 mm.....	55
Figure 3.20 Trilinear diagrams and P- δ curves for a-b) SF80/60_20 and c-d) SF80/60_40; Bilinear diagrams and P- δ curves for e-f) SF80/60_20 and g-h) SF80/60_40.....	56
Figure 4.1 Outline of Part III of the thesis, emphasizing the current chapter.....	60
Figure 4.2 Transport of slabs L to the Laboratory of Structure Technology Luis Agulló.....	62
Figure 4.3 Slump flow test: a) equipment and b) spread concrete after the test.....	63
Figure 4.4 a) Concrete pouring in the centre of the slab and b) flow of concrete to the edges.....	64
Figure 4.5 Setup for slab a) S, b) M, c) L and d) detail of the loading point.....	66
Figure 4.6 a) Detail of the supports and b) deflection measuring system.....	67
Figure 4.7 Evolution of cracking during the test of slab M_ _B	68
Figure 4.8 Crack patterns of slabs a) S_ _A ; b) S_ _B ; c) M_ _A ; d) M_ _B ; e) L_ _A and f) L_ _B	69
Figure 4.9 Detailed crack patterns of slabs a) S_ _A ; b) S_ _B ; c) M_ _A ; d) M_ _B ; e) L_ _A and f) L_ _B	70
Figure 4.10 Detail of cracking a) at the centre of slab L_ _A and b) near the edges of slab L_ _B	71
Figure 4.11 a) Measured and estimated deflections in the centre of slab L_ _A for a load of 272.4 kN and b) location of the displacement transducers.....	72
Figure 4.12 Load-deflection curves and maximum loads with corresponding deflection.....	73
Figure 4.13 Load-rotation angle curves and maximum loads.....	76
Figure 4.14 Energy absorption and load-rotation angle curves for slabs a) S_ _A , b) S_ _B , c) M_ _A , d) M_ _B , e) L_ _A and f) L_ _B	77
Figure 4.15 Evolution of the energy absorption capacity with the rotation angle.....	78
Figure 5.1 Location map of the cores in slab S_ _B	83
Figure 5.2 a) Slab with the core location marks before drilling and b) detail of the core drilling.....	83
Figure 5.3 Detail of a) cylindrical cores, b) cuts in cylindrical core and c) cuts in prismatic specimens.....	84
Figure 5.4 Equipment of the inductive method: a) coil and b) impedance analyser.....	85
Figure 5.5 a) Multidirectional method setup and b) cubic specimen after the test.....	86
Figure 5.6 Fibre content in the cubic specimens, average content in the slabs and standard deviation.....	86

Figure 5.7 Fibre orientation in specimens of slab S_B.....	88
Figure 5.8 Distribution of specimens in slab S_B.....	88
Figure 5.9 Alignment of fibres along X and Y axes for series a) 1-3 and b) 4-7 in slab S_B.....	89
Figure 5.10 Fibre orientation in specimens of slab M_A.....	89
Figure 5.11 Distribution of specimens in slab M_A.....	90
Figure 5.12 Alignment of fibres along X and Y axes for series a) 1-3 and b) 4-5 in slab M_A.....	90
Figure 5.13 Fibre orientation in specimens of slab M_B.....	91
Figure 5.14 Distribution of specimens in slab M_B.....	92
Figure 5.15 Alignment of fibres along X and Y axes for series a) 1-3 and b) 4-6 in slab M_B.....	92
Figure 5.16 Fibre orientation in specimens of slab L_A.....	93
Figure 5.17 Distribution of specimens in slab L_A.....	93
Figure 5.18 Alignment of fibres along X and Y axes for series a) 1-3 and b) 4- 6 in slab L_A.....	94
Figure 5.19 Fibre orientation in specimens of slab L_B.....	95
Figure 5.20 Distribution of specimens in slab L_B.....	95
Figure 5.21 Alignment of fibres along X and Y axes for series a) 1- 4 and b) 5-8 in slab L_B.....	96
Figure 5.22 Rotation of fibres while moving from the centre of the slabs to the edges.....	97
Figure 5.23 Division of slabs in zones depending on fibre orientation.....	97
Figure 5.24 a) Results from multidirectional method and b) transformed curves for the analysis...	99
Figure 6.1 Geometry of the model of slab S.....	107
Figure 6.2 Detail of the geometry of model of slab S: neoprene 2 and neoprene 3.....	108
Figure 6.3 . Stress-strain (σ - ϵ) curve used to model a) the SFRC and b) the neoprene.....	109
Figure 6.4 Real and predicted crack patterns: a) slab S_A; b) prediction for slab S; c) slab M_A; d) prediction for slab M; e) slab L_A and f) prediction for slab L.....	112
Figure 6.5 Experimental P- δ curves and simulation provided by ATENA with the RILEM and the EHE diagrams for slabs a) S, b) M and c) L.....	113
Figure 6.6 Trilinear diagram for SFRC and parameters considered in the preliminary study.....	115
Figure 6.7 Influence of the parameters a) σ_2 , b) σ_3 , c) ϵ_2 and d) ϵ_3	116
Figure 6.8 Influence of σ_2 in the P- δ curves for slabs a) S, b) M and c) L.....	118
Figure 6.9 Influence of σ_2 in the maximum load for slabs a) S, b) M and c) L.....	119
Figure 6.10 Influence of σ_2 in the slope E4 for slabs a) S, b) M and c) L.....	120
Figure 6.11 Influence of σ_2 in the energy absorption for slabs a) S, b) M and c) L.....	121
Figure 6.12 Influence of σ_3 in the P- δ curves for slabs a) S, b) M and c) L.....	122
Figure 6.13 Influence of σ_3 in the maximum load for slabs a) S, b) M and c) L.....	123
Figure 6.14 Influence of σ_3 in the slope E4 for slabs a) S, b) M and c) L.....	124
Figure 6.15 Influence of σ_3 in the energy absorption for slabs a) S, b) M and c) L.....	125

Figure 6.16 Influence of ε_2 in the P- δ curves ($\sigma_2=0.70\sigma_1$ and $\sigma_3=0.95\sigma_2$) for: a) S, b) M and c) L...	126
Figure 6.17 Influence of ε_2 in the maximum load for slabs a) S, b) M and c) L	127
Figure 6.18 Influence of ε_2 in the slope E4 for slabs a) S, b) M and c) L.....	128
Figure 6.19 Influence of ε_2 in the energy absorption for slabs a) S, b) M and c) L.....	129
Figure 6.20 P- δ curves resulting from the numerical fit of the parameters for slabs a) S, b) M and c) L.....	130
Figure 6.21 Constitutive models from RILEM, EHE and from the numerical fit of the parameters for slabs a) S, b) M and c) L	133
Figure 6.22 Fibre orientation in a) a smaller rectangular slab and b) a larger square slab.....	134
Figure 6.23 Evolution of the values of $\eta_{f\sigma 2}$ and $\eta_{f\sigma 3}$ with the b/a ratio of the slab.....	136
Figure 6.24 Method developed to obtain σ - ε diagrams for the design of SFRC slabs.....	137
Figure 6.25 Evolution of the values of $\xi_{\sigma 2}$ and $\xi_{\sigma 3}$ with the b/a ratio of the slab.....	138
Figure 7.1 Barcelona test specimen after cracking (frontal and top view).	145
Figure 7.2 Detail of a) interplay of forces and b) balance of forces at the conical wedge.....	146
Figure 7.3 Detail of a) interplay of forces and b) balance of forces at the conical wedge.....	147
Figure 7.4 Infinitesimal slice of a concrete segment.....	147
Figure 7.5 a) Lateral displacement of concrete segment and b) infinitesimal section of segment..	148
Figure 7.6 Circumferential deformation of the specimen.....	149
Figure 7.7 a) Opening of the specimen and b) measurements of the length of the conical wedge...150	
Figure 7.8 Simplified σ - ε diagram.	154
Figure 7.9 Vibration of the specimens: a) cylinders and c) beams.....	158
Figure 7.10 Results of series A40: a) Barcelona test and b) flexural test (EN14651:2005).....	159
Figure 7.11 Comparison of the σ - ε model with the simplified version for a) A40_C6, b) A60_C2, c) B30_C5, d) B50_C2, e) C5_C1 and f) C7_C2.	160
Figure.12 a) Specimen of the Barcelona test, b) half of the specimen modelled with FEM, c) definition of the conical wedge in the model and d) detail of the conical wedge.	161
Figure 7.13 . Stress-strain (σ - ε) curve to model the FRC.....	162
Figure 7.14 Experimental and numerical P- δ curves for: a) A40_C5, b) A40_C6, c) A60_C1, d) A60_C2, e) B30_C5, f) B30_C8, g) B50_C2, h) B50_C8, i) C5_C2, j) C5_C5, k) C7_C2 and l) C7_C5.....	164
Figure 7.15 Comparison of the formulation based on the Barcelona test with the constitutive models based on beam tests for the series with SF: a) A40, b) A60, c) B30 and d) B50.	167
Figure 7.16 Comparison of the formulation based on the Barcelona test with the constitutive models based on beam tests for the series with PF: a) C5 and b) C7.....	169
Figure 8.1 a) Pre-cracking test and b) beams with LVDT transducer for long-term test.....	178
Figure 8.2 a) Device to measure deflection and b) detail of the LVDT transducer.	178
Figure 8.3 Side view of the frame for the creep test.....	180

Figure 8.4 Preparation of the test before loading.	181
Figure 8.5 Location of the beams in the frames.	182
Figure 8.6 Long-term test in a) ambient conditions and b) climate-controlled room conditions....	183
Figure 8.7 Evolution of a) humidity and b) temperature in stage 1 (ambient conditions).....	183
Figure 8.8 Evolution of a) humidity and b) temperature in stage 2 (controlled conditions).	184
Figure 8.9 Average humidity and temperature in a) stage 1 and b) stage 2.....	185
Figure 8.10 Variation of the load during a) stage 1 and b) stage 2.	186
Figure 8.11 Loading history of a beam.....	187
Figure 8.12 Definition of initial crack width, crack width due to creep and total crack width.....	188
Figure 8.13 Initial crack width as a function of a) w_p and b) the load level.	189
Figure 8.14 Crack width due to creep for S1 - a) $w_p=0.25$ mm, b) $w_p=1.50$ mm and $w_p=2.50$ mm - and for S2 - c) $w_p \approx 0.34$ mm, d) $w_p=1.58$ mm and $w_p \approx 2.80$ mm -	190
Figure 8.15 Evolution of w_c^j for S1 - a) $w_p=0.25$ mm, b) $w_p=1.50$ mm and $w_p=2.50$ mm -	191
Figure 8.16 Crack width due to creep at 90 days as a function of a) w_p and b) the load level.....	192
Figure 8.17 Evolution of the rate of w_c^j with time.....	193
Figure 8.18 a) Deflection due to creep in beam S2_2.83_47.5% and b) relation between the crack width and the deflection due to creep in beam S2_2.83_47.5%.....	194
Figure 8.19 Creep coefficient for S1 - a) $w_p=0.25$ mm, b) $w_p=1.50$ mm and $w_p=2.50$ mm - and for S2 - c) $w_p \approx 0.34$ mm, d) $w_p=1.58$ mm and $w_p \approx 2.80$ mm -	195
Figure 8.20 Creep coefficient for S1 -a) $w_p=0.25$ mm, b) $w_p=1.50$ mm and $w_p=2.50$ mm - and for S2: c) $w_p \approx 0.34$ mm, d) $w_p=1.58$ mm and $w_p \approx 2.80$ mm -	196
Figure 8.21 Failure tests of beams of series a) S1 and b) S2.....	197
Figure 8.22 Evolution with time of the experimental and predicted creep coefficients for S2.....	201
Figure 8.23 a) Four-element viscoelastic model of creep in Findley et al. (1979) and b) simplified version of two-element viscoelastic model of creep.....	202
Figure 8.24 Experimental and predicted evolution of ϕ_w for beams of series S2.....	204

LIST OF TABLES

Table 1.1 Specific objectives.....	6
Table 2.1 Constitutive models in European codes and guidelines (Blanco et al. 2013).....	11
Table 2.2 Summary of the characteristics of the constitutive models (Blanco et al. 2013).....	12
Table 2.3 Main test methods for the characterization of the post-cracking behaviour of FRC.....	18
Table 2.4 Methods to determine fibre orientation.....	24
Table 2.5 Studies on the flexural creep post-cracking behaviour of FRC beams.....	29
Table 3.1 Characteristics of the fibres (provided by the manufacturer).....	33
Table 3.2 Series of casting and notation.....	34
Table 3.3 Compressive and residual flexural strengths at 28 days.....	34
Table 3.4 Average crack number and spacing and predicted crack spacing.....	39
Table 3.5 Crack width values for 40 kN and 80 kN and prediction with RILEM formulation.....	41
Table 3.6 Crack width values for different load levels: 150 kN and 200 kN.	42
Table 3.7 Slope of load-deflection curves for each of the aforementioned stages (in kN/mm).....	45
Table 3.8 Average absorbed energy up to a deflection of 40 mm.....	46
Table 3.9 Parameters of the constitutive models for SF2 0.25%_A and SF2 0.50%_B.....	53
Table 3.10 Load values for displacements of 6 mm, 15 mm and 45 mm (in kN) for SF2 0.50%_B....	57
Table 4.1 Dimensions of the slabs.....	61
Table 4.2 Concrete mix.....	62
Table 4.3 Characteristics of the fibres (provided by the manufacturer).....	63
Table 4.4 Date of production of the elements.....	63
Table 4.5 Results of the slump flow test for B1 and B2.....	64
Table 4.6 Modulus of elasticity, compressive strength and residual flexural strengths at 28 days..	65
Table 4.7 Load values for deflections of 1 mm, 5 mm, 10 mm, 20 mm and 40 mm.....	74
Table 4.8 Slopes in different stretches of the load-deflection curves.....	75
Table 4.9 Energy absorption at a given rotation angle.....	78
Table 5.1 Number of cores drilled from each slab.....	84
Table 5.2 Residual load and normalized residual load for slab S_B.....	100
Table 5.3 Residual load and normalized residual load for slab M_A.....	100
Table 5.4 Residual load and normalized residual load for slab M_B.....	101
Table 5.5 Residual load and normalized residual load for slab L_A.....	102
Table 5.6 Residual load and normalized residual load for slab L_B.....	102
Table 6.1 Dimensions of the elements in the model.....	108
Table 6.2 Material properties considered in the FEM model.....	110

Table 6.3 Data and results from the mesh size study.....	111
Table 6.4 Results of the prediction with the RILEM and the EHE and average results of slabs S, M and L.....	114
Table 6.5 Values of σ_1 , ε_1 and ε_3 for slabs S, M and L.....	117
Table 6.6 Variables of the parametric study for slabs S, M and L.....	117
Table 6.7 Slope of the tendencies in Figure 6.9.....	119
Table 6.8 Slope of the tendencies in Figure 6.11.....	121
Table 6.9 Slope of the tendencies in Figure 6.13.....	123
Table 6.10 Slope of the tendencies in Figure 6.15.....	125
Table 6.11 Slope of the tendencies in Figure 6.17.....	127
Table 6.12 Slope of the tendencies in Figure 6.19.....	129
Table 6.13 Values of the parameters σ_2 , σ_3 and ε_2 for slabs S, M and L.....	130
Table 6.14 Average experimental results and results of the numerical fit.....	131
Table 6.15 Average results of slabs S, M and L and results of the prediction of the RILEM and the EHE.....	132
Table 6.16 Fibre network effect factors for the slabs S, M and L.....	135
Table 6.17 Base factors associated with the reference slab.....	137
Table 7.1 Analytical expressions for the tensile strength.....	143
Table 7.2 Summary of the hypothesis assumed.....	144
Table 7.3 Friction coefficient for plain concrete according to the MC2010.....	151
Table 7.4 Main data from the study of Guàrdia (2008).....	152
Table 7.5 Main parameters defining the expressions for tensile strength.....	152
Table 7.6 Comparison of the tensile strength estimated by the expressions in the literature.....	153
Table 7.7 Summary of the parameters defining the simplified σ - ε diagram.....	155
Table 7.8 Series of FRC beams and cylinders.....	156
Table 7.9 Concrete mix.....	157
Table 7.10 Characteristics of the fibres (provided by the manufacturer).....	157
Table 7.11 Compressive strength and modulus of elasticity at 28 days.....	158
Table 7.12 Main results of the Barcelona test and the flexural test for series A40 and A60.....	159
Table 7.13 Material properties considered in the FEM model.....	163
Table 7.14 Differences between experimental and predicted load values for displacements of 1.0 mm, 3.0 mm and 5.0 mm.....	165
Table 7.15 Parameters defining the constitutive models of series A40, A60, B30 and B50.....	166
Table 7.16 Parameters defining the constitutive models of series C5 and C7.....	169
Table 8.1 Research parameters.....	175

Table 8.2 Concrete mix.....	175
Table 8.3 Characteristics of the fibres used (provided by the manufacturer).....	176
Table 8.4 Modulus of elasticity, compressive and residual flexural strengths at 28 days.....	176
Table 8.5 Activities for the preparation of the beams.....	177
Table 8.6 Main data of the pre-cracking of the beams.....	179
Table 8.7 Main data of the beams.....	182
Table 8.8 Maximum, minimum and average data of humidity and temperature in stage 1.....	184
Table 8.9 Maximum, minimum and average data of humidity and temperature in stage 2.....	184
Table 8.10 Significant dates of the long-term test.....	186
Table 8.11 Initial crack width.....	188
Table 8.12 Crack width due to creep at 30, 90 and 150 days.....	191
Table 8.13 Initial deflection, deflection due to creep and total deflection at 150 days.....	193
Table 8.14 Creep coefficient at 30, 90 and 150 days.....	196
Table 8.15 Experimental and predicted creep coefficients at 30, 90 and 150 days.....	201
Table 8.16 Experimental and predicted creep coefficient at 30, 90 and 150 days.....	204

SYMBOLS

α_c^f	Coefficient for long-term strength behaviour
α_{fcm}	Factor considering the strength of concrete according to Model Code 2010
α_{sys}	Coefficient for size effect according to the DBV
α_1	Factor considering the strength of concrete according to EHE-08
α_2	Factor considering the strength of concrete according to EHE-08
α_3	Factor considering the strength of concrete according to EHE-08
β	Failure angle of concrete
$\beta(f_{cm})$	Factor considering the strength of concrete in the basic creep coefficient according to EHE-08
$\beta(RH)$	Factor considering the relative humidity according to Model Code 2010
$\beta(t_0)$	Factor considering the age of concrete at the time of loading in the basic creep coefficient according to EHE-08
$\beta_{bc}(f_{cm})$	Factor considering the strength of concrete in the basic creep according to Model Code 2010
$\beta_{dc}(f_{cm})$	Factor considering the strength of concrete in the drying creep according to Model Code 2010
$\beta_c(t-t_0)$	Function that describes the development of creep with time according to EHE-08
$\gamma(t_0)$	Factor considering the age of concrete at the time of loading according to Model Code 2010
γ_{ct}^f	Safety factor according to DBV
γ_F	Partial safety factor according to Model Code 2010
δ	Deflection
δ_L	Lateral displacement
δ^j	Deflection due to creep at a time j
δ_i	Initial deflection
δ_p	Pre-cracking deflection
δ_P	Displacement caused by the plate in the Barcelona test
δ_{pr}	Residual pre-cracking deflection
δ^j	Total deflection at a time j
ε	Strain
ε_c	Strain of concrete
ε_s	Strain of steel
ε_u	Ultimate strain of concrete
ε_{Fu}	Ultimate strain of concrete according to Model Code 2010
ε_{SLS}	Strain associated with f_{Fts}
ε_{SLU}	Strain associated with f_{Ftu}
ε_T	Total strain
ε_0	Strain of a reference layer of the section

ε_1	Strain associated to the tensile strength σ_1 ; Strain of a spring element
ε_2	Strain associated to σ_2 ; Strain of a dashpot element
ε_3	Ultimate strain in a trilinear σ - ε diagram (strain associated to σ_3)
η	Damping coefficient
$\eta_{f\sigma 2}$	Fibre network effect factor associated with σ_2
$\eta_{f\sigma 3}$	Fibre network effect factor associated with σ_3
θ	Angle; rotation angle
κ_v	Coefficient to consider the coefficient of variation
κ_h	Size factor
λ	Empirical constant dependant of the material in the formulaton by Marti (1989)
μ_k	Kinetic friction coefficient of concrete
μ_s	Static friction coefficient of concrete
$\xi_{B\sigma 2}$	Base factor associated with σ_2
$\xi_{B\sigma 3}$	Base factor associated with σ_3
$\xi_{\sigma 2}$	Geometry factor associated with σ_2
$\xi_{\sigma 3}$	Geometry factor associated with σ_3
σ	Stress; Standard deviation
σ_c	Stress of concrete
σ_p	Pre-cracking stress
σ_s	Stress of steel
$\sigma_{0.5mm}$	Stress for a crack width of 0.5 mm
σ_1	Tensile strength in a trilinear σ - ε diagram
σ_2	Stress defining the second point of a trilinear σ - ε diagram
σ_3	Stress defining the third point of a trilinear σ - ε diagram (associated to the ultimate strain)
τ	Work
φ	Internal friction angle of concrete
$\varphi(t, t_0)$	Creep coefficient
φ_ε	Creep coefficient in terms of strain
φ_{bc}	Basic creep coefficient
φ_{dc}	Drying creep coefficient
φ_{HR}	Coefficient that considers the influence of the relative humidity
φ_w^j	Creep coefficient in terms of crack width at a time j
φ_0	Basic creep coefficient according to EHE-08
χ	Curvature of the section
ϕ	Diameter of steel rebar

$\Delta\delta$	Increment of deflection
ΔP	Increment of load
ΔM	Increment of bending moment
$\Delta\varphi$	Increment of rotation
a	Length of the slab
b	Width
c_{ref}	Concrete cover of reference
d	Effective depth of the section; Diameter
d'	Diameter of the plate in the Barcelona test
d_a	Maximum aggregate size
f_c	Compressive strength of concrete
f_{ck}	Characteristic compressive strength of concrete
f_{cm}	Average compressive strength of concrete
f_{ct}	Tensile strength of concrete
f_{ctd}	Design tensile strength of concrete
$f_{ctk,fl}$	Characteristic value of the flexural tensile strength of concrete
$f_{ctm,fl}$	Average flexural tensile strength of concrete
$f_{ctR,d}$	Design residual tensile strength of concrete
$f_{ctR1,d}$	Design residual tensile strength of concrete associated with f_{R1}
$f_{ctR3,d}$	Design residual tensile strength of concrete associated with f_{R3}
f_{eq}	Equivalent flexural tensile strength of concrete
f_{eq1}	Post-cracking equivalent strength of concrete for serviceability limit state
f_{eq2}	Post-cracking equivalent strength of concrete for ultimate limit state
$f_{eq,ctd,I}$	Design value of the equivalent tensile strength of concrete at deformation area I
$f_{eq,ctd,II}$	Design value of the equivalent tensile strength of concrete at deformation area II
$f_{eq,ctk,I}$	Characteristic value of the equivalent tensile strength of concrete at deformation area I
$f_{eq,ctk,II}$	Characteristic value of the equivalent tensile strength of concrete at deformation area II
f_{Fts}	Characteristic value of the tensile strength of concrete for serviceability limit state
f_{Ftu}	Characteristic value of the tensile strength of concrete for ultimate limit state
f_L	Limit of proportionality of concrete
f_R	Residual flexural tensile strength of concrete
f_{R1}	Residual flexural tensile strength of concrete for a CMOD of 0.5 mm
f_{R2}	Residual flexural tensile strength of concrete for a CMOD of 1.5 mm
f_{R3}	Residual flexural tensile strength of concrete for a CMOD of 2.5 mm
f_{R4}	Residual flexural tensile strength of concrete for a CMOD of 3.5 mm
$f_{R1,d}$	Design residual flexural tensile strength of concrete for a CMOD of 0.5 mm

$f_{R3,d}$	Design residual flexural tensile strength of concrete for a CMOD of 2.5 mm
f_y	Tensile strength of steel
h	Height of the section; Height of the specimen of the Barcelona test
h_{sp}	Distance between the notch tip and the top of the specimen
k	Coefficient for the type of stresses in the cross-section according to CNR-DT 204
k_1	Coefficient for the type of stresses in the cross-section according to EHE-08
l	Length of the conical wedge; Span
l_{cs}	Characteristic length
n	Number of cracks
s_{rm}	Average crack spacing
t	Time
t_0	Time of loading
x	Depth of the neutral axis
y	Height of the neutral axis
y_c	Height of the centre of mass of concrete
y_G	Height of the centre of mass
y_s	Height of the centre of mass of steel
w	Crack width
w_c^j	Crack width due to creep at a time j
w_{EN}	Average crack width in the flexural test according to EN14651:2005
w_{DIN}	Average crack width in the flexural test according to DIN1048
w_i	Initial crack width
w_p	Pre-cracking width
w_{pr}	Residual pre-cracking width
w_t^j	Total crack width at a time j
w_u	Ultimate crack width
w_{15}	Crack width measured 15 mm above the bottom surface
w_{i2}	Average crack width at the endpoint of the interval where f_{eq2} is evaluated
A	Area; Function considering the initial crack width and the load level
A_c	Area of concrete
A_s	Area of steel
B	Function considering the initial crack width and the load level
D_f	Diameter of flow spread in the slump flow test
E	Modulus of elasticity
E_c	Modulus of elasticity of concrete
E_{cm}	Average modulus of elasticity of concrete

$E1$	Slope of the P - δ curve in the stretch up to 40% of the maximum load
$E2$	Slope of the P - δ curve in the stretch between 50% and 80% of the maximum load
$E3$	Slope of the P - δ curve in the stretch between 90% and 99% of the maximum load
$E4$	Slope of the P - δ curve in the final stretch, after the maximum load
F_c	Average load applied during the long-term test
F_L	Force associated with the limit of proportionality
F_p	Force associated with w_p
F_P	Force applied by the plate in the Barcelona test
F_{Pmax}	Maximum force applied by the plate in the Barcelona test
$F_{P0.02mm}$	Force applied by the plate in the Barcelona test for a displacement of 0.02 mm
$F_{P0.75mm}$	Force applied by the plate in the Barcelona test for a displacement of 0.75 mm
$F_{P4.00mm}$	Force applied by the plate in the Barcelona test for a displacement of 4.00 mm
F_{fr}	Friction force
F_N	Normal force
F_R	Radial force
K	Orientation factor
K_f	Bending stiffness
L	Length
M	Bending moment
M_p	Pre-cracking moment
M_{ref}	Bending moment of reference
M_u	Ultimate bending moment
$M_{w=0.2 mm}$	Bending moment at a crack width of 0.2 mm
N	Axial force
P	Load
P_p	Pre-cracking load
R	Radius; Resistant parameter or spring constant
T_{50}	Time taken by the mixture to reach the 500 mm mark in the slump flow test

1. INTRODUCTION

1.1. SCOPE OF THE RESEARCH

Fibre reinforced concrete (FRC) has arisen as an alternative to traditional reinforcement in concrete with the same philosophy of bearing the tensile stresses and providing ductility to structures. The use of fibres to enhance the properties of brittle materials is not a novel idea. In fact, the ancient Egyptians already used fibrous elements such as straws or horsehair to reinforce mud bricks. The first studies on steel fibre reinforced concrete (SFRC) date from the 1960s. Since then significant research was carried out to reach deeper understanding on mechanical properties of the material.

Recent investigations led to the development of other types of FRC such as: high performance fibre reinforced concrete (HPFRC) characterized by multiple cracks and an increase of the strength after cracking (Walraven 2009); self-compacting fibre reinforced concrete (SCFRC) that combines the advantages of self-compacting concrete in the fresh state and the enhanced post-cracking performance of FRC (Grünewald 2004); or hybrid fibre reinforced concrete (HyFRC) characterized by the use of short straight fibres and long deformed fibres (Vandewalle 2006).

The fact that fibres are discrete and randomly distributed in the concrete mix leads to a 3-dimensional reinforcing mechanism different from that of conventional reinforced

concrete (RC). While steel rebars in RC are efficiently placed in the section with regard to the cracking plane, the fibres work, usually with less efficiency than RC. Nonetheless, this sort of 3-dimensional reinforcement provides an enhanced crack-bridging capacity, increasing concrete toughness and durability, which can be very convenient for certain applications such as tunnel linings.

In 2002, yearly worldwide production of fibres was estimated at 300,000 tons per year (Li 2002) with a growth rate of 20% in North America. However, the use of FRC remained a small fraction of the total consumption of concrete in the construction industry. The lack of international codes and guidelines for the design hindered FRC expansion as a competitive structural solution and its use was limited to improve cracking control without considering the fibre contribution to the bearing capacity. In Spain, the amount of steel fibres used in tunnels and pavements was estimated at 38,000 tons approximately (Serna *et al.* 2009). This amount was distributed among the traditional applications as depicted in Figure 1.1b. (see Figure 1.1a)

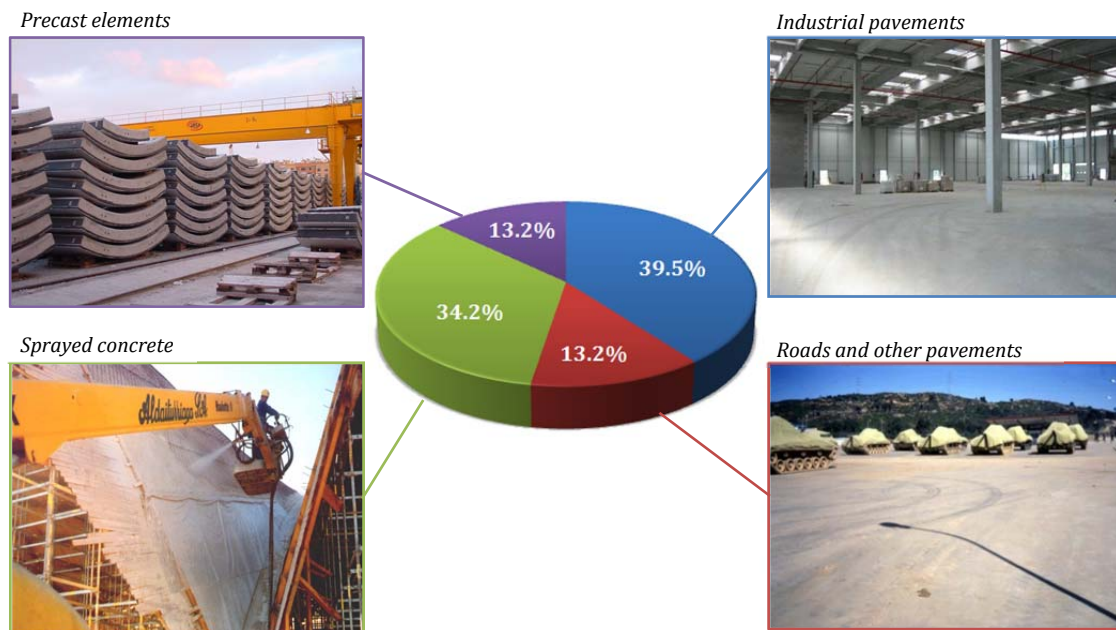


Figure 1.1 Traditional applications of SFRC: industrial pavements (BEKAERT), roads and other pavements, sprayed concrete (Serna *et al.* 2009) and precast segments.

The turning point regarding the incorporation of steel fibres as a reinforcing material in Europe occurred with the publication of design codes and recommendations (di Prisco *et al.* 2009), which provided the tools for the design of FRC structures. In this sense, it is worthwhile mentioning, in order of publication, the German guidelines (DBV 2001), the RILEM TC 162-TDF recommendations (Vandewalle *et al.* 2003), the Italian guidelines CNR-DT 204 (CNR 2006), the Spanish code EHE-08 (CPH 2008) and the Model Code 2010 (*fib* 2010). Since then, an increasing interest has grown among civil engineers regarding the use of fibres with bearing capacity in, for example, tunnel linings (Plizzari and Tiberti 2006; Cavalaro 2009; Chiaia *et al.* 2009b; de la Fuente *et al.* 2012b), pipes

(Figueiredo 2008; de la Fuente *et al.* 2012a) or slabs (Destrée and Mandl 2008; Maya *et al.* 2012; Michels *et al.* 2012).

Despite the remarkable advances in the steel fibre reinforcement technology and its increasing use in several applications, questions continue to arise regarding the performance of the material. In fact, there are several subjects that need to be addressed to ultimately propose an accurate and efficient design procedure. Some of these subjects were identified by the FRC research group at the Universitat Politècnica de Catalunya (UPC), responsible for coordinating the recommendations for FRC in the Spanish code published in 2008. In this context and given that the doctoral thesis represents the continuation of a research line that started with an undergrad thesis, a generalist study is herein proposed covering the subjects highlighted in green in Figure 1.2. Notice that most of them focus on concrete with steel fibres.

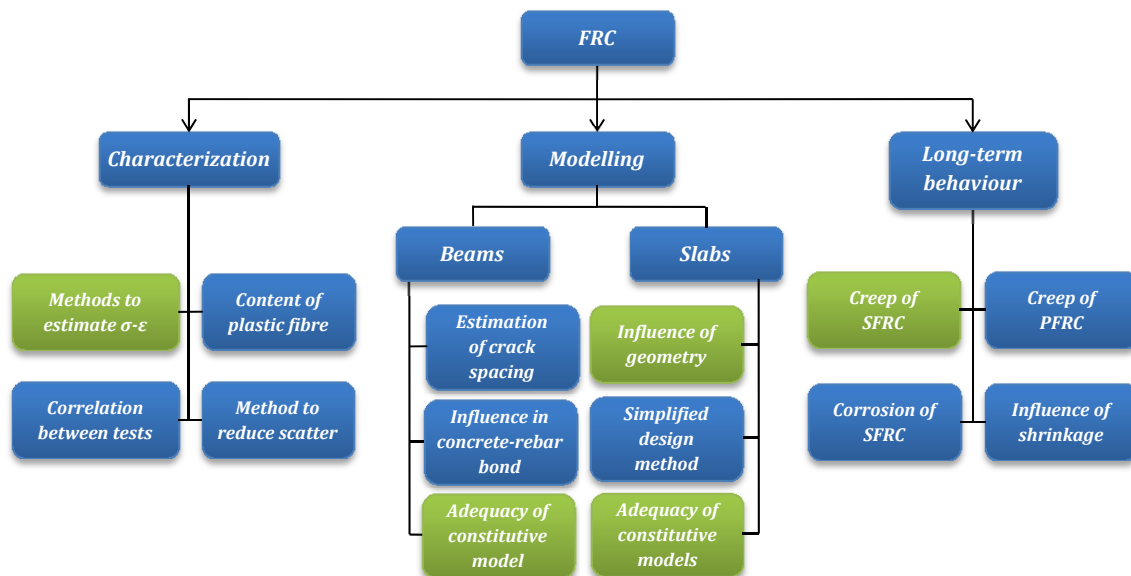


Figure 1.2 Subjects covered in the doctoral thesis and other subjects that require further study.

One subject that remains a matter of discussion in the scope of the design FRC structures is the identification of the most suitable constitutive model to reproduce the behaviour of the material when it is subjected to tension. After numerous proposals in the literature and in the European codes and guidelines, there is no constitutive model broadly accepted. This situation reveals the need to study which model is the most accurate in the prediction of the response of FRC.

Likewise, the representativeness of the test methods for the characterization of the material is equally important in the design. The current design procedures are based on the bending test of small beams (or beam test), which are known to exhibit significant scatter and may not be geometrically representative of structures other than beams. In fact, the structural response and the fibre orientation in small beams differ considerably

from slabs, an application in which steel fibres are increasingly used as the only reinforcement.

In this regard, it would be of great interest to study the capacity of the existing constitutive models to predict the behaviour of both typologies of structures: beams and slabs. Considering the abovementioned, it could be expected that the existing models would be more adequate to simulate the performance of beams rather than slabs. In such case, the lack of representativeness of the beam test regarding slabs or other type of structures should be taken into account. The concern regarding appropriate constitutive models and test methods stems from the aim to design efficient FRC structures.

A property that has a direct effect on the efficiency of FRC is fibre orientation, since the structural response depends on how fibres are oriented with respect to the failure plane. This means that, if controlled, fibre orientation may enhance the tensile behaviour (Grünwald *et al.* 2011). In some cases, preferential orientations may be advantageous for the structural response. A clear example are slabs, which tend to present fibres parallel to the main plane of the element. The concept of an improved tensile performance of FRC as a result of a certain fibre orientation may be very interesting. Although this was not considered in the design, numerous studies showing its influence in the structural response led to the proposal of an orientation factor in the Model Code 2010 (*fib* 2010) to take into account favourable or unfavourable orientations.

Even though the orientation factor is a step towards a more accurate design, some unresolved issues still remain. Research has provided evidence that, among other factors, the geometry influences the distribution of fibres within the concrete matrix. Bearing that in mind, should the dimensions of the structure be considered when determining the effect of a favourable fibre orientation? For example, focusing on the case of slabs, how are the orientation and its favourable effect affected by increasing the width of the element? Should a different structural response of FRC slabs be expected depending on their size? All these questions must be answered.

So far, the design procedures for FRC structures were discussed considering the bending test as the method for the characterization of the material. Nevertheless, there are alternative tests methods developed recently in order to overcome some of the disadvantages of the beam tests. One of them is the Barcelona test (AENOR 2010) based on a double punch test of cylindrical specimens and that was already used to characterize the SFRC in several stretches of the Line 9 of the Barcelona Metro.

Despite the advantages that the Barcelona test may present in comparison with the former, it is not as widely spread and so commonly used as the latter. Perhaps, the reason for that may be the lack of a constitutive model derived directly from the Barcelona test. In fact, at the moment, any alternative test method used for the characterization must be correlated to the beam test in order to be accepted in the design. A direct formulation from the Barcelona test would help to extend its use as interesting alternative to the beam test.

Within the framework of a complete design procedure of FRC elements, another subject yet to be included in design codes and guidelines is the long-term behaviour. In this sense, the post-cracking creep behaviour is one of the least studied properties of FRC up to the moment. Several experimental studies were performed recently on the subject, however further research is required to fully understand the phenomenon and to develop formulations able to predict the long-term deformations.

1.2. MOTIVATIONS

The industry is demanding SFRC with more structural responsibilities for applications beyond the traditional usage. Such expansion of the SFRC as a construction material requires a complete design procedure that includes all factors and conditions that may affect the short and long-term performance of the structure.

The most recent European codes and guidelines compiled and assimilated the experiences from the previous guidelines. However, several aspects still need to be further studied in order to reach full comprehension. The definition of the constitutive model of SFRC and the development of methods to characterize this material have been extensively studied. Nevertheless, their adequacy for certain applications still remains a problem. Moreover, properties such as the fibre orientation and the creep behaviour are not minor concerns that need to be properly considered in the design.

The incorporation of these aspects in the design procedure would lead to more efficient and cost-saving FRC structures, thus contributing to the consolidation of FRC. The motivations herein presented are discussed in detail in Chapter 2 of the thesis.

1.3. OBJECTIVES

Taking that into account, four general objectives that correspond to the main subjects addressed in this doctoral thesis are defined as follows.

- Analyse the current constitutive models and their adequacy to simulate the performance of SFRC beams.
- Study the influence of the element geometry and the fibre orientation in the structural response of SFRC slabs and assess the suitability of the existing constitutive models to simulate the performance of the structure.
- Propose an alternative constitutive model based on the Barcelona test.
- Study the post-cracking creep behaviour of SFRC.

In order to achieve these main goals several specific objectives are set. Table 1.1 shows the main specific goals for each subject treated in the thesis.

Table 1.1 Specific objectives.

Subject	Specific objectives
RC-SFRC beams	<ul style="list-style-type: none"> Assess the flexural response of real scale RC-SFRC beams in terms of cracking and bearing capacity. Identify the constitutive models that simulate best the response of the material based on the elements tested.
SFRC slabs	<ul style="list-style-type: none"> Evaluate the flexural behaviour of real-scale SFRC slabs, identifying the differences in terms of structural response due to their geometry. Assess fibre orientation in the SFRC slabs and propose a fibre orientation pattern depending on the width of the slabs. Analyse the adequacy of the current constitutive models to simulate the flexural response of the SFRC slabs. Perform a parametric study to determine the influence of the constitutive equation in the structural response of the slabs. Propose geometry factors that could be used in the design of specific elements.
Predicting the tensile behaviour of SFRC	<ul style="list-style-type: none"> Develop an analytical formulation to predict the tensile behaviour of the SFRC from the Barcelona test. Propose a simplification of the formulation that may be easily adopted. Compare the constitutive model proposed with the constitutive models based on beam tests.
Long-term behaviour of SFRC	<ul style="list-style-type: none"> Assess the post-cracking creep behaviour of SFRC beams with different pre-cracking widths and load levels. Evaluate the applicability of the formulations from codes to predict the creep coefficient to the post-cracking response of SFRC under sustained loads. Propose a simple model that could reproduce the creep deformations of SFRC in the post-cracking stage in terms of the creep coefficient.

1.4. METHODOLOGY

The thesis is subdivided in six parts as shown in Figure 1.3 (the chapters included in each part are indicated in parenthesis). Part I describes the motivations of the thesis. These were identified by means of the state of the art conducted in Chapter 2, which covered several subjects that will be addressed in the thesis.

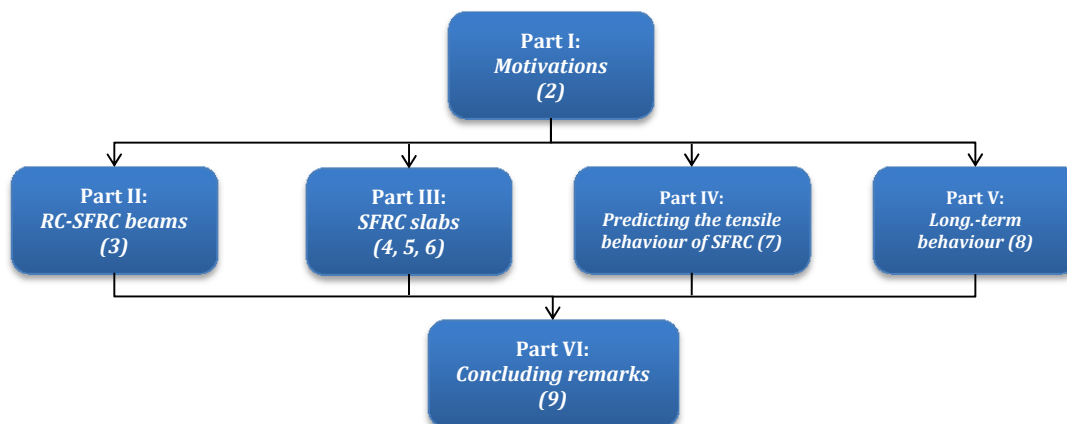


Figure 1.3 Outline of the thesis.

Part II of the thesis focuses on the application of SFRC to beams with traditional reinforcement. This subject is dealt by studying the flexural response of real-scale beams with combined reinforcement of steel fibres and rebars (hereinafter RC-SFRC). The experimental program conducted, involving different steel fibres and fibre contents allows deepening in the structural response of this type of elements both in terms of cracking and bearing capacity. The second part of the study focuses on the numerical simulation of the flexural response of the RC-SFRC using five different constitutive models available in European codes and guidelines. The differences among the models and their adequacy for the simulation of this type of structures are evaluated. This study, including both the experimental program and the modelling, was conducted in Chapter 3.

Part III deals with the experimental behaviour, fibre orientation and modelling of SFRC slabs with different dimensions. These subjects are addressed in three different chapters as represented in Figure 1.4.

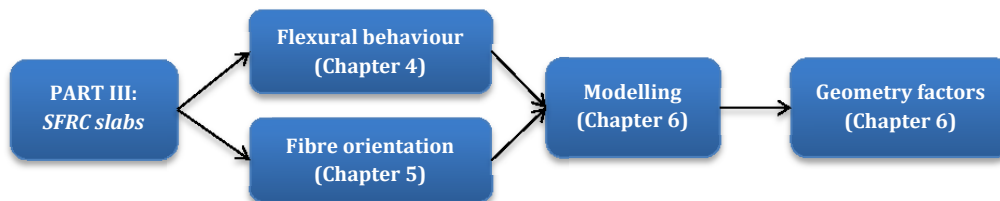


Figure 1.4 Outline of Part III of the thesis.

In Chapter 4, the flexural behaviour of SFRC slabs is studied, identifying the structural response in terms of cracking, bearing capacity and energy absorption capacity. Chapter 5 focuses on the study of the fibre orientation in cores drilled from several points of the slabs tested, thus enabling the definition of a fibre orientation pattern depending on the width of the element. The available test methods also allowed determining the fibre content in the different points of the slab.

Chapter 6 covers the simulation of the SFRC slabs with finite element software. The results obtained with two of the constitutive models based on the beam test are compared. In order to deepen in the analysis of an adequate constitutive model, a parametric study is conducted to assess the influence of each of the parameters in the flexural response of the slabs. Furthermore, the need for geometry factors is analysed based on the results obtained from the simulations. Part of the study conducted in this chapter was developed at Delft University of Technology.

Part IV presents an alternative formulation to predict the tensile behaviour of SFRC. The constitutive model developed is based on the performance of Barcelona tests for the characterization of the material. The constitutive model proposed is validated by simulating the results of an experimental program involving different types of fibres and fibre contents by means of finite element software. Moreover, the simplified formulation proposed is compared with constitutive models from European codes and guidelines. The

development of the formulation, the experimental program and the simulation are all included in Chapter 7.

In Part V, the post-cracking creep behaviour of SFRC is studied. A experimental program was performed on pre-cracked beams with sustained loads during approximately 6 months. The analysis of the results is conducted in terms of crack width and creep coefficient. The need of a new formulation to predict long-term deformations is assessed by comparing the experimental results and the predictions obtained with the existing formulations in the codes. Rheological models are used to propose simulate the experimental behaviour based on the limited number of specimens tested.

Finally, Part VI describes the conclusions of each of the subjects addressed in this thesis and presents the future perspectives of research.

The research conducted in this doctoral thesis takes place within the framework of a larger project regarding the structural design and applications of FRC. In the scope of this project, several aspects of the behaviour of SFRC and plastic fibre reinforced concretes (PFRC) are assessed, pursuing a global understanding of the material. For that reason, some of the experimental programs performed in this project were designed for both steel and plastic fibres. The doctoral thesis herein presented focuses on the behaviour of SFRC. The study regarding PFRC will be covered in the doctoral thesis entitled *Caracterización y diseño del hormigón reforzado con fibras plásticas* (in Spanish).

This approach is necessary due to the significant differences that might exist between the behaviour of each type of fibre. This is considered necessary in order to ensure an impartial analysis of each material, avoiding choosing paths that might end up favouring one type of fibre over the other.

2. STATE OF THE ART

2.1. INTRODUCTION

The identification of the most accurate and suitable procedure to design SFRC structures is a key aspect to help extending the use of this material. Such procedure should include an adequate constitutive model, test methods to characterize the performance of the material that are representative of the real application and several aspects that influence the structural response such as fibre orientation and distribution.

Over the past ten years, several national codes and guidelines were published (Soranakom and Mobasher 2009; Walraven 2009). However, no single design procedure was generally accepted, mainly due to the differences in the constitutive models proposed in each document. The first step to reach an agreement was taken by the Technical Group *fib* TG 8.3 “Fiber reinforced concrete” and TG 8.6 “Ultra high performance fiber reinforced concrete” in the Model Code 2010 (*fib* 2010). The latter is the reference for Eurocode 2 and future codes at a national level.

This chapter reviews the European codes and guidelines for the design of SFRC, focusing on the constitutive models and the test methods to characterize the material. Moreover, fundamental properties of the material that still require improvement are identified. Hence, this state of the art pursues two main goals: to identify the motivations

for this thesis and to briefly cover literature concerning several subjects that will be addressed in this dissertation¹.

2.2. CONSTITUTIVE MODELS FOR FRC IN CODES AND GUIDELINES

2.2.1. Brief overview

The European codes and guidelines for the design of FRC structures that are studied in this chapter are, according to the chronological order of publication, the DBV (DBV 2001), the RILEM recommendations (Vandewalle *et al.* 2003), the CNR-DT 204/2006 (CNR 2006), the EHE-08 (CPH 2008) and the Model Code 2010 (*fib* 2010). Hereinafter, they will be referred to as DBV, RILEM, CNR-DT 204, EHE-08 and MC2010, respectively.

Table 2.1 presents the constitutive models proposed in the previous documents grouped according to the type of diagram (namely rectangular, bilinear and trilinear or multilinear), indicating the parameters that define each one of the models. Likewise, Table 2.1 also includes the tests required to obtain the values of these parameters. In Table 2.2, the main criteria considered in each of the constitutive models are presented.

From what is presented in Table 2.1 and Table 2.2, the existing constitutive models are based on discontinuous equations and on an indirect approach since the parameters must be defined from experimental data. Likewise, most of them propose stress-strain (σ - ε) curves, even though the CNR-DT 204 and the MC2010 also provide the model in terms of stress-crack width (σ - w). Furthermore, a tendency towards the use of residual flexural strengths (f_R) instead of equivalent flexural strengths (f_{eq}) is observed, despite Barros *et al.* (2005) reported that f_R is more susceptible to local irregularities of the load-displacement curve than f_{eq} . Notice that the parameter f_{eq} is related to the energy absorption capacity of the material up to a certain deflection, while the parameter f_R corresponds to the stress associated to the force at a certain deflection. In spite of

One of the main differences of the earlier design guidelines (DBV and RILEM) from the ones published afterwards is that the former only refer to steel fibres whereas the latter distinguish between structural and non-structural fibres. This terminology implies a significant change in the design of FRC since it extends the range of fibres that may be used with structural purposes. Another common concept in the early design guidelines is the size effect, which consists in the effect of the specimen height over the bending behaviour.

A rather innovative approach is proposed by the MC2010 since it includes an orientation factor in the constitutive model that takes into account favourable or unfavourable orientations. A brief analysis of each one of the constitutive models introduced in Table 2.1 is conducted in subsequent sections.

¹ Part of this study was published in:
Blanco, A., Pujadas, P., de la Fuente, A., Cavalaro, S. and Aguado, A. Application of constitutive models in European codes to RC-FRC. *Construction and Building Materials*, 2013, vol. 40, p. 246-259.

Table 2.1 Constitutive models in European codes and guidelines (Blanco et al. 2013).

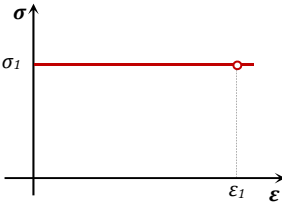
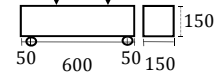
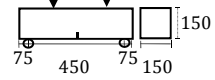
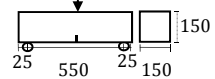
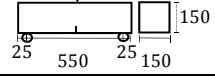
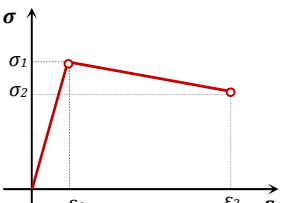
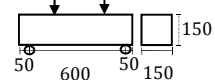
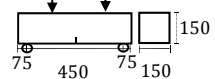
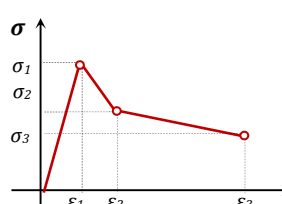
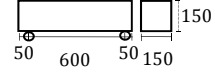
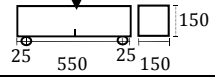
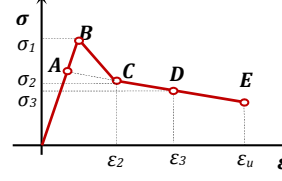
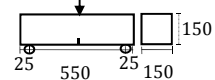
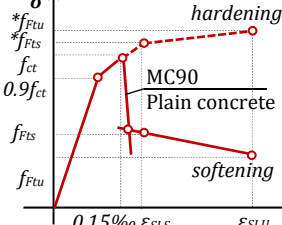
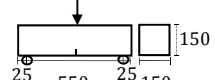
Diagram	Parameters	Characterization test	
	$\sigma_1 = f_{eq,ctd,II} = f_{eq,ctk,II} \cdot \alpha_d^f \cdot \alpha_{sys} / \gamma_{ct}^f \leq f_{eq,ctd,I}$ (α_{sys} : coefficient for size effect; α_d^f : coefficient for long-term strength behaviour) $\epsilon_1 = \epsilon_u = 10\text{‰}$	DIN 1048 	DBV
	$\sigma_1 = f_{FTu} = f_{eq,2}/3$ $\epsilon_1 = \epsilon_u = [20\text{‰ softening}; 10\text{‰ hardening}]$	UNI 11039 	CNR-DT 204
	$\sigma_1 = f_{ctR,d} = 0.33 f_{R,3,d}$ $\epsilon_1 = \epsilon_u = [20\text{‰ bending}; 10\text{‰ tensile}]$	UNE EN 14651 	EHE-08
	$\sigma_1 = f_{FTu} = f_{R,3}/3$ $\epsilon_1 = \epsilon_u = [20\text{‰ softening}; 10\text{‰ hardening}]$	UNE EN 14651 	MC2010
	$\sigma_1 = f_{eq,ctd,I} = f_{eq,ctk,I} \cdot \alpha_d^f \cdot \alpha_{sys} / \gamma_{ct}^f$ $\sigma_2 = f_{eq,ctd,II} = f_{eq,ctk,II} \cdot \alpha_d^f \cdot \alpha_{sys} / \gamma_{ct}^f \leq f_{eq,ctd,I}$ $\epsilon_2 = \epsilon_u = 10\text{‰}$	DIN 1048 	DBV
	$\sigma_1 = f_{FTS} = 0.45 f_{eq,1}$ $\sigma_2 = f_{FTu} = k [f_{FTS} - (w_u/w_{i2}) (f_{FTS} - 0.5 f_{eq,2} + 0.2 f_{eq,1})]$ $k = [0.7 \text{ pure tension, 1 other cases}]$ $\epsilon_2 = \epsilon_u = [20\text{‰ softening}; 10\text{‰ hardening}]$	UNI 11039 	CNR-DT 204
	$\sigma_1 = f_{ctd} = \alpha_c^f \cdot f_{ctk,fl} / \gamma_{ct}^f$ $\sigma_2 = f_{eq,ctd,I} = f_{eq,ctk,I} \cdot \alpha_d^f \cdot \alpha_{sys} / \gamma_{ct}^f$ $\sigma_3 = f_{eq,ctd,II} = f_{eq,ctk,II} \cdot \alpha_d^f \cdot \alpha_{sys} / \gamma_{ct}^f \leq f_{eq,ctd,I}$ $\epsilon_1 = \sigma_1 / E_c; \epsilon_2 = \epsilon_1 + 0.1\text{‰}; \epsilon_3 = \epsilon_u = 10\text{‰}$	DIN 1048 	DBV
	$\sigma_1 = 0.7 f_{ctm,fl} (1.6-d);$ $\sigma_2 = 0.45 \cdot k_h \cdot f_{R,1};$ $\sigma_3 = 0.37 \cdot k_h \cdot f_{R,4}$ $\epsilon_1 = \sigma_1 / E_c; \epsilon_2 = \epsilon_1 + 0.1\text{‰}; \epsilon_3 = \epsilon_u = 25\text{‰}$	RILEM TEST 	RILEM
	$\sigma_1 = f_{ct,d} = 0.6 f_{ct,fl,d}$ $\sigma_2 = f_{ctR,d} = 0.45 f_{R,1,d}$ $\sigma_3 = f_{ctR,3,d} = k_1 (0.5 f_{R,3,d} - 0.2 f_{R,1,d})$ $\epsilon_2 = 0.1 + 1000 \cdot f_{ct,d} / E_c$ $\epsilon_3 = 2.5 / l_{cs} (l_{cs}: \text{characteristic length})$ $\epsilon_u = [20\text{‰ bending}; 10\text{‰ pure tension}]$	UNE EN 14651 	EHE-08
	$f_{ctm} = 0.30 (f_{ck})^{2/3}$ $f_{FTS} = 0.45 f_{R1}$ $f_{FTu} = k [f_{FTS} - (w_u / CMOD_3) (f_{FTS} - 0.5 f_{R3} + 0.2 f_{R1})]$ $\epsilon_{SLS} = CMOD_1 / l_{cs}$ $\epsilon_{SLU} = w_u / l_{cs} = \min(\epsilon_{FTu}, 2.5 / l_{cs} = 2.5 / y)$ $\epsilon_{Fu} = [20\text{‰ softening}; 10\text{‰ hardening}]$	UNE EN 14651 	MC2010

Table 2.2 Summary of the characteristics of the constitutive models (Blanco et al. 2013).

Assumptions	DBV	RILEM	CNR-DT 204	EHE-08	MC2010
Stress- strain (σ - ε) / Stress-crack width (σ - w)	σ - ε	σ - ε	σ - ε / σ - w	σ - ε	σ - ε / σ - w
Direct approach (DA) / Indirect approach (IA)	IA	IA	IA	IA	IA
Continuous equation (CE) / Discontinuous equation (DE)	DE	DE	DE	DE	DE
Residual strengths		•		•	•
Equivalent strengths	•		•		
Differentiates the ultimate strain (20‰; 10‰)			•	•	•
Conversion factors regarding the linear-elastic distribution of stresses	•	•		•	
Characteristic length to obtain strain			•	•	•
Safety coefficients	•		•	•	•
Size effect	•	•			
Effect of long-term strength behaviour	•				
Terminology of “structural fibre”			•	•	•
Contribution of fibres in the crack spacing		•	•		•
Effect of fibre orientation					•

2.2.2. German guidelines: DBV-Merkblatt Stahlfaserbeton (1992/2001)

The German Concrete Society was the promotor of the first guidelines including a σ - ε constitutive model for the design of FRC, specifically for metallic fibers (DBV 1992b). This document was published in order to provide a diagram for the structural design of tunnels. In 2001, a new guide was published in which a trilinear model is proposed for the Serviceability Limit State (SLS) with the possibility of using a bilinear diagram (or even a rectangular diagram) for the Ultimate Limit State (ULS). Both diagrams, represented in Figure 2.1, are defined by equivalent strengths deduced from the results of 4-point bending tests. The peak stress (f_{ctd}) in the trilinear model corresponds to the maximum load during the test in a deflection of up to 0.1 mm.

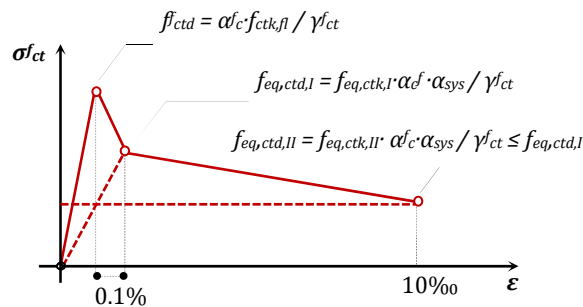


Figure 2.1 Constitutive models proposed by the DBV.

Among the aspects to highlight from the DBV model are the use of a coefficient to consider the coefficient of variation (k_v), safety factors (γ_{ct}) and the effect of long-term strength behaviour by means of the a coefficient (α_c), with reductions up to 25% in

lightweight concrete and up to 15% in conventional concrete. This model also introduces the concept of size effect (α_{sys}) that takes into account the effect of the height of the specimen in the flexural tensile behaviour penalizing (up to 20%) the sections with larger heights. In the version of 2001, the ultimate strain (ϵ_u) increased to 10‰, while the previous version suggested 5‰.

2.2.3. RILEM TC 162-TDF Recommendations (2003)

The first proposal of a constitutive model by RILEM TC 162-TDF in 2000 consisted of a σ - ϵ trilinear diagram defined by means of equivalent flexural strengths ($f_{eq,i}$). The main differences with the German model was the use of a 3-point bending test and the absence of parameters to take into account the size effect.

After numerous investigations conducted in the scope of the Brite Euram project BRPR-CT98-0813 (Brite-Euram 2002), a new σ - ϵ trilinear model for SFRC was proposed in 2003 (see Table 2.1). The most significant change was the use of residual flexural strengths (f_R) and the inclusion of a size factor. The value of ultimate strain (ϵ_u) proposed by RILEM was 25‰. This is the result of considering a height of the neutral axis of 140 mm above the point where the CMOD is measured and assuming a characteristic length equal to that distance. Consequently for a CMOD of 3.5 mm, a strain value of $(3.5/140)=25‰$ is obtained, as indicated in Figure 2.2a.

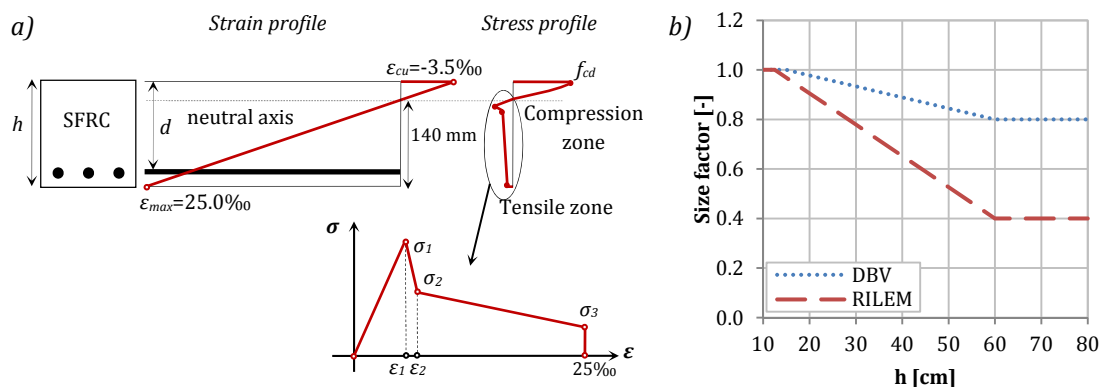


Figure 2.2 a) σ - ϵ distribution in cross section and σ - ϵ diagram and b) size factors in DBV and RILEM.

The stresses are obtained by affecting $f_{R,1}$ and $f_{R,4}$ with a size factor (κ_h) to consider the geometric differences between the test specimens and the real structure. As observed in Figure 2.2b, the RILEM size factor presents lower values than the DBV, thus indicating a more conservative approach.

2.2.4. Italian guidelines: CNR-DT 204 (2006)

In 2006, the Italian National Research Committee published the Guide CNR-DT 204 for the Design, and Construction of Fibre Reinforced concrete structures. This document proposes two different relations for the tensile behaviour of FRC: the linear-elastic model and the plastic-rigid model, both expressed in terms of σ - ϵ and σ - w diagrams. The plastic

rigid model is used for the ULS design while the linear-elastic model can be applied either to ULS and SLS.

In Figure 2.3, cross section with the stress distribution of each model is schematized. These diagrams are defined by using equivalent flexural strength and characterizing the tensile behaviour of the material by means of 4-point bending tests or uniaxial tensile tests according to the Italian standards UNI 11039 (UNI 2003) and UNI 11188 (UNI 2004), respectively.

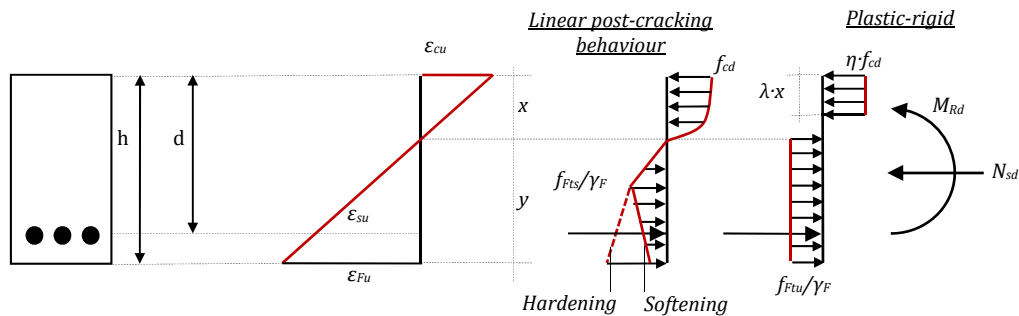


Figure 2.3 Linear post-cracking model and rigid-plastic model in CNR-DT 204 (CNR 2006).

The linear post-cracking behaviour model differentiates between strain-hardening and strain-softening materials. In the first case, multi-cracks occur and the average strain may be directly obtained from the experimental tests. The value of ultimate strain for strain-hardening materials is assumed to be 10‰. In the case of strain-softening materials, when only one main crack appears, the ultimate strain (ϵ_{Fu}) is related to the ultimate crack width (w_u) and the equivalence is carried out by means of a characteristic length (l_{cs}). The value of l_{cs} is determined from the minimum between the average crack spacing (s_{rm}) and the height of the neutral axis (y). In this case, the ultimate tensile strain is 20‰ and the w_u must follow the condition: $w_u = \epsilon_{Fu} \cdot l_{cs} \leq 3$ mm.

Another aspect worthwhile highlighting in the Italian guidelines is the recommendation of partial safety factors for the design in ULS and SLS.

2.2.5. Spanish code: EHE-08 (2008)

The Spanish code (EHE-08) includes recommendations for the use of FRC without specifying the type of fibre, as long as they are structural. In this code, two σ - ϵ diagrams are presented: a rectangular diagram and a multilinear diagram. In the case of ULS calculations, as a general rule, the rectangular diagram may be used, while for particular cases that require a higher level of accuracy the simplified bilinear model (defined by the points A-C-D-E of the multilinear diagram, see Table 2.1) is suggested. For SLS cases, the multilinear diagram may be used (defined by A-B-C-D-E, see Table 2.1) since the additional strength provided by the peak A-B-C allows a better approximation and an improved accuracy.

The parameters defining these diagrams are residual flexural strengths obtained from a 3-point bending test according to EN 14651:2005 (CEN 2005). Alternatively, the Spanish code indicates that other test methods to characterize the tensile behaviour of FRC may be used such as the Barcelona test (UNE 83515 (AENOR 2010)).

Regarding the definition of the strain values, this model uses the concept of the characteristic length (l_{cs}) to determine the strain associated to a crack width of 2.5 mm (in the bending test). In this case, the value of l_{cs} corresponds to the minimum between the average crack spacing (s_{rm}) and the height of the neutral axis (y). Likewise, the Spanish code differentiates two values for the ultimate strain depending on the type of forces to which the section is subjected to: 20‰ for bending and 10‰ for tension.

From the comparison of these models with the previously described, it may be noticed that the rectangular model follows the same philosophy of the rigid-plastic model in the Italian guidelines and the multilinear is similar to the trilinear models suggested in the German standard and in the RILEM recommendations. Although the Spanish code does not introduce significant advances, it gathers the knowledge and main concepts from the previous recommendations.

2.2.6. *fib* Model Code (2010)

The experience on FRC over the past twenty years and the publication of design codes and guidelines at a national level led the *fib* (Fédération Internationale du Béton) to introduce FRC in the update of the previous CEB-FIP Model Code 90. With the aim of providing a tool for the design of FRC structural elements, the new MC2010 proposes two different models for the tensile behaviour of FRC following the approach of the Italian guidelines: the plastic-rigid behavior and the linear-postcracking behavior, shown in Figure 2.4. These models are presented in terms of simplified σ - w constitutive diagrams and may reproduce both hardening and softening behaviour.

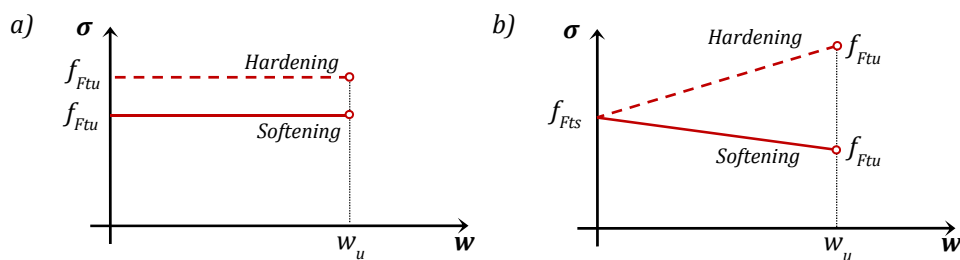


Figure 2.4 Simplified σ - w diagrams: a) rigid-plastic and b) linear post-cracking.

The parameters in both diagrams are defined by means of residual flexural tensile strengths, determined by performing a 3-point bending test according to EN 14651:2005 (CEN 2005). The parameter f_{Fts} represents the serviceability residual strength, defined as the post-cracking strength for crack openings at SLS. On the other hand, f_{Ftu} represents the

ultimate residual strength and it is associated with the ULS crack opening (w_u), which is the maximum crack opening accepted in structural design.

For the rigid-plastic model w_u is 2.5 mm and for the linear-elastic it depends on the ductility required but it will not exceed 2.5 mm. The equations to determine the parameters f_{Fts} and f_{Ftu} were presented in Table 2.1. Since these two models are simplifications, the *fib* Model Code recommends the use of more advanced constitutive diagrams for numerical analysis (including the first crack tensile strength).

In order to define the σ - ε diagram it is necessary to distinguish between strain-softening and strain-hardening materials. A material is regarded as strain-hardening if it shows hardening behaviour in tension up to an ultimate strain $\varepsilon_{Fu}=1\%$, otherwise the material is considered as strain-softening.

For strain-softening materials, the σ - ε diagram is defined by identifying the crack width and the corresponding structural characteristic length (l_{cs}) of the structural element. Hence, the strain can be expressed as $\varepsilon=w/l_{cs}$. The value of l_{cs} corresponds to the minimum between the average crack spacing (S_{rm}) and the distance between the neutral axis and the tensile side of the cross section (y).

In the case of elements with rebars, y is evaluated in the cracked phase assuming no tensile strength of the fibre reinforced concrete and a load configuration corresponding to the serviceability state of crack width and spacing (see Figure 2.5a). In sections without traditional reinforcement under bending (or under combined tensile-flexural and compressive-flexural forces with the resulting force external to the section), the value of y is assumed equal to the height of the section (see Figure 2.5b). Therefore, the ultimate crack width w_u be calculated as $w_u=l_{cs} \cdot \varepsilon_{Fu}$. The ultimate strain ε_{Fu} equals 2% for variable strain distribution along the cross section and 1% for uniform tensile strain distribution along the cross-section.

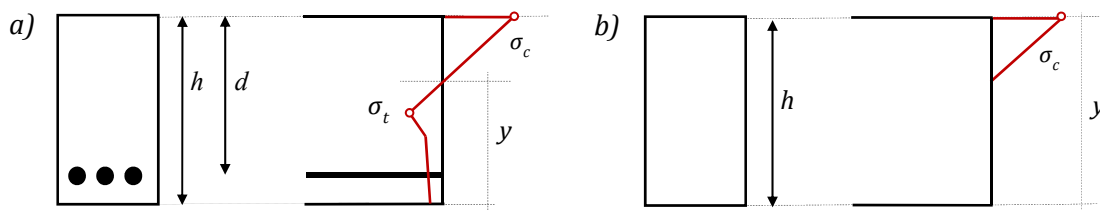


Figure 2.5 Definition of the parameter y for a) RC section and b) plain concrete section.

For strain-hardening materials, l_{cs} is not necessary and the σ - ε diagram is defined by assuming ε_{Fu} equal to 2% for variable strain distribution along the cross section and equal to 1% for uniform tensile strain distribution along the cross section.

The resulting σ - ε diagram was presented in Table 2.1. The second branch suggested in the pre-cracking stage corresponds to the constitutive diagram for plain

concrete until the intersection between the residual post-cracking behaviour and the unstable crack propagation occurs, for strain-softening materials. This is indicated as “MC90 Plain concrete” in Table 2.1. For strain-hardening another branch is proposed (see dash line in Table 2.1).

Regarding the characterization of the tensile behaviour, it was previously mentioned that the MC2010 recommends the bending test specified in EN 14651:2005 (CEN 2005). Nevertheless, other tests may be accepted if correlation factors with the parameters of EN 14651:2005 are proven. In this sense, the MC2010 advises not to use uniaxial tensile tests for new concrete mixtures due to the difficulty of execution and interpretation of the results.

Additionally, the long-term behaviour of cracked FRC under tension must be considered in case reinforcing materials affected by creep deformations such as organic or natural fibres are used. Following the example set by the CNR-DT 204 and EHE-08, the MC2010 specifies that fibre reinforcement can partially or totally substitute conventional reinforcement at ULS if certain requirements are fulfilled. The MC2010 also presents partial safety factors for materials.

An aspect that differentiates MC2010 from other models is the recommendation of an orientation factor (K) for the design. This factor equals 1 when an isotropic fibre distribution is assumed and should be lower or higher than 1 if favourable or unfavourable effects are experimentally verified. A recent study by di Prisco *et al.* (2012) proposed a methodology for the quantification of K based on mechanical tests on SCFRC. The MC2010 is also the first to suggest the performance of special tests to determine the effect of fibre orientation by using structural specimens, which reproduce better the material in the real-scale element.

This brief review of the design codes and guidelines for FRC allows identifying some key aspects that should be taken into account in the design of FRC structures. These are the need for representative test methods, the influence of fibre orientation in the performance of the material and the consideration of the long-term behaviour of cracked FRC. Each one of these topics is discussed in subsequent sections.

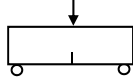
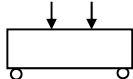

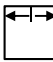
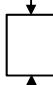

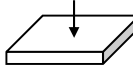
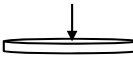
2.3. TEST METHODS TO CHARACTERIZE THE TENSILE BEHAVIOUR OF FRC

2.3.1. Brief overview

Most European codes and guidelines use bending tests to characterize the post-cracking response of FRC and to determine the parameters defining their constitutive models. However, there are several test methods to identify, directly or indirectly, the post-cracking response of FRC. Some of them and their corresponding standard are gathered in Table 2.3. Notice that some of these test methods (or with similar test setup and dimensions) may also be found in standards from other countries. It should be

remarked that the EFNARC panel test (EFNARC 1996) and the round determinate panel test (ASTM 2010b) were conceived to characterize fibre reinforced shotcrete (FRS).

Table 2.3 Main test methods for the characterization of the post-cracking behaviour of FRC.

Test	Standard / Reference	Setup	Dimensions ¹ [mm]
3-point bending test	EN 14651:2005		600 x 150 x 150
4-point bending test	NBN B 15-238		600 x 150 x 150
Uniaxial tensile test	RILEM TC 162-TDF recommendations		Φ150 x 150
Wedge-splitting test	Tschegg and Linsbauer (1986)		150 x 150 x 150
Barcelona test	UNE 83515:2010		Φ150 x 150
Double-edge wedge splitting test	di Prisco <i>et al.</i> (2010)		150 x 150 x 150
EFNARC panel test	EFNARC European Specification for Sprayed Concrete		600 x 600 x 10
Round panel test	ASTM C1550 - 10a		Φ800 x 75

1: The dimension preceded by the symbol Φ indicates a diameter.

The uniaxial test is the most direct method to obtain the tensile response, whereas the bending tests (IBN 1992; CEN 2005) or the wedge-splitting test (Tschegg and Linsbauer 1986) require an inverse analysis to obtain these results. Nevertheless, the MC2010 does not recommend the use of uniaxial tensile tests in certain cases given the complexity of execution and the reliability of the results. Under this circumstance, the question of which are the criteria to decide the most adequate method to characterize the post-cracking behaviour of FRC may be raised. According to Kooiman (2000), some of the aspects that should be considered are:

- The complexity of the test (set-up, preparation of specimens and execution).
- The reproducibility of the test.
- The costs and the applicability in practice.
- The complexity of processing the test results into a uniaxial material relation and
- The reliability and the scatter of the test results.

Based on these criteria, the use of the bending tests to systematically characterize the post-cracking response of FRC may be questioned. While in terms of execution beam tests may be simpler to perform than uniaxial tests and panel tests, they are more complex than the Barcelona test, the wedge-splitting test and the double-edge wedge splitting test.

Furthermore, several studies in the literature report a significant scatter in the results (Dupont and Vandewalle 2004; Molins *et al.* 2009; Buratti *et al.* 2011), frequently around 20%. Parmentier *et al.* (2008) analysed the variation of the results obtained with the bending tests and the panel tests for two types of FRC: normal concrete (NC) and high strength concrete (HSC). The results obtained (see Figure 2.6) reveal a variation over 15% for the beam tests for both types of concrete. Notice that these values are between 2 to 3 times higher than the obtained for the panel tests by the same author.

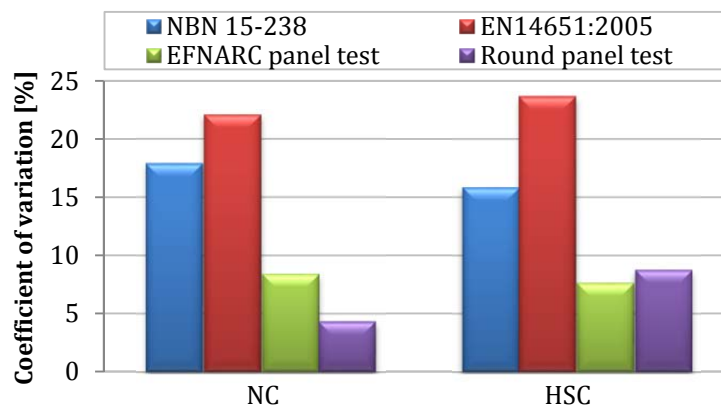


Figure 2.6 Coefficient of variation in the bending tests and panel tests (Parmentier *et al.* 2008).

The high scatter of the bending tests may be attributed to the amount of fibres and their distribution in the cracked section. In addition to the scatter, Wille and Parra-Montesinos (2012) observed significant differences in the flexural behaviour of FRC by changing the beam size, the casting method and the support system, reaching differences of up to 200%.

Recently, Dozio (2008), Laranjeira (2010) and Ferrara *et al.* (2011) emphasized the importance of performing tests that are geometrically representative of the structural application for what the material is intended. Hence, the representativeness of testing small beams to design any type of structural elements is arguable. In fact, a recent study on the mechanical performance of SFRC flat slabs (Michels *et al.* 2012) confirms this statement and points out the necessity to introduce realistic geometry factors in the design. This reinforces the need to consider new design approaches that take into account the differences in the responses of the characterization test and the real scale structure or to propose tests that are tailored to each structural application.

2.3.2. Barcelona test (UNE 83515:2010)

An alternative test method was presented by Molins *et al.* (2007) based on the double punch test (DPT hereinafter) developed by Chen (1970). The Barcelona test is now a standardized method according to UNE 83515:2010 (AENOR 2010). The cylindrical FRC specimen used presents a diameter and a height of 150 mm. During the test, it is located between two steel cylindrical punches located at the centre of the top and the bottom surfaces (see Figure 2.7a). The steel punches have a height of 24 mm and a diameter of 37.5 mm.

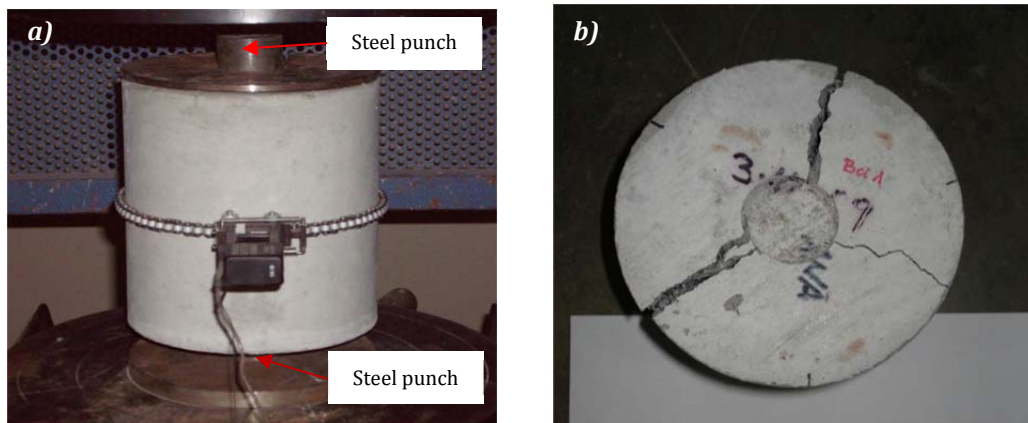


Figure 2.7 a) Barcelona test setup and b) top surface of a specimen after the test.

This test is characterized by the appearance of 2 to 4 radial cracks (Carmona *et al.* 2012) as shown in Figure 2.7b. The test is controlled by measuring the total crack opening displacement (TCOD) with a circumferential extensometer placed at half-height of the specimen (see Figure 2.7a).

Several researchers (Molins *et al.* 2009; Chao *et al.* 2011; Carmona *et al.* 2012) highlighted the advantages of this test in comparison with the bending test such as material and time saving, larger specific failure surface and, therefore, less scatter in the results, lighter specimens and the possibility of testing cores bored from real structural elements.

Despite these advantages, the fact that a circumferential extensometer is necessary to measure the TCOD restricts the widespread use of the Barcelona test. In order to overcome such drawback, Carmona *et al.* (2012) proposed an experimental correlation between the axial displacement and the TCOD. A more recent study by Pujadas *et al.* (2012) presented an analytical correlation between the axial displacement and the TCOD that is valid for the whole extent of the curve and for any type of FRC. Nevertheless, a formulation that provides the stress-strain (σ - ϵ) relation and that applies for both the linear-elastic and post-cracking stages is still required.

2.4. ORIENTATION

2.4.1. Factors influencing fibre orientation

Production conditions to which FRC is subjected affect the distribution and orientation of fibres in the concrete matrix. The fibres may not provide a uniform reinforcement with the same efficiency in all directions. In most cases, preferential orientations in the concrete matrix occur as a result of several factors (see Figure 2.8): the fresh-state properties, the concrete pouring, the geometry of the formwork, the type of vibration and the production method.

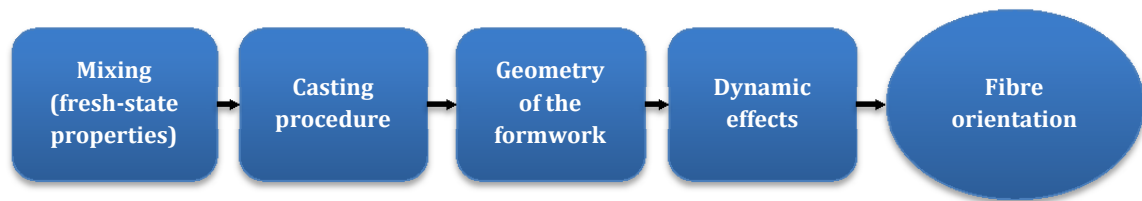


Figure 2.8 Main stages of the production process that affect fibre orientation.

Studies on the fresh-state properties (mainly rheological properties) of FRC (Kooiman 2000; Grünewald 2004; Markovic 2006; Ferrara *et al.* 2008; Stähli 2008; Martinie *et al.* 2010) reported that the flow of concrete affects the fibre orientation and, consequently, the hardened material properties. The study by Martinie and Roussel (2011) sets two main reasons for the preferential orientation of the fibres: the wall-effects that depend on the geometry of the formwork and the flow of concrete, which depends on the rheological properties of the material, the geometry of the formwork and the casting procedure.

Figure 2.9 shows how the orientation of fibres in a certain concrete volume is affected by the presence of boundaries. If the volume of FRC is subjected to no restrictions, the fibres are distributed randomly and no preferential orientations occur (see Figure 2.9a). However, if it is located between two surfaces (top and bottom surfaces in Figure 2.9b) the fibres near the boundaries will tend to align parallel to them. From a geometrical point of view, it is not possible to find a fibre perpendicular to a wall at a distance lower than half of the length of the fibre (Dupont and Vandewalle 2005).

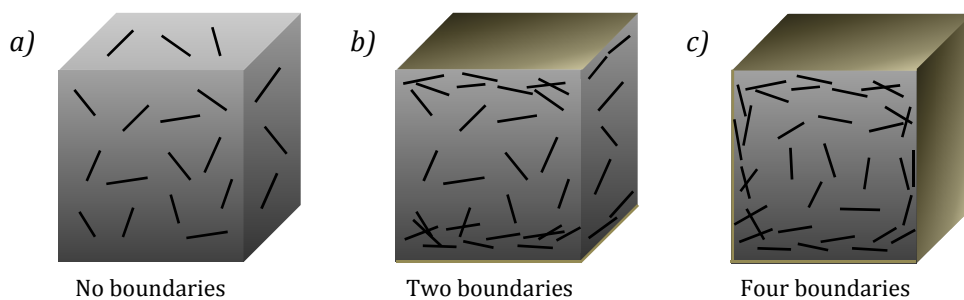


Figure 2.9 Influence of boundary conditions in fibre orientation.

This phenomenon, known as the wall-effect (Romualdi and Mandel 1964; Krenchel 1975; Kameswara Rao 1979; Soroushian and Lee 1990; Hoy 1998; Kooiman 2000; Van Gysel 2000; Dupont and Vandewalle 2005), is more noticeable as the FRC volume becomes exposed to more boundaries, as represented in Figure 2.9c.

Even though the wall-effect has a local nature and should not have a significant influence in the structural response of a big element, the restrictions imposed by the rigid surfaces of the formwork can affect the post-cracking response of smaller specimens (Stroeven and Hu 2006). For example, in the case of the small beams (150 x 150 x 600 mm) used in the bending tests the wall-effect and a preferential orientation in the perpendicular plane to the casting direction due to the vibration of the specimen were experimentally verified (Gettu *et al.* 2005; Torrents *et al.* 2012).

Cementitious materials only flow if a stress higher than a critical value (yield stress) is applied (Roussel 2006; Roussel 2007). Two channel flow patterns are considered: a free surface flow and a confined flow. In the first one, the concrete flows above one wall and the velocity profile and the distribution of the drag forces are characterized by a parabolic shape. Such statement is true for a Newtonian fluid, however for a yield stress fluid the profile of the velocity presents a plug-flow zone where the shear stresses are lower than the yield stress and, therefore, the velocity is constant (Martinie and Roussel 2011). The extension of the plug-zone is determined by the value of the yield stress, being the former thicker as the latter increases. The velocity profile of a high yield stress fluid such as a conventional FRC may be observed in Figure 2.10a.

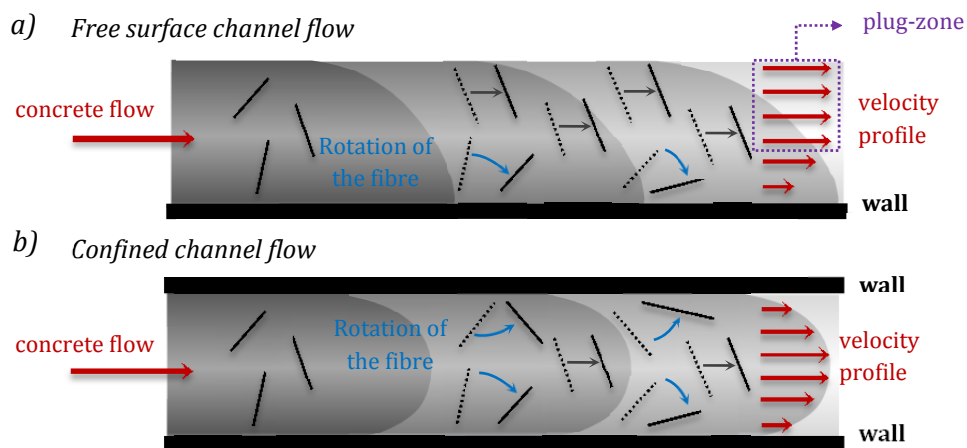


Figure 2.10 Mechanisms of flow-induced in a) a free surface flow and b) a confined flow.

The drag forces exert a torque on the fibres which makes them rotate and align along the direction of the flow. In the plug-zone the torque is considered to be negligible since the velocity is constant (Ferrara 2012). In such cases, the effect of fibre alignment along the direction of the flow is restricted to the zone where the velocity is not constant, as observed in Figure 2.10a.

In the case of a confined channel flow, the velocity profile differs from the one described in a free surface channel flow. Stähli (2008) verified that the fibres in a SCFRC tend to align with the direction of the confined flow (see Figure 2.10b). Moreover, the author concluded that this orientation is affected by the flow velocity and time. This effect is stronger for concretes with lower viscosity.

Another phenomenon occurs when the flow is dominated by extensional stresses instead of shear stresses (such as in radial flows), in which the fibres tend to align perpendicularly to the flow. This type of orientation was already observed by Grünwald (2004) in SCSFRC tunnel segments. Barnett *et al.* (2010) reported that in UHPFRC circular panels with extensional or radial flow short fibres align perpendicular to the radius of the panel. Likewise, the study by Boulekbache *et al.* (2010) assessed the orientation of long fibres in a homogeneous and plastic fluid subjected to a radial flow and a free surface channel flow. The authors detected that the fibres aligned perpendicularly to the flow in the first case and along the flow in the second.

Research has provided evidence that another factor influencing the orientation of fibres in the matrix is the casting procedure (Toutanji and Bayasi 1998; Markovic 2006; Torrijos *et al.* 2008; Barnett *et al.* 2010). Barnett *et al.* (2010) presented the results for several round plates of UHPFRC cast following different procedures (from the centre, from the perimeter and randomly). Electrical resistivity measurements and X-ray CT imaging confirmed that these casting procedures led to different fibre orientation in the plates. Moreover, a significant variation of the flexural performance of the panels was reported (depending on the casting method, changes up to 67% and 120% were observed in the maximum load and the flexural toughness of the panel, respectively).

Further research on the tensile behaviour of UHPFRC dog-bone shape specimens (Kang and Kim 2011) and the flexural behaviour of UHPFRC small beams (Kang and Kim 2012) revealed that when the casting procedure favoured a fibre alignment parallel to the tensile stresses, the specimens showed an improved mechanical performance. In fact, these beams and dog-bone shape elements exhibited, respectively, a maximum load 20% and 45% higher than the measured for the equivalent specimens produced favouring a fibre alignment perpendicular to the tensile stresses.

The last factor included in Figure 2.8 is the dynamic effects. Several researchers highlighted that external vibration of SFRC leads to segregation and a preferential alignment in horizontal planes (Edgington and Hannant 1972; Stroeven 1977; Stroeven 1979; Soroushian and Lee 1990; Toutanji and Bayasi 1998).

2.4.2. Fibre orientation in specimens with different sizes

In the previous section, the influence of the geometry of the formwork was introduced, focusing on the boundary conditions. Nevertheless, it is also interesting to discuss how a change in the geometry of the cross section (in the width or the thickness) may affect fibre orientation and, consequently, the structural response.

Kooiman (2000) conducted an experimental study on the flexural behaviour of SFRC beams with the span ranging from 500 to 1500 mm and the width from 150 mm to 450 mm (keeping constant the span to beam depth ratio and the notch depth to beam depth ratio). While the beam depth seemed to have no significant influence, the author reported an increase in the average energy absorption capacity and a reduction of the scatter as the width of the beam increased. The number of fibres in the cross-section indicated that the average number of fibres per cross-sectional area was not significantly influenced by width as long as the casting and compacting procedures were the same.

However, Michels *et al.* (2012) tested large-scale octagonal plates with increasing thickness and observed that the post-cracking residual strength decreased with thickness. Likewise, the analysis revealed that the orientation factor has a small variation in the horizontal plane and a remarkable variation over the thickness of the plate. The author also reported a more pronounced orientation in the horizontal plane in slender plates.

In this regard, it would be interesting to identify if changes in geometry may accentuate the advantageous effect of certain preferential orientations for instance, in slabs, which usually present a preferential fibre orientation perpendicular to the casting direction. For that, further experimental research on the fibre orientation and structural response of real-scale elements with different dimensions is required.

2.4.3. Methods to determine fibre orientation

Significant research was conducted in the past years with the aim of developing techniques capable of identifying the fibre orientation in hardened concrete as shown in Table 2.4. These techniques may be classified as destructive or non-destructive methods, being based on either direct or indirect measurements.

Table 2.4 Methods to determine fibre orientation.

Method	Measurements	Technique	References
Destructive	Indirect	<ul style="list-style-type: none"> Manual counting + theoretical expression by Krenchel (1975) 	Soroushian and Lee (1990); Gettu <i>et al.</i> (2005); Dupont and Vandewalle (2005)
		<ul style="list-style-type: none"> Mechanical testing 	Kooiman (2000); Barragán (2002); Grünewald (2004); Pujadas <i>et al.</i> (2011)
Non-destructive	Direct	<ul style="list-style-type: none"> Image analysis X-Ray method Computarized tomography 	Grünewald (2004); Lappa (2007) Van Gysel (2000); Robins <i>et al.</i> (2003); Vandewalle <i>et al.</i> (2008) Stähli and van Mier (2007)
		<ul style="list-style-type: none"> Alternating current-impedance spectroscopy (AC-IS) Open coaxial transmission line Dielectric waveguide antennas Electrical resistivity methods Inductive method 	Ozyurt <i>et al.</i> (2006); Ferrara <i>et al.</i> (2008) Torrents <i>et al.</i> (2009) Roqueta <i>et al.</i> (2011) Lataste <i>et al.</i> (2008) Torrents <i>et al.</i> (2012)

In general, the scope of the destructive methods remains limited to research purposes due to the size of the specimens, the complexity, the time required and the cost associated to these techniques. Hence, the interest in developing non-destructive methods that may be applied to real-scale structures. It must be remarked that from the non-destructive methods included in Table 2.4, only the inductive methods remains restricted to a small cubic specimen (150 x 150 x 150 mm), whereas the others may be applied to large elements.

2.5. LONG-TERM BEHAVIOUR OF SFRC

2.5.1. Basic concepts

The study conducted on the long-term behaviour of SFRC in this thesis focuses on creep deformations. However, long-term deformations may be of various origins and in order to define the scope of the study it is worthwhile reviewing them briefly.

Origin of long-term deformations

The hydrated cement paste plays a key role in the long-term deformations since it is the source for drying shrinkage and creep deformations. The hydrated cement paste contains water in several forms that may be classified according to the firmness with which it is hold (Neville 2004), as indicated in Figure 2.11.

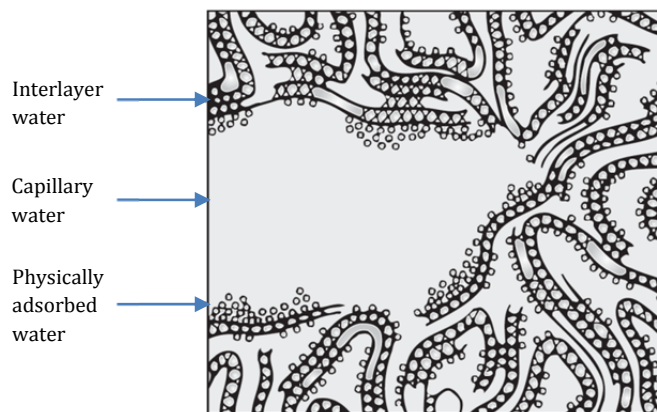


Figure 2.11 Types of water in the hydrated cement paste (Mehta and Monteiro 2006).

The capillary water is in the voids of the hydrated cement paste, free from the attractive forces exerted by the solid surface. Such forces are responsible for the water adsorbed to the solid surface. The interlayer water is linked to the C-S-H structure and it is only lost on strong drying processes according to Mehta and Monteiro (2006). Additionally, part of the water is chemically bounded with the cement hydrated phases.

Drying shrinkage develops when a cement paste is exposed to ambient conditions where the humidity is lower than saturation humidity. In such cases, a loss of physically

adsorbed water from C-S-H occurs. If, however, the loss of adsorbed water in a hydrated cement paste is caused by the application of a sustained stress, the resulting deformations are attributed to the creep phenomenon. Even though, there may be other causes contributing to creep in concrete, the loss of adsorbed water seems to be the most important (Acker and Ulm 2001; Mehta and Monteiro 2006).

Notice that drying shrinkage and creep develop over time and are significantly influenced by the degree of hydration. Other volume changes may occur at early stages, for example, due to the decrease in the temperature after the dissipation of hydration heat (thermal shrinkage), to evaporation on the surface (plastic shrinkage) and to the internal removal of capillary water in moisture-sealed conditions as a result of chemical combination during hydration (autogenous shrinkage). Further detail on these volume changes of concrete may be found in Neville (2004) and Mehta and Monteiro (2006).

Classification of long-term deformations

The total strain of concrete at any time may be understood as the result of the elastic strain, shrinkage and creep (see Figure 2.12a). The initial strain at the application of the load is primarily elastic, even though it may include a non-elastic component (Neville *et al.* 1983). It was previously introduced that there are several types of shrinkage. However, only carbonation shrinkage (Bažant 1988; Ferretti and Bažant 2006) develops in the same time scale as drying shrinkage.

Creep is defined as the addition of two components that depend on the ambient humidity. Basic creep is the deformation under sustained load when no moisture exchange occurs with the ambient (hygral conditions or equilibrium). Drying creep is the additional deformation that occurs when the concrete is also drying. Other types creep such as transitional thermal creep or wetting creep (Bažant 1988) are not discussed in this study.

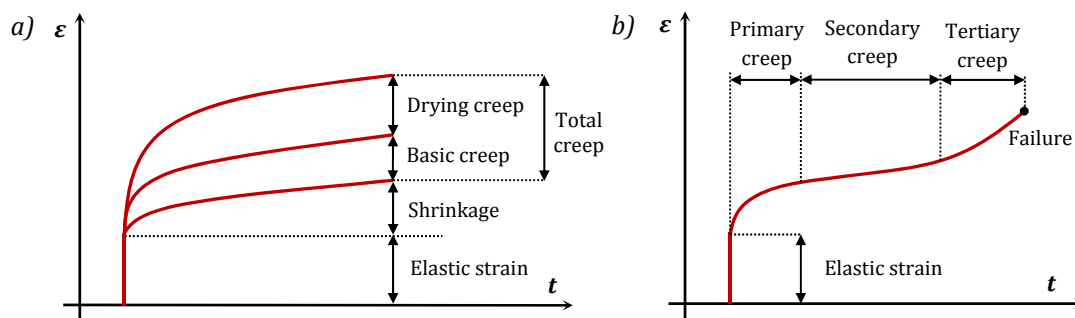


Figure 2.12 a) Total strain of concrete with time and b) general form of ϵ - t curve for materials subjected to creep (Neville *et al.* 1983).

The general form of the strain-time (ϵ - t) curve for a material subjected to creep is presented in Figure 2.12b. After the initial elastic strain three stages may be identified: the primary creep, the secondary creep and the tertiary creep. During the primary creep the creep rate decreases with time, whereas the secondary creep corresponds to a steady

state creep rate. For normal levels of stress (up to 40% of the compressive strength), the primary creep may not be distinguished from the secondary creep. Tertiary creep occurs when concrete is subjected to high levels of stress (over 40% of the compressive strength).

The results of creep may be expressed by the creep coefficient which is the ratio between creep strain and elastic strain. When the stress is removed from concrete, the material exhibits an instantaneous recovery followed by a time-dependant recovery (creep recovery). Thus, concrete subjected to sustained stress presents an irrecoverable or residual strain after the unloading (Neville *et al.* 1983).

Factors affecting creep

According to Neville *et al.* (1983), the main factors influencing creep are aggregate to cement paste proportion, aggregate characteristics, water and cement content, age of concrete at time of lading, curing history, storage conditions, the admixtures and the applied stress to strength ratio. Some of these factors are discussed subsequently.

The hydrated cement paste is the main source of the deformations related to moisture variations. In general, creep appears to be inversely proportional to the rate of hardening. Therefore, ordinary Portland cement generally shows higher creep than the corresponding concrete containing high-early-strength cement. Additionally, for a cement content, an increase in the water-cement ratio leads to higher creep due to a probable reduction in the concrete strength and a more permeable system (Mehta and Monteiro 2006).

The relative humidity has a significant influence on creep deformations when there is no hygral equilibrium and the concrete undergoes a drying process. Once the hygral equilibrium is attained, the rate of creep turns independent of the relative humidity and the deformations correspond to those of the basic creep (Neville *et al.* 1983). In this regard, it is important to notice that real structures are subjected to drying process and hygral conditions are only possible to reproduce in the laboratories. The temperature is another factor to consider in the long-term deformation of concrete since its increase accelerates the rate of loss of moisture. However, when all the moisture is removed, the rate of creep is reduced and equal to that of pre-dried concrete.

The curing history is another fundamental aspect in the long-term deformations that is closely linked to the relative humidity and temperature. The concrete cured under moist conditions and exposed afterwards to ambient conditions exhibits higher drying creep rate and creep deformations than the concrete that remains wet or remains dry. In fact, Acker and Ulm (2001) indicated that the creep deformations of concrete in a dry atmosphere could be up to five times greater than the basic creep of concrete with the higher water content. This phenomenon reveals that not only the loss of water under sustained stress but also the amount of water present at the time of loading is relevant. In

fact, the concrete pre-dried at a high temperature presents little or no creep if compared with water-cured concrete.

From the abovementioned, it may be concluded that the creep deformations may vary depending on when the drying process takes place. If the drying occurs prior to the application of load, the creep is smaller than if the drying occurs while the load is applied. Furthermore, it is known that alternating humidity between two limits leads to higher values of creep than the ones resulting from a constant humidity within the two limits.

Several theories and mechanisms have been proposed over the years to explain creep in concrete. Despite the efforts of the scientific community, none of the theories is capable of explaining all the experimental evidence; hence the phenomenon of creep remains uncertain according to some authors (Neville *et al.* 1983; Bažant 2001).

2.5.2. Creep of SFRC

Basic concepts on the creep of plain concrete were reviewed in the previous section. Nonetheless, for fibre reinforced composites it is also important to know the creep behaviour of the fibre. Some deformations under sustained stress were reported (ASM-International 1990) when steel is exposed to temperatures over 370°C; however for temperatures under this value steel does not present creep.

The research regarding the long-term performance of SFRC is still limited if compared to that of conventional concrete. However, some early studies already proved the capacity of fibres to reduce creep deformations in compression and the shrinkage of concrete (Mangat and Azari 1986) as well as creep deformation due to flexural forces in uncracked specimens (Swamy and Theodorakopoulos 1979). A study on the long-term deformations of full-scale RC-SFRC beams subjected to flexural forces for ten years was conducted by Tan and Saha (2005). The authors reported a reduced long-term deflection and an enhanced cracking control.

Recent studies on the post-cracking creep behaviour of FRC under flexural forces confirm the results of the early studies with regard to the contribution of the steel fibres to control the long-term deformations. A summary of these studies is presented in Table 2.5, including main data such as the specimen size, the fibre type and content, the variables measured, the reference parameter defining the value of the preload (in terms of crack width or deflection) and the load level applied.

The following notation was used: W (width), H (height), L (length), VM (variables measured), DP (definition of preload), SF (steel fibre), PF (plastic fibre), BF (basalt fibre), w (crack width), δ (deflection), M_p (pre-cracking moment), F_p (pre-cracking load), σ_p (pre-cracking stress), ARS (average residual strength) and $\sigma_{0.5mm}$ (stress for a crack width of 0.5 mm during the characterization test). Notice that a number was appended to SF or PF (e.g. PF¹ and PF²) in case that more than one fibre of that type was used.

Table 2.5 Studies on the flexural creep post-cracking behaviour of FRC beams.

Reference	$W \times H \times L$ [cm]	Fibre type and content	VM [-]	DP [mm]	Load level
Chanvillard and Roque (1999)	15x20x70	SF:60 kg/m ³	w, δ	$w=0.3$ $w=0.6$	72% M_p 80% M_p
Granju <i>et al.</i> (2000)	15x20x70	SF:65 kg/m ³	w, δ	$w=0,3$	60% of F for a $\delta=l/300$ in bending
Kurtz and Balaguru (2000)	10x10x35	PF ¹ :0.9 kg/m ³ PF ² :0.9 kg/m ³	δ	$\delta=0.75$	22%-88% ARS (ASTM C1399/C1399M-10)
MacKay (2002) MacKay and Trottier (2004)	10x10x35	SF:24 kg/m ³ PF:4.5 kg/m ³	δ	$\delta<0.2$	20%, 40%, 60%, 80% ARS (ASTM C1399/C1399M-10)
Cochrane (2003)	10x10x35	SF:25 kg/m ³ PF:4.6 kg/m ³	δ	$\delta<0.2$	20%, 40% ARS (ASTM C1399/C1399M-10)
Bast <i>et al.</i> (2007) Kusterle (2009)	15x15x60	SF:30 kg/m ³ PF:4.5 kg/m ³	δ	$\delta=1.75$	47%, 60%, 71%, 80% of F for a $\delta=1.75$ mm
Barragán and Zerbino (2008)	15x15x60	SF:40 kg/m ³	w, δ	$w=0.2-3.5$	46%-100% σ_p
Arango (2010)	15x15x60	SF:40 kg/m ³ SF:70 kg/m ³	w	$w=0.5$ $w=1.5$	60%, 80% and 90% F_p
Kanstad and Zirgulis (2012)	12x15x60	SF:40 kg/m ³ PF ¹ : 1.0%* PF ² :0.7%* BF: 1.0%*	δ	$w=0.2$	Residual bending stress of 0.5 f_{Rm} at CMODs of 0.5 mm and 2.5 mm.
Buratti and Mazzotti (2012)	30x12x200	SF ¹ : 25 kg/m ³ SF ¹ : 35 kg/m ³ SF ¹ + SF ² +PF: 17+3+0.3 kg/m ³	w, δ	$w=0.2$	50% M_p
Serna <i>et al.</i> (2012)	15x15x60	PF ¹ , PF ² , PF ³ , PF ⁴ : 4.5 kg/m ³	w	$w=0.5$	75% $\sigma_{0.5mm}$

* The fibre content in kg/m³ was not available.

It should be remarked that only the studies by Arango (2010), Kanstad and Zirgulis (2012), Buratti and Mazzotti (2012) and Serna *et al.* (2012) specify that the pre-crack width corresponds to the crack mouth opening displacement (CMOD). Likewise, notice that Cochrane (2003) focuses on the behaviour under high temperature and Serna *et al.* (2012) study different ambient conditions.

The studies presented in Table 2.5 correspond to elements with fibres as the only reinforcement. However, there are also recent studies on full-scale RC-SFRC beams conducted by Vasanelli *et al.* (2012) and Nakov and Markovski (2012). Another study worthwhile mentioning is the one conducted by Mendes *et al.* (2012) on the creep behaviour of SCSFRC pedestrian bridges, in which two prototypes were built and monitored to assess their long-term deformations.

Even though the experimental research on the creep behaviour of SFRC is growing, the studies focused on the modelling are still scarce. Mangat and Motamedi Azari (1985) presented a theoretical model to predict creep of steel fibre reinforced cement matrices under compression. Chanvillard and Roque (1999) and Cochrane (2003) propose expressions obtained from regressions of the experimental data. Bernard (2010) indicated

that the behaviour of the concrete cannot be dissociated from that of the fibres due to the interactions between both materials. The author also proposed an expression based on rheological models to reproduce post-cracking creep behaviour of fibre reinforced shotcrete (FRS). Nevertheless, some of the parameters of the expression remain to be determined.

2.6. CONCLUDING REMARKS

The first part of this chapter reviewed the main European codes and guidelines for the design of FRC structures. The advantages and limitations of the current design procedures were discussed, identifying fundamental aspects regarding the properties and the characterization of FRC that still need to be considered.

The post-cracking response of FRC should be characterized with test methods that are representative of the real structure. Hence, the use of bending tests of small beams for any structural application may be arguable due to differences in the fibre orientation and the structural behaviour. The MC2010 proposes a novel approach by introducing an orientation factor that considers favourable or unfavourable orientations. Nevertheless, the assessment of this factor and its application is still a subject of study. Moreover, none of the current codes and guidelines takes into account the long-term behaviour of the material. The lack of extensive research on the topic is the main reason for that.

Once the motivations of this research were identified, the second part of the chapter covered the state of the art of the subjects addressed in this thesis. Firstly, the current test methods to determine the post-cracking response of FRC and the criteria upon which a test method should be chosen were reviewed. The low representativeness of the beam test for certain applications (e.g. slabs) and the high scatter suggests that a different approach should be considered. In this sense, it is advisable either to use specific tests for each structural application or consider the differences between the response of the test specimen and the real structure by means of geometry factors.

Secondly, the factors influencing fibre orientation were described. These factors lead to preferential orientations of the fibres in the concrete matrix that may be advantageous in certain structures. The possibility that the dimension of the element might favour a certain orientation and, therefore, improve the structural response would be very interesting in the design. With regard to the techniques to measure fibre orientation, a tendency towards the development of non-destructive methods that may be used in real structures is observed in the most recent studies.

Finally, some basic concepts of the creep behaviour of concrete and the most recent advances in the study of post-cracking creep behaviour of FRC were reviewed. It was concluded that, despite the growing experimental research on this subject, the studies focused on the modelling and prediction are scarce.

3. FLEXURAL BEHAVIOUR AND MODELLING OF RC-SFRC BEAMS

3.1. INTRODUCTION

The Part I of the thesis revealed a common philosophy in the design procedures in the European codes and guidelines: an approach based on simplified continuous non-differentiable constitutive diagrams whose parameters are identified by using inverse analysis procedures calibrated with the results of bending tests on small specimens. Despite their common approach, none of these guidelines was generally accepted for the design of FRC structures until the publication of the MC2010, which may be considered as an advance towards a single consistent design framework across Europe.

Given that small-scale bending tests are used for the characterization of the post-cracking behaviour of SFRC, it may be expected that the constitutive model in these design procedures are adequate to simulate the structural response of real-scale beams. Nevertheless, the differences identified in Part I of the thesis among the constitutive models in terms of the shape of the diagram as well as the parameters defining model may lead to variations in the predictions that should be analysed.

In this sense, a comparative study on of the capacity of the constitutive models in European codes and guidelines, including the new MC2010, to predict the behaviour of real-scale beams may be of great interest in order to identify the most suitable procedure to simulate the tensile post-cracking behaviour of SFRC.

3.1.1. Objectives

In view of the exposed, the objective of this chapter is to analyse the suitability of the constitutive models in European design codes and guidelines for the design of SFRC structures based on the flexural response of beams with steel fibres and rebars. In order to achieve the aforementioned goal, the following specific objectives are defined:

- Assess the structural response of real-scale RC-SFRC beams in terms of cracking, bearing capacity and energy absorption;
- Evaluate the influence of different steel fibre types and content on the post-cracking behaviour of the RC-SFRC beams;
- Simulate the response of the RC-SFRC beams by means of a non-linear sectional analysis using the constitutive models presented in five different design codes and guidelines and
- Identify the constitutive models that reproduce better the response of the material based on the experimental results.

3.1.2. Outline of the chapter

In section 3.2, an experimental program is presented to study the structural behaviour of elements with a combined reinforcement of rebars and steel fibres. Subsequently, in section 3.3 the results are analysed, focusing in the cracking, the efficiency of the fibres and the results of the load-displacement curve¹.

By means of a numerical model, briefly presented in section 3.4, the tests of the RC-SFRC beams are simulated with each of the constitutive models proposed in the European design codes and guidelines studied in Chapter 2. In section 3.5, the results of the simulations are compared to the experimental data in order to evaluate which model provides a better prediction². Finally, in section 3.6, the main conclusions of the study are highlighted.

3.2. EXPERIMENTAL PROGRAM

3.2.1. Specimens

The elements tested were simply-supported beams with a length of 3.0 m, a width of 1.0 m and a height of 0.2 m. The reinforcement was composed by rebars and steel fibres (except in the case of two control beams reinforced only with rebars). The conventional

¹ The experimental study conducted in this chapter and their results were published in: Pujadas, P., Blanco, A., Fuente, A. and Aguado, A. Cracking behavior of FRC slabs with traditional reinforcement. *Materials and Structures*, 2012, vol. 45, no. 5, p. 707-725.

² The numerical study and the comparative analysis performed were published in: Blanco, A., Pujadas, P., de la Fuente, A., Cavalaro, S. and Aguado, A. Application of constitutive models in European codes to RC-FRC. *Construction and Building Materials*, 2013, vol. 40, p. 246-259.

reinforcement (B500S) consisted of seven bars with a diameter of 16 mm in longitudinal direction and bars with a diameter of 8 mm every 20 cm in transversal direction (see Figure 3.1). The nominal concrete cover in the longitudinal and in the transversal reinforcement was 35 mm and 50 mm, respectively. Although the configuration of the reinforcement corresponds to a slab, the element behaves like a beam due to the test setup defined for this experimental program (see section 3.2.3). The beams were produced at the BEKAERT S.A facilities in Belgium.

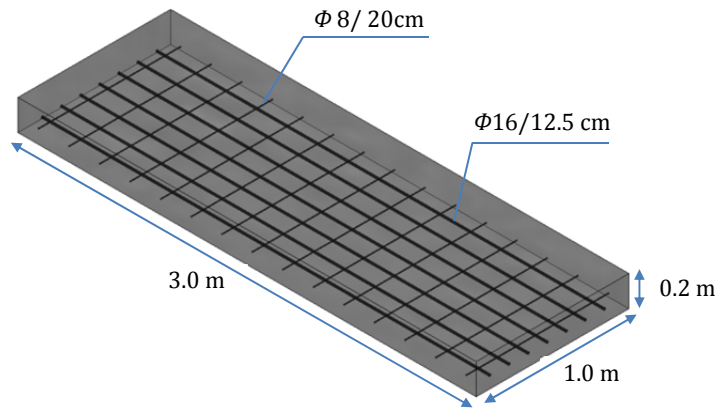


Figure 3.1 Traditional reinforcement of the beams.

3.2.2. Materials and concrete mix

Four SFRC mixes were prepared varying the fibre type and content, as well as a conventional concrete for the control beams. In this sense, even though fibres reduce the workability of concrete, a change of the SFRC mix was not considered necessary due to the satisfactory fresh-state aspect of the material. The main characteristics of the mix used are: a water/cement ratio of 0.55, a cement content of 300 kg/m³, a maximum aggregate size of 16 mm and a super-plasticizing content of 1.5%. The consistency of the mixture is soft (S4) according to Eurocode 2 (CEN 1992). The strength class of the SFRC was C25/30.

Fibre contents of 0.25% and 0.50% in volume (20 kg/m³ and 40 kg/m³, respectively) were tested. Two types of hooked-end steel fibres gathered into bundles by water-soluble glue (SF1 and SF2) were used. The main characteristics of the steel fibres are shown in Table 3.1.

Table 3.1 Characteristics of the fibres (provided by the manufacturer).

Characteristics		SF1	SF2
Length (L)	[mm]	35	60
Diameter (d)	[mm]	0.55	0.75
Aspect ratio (L/d)	[-]	64	80
Tensile strength (f_f)	[MPa]	1100	1050
Modulus of elasticity (E)	[GPa]	210	210
Number of fibres per kg	[-]	14500	4600

The beams were cast by pouring the concrete from a skip with a lateral outlet and moveable flow control chute placed, approximately, at a height of 40 cm over the bottom surface of the formwork. The concrete was vibrated externally to ensure a uniform distribution. The beams were removed from the moulds within 48 hours of casting and were moist cured under a plastic sheet. Subsequently, the beams were transported to the Laboratory of Structure Technology Luis Agulló at UPC to be tested.

Table 3.2 shows the date of the production and the notation used to refer to the beams. The notation indicates the type of reinforcement (RC, SF1 o SF2), the fibre dosage (0.25% or 0.50%) and the specimen (A or B; this corresponds to each of the two beams per type of reinforcement and fibre dosage). The RC abbreviation corresponds to the beams with conventional reinforcement without fibres, whereas SF1 and SF2 correspond to the elements with mixed reinforcement according to the type of fibre.

Table 3.2 Series of casting and notation.

Series	Date	Notation of the beams	
RC	18/02/2008	RC_A	RC_B
SF1 0.25 %	04/02/2008	SF1 0.25%_A	SF1 0.25%_B
SF1 0.50 %	04/02/2008	SF1 0.50%_A	SF1 0.50%_B
SF2 0.25 %	03/03/2008	SF2 0.25%_A	SF2 0.25%_B
SF2 0.50 %	03/03/2008	SF2 0.50%_A	SF2 0.50%_B

A total of ten concrete specimens as the one described in Figure 3.1 were cast (two elements per each fibre type and dosage). Additionally, six cubic samples (150 x 150 x 150 mm) and six prismatic samples (150 x 150 x 600 mm) were cast for the characterization of the compressive and residual flexural strengths, respectively. The notation used in the case of the samples is the same as the ones used for the beams.

The results of the compression test according to EN 12390-3:2009 (CEN 2009) and the flexural test according to EN14651:2005 (CEN 2005) are included in Table 3.3. These are presented in terms of average compressive strength (f_{cm}), limit of proportionality (f_l) and residual flexural strengths (f_{R1} , f_{R2} , f_{R3} and f_{R4}) for crack mouth opening displacements of 0.05 mm, 0.5 mm, 1.5 mm, 2.5 mm and 3.5 mm, respectively. Notice that the characterization of the mixes was performed at BEKAERT S.A. facilities.

Table 3.3 Compressive and residual flexural strengths at 28 days.

Property	RC		SF1 0.25%		SF2 0.25%		SF1 0.50%		SF2 0.50%	
	Average [MPa]	CV [%]	Average [MPa]	CV [%]	Average [MPa]	CV [%]	Average [MPa]	CV [%]	Average [MPa]	CV [%]
f_{cm}	22.0	5.57	36.5	5.07	29.0	4.22	30.5	1.34	26.0	5.98
f_l	-	-	3.84	8.48	3.35	5.19	3.62	12.33	3.12	11.91
f_{R1}	-	-	2.55	34.94	2.96	22.50	4.10	21.75	3.93	17.56
f_{R2}	-	-	2.44	38.76	3.16	26.21	4.18	22.95	4.49	21.54
f_{R3}	-	-	2.22	38.27	3.23	27.03	3.94	23.37	4.56	22.64
f_{R4}	-	-	1.99	35.91	3.10	26.56	3.49	24.10	4.62	20.07

The results show that the compressive strength decreases with the fibre content for both types of fibres. This is explained by the influence of high fibre contents that may lead to bigger pore volume in the granular skeleton (Markovic 2006). Fibres SF2, which have a higher ratio than SF1 (see Table 3.1), present a lower compressive strength value for both contents. A similar outcome may be observed in Bencardino *et al.* (2008).

The values of residual flexural strengths of the four series present a high scatter, above 20 % in almost all cases. This order of magnitude in the scatter of the flexural test was already reported in the literature by several researchers (Dupont and Vandewalle 2004; Parmentier *et al.* 2008; Molins *et al.* 2009). In this sense, regarding the global results presented in subsequent sections, the use of rebars helped to reduce the scatter in the mechanical response of the beams.

The long fibres (SF2) turn out to be more active in bridging the cracks when the cracks are bigger, providing a more stable post-cracking response. However, the shortest fibres (SF1), in spite of being very efficient for the control of smaller cracks, become less active as the crack increases due to the fact that they are subjected to a higher pull-out. Finally, a point is reached when the fibre length embedded in the concrete is insufficient for them to take part in the transfer of stress mechanisms. This behaviour results in lower residual strength values for large crack widths. The residual strength for a CMOD of 3.5 mm for SF2 is 55.8% higher than for SF1 for a fibre volume of 0.25% and 32.4% higher for a volume of 0.50%. This behaviour of fibres will be further discussed in section 3.3.

3.2.3. Test setup

The tests were conducted using a MTS® load frame with a maximum capacity of 1000 kN. A piston connected to the load frame by means of a tridimensional joint applied the load on a stiffened steel beam (IPN 550), which transfers the load to two HEB 140 steel beams as shown in Figure 3.2a. The latter were located all along the width of the elements to ensure a continuous loading line and were designed to have a minimum influence in the results of the test. Between the HEB 140 beams and the top of the concrete beam, a layer of neoprene of 5 mm, was placed to ensure full contact in the loading surface. The concrete beams were supported along the two short sides on top of steel beams (see Figure 3.2a).

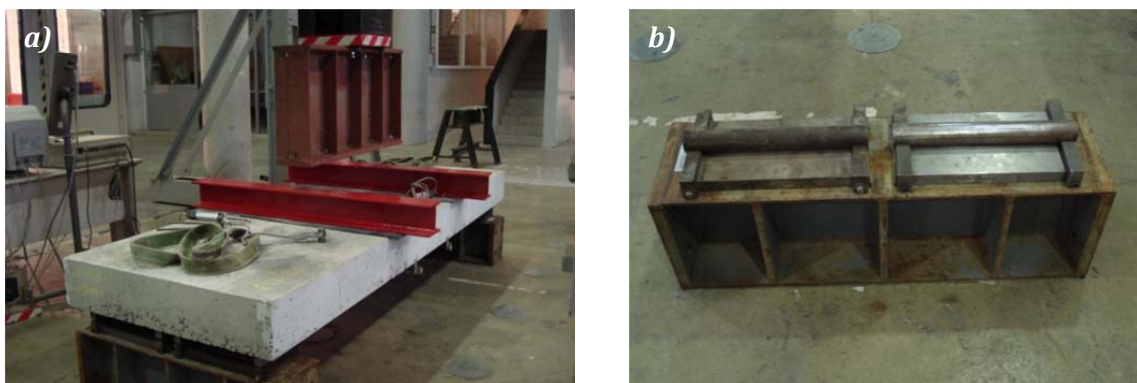


Figure 3.2 Details of a) the loading system and b) the joints in the supports.

Steel joints were placed between the concrete and the supports (see Figure 3.2b) in order to ensure the free rotation. The joints were arranged so that the horizontal movements were restrained only in one of them. As a result, the setup follows an isostatic configuration similar to a four point bending test with a span of 2.7 m and a distance between loading lines of 0.9 m, as indicated in Figure 3.3.

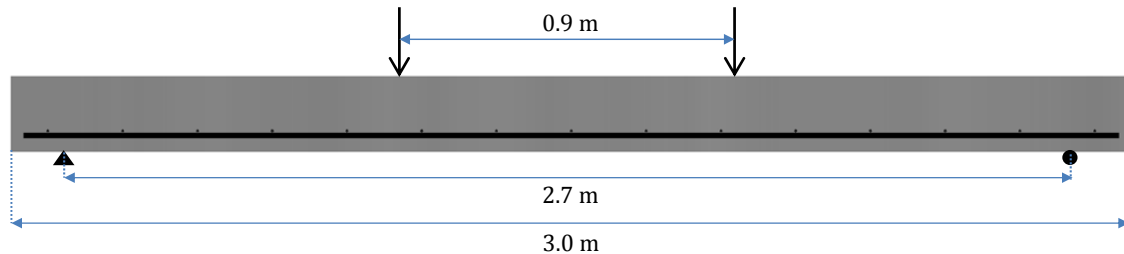


Figure 3.3 Isostatic setup of the test and dimensions.

Two displacement transducers, placed horizontally on both sides of the elements, measured the crack width in the central 45 cm during the loading procedure. In order to obtain more detailed information regarding the crack width at the early stages of the loading procedure, twenty fixed points were located in both sides of the elements (ten per side). These points were placed 2 cm above the bottom of the slab and with an approximate spacing of 15 cm (see the numbered points in Figure 3.4). The fixed points covered a length of 135 cm in both sides. The distance between these points was measured before the loading and at different stages of the test with an extensometer in order to determine the width of the cracks that appear in each stretch.

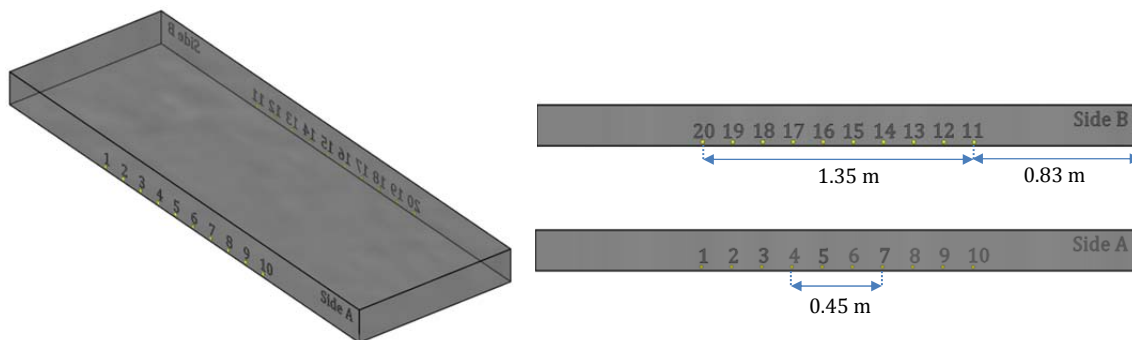


Figure 3.4 Location of the fix points in both sides of the beam.

In Figure 3.5 a detail of the fixed points and the extensometer are presented. Besides measuring the crack width, a third displacement transducer was placed vertically at the midspan section in order to measure the deflection. Moreover, the displacement and the load applied by the jack were also measured during the test.

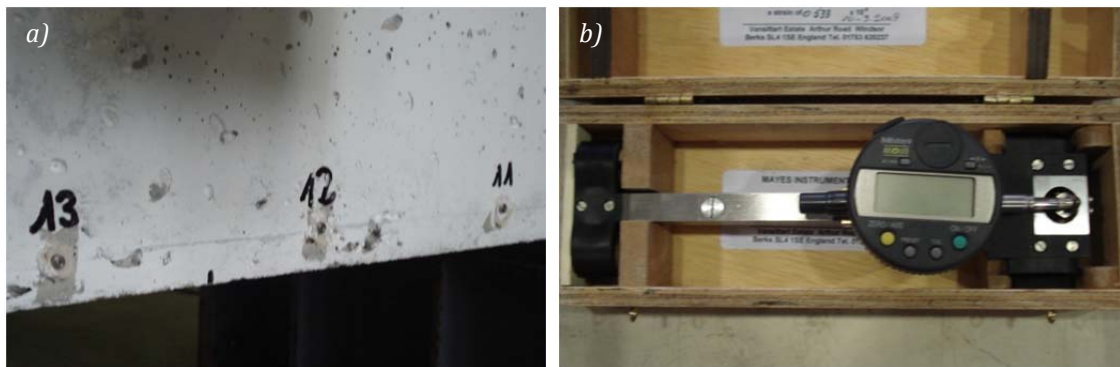


Figure 3.5 a) Detail of the fixed points and b) Digital extensometer.

The test is performed with displacement control and the loading procedure was divided in six sequential stages. In each of the first five stages, the displacement was applied in incremental stretches of 20 kN. After each stretch, the load was sustained for approximately 20 minutes. The first ten minutes served to stabilize the deformation of the beam. Then, the cracks were marked and photographed in both sides of the beams, thus recording the crack propagation. Additionally, the distance between the fixed points was also measured. In the sixth stage, the loading was continuously applied until the end of the test. A constant displacement rate of 0.025 mm/s was used.

3.3. RESULTS

The analysis of the results is structured in three sections according to the studied variables: the crack pattern, the crack width and the load-displacement curves. Given the amount of traditional reinforcement used, the rebars have a major influence in the behaviour of the beams. Nevertheless, the addition of steel fibres provides more ductility and enhances the bearing capacity.

3.3.1. Crack pattern

The crack patterns of both sides (side A and B) of the beams are presented in Figure 3.6 according to the notation previously described in section 3.2.2. The crack pattern of side B is represented symmetrically taking the bottom surface of the beam as a symmetry axis. The cracks are plotted in different colours that represent the history of propagation depending on the load level. The legend of colours for the crack propagation is: green up to 40 kN, blue up to 60 kN, red up to 80 kN, black up to 100 kN and yellow up to the end of the test.

The crack patterns indicate that the addition of steel fibres leads to the formation of more cracks with smaller spacing, as previously reported by Tan *et al.* (1995). This is mainly influenced by the post-cracking behaviour of SFRC and the improvement in adherence between the passive reinforcement and the concrete due to the presence of fibres, leading to the reduction of the bond transfer length (Bischoff 2003).

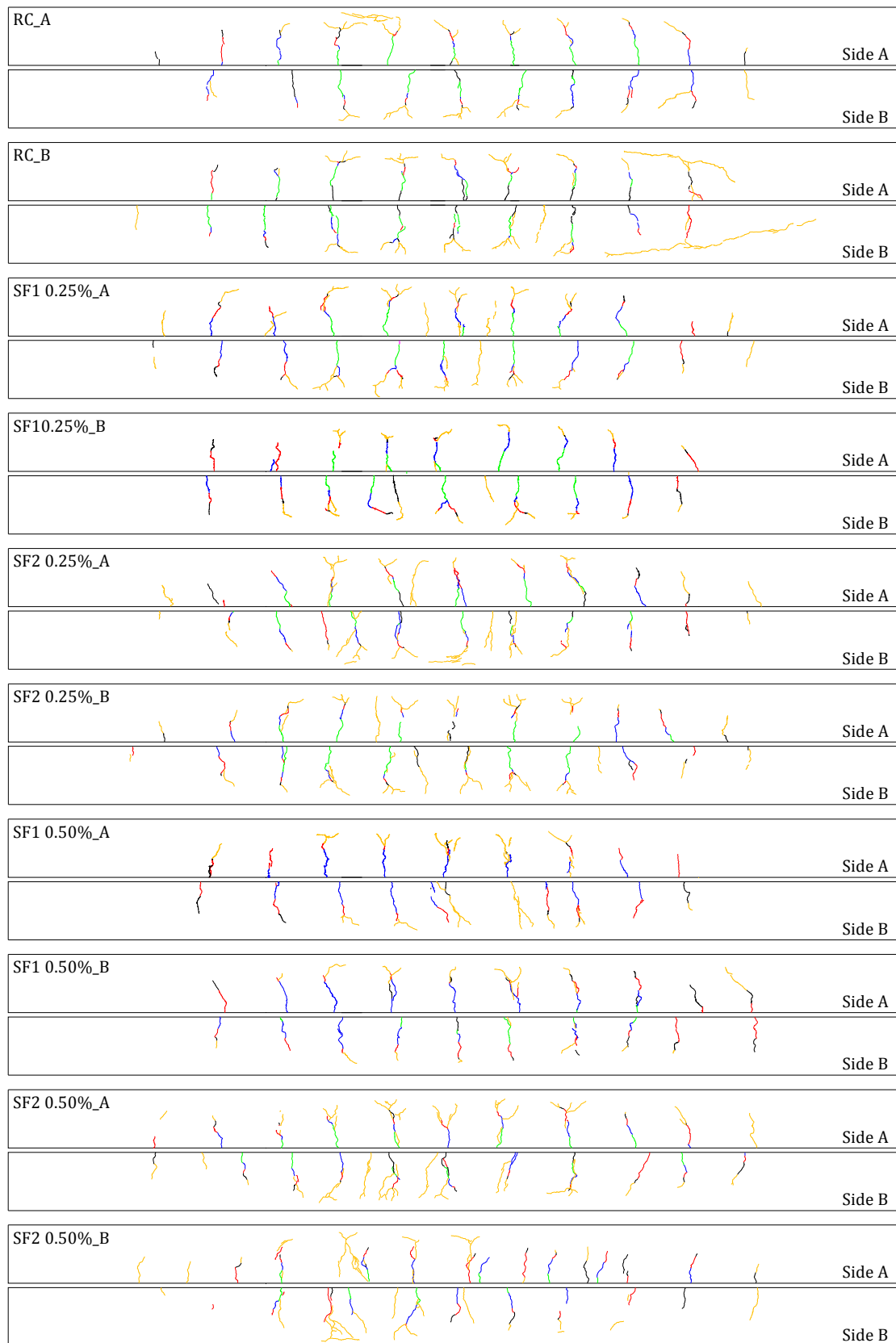


Figure 3.6 Crack patterns.

Furthermore, significant crack ramification was detected in the SF elements, especially those with a higher fibre content (see SF2 0.50%_A and SF2 0.50%_B in Figure 3.6). A common feature observed in all the elements is the symmetry in the formation of the cracks in both sides.

Regarding the history of the crack propagation, the patterns reveal that the first cracks become noticeable for the naked eye at different load levels depending on the fibre content. In the case of the SF elements with higher fibre content, the bridging effect provided by the fibres makes that the first cracks become visible at 60 kN (plotted in blue in Figure 3.6), whereas for lower contents and for the RC elements the first cracks are observed at 40 kN (plotted in green in Figure 3.6). Almost all of the cracks had already appeared at 80kN, however from that load until the end of the test a significant growth and ramification occurred.

After the fifth stage of loading (for loads higher than 100 kN) secondary cracks appeared in the SF beams. Only in the case of the beam RC_B shear cracks developed on both sides. Additionally, in some cases, horizontal small cracks along the compression block were observed for advances loading stages. This was particularly evident in the beams RC_A (side B), SF2 0.25%_A (side B) and SF2 0.50%_A (side B).

Table 3.4 shows the average number of cracks and crack spacing as well as the crack spacing predicted with the formulation proposed by the RILEM-TC162-TDF recommendations (Vandewalle *et al.* 2003) and Italian code CNR-DT 204 (CNR 2006). The study was limited to the central 90 cm of the beam in order to avoid the interaction with shear cracks observed in RC_B near the supports.

Table 3.4 Average crack number and spacing and predicted crack spacing.

Type of fibre	Fibre content [%]	Average number of cracks	Average crack spacing [cm]	Crack spacing prediction in RILEM and CNR-DT 204 [cm]
RC	-	10	19.0	17.2
SF 1	0.25	11	15.6	13.5
SF 1	0.50	10	18.6	
SF 2	0.25	12	15.9	10.8
SF 2	0.50	13	14.1	

The average value of crack spacing observed in the RC beams points out the influence of the transversal reinforcement location - separated 20 cm (see Figure 3.1) - in the formation of the cracks. Due to the reduction of the area of concrete in the sections where the transversal reinforcement is located, the cracks tend to line up with it. Detailed studies about the contribution of the transversal reinforcement may be found in Lee *et al.* (1989) and Fernández Ruiz (2003). A reduction of the average crack spacing is detected in the beams with SF if compared to that of RC beams. In the case of the SF2 beams, the increase of fibre content results in a higher average number of cracks and lower average crack spacing. Nevertheless, for the SF1 beams the increase of fibre content does not imply a decrease in the crack spacing.

This phenomenon was previously observed by Dupont (2003), who reported that increasing the fibre content from 0.25% to 0.50% can result in either a small reduction of the crack spacing (around 6%) or no reduction in some cases. The results from another study by Vandewalle (2000) also indicate that increasing the amount of fibres from 0.40% to 0.60% did not lead to a reduction of the crack spacing in all the cases studied. However, Dupont (2003) reported that if the fibre content increases to 0.75%, the crack spacing can be reduced 30% with respect to the beams with 0.25% of fibres. This behaviour suggests that, for low and moderate contents (below 0.75%), the increase in fibre content does not always lead to a reduction of the crack spacing.

In Table 3.4, the crack spacing predicted by the formulation in the RILEM and the CNR-DT 204 underestimates the value of the average crack spacing. This difference might be due to the presence of the transversal reinforcement.

3.3.2. Crack width

Analysis at serviceability

The curves presented in Figure 3.7 correspond to the average crack width measured in the fixed points located in the central 45 cm of each side (points 4-7 in side A and points 14-17 in side B in Figure 3.4). Notice that the distance between the points was not measured during all the loading procedure, only for certain values of load: 20 kN, 40 kN, 60 kN, 80 kN and 100 kN. The average value of crack width is obtained by dividing the distances measured by the number of cracks that appeared in each stretch.

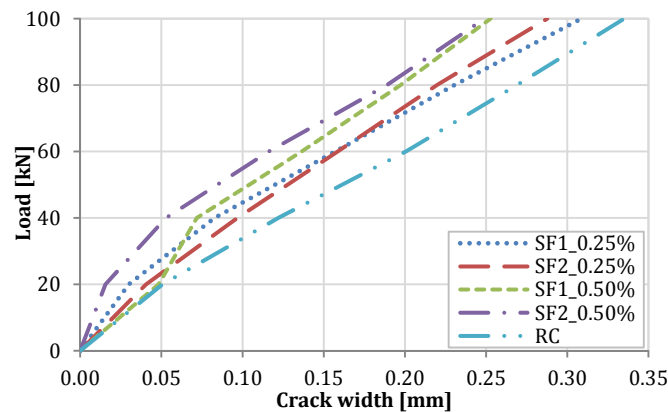


Figure 3.7 Load-crack width curves up to 0.40 mm.

The results of the SF elements with lower fibre content indicate that the shortest fibres (SF1) enabled a better cracking control for crack widths lower than 0.15 mm, but the longest fibres (SF2) turn out to be more active in bridging the cracks when these grow. Nevertheless, the described behaviour is not so evident if the content of fibres doubles since SF2 elements exhibits a better performance than SF1 in terms of cracking control up to 0.20 mm, moment at which both types present a very similar response.

Table 3.5 presents the corresponding average crack widths (from beams A and B) for the load values of 40 kN and 80 kN. Additionally, the crack width prediction provided by the formulation in the RILEM for those two load levels were calculated by means of the numerical model presented in section 3.4.1.

Table 3.5 Crack width values for 40 kN and 80 kN and prediction with RILEM formulation.

Element	Fibre content [%]	Crack width [mm]			
		For 40 kN		For 80 kN	
		Experimental	RILEM	Experimental	RILEM
RC	-	0.120	-	0.270	-
SF1	0.25	0.080	0.039	0.230	0.203
SF2	0.25	0.100	0.063	0.220	0.226
SF1	0.50	0.070	0.035	0.200	0.200
SF2	0.50	0.050	0.044	0.190	0.215

From the results, a significant reduction in the crack width values is observed when compared to the RC beams. In this sense, the addition of 0.50 % in volume of SF1 and SF2 leads to a reduction of the average crack widths of 41.7 % and 58.3 %, respectively, for a load of 40 kN. In the case of 80 kN, the value of crack width decreases 25.9% and 29.6% for SF1 and SF2, respectively. The different behaviour of the fibres SF1 and SF2 will be further discussed later in this section.

Regarding the estimation provided by the RILEM formulation for a load of 40 kN, an underestimation of the crack widths is observed in all cases, being in some cases the estimated value 50% lower than the one experimentally observed. Nevertheless, the reason for such difference is that the formulation is conceived for stabilized cracking, whereas the prediction is made for early stages of the loading (only 40 kN). In fact, for the load level of 80 kN, when it can be assumed that cracking is stabilized, this tendency changes and the prediction is very close to the experimental data. The estimated values are 12% lower for SF1 0.25%, 3% higher for SF2 0.25% and 13 % higher for SF2 0.50%. In the case of SF1 0.50 %, the prediction equals the measured value.

Analysis at failure

The curves presented in Figure 3.8 correspond to the average crack width measured with the displacement transducers located in the central 45 cm of both sides of the beam. The values of average crack width are obtained by dividing the distance measured during the loading by the number of cracks that appeared in that stretch.

The curves show that for large crack widths, the SF2 elements exhibited an improved response when the fibre content is doubled (see Figure 3.8a for 0.25% in volume and Figure 3.8b for 0.50%), whereas for the SF1 beams the difference was not so noticeable. For a more detailed analysis, the experimental crack widths measured for the load values of 150 kN and 200 kN are presented in Table 3.6. Even though the values of crack width associated to this load levels are above the range of serviceability, the analysis is conducted to compare the bridging action of the two types of fibres for high loads.

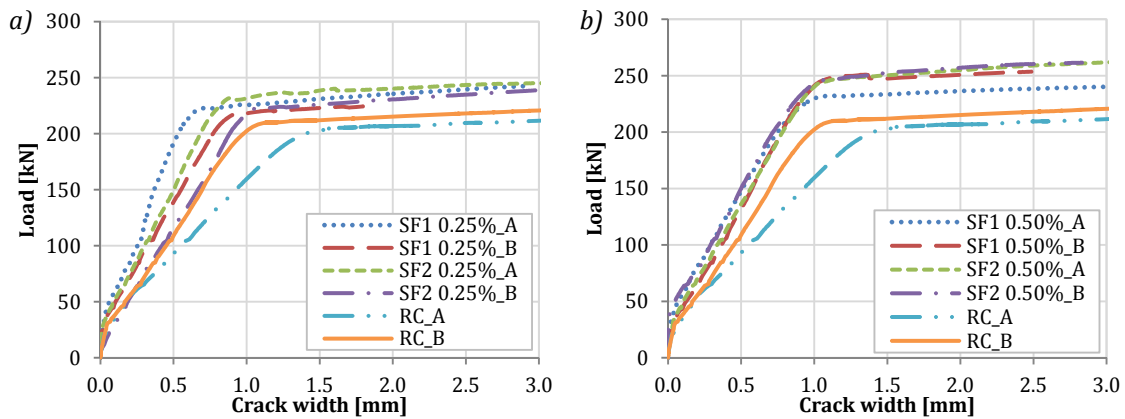


Figure 3.8 Load-crack width for fibre contents of a) 0.25% and b) 0.50% in volume.

Table 3.6 Crack width values for different load levels: 150 kN and 200 kN.

Element	Fibre content [%]	Crack width for 150 kN [mm]	Crack width for 200 kN [mm]
RC	-	0.80	1.19
SF1	0.25	0.55	0.77
SF1	0.50	0.54	0.77
SF2	0.25	0.58	0.78
SF2	0.50	0.53	0.75

From the results in Table 3.6, a noticeable reduction of the crack width is detected when fibres are added, as reported in other studies by Tan *et al.* (1995), Vandewalle (2000), Dupont (2003) and Altun *et al.* (2006). At 150 kN, this reduction with respect to the RC beams represents 31.3% for SF1 0.25%, 32.5% for SF1 0.50%, 27.5% for SF2 0.25% and 33.8% for SF2 0.50%. In the case of 200 kN, this reduction increases to 35.3% for both SF1 0.25% and SF1 0.50%, to 34.5% for SF2 0.25% and to 37.0% for SF2 0.50%.

The results for the SF1 beams indicate that, despite increasing the dosage from a low (0.25%) to a moderate content (0.50%), a reduction of the crack width practically does not occur. Such behaviour suggests that, for this type of fibres, a high content (0.75% or higher) might be necessary to observe a significant reduction of the crack width. For the SF2 beams, a more noticeable cracking control is detected when doubling the amount of fibres. Nonetheless, an even greater reduction could be obtained with higher fibre contents.

Analysis of the load increase-crack width relation

An analysis of the crack width in relative terms (taking as a reference the RC beams) to study the differences between the two fibres was conducted. Figure 3.9 shows the load increment of the SF beams presented relatively to the load measured for the RC beams at the same crack width.

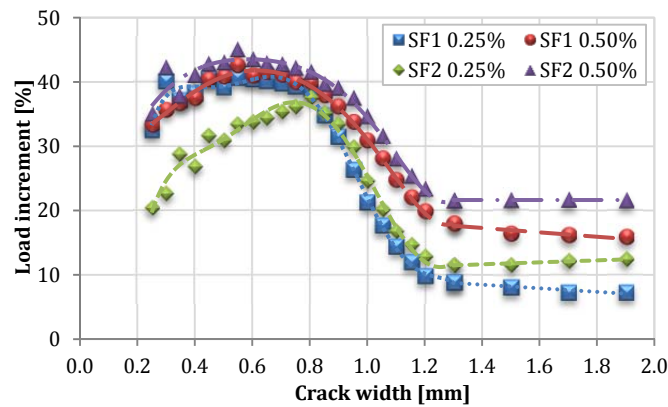


Figure 3.9 Load increase [%]-crack width curve.

From the curves, a common tendency is identified: the increment of average load increases up to a certain value (corresponding to a crack width around 0.6 mm) after which it decreases until stabilizing around 1.3 mm. Both types of fibres present a high aspect ratio, however SF2 is almost twice as long as SF1 (see Table 3.1). The difference in length influences the behaviour of the material as short fibres (SF1) start working at earlier stages than the long ones (SF2), thus becoming more efficient at smaller crack widths. As cracks grow, the short fibres lose anchorage and the long ones become more active in the bridging process, enhancing ductility and residual strength (Markovic 2006). This phenomenon was reported in the studies by Lawler *et al.* (2005) and Sorelli (2006).

Considering a content of 0.25%, the load increment for crack widths smaller than 0.5 mm is higher for SF1 beams. Nevertheless, at a crack width around 0.8 mm, the SF2 beams show higher load increments. In the case of a content of 0.50%, both types of fibres present very similar response with slightly higher increments for SF2. In the final stretch of the curve, the load increment stabilizes and remains almost constant from 1.3 mm. On this stage of the cracking, the load increments relative to the RC beams for the lower fibre content are 8.8% and 11.6% for SF1 and SF2, respectively. For higher contents, these increments are 18.0% and 21.6% for SF1 and SF2, respectively.

The shape of the curves of Figure 3.9 may be explained by the different stages of the stress profile of the cross section presented in Figure 3.10.

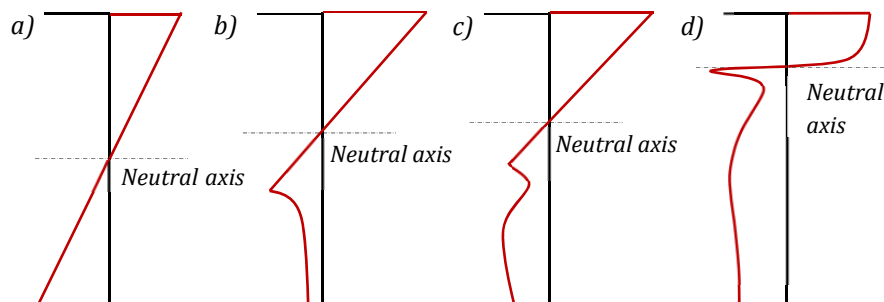


Figure 3.10 Stress profile of a SFRC section at different stages: a) linear-elastic behaviour; b), c) and d) post-cracking behaviour at different stress levels.

The stress profile in Figure 3.10a corresponds to the linear-elastic behaviour prior to cracking. The contribution of the fibres occurs after the instantaneous loss of stiffness due to the cracking of the matrix (as shown in Figure 3.10b). Subsequently, the fibres reach their maximum contribution at a certain point with a stress profile similar to the one in Figure 3.10c. This maximum contribution is determined by the type and amount of fibres. Afterwards, the fibres lose adherence and slide from the cement matrix (see Figure 3.10d). This pull-out mechanism results in a reduction of the load increment until it becomes stable as previously observed in Figure 3.9.

3.3.3. Load-deflection curves

Analysis at serviceability

The load-deflection curves up to a deflection of 5 mm are presented in Figure 3.11 for each pair of beams (for e.g.: SF1 0.25%_A y SF1 0.25%_B). The curves in Figure 3.11a correspond to a fibre content of 0.25%, whereas Figure 3.11b presents the curves of the beams with a content of 0.50%. In both cases the curves corresponding to the RC elements are also included.

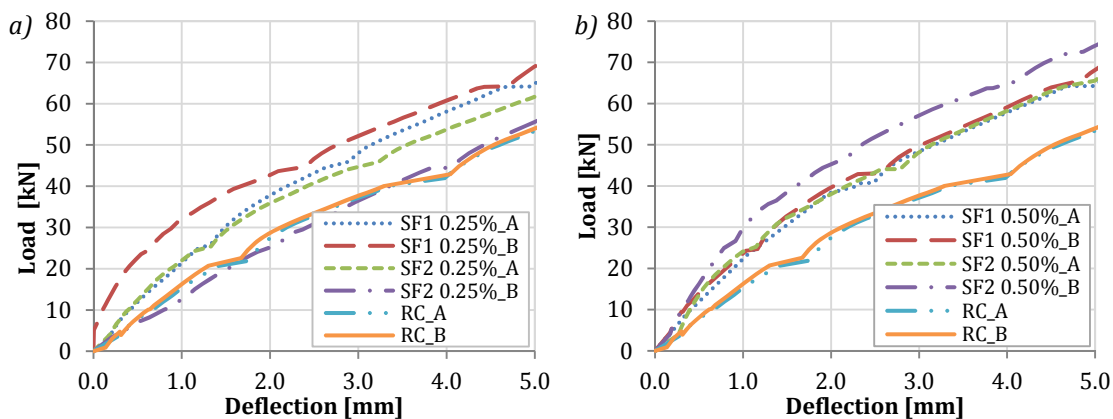


Figure 3.11 Load-deflection curves up to 5 mm for a) 0.25% and b) 0.50% in volume.

The load-deflection curves reveal that the fibre leading to a better performance for small deflections is SF1. Nevertheless, when the amount of fibres doubles, the SF2 0.50% elements exhibit a better response in general terms (see Figure 3.11b).

Analysis at failure

The analysis of the load-deflection curves is extended to failure in this section. For that purpose, the complete load-deflection curves are presented in Figure 3.12a for the case of 0.25% and in Figure 3.12b for the case of 0.50%. The curves for the RC beams are also included in both cases.

Three stages can be distinguished in the curves presented in Figure 3.12: the pre-cracking stage, the post-cracking stage and the pre-failure of the beam. In the first stage, a

linear behaviour may be assumed for all the materials of the cross-section. This linear behaviour between stresses and strains of the materials is maintained until concrete cracks (when it reaches a stress f_{ct} , which takes place for the bending moment M_{cr}). During the cracking process, the stresses endured by the tension block of concrete are transmitted to the steel through the mechanisms of adherence and strain compatibility between them. During the second stage, concrete has cracked and both the steel bars and the fibres begin to develop their resistance mechanism. Finally, the third stage corresponds to the stretch subsequent to the yielding of the reinforcement.

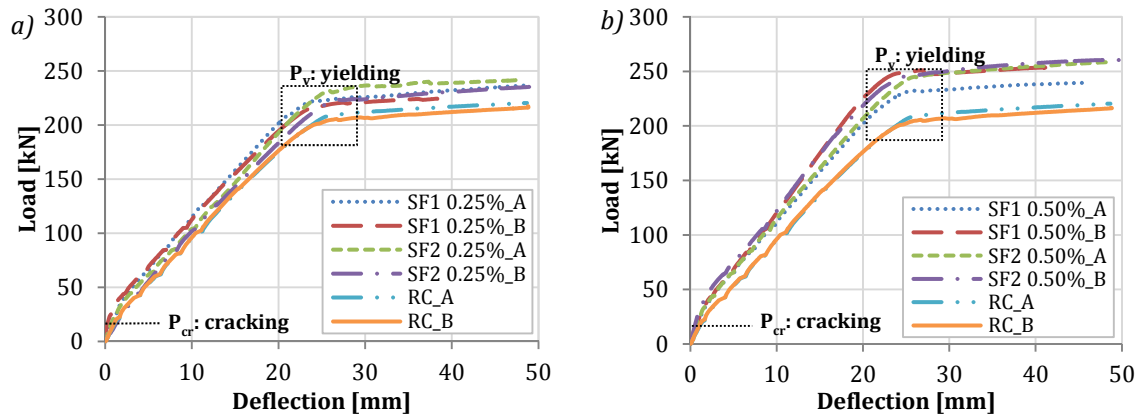


Figure 3.12 Load-deflection curves for a) 0.25% and b) 0.50% in volume.

The results in Figure 3.12 indicate that for a reference deflection of 30 mm (corresponding to a stabilized contribution of the fibre according to the study in section 3.3.2 in terms of crack width) the increase in load with respect to the RC elements is 5.7%, 8.7% for SF1 and SF2 with a fibre content of 0.25%, respectively (see Figure 3.12a). For content of 0.50% in volume, the increment in load for 30 mm doubles, reaching values of 13.9%, 17.7% for SF1 and SF2, respectively.

The behaviour in each stage is evaluated through the slopes of the curves, calculated by considering each of the stages as a straight line. The values of the slopes (in kN/mm) for each stage are presented in Table 3.7.

Table 3.7 Slope of load-deflection curves for each of the aforementioned stages (in kN/mm).

Element	Fibre content [%]	Stage 1: Pre-cracking	Stage 2: Post-cracking	Stage 3: Yielding of reinforcement
RC_A	-	16.5	7.90	0.373
RC_B	-	14.6	7.90	0.389
SF1_A	0.25	20.7	8.80	0.548
SF1_B		38.4	8.40	0.457
SF2_A	0.25	21.9	8.90	0.682
SF2_B		12.5	8.20	0.577
SF1_A	0.50	20.7	9.20	0.711
SF1_B		22.7	10.90	0.687
SF2_A	0.50	31.7	9.40	0.751
SF2_B		34.1	10.40	0.805

The results confirm the behaviour described above since. Despite the limited experimental results, the addition of fibres implies an increase in the value of the slope in all cases. The increase is particularly significant in stage 1 and stage 3. When the cracking of the matrix occurs, in the second stage, a decrease in the stiffness is detected. It must be remarked that in stage 2, the addition of fibres also involves an increase in the value of slope, even though not as pronounced as in the other stages with small differences between the type and amount of fibres used.

Given that the only difference among the elements (regarding the material) is the type of fibre, no differences should be observed in the slopes prior to cracking (stage 1) since the strengthening action of the fibres has not yet been activated. Therefore, the differences observed in the values in Table 3.7 might be attributed to the accommodation between the elements involved in the test setup. On the other hand, the significant influence of the rebar reinforcement in stage 2 partially eclipses the contribution of the fibres, thus justifying the small differences observed in the slopes in relative terms. Once the rebars yield (stage 3), the relative differences in the slopes attributed to the fibre contribution increases, despite the small differences in absolute terms.

Analysis of the energy absorption capacity

Several approaches to assess the energy absorption capacity such as tenacity indexes or factor of tenacity under deflection and fracture energy may be found in the literature (Hillerborg *et al.* 1976; ASTM 1991). The tenacity according to JSCE-SF4 (1984) is calculated for a standard-sized sample as the area under the load-deflection curve up to a limit of $L/150$. There are similar indexes proposed in other regulations such as DBV (1991); DBV (1992a); DBV (1992b); AENOR (2004a).

In this study, the absorbed energy was assessed by calculating the enclosed areas by the load-deflection curves up to a midspan deflection of 40 mm. Table 3.8 presents the absorbed energy, the increase of this parameter with regard to the RC beams and the average increment for a content of 0.25% and 0.50%.

Table 3.8 Average absorbed energy up to a deflection of 40 mm.

Element	Absorbed energy [kNmm]	Increment [%]	Average increment [%]
RC	5997.5	-	-
SF1 0.25%	6646.6	10.82	9.76
SF2 0.25%	6520.0	8.71	
SF1 0.50%	7092.3	18.25	19.67
SF2 0.50%	7262.5	21.09	

The results show a significant improvement in the energy absorption capacity of the SF1 and SF2 beams with regard to the RC beams. Such outcome is consistent with what was already reported for small beams (Gopalaratnan 1991) and full-scale beams (Barros and Cruz 2001). The values for SF1 and SF2 beams are very close for both fibre contents,

which suggest that for low and moderate fibre contents the type of fibre does not have a critical influence in the absorbed energy. Nevertheless, it is interesting to notice that when the amount of fibres doubles, the average increment doubles too.

3.4. NUMERICAL MODEL

In order to simulate the tests performed in the experimental program, a model capable of carrying out a non-linear sectional analysis and accounting for the cracking, post-cracking and post-failure behaviour of the materials is required. With this purpose, the model AES (Analysis of Evolutionary Sections) presented in de la Fuente *et al.* (2012a) was used. Likewise, a numerical subroutine for the structural analysis of the elements was also developed by the same author and included in the AES model. Such subroutine allows assessing the behaviour of the beams with several combinations of reinforcements under the test setup conditions. The main basis and the hypotheses implemented in both models are presented in this section to provide a general overview on how these numerical tools were conceived.

3.4.1. Numerical modelling of the sectional behaviour

The concrete was discretized in layers with constant thickness, whereas steel rebars was simulated as concentrated-area elements. Subsequently, the suitable constitutive model was assigned to each element in order to integrate the stresses resulting from a given deformation plane defined by a strain of a reference layer (ε_o) and the curvature of the section (χ) (see Figure 3.13a).

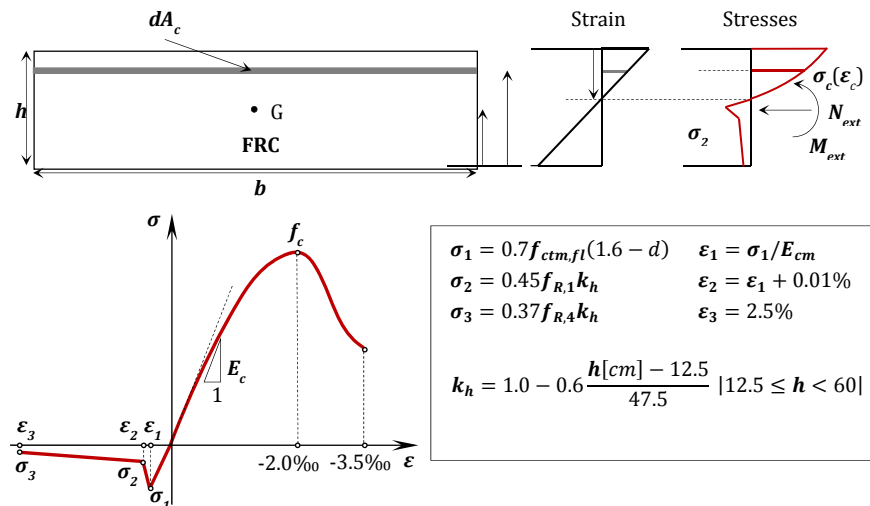


Figure 3.13 a) Sectional discretization and b) constitutive equations to simulate the stress-strain behaviour of the FRC (de la Fuente 2012b).

The response of SFRC under uniaxial compression was simulated with the expression suggested by Barros and Figueiras (1999). On the other hand, the simulation of its post-cracking behaviour was dealt with the constitutive models presented in Chapter 2.

The assessment of the crack width (w) depends on the type of reinforcement of the section. For RC sections the formulation proposed in Eurocode 2 (CEN 1992) was used, whereas in the case of RC-SFRC sections an extension of the previous formulation proposed by the RILEM was used. The steel of the rebars was simulated with the bilinear diagram presented in Figure 3.13c. The following hypotheses were considered in the simulation: perfect bond of the materials, the sections plane sections before applying external forces or after imposing fixed strains and shear strains are negligible; therefore, these were not taken into account.

Once the suitable constitutive equations have been assigned to each of the materials, a Newton–Raphson iterative method is used to solve the nonlinear equation system resulting from considering the equilibrium conditions (equations (3.1) and (3.2)) and compatibility (equation (3.3)).

$$N = \int_{A_c} \sigma_c(\varepsilon_c) dA_c + \sum_{i=1}^{n_b} \sigma_{s,i}(\varepsilon_{s,i}) A_{s,i} \quad (3.1)$$

$$M + N \cdot y_G = \int_{A_c} \sigma_c(\varepsilon_c) \cdot y_c dA_c + \sum_{i=1}^{n_b} \sigma_{s,i}(\varepsilon_{s,i}) \cdot y_{s,i} A_{s,i} \quad (3.2)$$

$$\varepsilon(y) = \varepsilon_{c,inf} - y \cdot \chi \quad (3.3)$$

3.4.2. Simulation of the tests

A subroutine included in AES was implemented in order to assess the P - δ curves considering the test configuration as well as different constitutive equations to simulate the FRC post-cracking behaviour. The algorithm implemented in the model to obtain the P - δ laws consists of:

- Dividing the half span of the element into intervals of magnitude Δx (Figure 3.14a).
- Obtaining the M - χ (Figure 3.14b) diagram of the cross section considering the mechanical properties of each material.
- Fixing an increment of the midspan deflection $\Delta\delta$.
- Fixing tolerances for the values $\Delta\delta$ and ΔP , $tol_{\Delta\delta}$ and $tol_{\Delta P}$ respectively.
- Assuming a trial value of the load ΔP .
- Evaluating the increment of bending forces ΔM_i in each point x_i by means of the expression (3.4).
- Calculating the accumulated bending force M_i in each point x_i .
- Finding the bending stiffness $K_{f,i}$ of each section by means of the M - χ diagram.
- Solving equation (3.5) in order to obtain $\Delta\delta_{ev}$ (increment of midspan evaluated).
- Verifying that $|\Delta\delta_{ev} - \Delta\delta| \leq tol_{\Delta\delta}$.
- Returning to the step 5 when the condition of the step 8 is not verified.

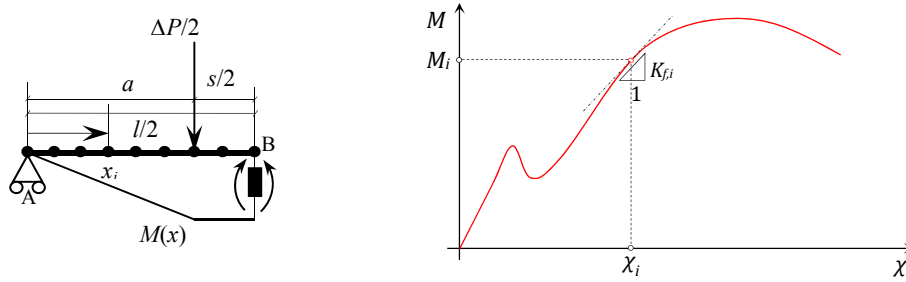


Figure 3.14 a) Discretization of the element and b) generic $M-\chi$ diagram (Blanco et al. 2013).

$$\Delta M = \begin{cases} \frac{\Delta P}{2}x & \text{for } 0 \leq x < a \\ \frac{\Delta P}{2}a & \text{for } a \leq x < a + \frac{s}{2} \end{cases} \quad (3.4)$$

$$\Delta \delta_{ev} = \Delta P \left[\int_0^a \frac{l - (2+l)x}{4K_f(x)} dx - \frac{as}{16K_f(x)_{x=a}} (2l + 4a + s) \right] \quad (3.5)$$

The rotation in A ($\Delta\varphi_A$) is evaluated by means of the first theorem of Mohr (3.6) and the increment of deflection in the midspan $\Delta\delta_B$ by means of the second one (3.7).

$$\Delta\varphi_B = \Delta\varphi_A + \int_0^{a+\frac{s}{2}} \frac{\Delta M(x)}{K_f(x)} dx \quad (3.6)$$

$$\Delta\delta_B = \Delta\delta_A + \Delta\varphi_A \frac{l}{2} + \int_0^{a+\frac{s}{2}} \frac{\Delta M(x)}{K_f(x)} \left(\frac{l}{2} - x \right) dx \quad (3.7)$$

The values of $\Delta\varphi_B$ and $\Delta\delta_A$ are zero due to the symmetry condition. Likewise, substituting (3.4) in (3.6) and in (3.7), the expressions (3.8) and (3.9) are obtained.

$$0 = \Delta\varphi_A + \int_0^a \frac{\Delta P}{2K_f(x)} x dx + \int_a^{a+\frac{s}{2}} \frac{\Delta P}{K_f(x)} a dx \quad (3.8)$$

$$\Delta\delta_B = \Delta\varphi_A \frac{l}{2} + \int_0^a \frac{\Delta P(x)}{2K_f(x)} x \left(\frac{l}{2} - x \right) dx + \int_0^{a+\frac{s}{2}} \frac{\Delta P}{2K_f(x)} a \left(\frac{l}{2} - x \right) dx \quad (3.9)$$

Integrating the expressions (3.8) and (3.9), and designating $K_f(x=a) = K_a$, the values of $\Delta\varphi_A$ and $\Delta\delta$ expressed in function of both the unknown ΔP and the bending stiffness ((3.10) and (3.11), respectively) are obtained.

$$\Delta\varphi_A = -\frac{\Delta P}{4} \left[2 \int_0^a \frac{x}{K_f(x)} dx + \frac{as}{K_a} \right] \quad (3.10)$$

$$\Delta\delta_B = \Delta\varphi_A \frac{l}{2} + \frac{\Delta P}{4} \left[\int_0^a \frac{l}{K_f(x)} dx + \frac{as}{4K_a} (2l - 4a - s) \right] \quad (3.11)$$

Substituting (3.10) in (3.11) the relation between $\Delta\delta_B$ and ΔP is derived in (3.12).

$$\Delta\delta_B = \frac{\Delta P}{4} \left[\int_0^a \frac{\xi(x)}{K_f(x)} dx - \frac{as}{4K_a} (2l - 4a - s) \right] \quad (3.12)$$

where:

$$\xi(x) = l - (2 + l)x \quad (3.13)$$

Finally, the analytical expression (3.13) is solved iteratively by using (3.14):

$$\Delta\delta_B^{k+1} = \frac{\Delta P^{k+1}}{4} \left\{ \frac{\xi(0)}{K_f(0)} + \sum_{i=1}^{n_p-1} \frac{\xi(x_i)}{K_f(x_i)} + \frac{\xi(a)}{K_f(a)} - \frac{as}{4K_a}(2l - 4a - s) \right\} \quad (3.14)$$

3.5. CONSTITUTIVE MODELS IN EUROPEAN CODES AND GUIDELINES

A comparative analysis is conducted in this section with the aim of studying the differences between the current constitutive models and their capacity to predict the behaviour of the beams previously described.

3.5.1. Assumptions in the numerical simulation

The numerical simulation was performed considering only the multilinear and the bilinear models due to their higher accuracy in the SLS (see Table 2.1). Furthermore, given that the characterization of the material was performed by means of the 3-point bending test specified in the standard EN14651:2005 (CEN 2005), it is necessary to correlate this test with the 4-point bending test used in the DBV (DIN1048). Since the test in EN14651:2005 measures the crack mouth opening displacement (CMOD) and the test in DIN1048 (DIN 1991) measures deflections, these are the two parameters to correlate. In fact, a correlation between EN14651:2005 and NBN 15-238 (IBN 1992) was already found in (Monsó 2011). In this case, the correlation will be adapted to the dimensions of the specimen in DIN1048. The failure mechanisms of the 4-point and 3-point bending test may be schematized as indicated in Figure 3.15.

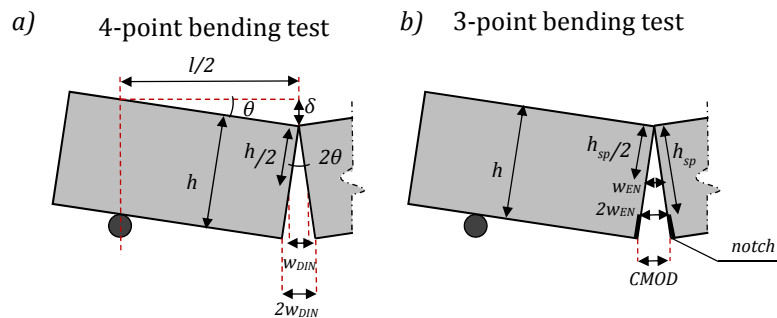


Figure 3.15 Failure mechanism of a) 4-point bending test (unnotched specimen) and b) 3-point bending test (notched specimen).

According to the notation indicated in Figure 3.15a, the equivalences shown in (3.15) and (3.16) may be deduced for the 4-point bending test.

$$\theta = \frac{\delta}{l/2} \quad (3.15)$$

$$2\theta = \frac{2w}{h}; \quad \theta = \frac{w}{h} = \frac{w_{DIN}}{h} \quad (3.16)$$

The values of h and $l/2$ for the specimen in DIN1048 are 150 mm and 300 mm (Table 2.1). The expressions (3.15) and (3.16) may be rewritten as indicated in (3.17).

$$w_{DIN} = w = \frac{\delta}{2} \quad (3.17)$$

Regarding the 3-point bending test, the equivalence in (3.18) may be considered according to Figure 3.15b.

$$\frac{CMOD}{h} = \frac{2w}{h_{sp}} = \frac{2w_{EN}}{h_{sp}}; \quad w_{EN} = \frac{h_{sp}}{2h} CMOD \quad (3.18)$$

Assuming the average values of crack width for the 4-point bending test (w_{DIN}) and the 3-point bending test (w_{EN}) are equal for a certain deflection and taking value of $h_{sp}=125$ mm and $h=150$ mm, expressions (3.19) and (3.20) may be written. The correlation in (3.20) may be used to find the equivalence between the experimental results obtained from the test in EN14651:2005 and the results from the test in DIN1048.

$$\frac{\delta}{2} = \frac{h_{sp}}{2h} CMOD \quad (3.19)$$

$$\delta = 0.833 CMOD \quad (3.20)$$

For the purpose of this study, it was assumed that the value of the characteristic length equals the experimental average spacing ($l_{cs} = s_{rm}$) which are 156 mm, 118 mm, 138 mm and 176 mm for SF_0.25, SF_0.50, PF_0.25 and PF_0.50, respectively.

Additionally, another assumption was made concerning the constitutive model in the MC2010. In this model, the intersection between the post-cracking branch of the MC90 (CEB-FIP 1993), which depends on the value of the l_{cs} , and the softening branch defined by the parameters in the MC2010 must be obtained (see Figure 3.16a). For three of the four cases studied (SF_0.25, PF_0.25 and PF_0.50), the intersection corresponded to a value of strain lower than that for the tensile strength f_{ct} . This situation might be associated with the values of l_{cs} assumed in the study, which could be smaller than the considered in such cases. Since there is no physical sense in a lower value of strain than that for f_{ct} , no contribution of the concrete matrix was considered after the tensile strength was reached in cases SF_0.25, PF_0.25 and PF_0.50 (see Figure 3.16b).

The value of strain assumed (0.15‰) is 8%, 3% and 21% higher than the value obtained by applying the MC2010 for SF_0.25, PF_0.25 and PF_0.50 respectively. The difference in the value of stress is hardly noticeable (in all cases it is inferior to 1%).

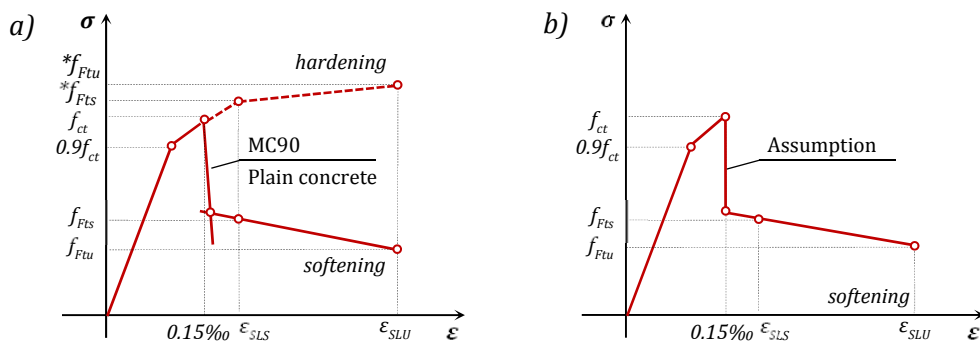


Figure 3.16 a) MC2010 and b) assumption made for this study for the case of SF2 0.25 %_A.

During the experimental program, variations in the concrete cover with respect to the theoretical (35 mm) were detected in some of the beams. The identification of these variations was possible since in some cases the longitudinal reinforcement was visible, as shown in Figure 3.17a. This variation in the concrete cover has a significant influence in the response of the beams. In Figure 3.17b, the variation of the values of the bending moment associated to a crack width of 0.2 mm ($M_{w=0.2mm}$) and the ultimate bending moment (M_u) due to the increase of the concrete cover is studied. These curves correspond to the beam SF2 0.50%_B and were obtained with the model AES, using the EHE constitutive model and taking as a reference the theoretical concrete cover (c_{ref}) and their corresponding values of bending moment (M_{ref}).

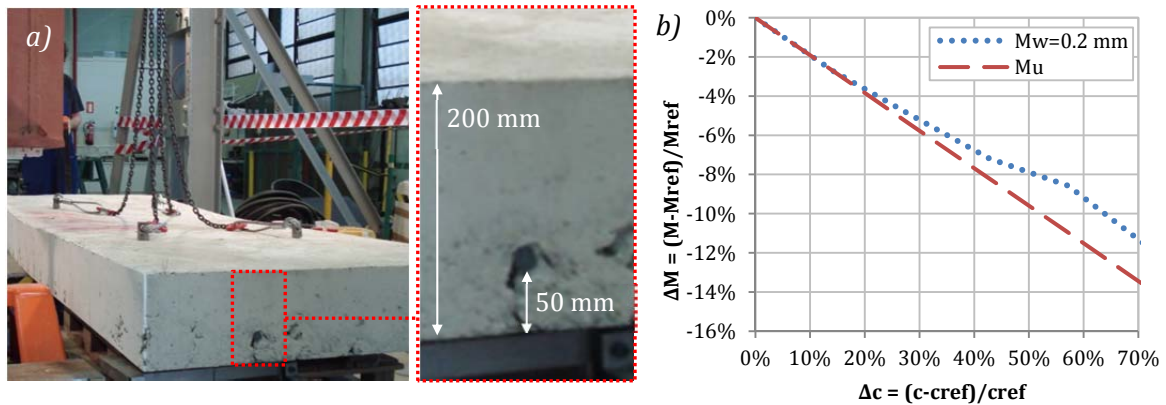


Figure 3.17 a) Variations in the concrete cover for the element SF2 0.50%_B and b) decrease of the bending moment due to the variation of the concrete cover.

The value of 50 mm indicated in Figure 3.17a represents an increase slightly over 40% with respect to the theoretical cover, which results in a value of M_u 8% lower than the expected with the theoretical cover. Therefore, given the influence of the traditional reinforcement in the response of these elements, it is necessary to take into account the real concrete cover in the numerical simulation. For the two elements simulated in this section, SF2 0.25%_A and SF2 0.50%_B, concrete covers of 60 mm and 50 mm were considered, respectively.

3.5.2. Constitutive models

The parameters defining each of the constitutive models are presented in for the two elements studied in this section: SF2 0.25%_A and SF2 0.50%_B. A total of four multilinear models and three bilinear models were analysed. As previously described in Chapter 2, the multilinear models were conceived to reproduce accurately the behaviour of FRC, since they simulate the linear-elastic behaviour before cracking by considering the peak stress and the loss of stiffness after the cracking, in the case of strain softening materials, as observed in Figure 3.18a. The bilinear models reproduce a simplified behaviour that does not consider this phenomenon (see Figure 3.18b).

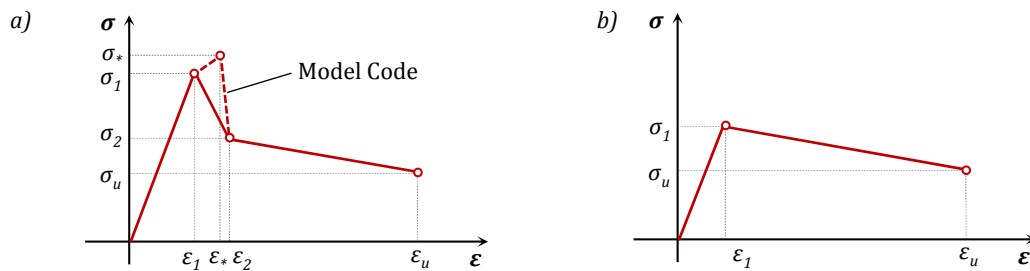


Figure 3.18 a) Multilinear model and b) bilinear model.

The values of the parameters defining each of the constitutive models studied in this section are presented in Table 3.9. The notation used corresponds to the one in Figure 3.18. Notice that the tensile strength is σ_1 for all models except the MC2010, in which the tensile strength is represented by σ^* . Additionally, it should be pointed out that partial safety factors were not used to obtain any values of stress and strain.

Table 3.9 Parameters of the constitutive models for SF2 0.25%_A and SF2 0.50%_B.

Beam	Models	σ_1 [MPa]	ϵ_1 [‰]	σ^* [MPa]	ϵ^* [‰]	σ_2 [MPa]	ϵ_2 [‰]	σ_u [MPa]	ϵ_u [‰]
SF2 0.25%_A	DBV trilinear	2.219	0.089	-	-	0.176	0.189	0.183	10.000
	RILEM	4.369	0.161	-	-	1.206	0.261	1.038	25.000
	EHE trilinear	2.155	0.089	-	-	1.332	0.189	0.895	20.000
	MC2010	2.321	0.096	2.579	0.150	1.388	0.150	1.023	20.000
	DBV bilinear	0.353	0.014	-	-	-	-	0.197	10.000
	CNR-DT 204	1.332	0.055	-	-	-	-	0.817	20.000
	EHE bilinear	1.336	0.055	-	-	-	-	0.895	20.000
SF2 0.50%_B	DBV trilinear	2.228	0.090	-	-	0.288	0.190	0.335	10.000
	RILEM	4.369	0.167	-	-	1.601	0.267	1.547	25.000
	EHE trilinear	2.155	0.092	-	-	1.769	0.192	1.404	20.000
	MC2010	2.321	0.099	2.579	0.150	1.840	0.152	1.494	20.000
	DBV bilinear	0.512	0.021	-	-	-	-	0.368	10.000
	CNR-DT 204	1.769	0.076	-	-	-	-	1.311	20.000
	EHE bilinear	1.772	0.076	-	-	-	-	1.404	20.000

For the multilinear models, it is observed that the tensile strengths (σ_1 or σ^* in the case of the MC2010) are very similar with the exception of the RILEM model, whose value is 41%, 97% and 103% higher than the tensile strengths of the MC2010, the DBV and the EHE-08, respectively. In the case of the bilinear models, the lowest value of σ_1 corresponds

to the DBV model which is approximately 74% and 71% lower than the values of the other bilinear models for the beams SF2 0.25%_A and SF2 0.50%_B, respectively.

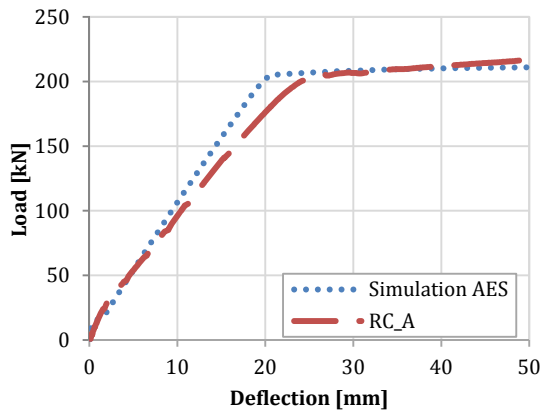
For the multilinear models, the values of σ_2 represent only 16 % and 28 % of σ_1 for the DBV and RILEM models, whereas for the MC2010 and the EHE-08 models corresponds to 54% and 62 % for beam SF2 0.25%_A. When the amount of fibres is doubled, for beam SF2 0.50%_B, these values turn into 23%, 37%, 71% and 82% for the DBV, the RILEM, the MC2010 and the EHE-08, respectively. These results indicate that the earliest constitutive models, the DBV and the RILEM, are conservative regarding the contribution of the fibres after cracking. Nevertheless, in the case of the RILEM, the other values of stress associated to larger strains are of the same order of magnitude as the most recent models.

Regarding the stress associated to the ultimate strain (σ_u), there is a significant difference between the DBV models (both bilinear and multilinear) and the others, being the former very conservative. In fact, the values of the DBV models represent less than 30% of the stress associated to the ultimate strain in the other models, which could lead to the underestimation of the performance of the material. If compared to σ_2 , the values of σ_u in beam SF2 0.25%_A represents 56%, 67%, 76% and 86% for the DBV, the EHE-08, the MC2010 and the RILEM, respectively. In the case of beam SF2 0.50%_B, this percentages are 72%, 79%, 81% and 97% for the DBV, the EHE-08, the MC2010 and the RILEM, respectively.

The low values observed in the models proposed by the DBV may be partially attributed to the use of a coefficient that takes into account the coefficient of variation in the flexural tests. Given the significant scatter associated to these tests and, in particular, the values observed in section 3.2.2, the reduction in the values of the equivalent tensile strengths is remarkable. Likewise, the high values of the RILEM model may lead to unsatisfactory predictions of the post-cracking response. The reason for the overestimation of the RILEM lies in the use of higher values in the parameters that define the post-cracking stage in the constitutive model, as other authors have pointed out (Tlemat *et al.* 2006). In order to improve the accuracy of the model, new values for those parameters were proposed by Barros *et al.* (2005).

3.5.3. Results

In order to facilitate the interpretation of the performance and the suitability of the models for simulating the post-cracking behavior of FRC elements, the prediction of the control slab R_A provided by the model AES and the experimental P - δ curve are shown in Figure 3.19. Additionally, the load values for deflections of 6 mm, 15 mm and 45 mm, which are representative of different stages of the P - δ curve, are presented in the table of Figure 3.19. The curves indicate that the prediction of the response for the control slab RC is satisfactory, particularly at the early stages of the loading and after the yielding of the reinforcement occurs.



δ [mm]	Load [kN]		Relative error [%]
	Experimental	Simulation AES	
6	62.7	64.6	3.0
15	139.4	156.4	12.2
45	214.3	210.7	-1.7

Figure 3.19 a) Experimental and prediction P - δ curves for slab RC_A and b) load values for deflections of 6 mm, 15 mm and 45 mm.

From the results presented in the table in Figure 3.19, it is observed that for a deflection of 6 mm the prediction overestimates the experimental results in 3.0% and for 45 mm there is an underestimation of only 1.7%. The biggest differences between both curves are detected for values of load over 100 kN and until the yielding of the reinforcement. For example, the prediction for 15 mm is a 12.2% higher than the load value registered during the test.

Subsequently, the predictions regarding the RC-SFRC beams are presented and analyzed. The diagrams of the constitutive models and the P - δ curves for SF2 0.25%_A and SF2 0.50%_B are shown in Figure 3.20. First, the multilinear models and their corresponding load-deflection results are presented and then the bilinear models and their results.

The high value of tensile strength adopted by the RILEM model, as observed in Figure 3.20a and 3.20c, can lead to an overestimation of the structural response of the beams (see P - δ curves in Figure 3.20b and 3.20 d), particularly in serviceability. Contrarily, the DBV model presents the lowest values if compared with the RILEM, the EHE-08 and the MC2010, as previously discussed in section 3.5.2, resulting in a conservative prediction of the behaviour for large deflections. The EHE-08 and the MC2010 overestimate the results for small deflections but for large deflections, the prediction remains on the safe side or slightly over the experimental results (see Figure 3.20b and 3.20d).

In Figure 3.20e and 3.20g, despite fitting satisfactorily the serviceability limit state, the DBV model underestimates noticeably the behaviour at pre-failure. The CNR-DT 204 and EHE-08 models present the same value of tensile strength; nevertheless, the stress associated to the ultimate strain is lower in the case of the CNR-DT 204. This difference results in a slightly lower response in the pre-failure regime of the beam when using the CNR-DT 204 model (see Figure 3.20f and 3.20h).

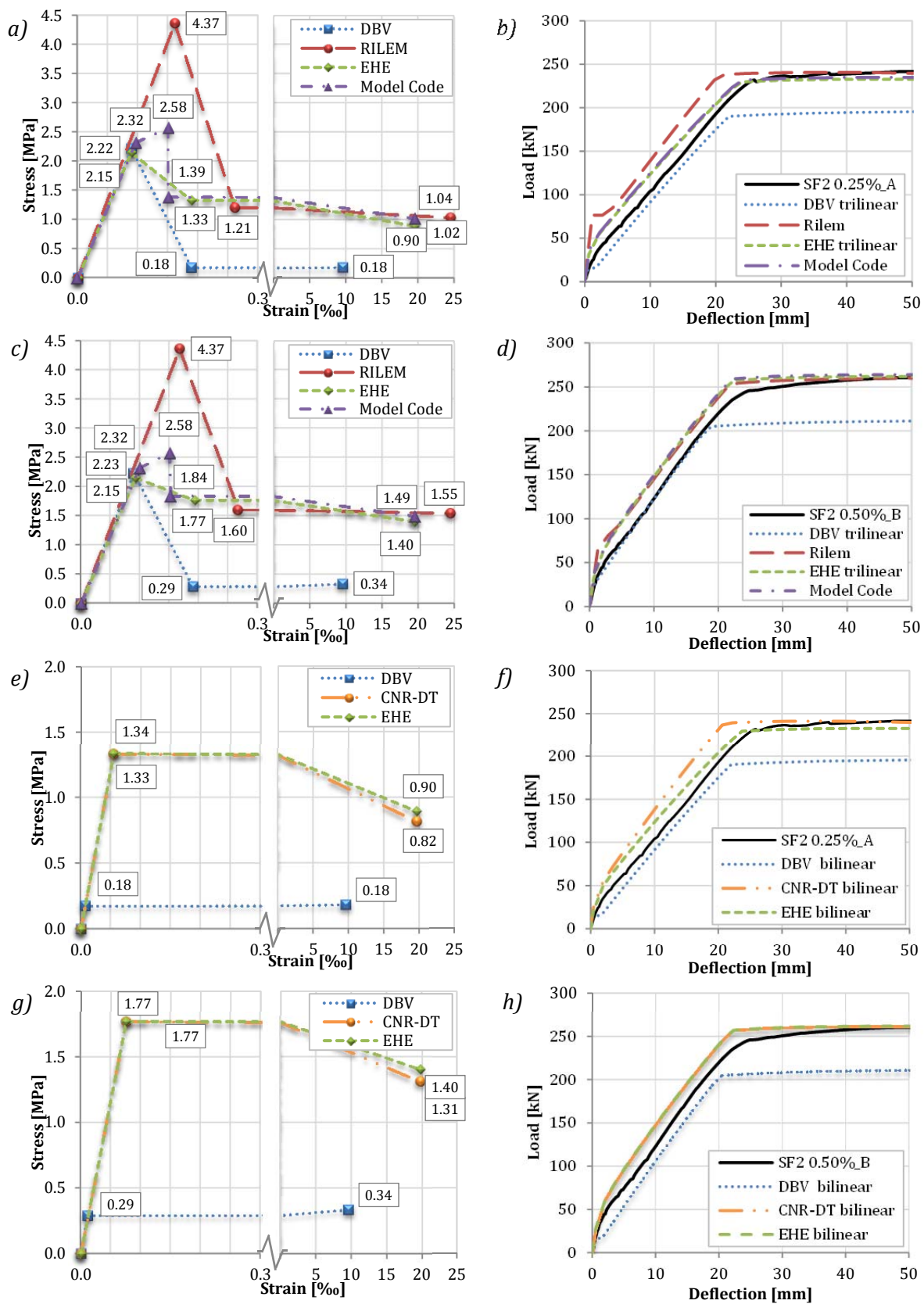


Figure 3.20 Trilinear diagrams and P- δ curves for a-b) SF80/60_20 and c-d) SF80/60_40; Bilinear diagrams and P- δ curves for e-f) SF80/60_20 and g-h) SF80/60_40.

In Table 3.10, the load values for deflections of 6 mm, 15 mm and 45 mm, which are representative of different stages of the curve, are presented for the beam SF2 0.50 %_B. The corresponding load for 45 mm will indicate which models are on the safe side for large deflections close to failure.

Table 3.10 Load values for deflections of 6 mm, 15 mm and 45 mm (in kN) for SF2 0.50%_B.

Models		6 mm	15 mm	45 mm
Experimental data		82.9	175.1	259.8
DBV	<i>Trilinear</i>	81.0	171.3	210.8
	<i>Bilinear</i>	64.8	156.9	210.7
RILEM	<i>Trilinear</i>	120.6	192.9	259.6
CNR-DT 204	<i>Linear-elastic</i>	107.4	195.9	261.3
EHE	<i>Trilinear</i>	106.4	195.2	261.8
	<i>Bilinear</i>	106.4	195.4	261.8
Model Code	<i>Multilinear</i>	108.3	197.5	263.9

The models proposed by the DBV provide the best fit of the experimental data for small deflections. In fact, the prediction of the DBV trilinear is only 2.3% lower for 6 mm and 2.2% lower for 15 mm than the measured value, while the other trilinear models and the CNR-DT 204 largely overestimate the experimental results for 6 mm and 15 mm: the RILEM 45.5% and 43.2%, the CNR-DT 204 29.6% and 11.9%, the EHE 28.8% and 11.7% and the Model Code 30.6% and 12.8%, respectively.

On the other hand, the RILEM, the CNR-DT 204, the EHE-08 and the MC2010 provide the best fit for larger deflections, with a difference of less than 1.6% with the experimental data. In this sense, the model that presents a larger difference with the experimental result is the DBV trilinear that provides a very conservative prediction (the load for 45 mm is nearly 19% lower than those experimentally obtained).

3.6. CONCLUDING REMARKS

Chapter 3 presented the results of an experimental program involving flexural tests on full-scale RC-SFRC beams and the numerical modelling of such beams. The following conclusions may be derived from the experimental results:

- The addition of fibres reduces the crack spacing due to a higher transmission of stresses to concrete through adherence mechanisms. Even though this is generally true, in certain cases is not so clear. The formulation proposed by the RILEM (and adopted by the CNR-DT 204) to predict the crack spacing underestimate the experimental results. This difference might be attributed to the presence of the transversal reinforcement in the beams.
- The crack width is significantly reduced by the addition of fibres, particularly when the amount of fibres increases. In fact, the crack width associated to a load of 40 kN for a beam with a fibre content of 0.50% in volume is approximately 50%

smaller than the measured for a beam with a content of 0.25% subjected to the same load level. The estimation of the crack width with the RILEM formulation is satisfactory for stabilized cracking.

- The contribution of the fibres to the cracking control reaches its maximum value for crack widths between 0.55 mm and 0.8 mm (depending on the type and amount of fibres), stabilizing around 1.2 mm and 1.4 mm. The short fibres are more active in the first stages of the cracking, whereas the long fibres continue to provide ductility and control the cracking for larger deflections.
- The load-deflection curves of the RC-SFRC beams indicate the influence of the fibres in the control of the deflection and the increase of slopes of the curves or stiffness. In addition to that, the energy absorption increment relative to the control beams is remarkable, doubling its value when the fibre content doubles.
- The constitutive models proposed in the DBV predict satisfactorily the flexural response of the RC-SFRC beams for small deflection but underestimate by, approximately, 19% the load values for large deflections. This difference may be caused by the use of a coefficient that takes into account the scatter of the flexural tests, penalizing the post-cracking strengths in case of high coefficients of variation.
- The constitutive model suggested by the RILEM presents significant differences with the experimental results for small deflections, overestimating the load values by 45%. Nevertheless, for large deflections the model reproduces accurately the experimental curves.
- The models proposed in the CNR-DT 204 and in the EHE-08 provide almost identical predictions. In both cases, the models overestimate the response for small deflections by 30%. However, their predictions become closer to the experimental data as the deflections increase.
- The model proposed in the MC2010 provides a similar prediction to that of the trilinear model in the EHE-08. In general, the Model Code 2010 predicts satisfactorily the structural response although overestimates the response for small deflections.

4. FLEXURAL BEHAVIOUR OF SFRC SLABS

4.1. INTRODUCTION

The Part II of this thesis showed that numerical models of RC-SFRC beams with the constitutive models from European codes reproduce satisfactorily the behaviour of the real-scale elements. Nevertheless, the beams are just one of the typologies of structural elements constructed with SFRC. In fact, the material is also used in a wide range of elements such as pavements, tunnel lining segments and flat slabs. It is obvious that all these elements hold a small resemblance in terms of fibre distribution and structural behaviour with the specimens used to obtain the constitutive models from European codes. Uncertainties regarding the capability of these models to reproduce well the behaviour of pavements or slabs in simulations are evident.

With a material so sensible to variations, the design of SFRC structures using the results of tests representative of the structure is of paramount importance. To avoid the specification of an endless number of test configurations, the design codes and recommendations should provide tools to compensate the lack of representativeness of the standard tests (for example geometry factors, orientation factors, among others) taking into account the own characteristics of each structural application. The use of these types of factors in the design procedure is not a novel idea. Indeed, two European guidelines (DBV and RILEM) already introduced a size factor in order to consider the effect of the height of the element over the bending behaviour of the cross section. The definition of this size factor was mainly based on the experience with the test of real scale beams.

A recent study on the mechanical performance of flat slabs (Michels *et al.* 2012), already introduced in Chapter 2, revealed the need to introduce realistic geometry factors in the design of SFRC slabs. Michels *et al.* (2012) concluded that the fibre orientation and the residual strength in the cracked state decreased as the thickness of the slab increased. Two geometry factors were implemented in a simplified bilinear σ - ε law in tension to account for this size effect in the design. However, other factors besides the thickness might affect the structural behaviour of the elements. Clear examples are the width or the length, which might influence the fibre orientation and the localized mechanical properties of the concrete and the global structural response.

In this context, several questions might arise. How does the fibre orientation in the slabs change as the width increases? How does the global structural response of real scale SFRC slabs vary depending on the size of the element? In order to work towards a more robust design method for SFRC slabs, these questions must be answered. For that, further research is required on the mechanical performance of SFRC slabs, the orientation of fibres and its variation with the size of the element as well as the influence of using constitutive models based on the tests of small beams to simulate the structural behaviour in numerical models.

With the aim of providing fundamental information to the proposal of more reliable design methods, the Part III of this thesis focuses on questions related with the flexural behaviour and the orientation of fibres in real-scale SFRC slabs (without traditional reinforcement) with different dimensions. For that purpose, the Part III is divided in three chapters as indicated in Figure 4.1.

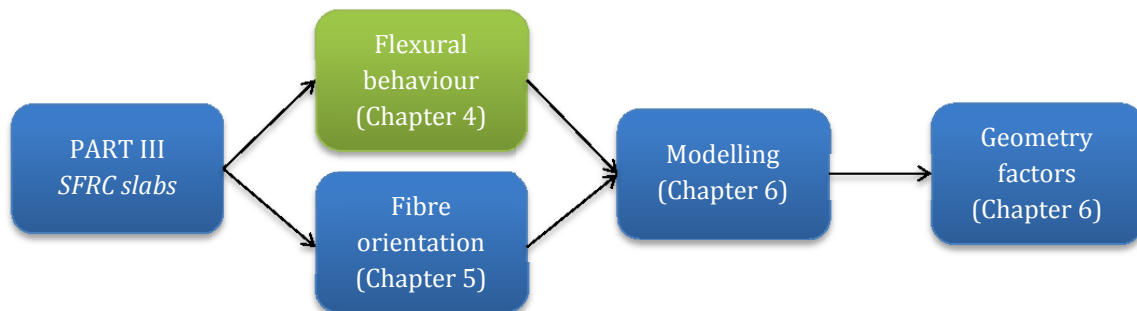


Figure 4.1 Outline of Part III of the thesis, emphasizing the current chapter.

The flexural behaviour of SFRC slabs is studied in the current chapter whereas the fibre orientation is evaluated in Chapter 5. Then, the flexural behaviour of the slabs is modelled and the suitability of the current constitutive models to predict their structural response is analysed in Chapter 6. Finally, geometry factors that take into account the influence of the slab geometry are proposed and integrated in a design method.

4.1.1. Objectives

The main goal pursued in this chapter is to evaluate the structural behaviour of real scale SFRC slabs with different widths. For that, the following specific objectives are defined:

- Assess the crack pattern of the real-scale SFRC slabs and identify the differences due to their geometry;
- Evaluate the flexural behaviour of the real-scale SFRC slabs in terms of bearing capacity and ductility based on the load-deflection and load-rotation curves registered during the tests and
- Assess the energy absorption capacity of the real-scale SFRC slabs depending on their geometry.

4.1.2. Outline of the chapter

Initially, in section 4.2, an experimental program is proposed to study the structural response of real-scale SFRC slabs with different widths. In this section, the main properties of the material as well as the tests that performed are described. In section 4.3, the results obtained from tests are analysed in terms of crack pattern, load-deflection curves, load-rotation angle curves and energy absorption capacity. Finally, in section 4.4, the main conclusions of the study are highlighted.

The slabs described in this chapter and the results obtained provide the basis to the studies developed in Chapter 5 and Chapter 6 regarding the orientation of fibres in SFRC slabs and the modelling of the flexural behaviour of SFRC slabs, respectively.

4.2. EXPERIMENTAL PROGRAM

4.2.1. Specimens

In order to study the flexural behaviour of SFRC in these elements, a total of 6 slabs with 3.0 m of length and 0.2 m of thickness and three different widths were cast to evaluate the influence of this parameter in the structural response. According to the notation adopted in Table 4.1, the slabs could be either small (S), medium (M) or large (L) depending on whether the width was 1.5 m, 2.0 m or 3.0 m, respectively.

Table 4.1 Dimensions of the slabs.

Notation	Dimensions [m]
S_A and S_B	1.5 x 3.0 x 0.2
M_A and M_B	2.0 x 3.0 x 0.2
L_A and L_B	3.0 x 3.0 x 0.2

The letters A or B were appended to the end of the notation to indicate each of the two slabs with the same dimension. The slabs were cast at ESCOFET S.A facilities and then transported to the Laboratory of Structure Technology Luis Agulló at the UPC to be tested (see Figure 4.2).



Figure 4.2 Transport of slabs L to the Laboratory of Structure Technology Luis Agulló.

4.2.2. Materials and concrete mix

Since the main research parameter is the width of the slabs, only one concrete mix was used. The concrete was produced in a 750 litres vertical axis mixer with the following mixing process: initially the dried components were mixed during one minute, subsequently the water was added and the paste was mixed during two minutes, afterwards the superplasticizer was added and finally the steel fibres were included. After that, the concrete was mixed for two additional minutes. The total time of mixing ranged from five to seven minutes. The details of the concrete mix are presented in Table 4.2.

Table 4.2 Concrete mix.

Materials	Characteristics	Quantities [kg/m ³]
Gravel (6/15 mm)	Granite	520
Gravel (2.5/6 mm)	Granite	400
Sand (0/3 mm)	Granite	510
Cement	CEM I 52,5 R	350
Filler	Marble dust	300
Water	-	178
Superplasticizer	Adva® Flow 400	12
Fibres	Steel fibres	40

The steel fibres used were of type Dramix® RC80/50BN with circular cross-section and hooked ends. These fibres are made of low carbon steel and are gathered into bundles by water-soluble glue. Additional characteristics of the fibres used are summarized in Table 4.3.

Table 4.3 Characteristics of the fibres (provided by the manufacturer).

Characteristic	Unit	Value
Length (L)	[mm]	50
Diameter (d)	[mm]	0.62
Aspect ratio (L/d)	[-]	83
Tensile strength (f_y)	[MPa]	1270
Modulus of elasticity (E)	[GPa]	210
Number of fibres per kg	[-]	8100



Notice that three batches (namely B1, B2 and B3) with the same mix proportion were required to cast all slabs. Due to limitation of the moulds available at the manufacturer's facilities, it was decided that the slabs would be produced in three different days. Table 4.4 shows the dates and the elements cast with each batch.

Table 4.4 Date of production of the elements.

Batch	Date	Elements
B1	09/11/2010	L_A M_A
B2	11/11/2010	L_B M_B
B3	23/11/2010	S_A S_B

The concrete mix was designed to obtain a fluid concrete with characteristics close to self-compactability. Therefore, the fresh state properties of the SFRC were evaluated by means of the slump flow test (see Figure 4.3) according to UNE-EN 12350-8:2011 (AENOR 2011), which assesses the filling ability of the mixture through the average diameter of flow spread (D_f) and the time taken by the mixture to reach the 500 mm mark (T_{50}). The test also allows a qualitative evaluation of the material stability by analyzing signs of segregation such as irregular distribution of coarse aggregates, existence of coarse aggregates without mortar or separation of the paste around the perimeter.

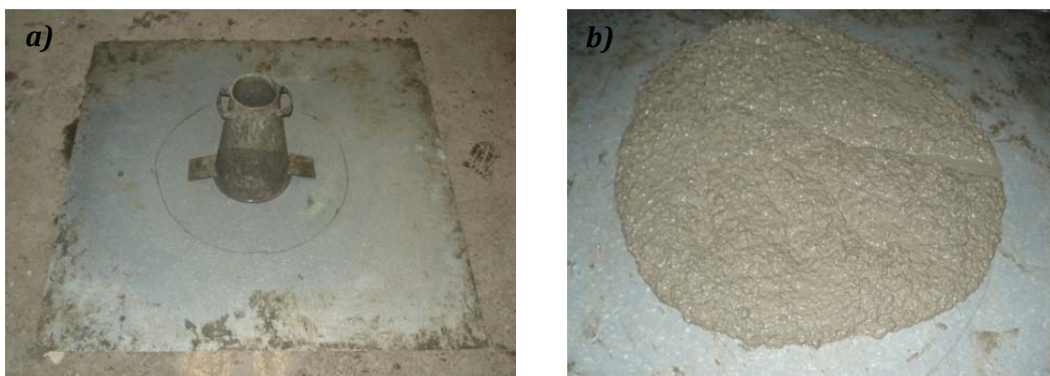


Figure 4.3 Slump flow test: a) equipment and b) spread concrete after the test.

Table 4.5 shows the fresh state properties measured and the time passed from the production of the concrete to the conclusion of the slump flow test for batches B1 and B2. Values for batch B3 were not assessed since the fresh aspect of the concrete was similar to the observed in B1.

Table 4.5 Results of the slump flow test for B1 and B2.

Properties		B1	B2
D_f	[mm]	535	345
T_{50}	[sec]	20	10
T_{delay}	[min]	10	20

Even though the same materials and production process was used, B1 and B2 had some differences in the fresh state properties measured. The former presented a D_f 55% bigger and a T_{50} twice as big as the latter. It is important to remark that, due to the current practice, all tests were performed after the slabs were cast, which conditioned the beginning of the slump flow measurement. Therefore, at least part of the decrease on the values measured for D_f and T_{50} may be attributed to the delay on the characterization of batch B2. Despite that, all batches presented similar aspect before and during the production of the slabs.

Due to the influence of the pouring method on the fibre orientation and on the mechanical properties, the same casting procedure was used to produce all slabs so as to avoid introducing additional variables to the study. All slabs were cast from the centre (see Figure 4.4), pouring the concrete from a skip with straight outlet and a discharge gate placed at a height of 50-60 cm over the bottom surface of the formwork. Given the dimensions of the M and L slabs, more than one discharge from the skip was required to fill the formwork. After that, the concrete was vibrated externally with a portable system attached to the walls of the formwork during 15 to 20 seconds in order to ensure a uniform distribution in the mould. The slabs were removed from the moulds within 24 hours of casting and were moist cured under a plastic sheet during 20 days.

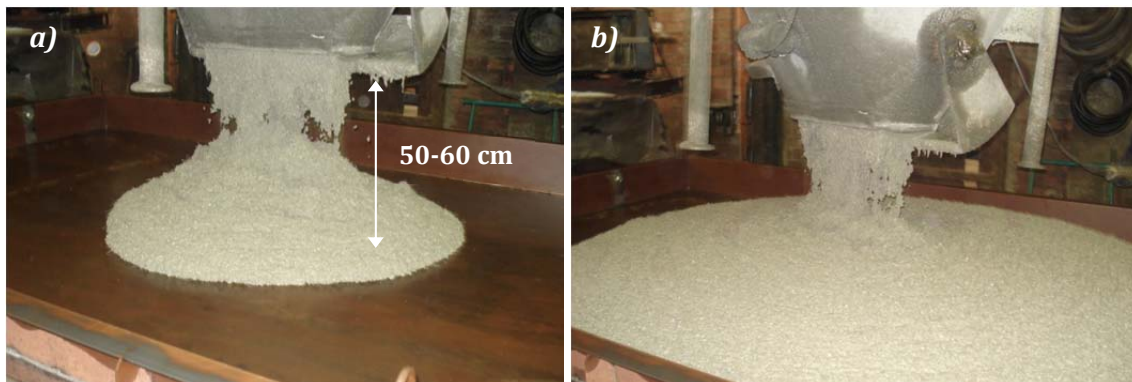


Figure 4.4 a) Concrete pouring in the centre of the slab and b) flow of concrete to the edges.

The following specimens were cast for each concrete batch; six prismatic beams (150 x 150 x 600 mm) for the characterization of the flexural strength (EN 14651:2005 (CEN 2005)), three cylindrical samples (150 x 300 mm) for the assessment of the compressive strength (UNE 83507:2004 (AENOR 2004b)) and three cylindrical samples (150 x 300 mm) for the measurement of the modulus of elasticity (UNE 83316:1996 (AENOR 1996)). All specimens were vibrated externally by means of a vibrating table at 3000 rpm during 10 seconds approximately. The elements were removed from the moulds

within 24 hours of casting and were moist cured under a plastic sheet for a week, after which they transported from the ESCOFET S.A facilities to the Laboratory of Structure Technology Luis Agulló at the UPC. Then, the specimens were kept in a curing room at 20 ± 2 Celsius degrees and 95% of relative humidity.

The average results at 28 days for the compressive strength (f_{cm}) and modulus of elasticity (E_{cm}) of each batch are presented in Table 4.6 as well as the respective coefficient of variations (CV). The table also shows the limit of proportionality (f_L) and the residual flexural tensile strengths (f_{R1} , f_{R2} , f_{R3} and f_{R4}) corresponding to the CMOD of 0.05 mm, 0.50 mm, 1.50 mm, 2.50 mm and 3.50 mm, respectively. Notice that the average residual flexural strengths of batch B3 correspond to the testing of two beams instead of six since the other three were used in the experimental program described in Chapter 7 and one failed due to problems with the CMOD control device.

Table 4.6 Modulus of elasticity, compressive strength and residual flexural strengths at 28 days.

Property		B1		B2		B3	
		Average [MPa]	CV [%]	Average [MPa]	CV [%]	Average [MPa]	CV [%]
Modulus of elasticity	E_{cm}	29030	0.96	28640	2.79	30160	2.20
Compressive strength	f_{cm}	46.73	0.77	49.46	0.59	46.77	2.54
	f_L	5.42	7.05	5.29	2.23	3.76	7.96
Residual flexural strengths	f_{R1}	6.25	12.50	6.13	13.71	3.75	22.29
	f_{R2}	7.02	12.39	7.04	15.77	4.24	17.91
	f_{R3}	7.05	11.59	7.08	15.05	4.30	15.88
	f_{R4}	6.62	12.08	6.62	12.08	4.17	15.68

The scattering observed in the results is high but smaller than the 20% reported by Parmentier *et al.* (2008) and Molins *et al.* (2009). The comparison of residual flexural tensile strengths show that batches B1 and B2 present almost identical average values whereas B3 exhibits lower values. Given that the concrete mix used in the three series is the same and the other tests (compressive strength and modulus of elasticity) provide similar results for all series, the difference in the post-cracking performance of B3 is attributed to the reduced number of specimens tested. Therefore, it will be assumed for subsequent steps of this study that the performance of the material of B3 is equivalent to B1 and B2.

4.2.3. Test setup

The tests of the slabs were conducted using a MTS® load frame with a maximum capacity of 1000 kN. A piston connected to the load frame by means of a tridimensional joint applies the load in a surface of 200 x 200 mm in the centre of the slabs. Between the piston and the top of the slab, a neoprene sheet (200 x 200 x 20 mm) was placed to ensure full contact in the loading surface. The slabs are supported along their four sides on top of steel trestles. Given that the corners of the slabs would eventually rise during the loading and to enable a simpler setup preparation (avoiding the contact of two consecutive

supports) it was decided to support the element only in the central part of each side, along half of the total length. In other words, a quarter of the length of each side was not supported near the corners of the slabs. The setup is shown in Figure 4.5 for the three types of slabs (S, M and L). A detail of the loading surface is also presented in Figure 4.5d.

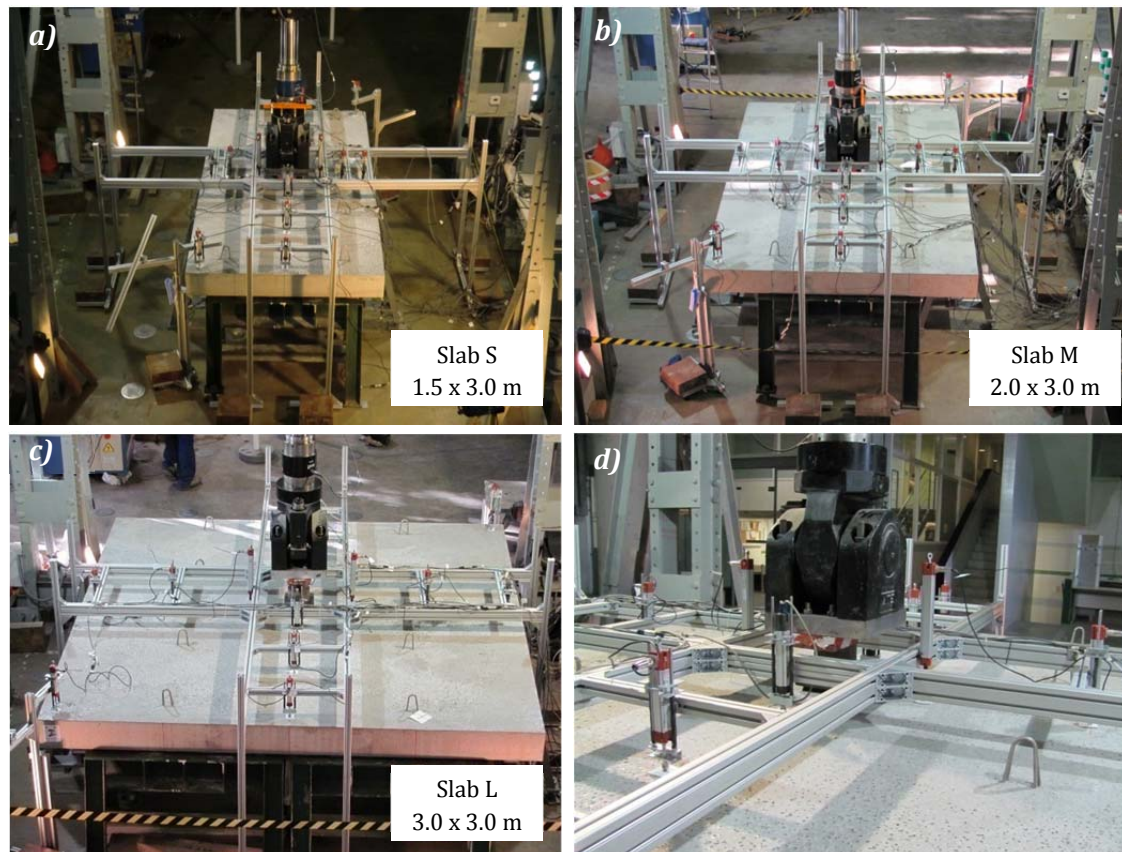


Figure 4.5 Setup for slab a) S, b) M, c) L and d) detail of the loading point.

Neoprene sheets were placed between the slab and the steel trestles to limit the contact area and to guarantee a more uniform load transmission (see Figure 4.6a). The layer of neoprene was 2 cm thick, 20 cm wide and 1.5, 1 or 0.75 m long depending on the length of the supported side. This setup intends to simulate a hyperstatic support configuration that should allow a redistribution of moments and the contribution of fibres in more than one direction.

In total, fourteen displacement transducers measured the deflection at different points of the slabs (Figure 4.6b) during the loading procedure. Two of them were located at diagonally opposed corners in order to assess the expected raising of these points. The remaining transducers were located at the symmetry axes of the slabs forming a cross (6 in each direction) parallel to the sides. Four of these transducers were placed in the axis of the support to measure the behaviour of the neoprene layer. No transducer was placed in the centre of the slabs due to the presence of the loading surface. The deflection at this point was estimated from the readings of the other transducers (as explained later in the

text). Besides that, the displacement and the load applied by the jack are also measured during the test.



Figure 4.6 a) Detail of the supports and b) deflection measuring system.

The test was performed with displacement control and the loading procedure was divided in two sequential stages. At the first stage, a smaller displacement rate was used to allow a clear appreciation of the arising and the propagation of cracks. Once the extent of the major cracks had stabilized, a bigger displacement rate was used in order to assess the behaviour of the slabs reaching high displacement values. For the smaller slabs the displacement was applied at a rate of 0.15 mm/min until the jack reached a displacement of 6 mm and then the rate was increase to 0.20 mm/min. The medium slabs were loaded at 0.20 mm/min and after reaching 6 mm of displacement the rate was changed to 0.30 mm/min. Finally, the large slabs were loaded at 0.25 mm/min up to a total deflection of 5 mm, after which the rate was raised to 0.40 mm/min.

4.3. RESULTS

4.3.1. Crack patterns

The crack pattern in slabs subjected to concentrated load usually consists of radial cracks that appear from the loading point to the edges of the slab (not necessarily to the corners). This was demonstrated in the yield line theory and validated experimentally (Johansen 1962). The crack patterns observed in the present study agree with the previous description.

Figure 4.7 shows an example of the evolution of the cracking during the test of slab M_B in pictures taken at different loading stages. The evolution of cracking from Figure 4.7a to Figure 4.7e corresponds to an increasing load stage up to a registered maximum of 297.1 kN whereas Figure 4.7f corresponds to the post-peak stage. These pictures highlight how a significant crack width growth occurs during the test.

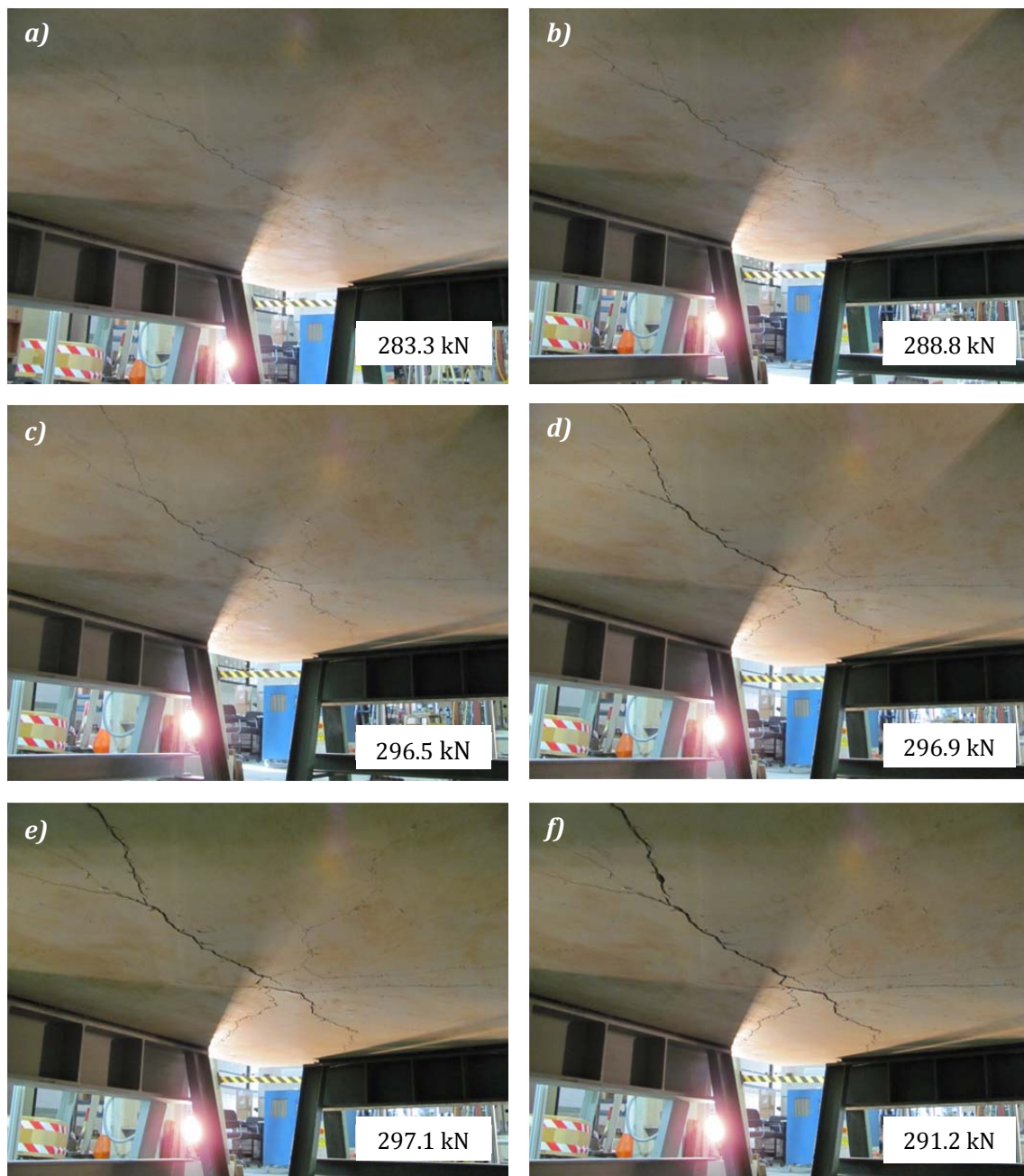


Figure 4.7 Evolution of cracking during the test of slab M_B.

After the test, each slab was turned over for the assessment of the crack pattern. This operation was possible due to the significant residual strength provided by the steel fibres even after advanced damage. The pictures of the crack patterns presented in Figure 4.8 indicate that, in general, there are four main cracks and several secondary cracks (which are not visible in Figure 4.8). In almost all cases the cracks approaches the points where the supports end.

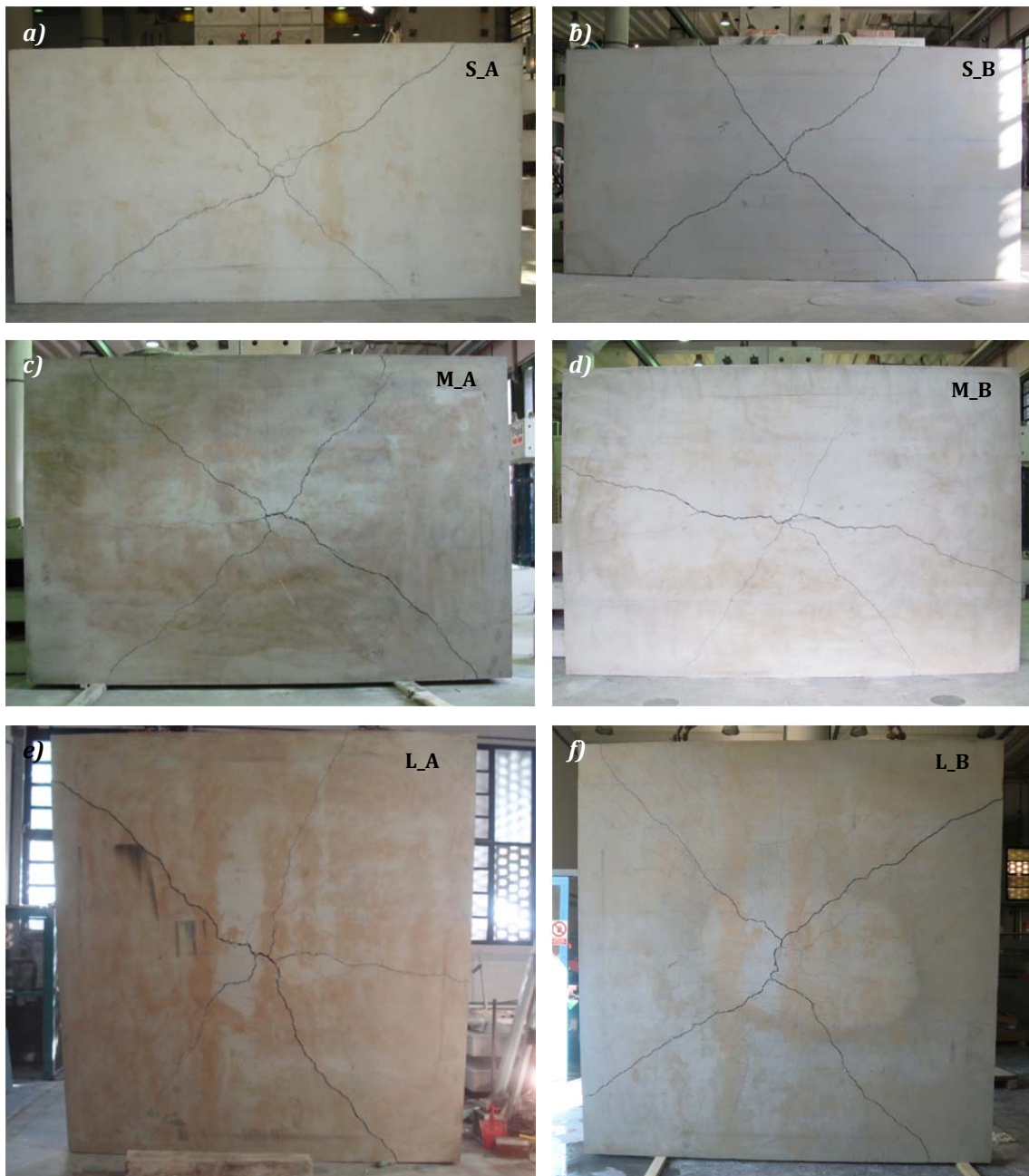


Figure 4.8 Crack patterns of slabs a) S_A; b) S_B; c) M_A; d) M_B; e) L_A and f) L_B.

In order to provide a more detailed view, a map was drawn with the main and the secondary cracks visible to the naked eye. The resulting crack patterns are presented in Figure 4.9. The main cracks, already identified in Figure 4.8, are represented by black lines and the secondary cracks are depicted by grey lines.

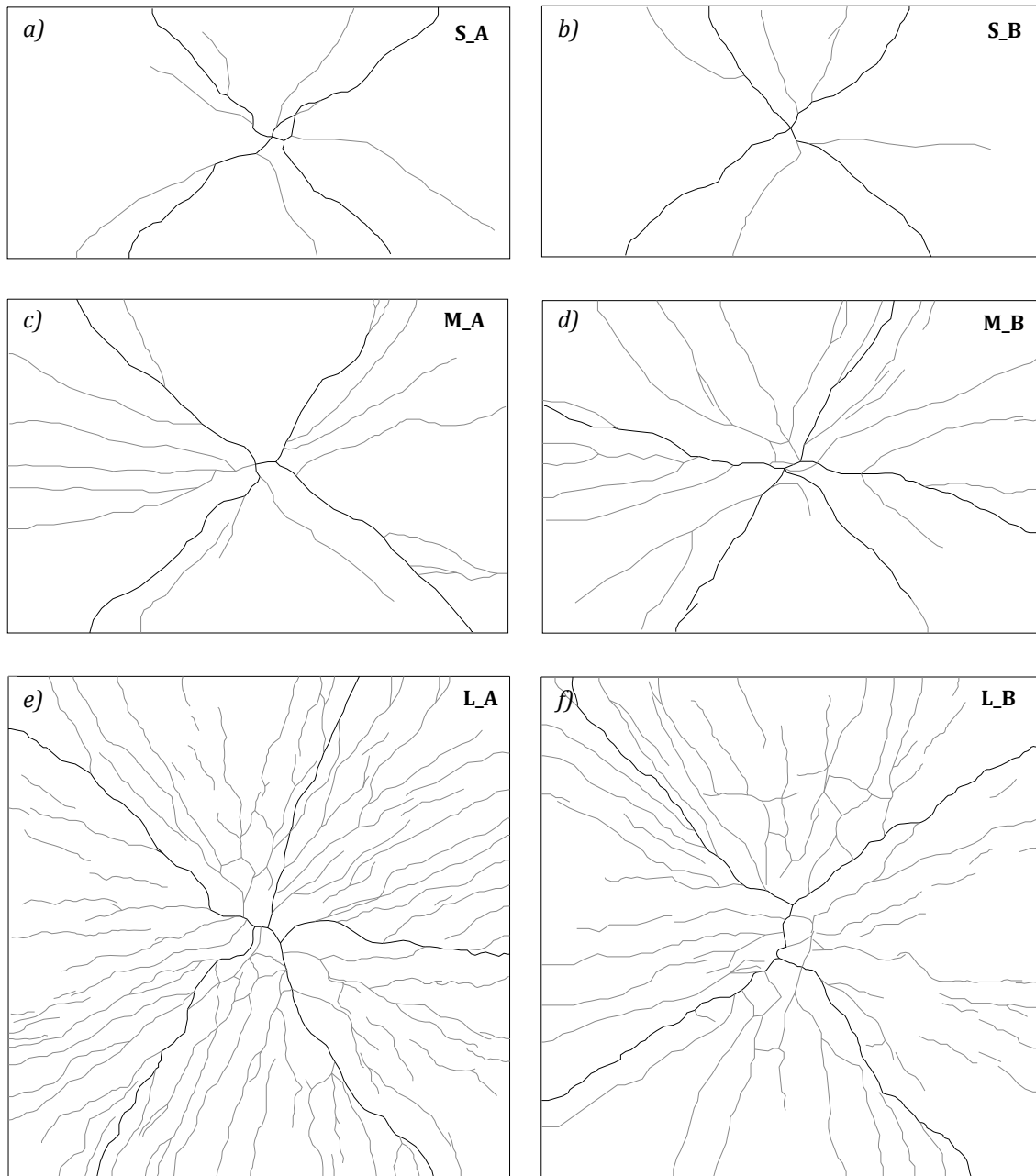


Figure 4.9 Detailed crack patterns of slabs a) S_A; b) S_B; c) M_A; d) M_B; e) L_A and f) L_B.

The maps indicate that in general four main cracks are formed. The only exceptions are slabs M_B and L_A (Figures 4.9d and 4.9e, respectively), which present five main cracks. These differences in the crack patterns indicate that slabs M_B and L_A are more likely to exhibit differences in the post-cracking behaviour with respect to their corresponding pairs (M_A and L_B). By the same rule, the slabs S, with very similar crack patterns, should be more likely to present similar post-cracking behaviour. The higher density of secondary cracks observed in slabs M (Figures 4.9c and 4.9d) and L (Figures 4.9e and 4.9f) may be attributed to the bigger deflection reached during the test of these slabs (especially in slabs L).

At large, the behaviour of the steel fibres in the cracks responds to a pull-out mechanism (which ultimately would lead to the complete removal of the fibre from the concrete matrix). Matrix spalling close to the crack mouth edge was detected during the test. Details of the cracking observed in slabs L_A and L_B after the test are presented in Figure 4.10. Figure 4.10a focus on a main crack in the centre of the slab (L_A), where the crack opening approached 10 mm. The detail shows that some fibres still bridge the crack whereas others were partially removed. Figure 4.10b corresponds to a main crack near the edges of the slab (L_B). In this case, the crack opening is smaller (only 6 mm) and most of the fibres are still bridging the crack. It is also clear that small pieces of the matrix have spall near the crack due to the debonding of the fibres and to the brittle nature of the cementitious matrices (Laranjeira 2010).

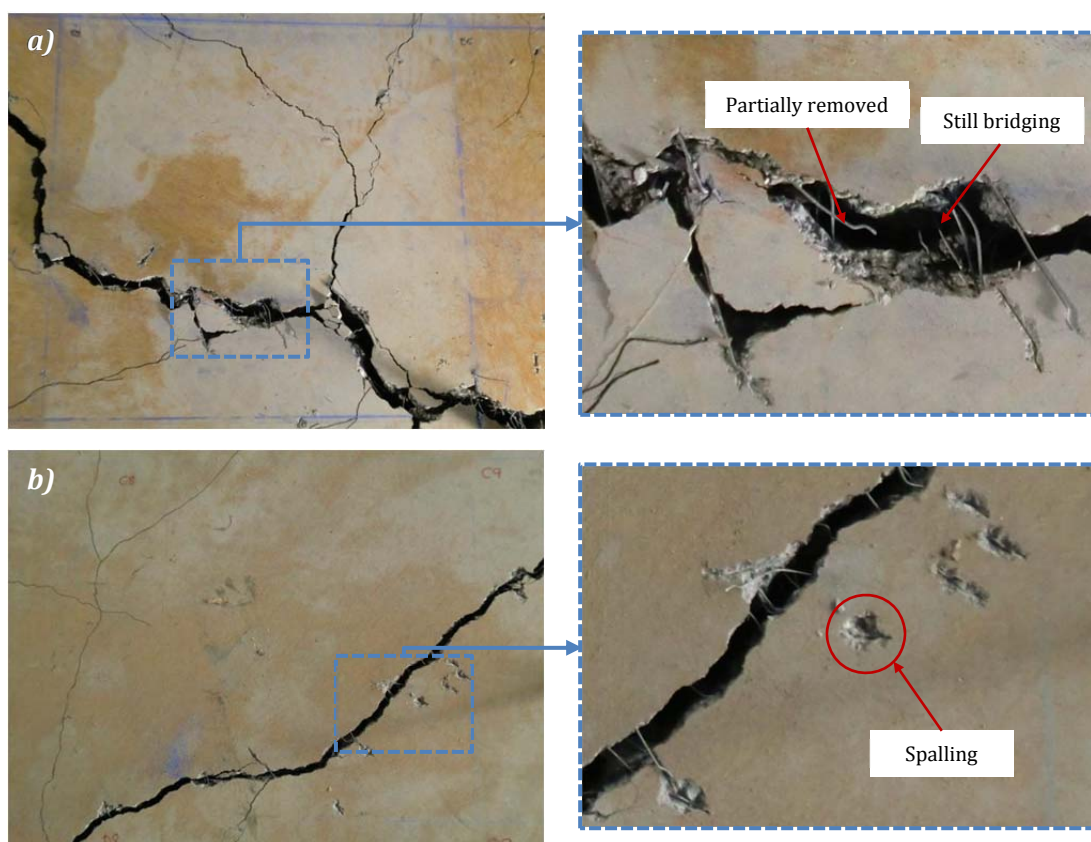


Figure 4.10 Detail of cracking a) at the centre of slab L_A and b) near the edges of slab L_B.

4.3.2. Load-deflection curves

Estimation of the deflection at the centre of the slabs

As mentioned in section 4.2.3, no displacement sensor was placed at the centre of the slab, which coincides with the point of application of the load. . Therefore, the deflection at the centre of the slab must be estimated before presenting the load-deflection curves of each test.

Figure 4.11a shows the deflections measured for a load of 226.7 kN by the twelve displacement transducers located in the two symmetry axis of the slab L_A (blue represents one direction and red the perpendicular direction). The symmetry axis and the location of the transducers in such slab are presented in Figure 4.11b. The results indicate a linear relation between the deflection measured and the position of the transducers, with a $R^2=0.999$ in all cases. Therefore, a linear regression was used to estimate the deflection in the centre of the slab considering each direction separately (see circled deflections at location 0 cm). The average of values in both directions is then estimated.

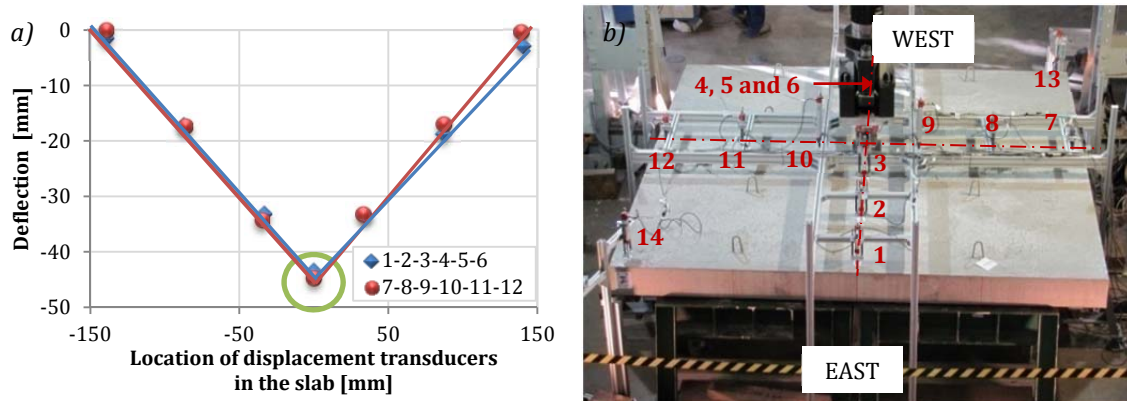
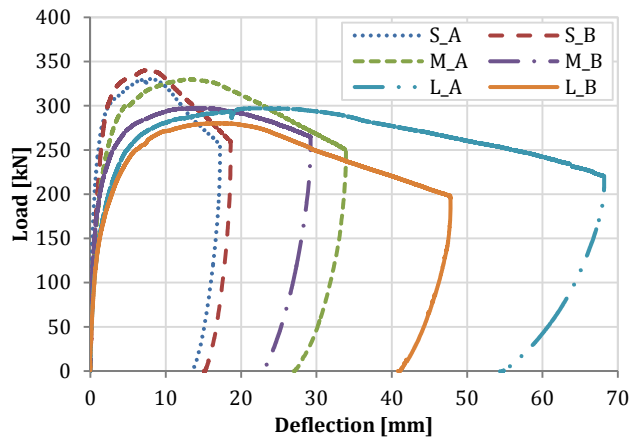


Figure 4.11 a) Measured and estimated deflections in the centre of slab L_A for a load of 272.4 kN and b) location of the displacement transducers.

Notice that the average deflection estimated must be subtracted by the normal deflection of the neoprene layers. The latter may be estimated through the average of the measures registered by the four displacement transducers placed at the axis of the support (namely 1, 6, 7 and 12). Such correction should also consider that the slabs may lose contact with part of the neoprene sheet during the test so that the support centreline moves towards the loading point. Since the deflection of the support centreline should be minor, only the normal deflection of the neoprene layers is considered to obtain the final deflection. The same procedure is repeated for all load values recorded during the test.

Analysis of the load-deflection curves

The experimental results are initially presented in terms of vertical load versus the deflection at the centre of the slab as shown in Figure 4.12. In the table in Figure 4.12 the maximum load values and their corresponding deflection are presented. A considerable difference in the structural response of slabs S, M and L was expected as a result of the significant variation on the shape of the elements. Nevertheless, the bearing capacity of the steel fibres as the only reinforcement compensates for the influence of the geometry providing a ductile behaviour, particularly in the case of the slabs L. Therefore, the fibre reinforcement allowed the larger slabs (M and L) to reach load levels close to those of the slabs S. In fact, the maximum load measured ranges from 280.1 kN (L_B) to 340.7 kN (S_B), thus showing a variation of only 21.4% despite the change in the width.



Slab	Maximum load [kN]	Deflection [mm]
S_A	330.3	8
S_B	340.7	7.7
<i>Average S</i>	<i>335.5</i>	<i>7.85</i>
M_A	329.9	13.3
M_B	297.1	15.1
<i>Average M</i>	<i>313.5</i>	<i>14.2</i>
L_A	297.1	22.4
L_B	280.1	16.9
<i>Average L</i>	<i>288.6</i>	<i>19.65</i>

Figure 4.12 Load-deflection curves and maximum loads with corresponding deflection.

Another parameter that indicates the structural contribution of the fibres and the ductile behaviour of FRC is the high residual load in comparison with the maximum load reached during the test. In the case of the slab L_A the residual load is 217.7 kN for the maximum deflection reached (68.2 mm) whereas the slab L_B presents a residual load equal to 184.5 kN for the maximum deflection reached (47.8 mm). These values correspond to 73% and 66% of the highest load measured for L_A and L_B, respectively.

It should be pointed out that the use of other types of fibres with a lower modulus of elasticity (in an equivalent fibre content) could enhance the ductility of the slab. However the load registered in this case would be smaller and a bigger difference should appear between load levels of the three types of slabs.

In terms of average loads, a difference is observed between the slabs: the maximum loads of the slabs S and M are, respectively, 16.3% and 8.6% higher than the registered for the L slabs. However, if studied individually the difference is not so evident since the slab M_A presents a maximum load close to the value of the slabs S. Likewise, the value measured for slab M_B is similar to that of slabs L. The same observation is not verified for the average deflections at which the maximum load occurs. This deflection in the slabs S is different from the measured for the slabs M and L.

A general overview of the response of the slabs is introduced in Table 4.7 in terms of the load measured for a given deflection. The selected values of deflection range from small to large deflections, namely: 1 mm, 5 mm, 10 mm, 20 mm and 40 mm. The results indicate that the pairs of slabs present a rather similar behaviour for small deflections. For example, the values measured in the slabs L for 1 mm only differ a 0.7%; whereas for 20 mm and 40 mm the difference increases up to 6.5% and 25.7%, respectively.

Table 4.7 Load values for deflections of 1 mm, 5 mm, 10 mm, 20 mm and 40 mm.

Slab	Load [kN]				
	1 mm	5 mm	10 mm	20 mm	40 mm
S_A	245.8	320.7	321.6	-	-
S_B	206.4	331.1	330.3	-	-
<i>Average S</i>	<i>226.1</i>	<i>325.9</i>	<i>326.0</i>	-	-
M_A	181.0	300.5	325.2	312.2	-
M_B	185.0	273.5	293.5	291.2	-
<i>Average M</i>	<i>183.0</i>	<i>287.0</i>	<i>309.4</i>	<i>301.7</i>	-
L_A	138.7	251.6	280.8	296.5	277.1
L_B	137.6	238.9	271.2	278.3	220.4
<i>Average L</i>	<i>138.2</i>	<i>245.3</i>	<i>276.0</i>	<i>287.4</i>	<i>248.8</i>

The reason for the increasing difference in load values with large deflections may be the fibre reinforcement itself. Before cracking occurs, the response of the slabs of each pair is almost identical since their performance depends on the concrete properties. Therefore, the first crack is determined by the concrete matrix properties and the existing level of stress. Nevertheless, after the first crack appears, the development of new cracks depends on the distribution and orientation of the fibres in the concrete matrix. This means that dispersions on the distributions or orientation will lead to the development of different crack patterns, ultimately producing a variation on the structural response. .

As the deflection increases the fibres are more active and the influence of the dispersion on their distribution becomes more evident on the overall response of the slabs. This justifies the bigger dissimilarities verified between the results of the two slabs of each geometry for increasing deflections. The described behaviour is confirmed by the results presented in Table 4.7, particularly for slabs M and L which present differences in the crack pattern (as shown in Figure 4.9).

Identification of the stages in the load-deflection curves

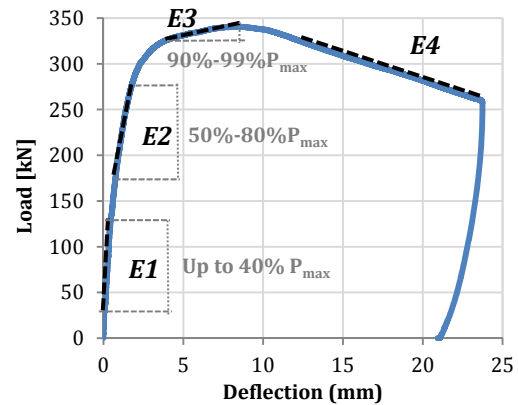
Four stages may be distinguished in the load-deflection curves of Figure 4.12. In the first stage, before concrete cracks, a linear behaviour may be assumed. When cracking occurs, the stress resisted by the concrete is transmitted to the steel fibres, which initiate their bearing activity through a mechanism of adherence, strain compatibility and the debonding. This second stage is characterized by a non-linear behaviour of the element. When the main cracks of the elements are formed and the fibres are fully debonded, the embedded fibres are subjected to pull-out. In this third stage, the fibres can still carry stresses, causing small increments in the load for increasing deflections. Finally, a fourth stage is identified after the peak load. This is characterized by a slight reduction of the load due to the partial removal of the fibres.

To further analyse the behaviour of each of the slabs, the average slope of the lines which make up each stage described above was calculated. Given the different performance of the slabs depending on their geometry, the three first stages were defined in terms of percentage of the maximum load in order to allow a better comparison of the

results. The slope of the first stage (*E1*) corresponds to the stretch up to 40% of the maximum load. The slope of the second stage (*E2*) is calculated in the stretch going from 50% to 80% of the maximum load while the slope of the third stage (*E3*) is evaluated in the stretch defined between 90% and 99% of the maximum load. Since the fourth stage is easily identified in the load-deflection curves, there was no need to define percentages of load. The values of the slopes (expressed in kN/mm) are presented in Table 4.8.

Table 4.8 Slopes in different stretches of the load-deflection curves.

Slab	Slopes [kN/mm]			
	<i>E1</i>	<i>E2</i>	<i>E3</i>	<i>E4</i>
S_A	405.0	107.4	7.3	-8.9
S_B	269.0	104.9	6.7	-8.0
Average S	337.0	106.2	7.0	-8.5
M_A	238.9	52.1	4.9	-4.5
M_B	344.3	46.0	4.1	-3.3
Average M	291.6	49.0	4.5	-3.9
L_A	143.8	30.6	1.8	-2.0
L_B	150.6	27.7	3.9	-3.0
Average L	147.2	29.2	2.8	-2.5



The values in Table 4.8 confirm the previously described behaviour. In the second stage, there is a decrease in the stiffness caused by the cracking of the matrix. The reduction in the values of stiffness is 69%, 83% and 80% for slabs S, M and L, respectively. Another decrease in stiffness is observed in the third stage, which shows values of slope 93%, 91% and 90% smaller than *E2* for slabs S, M and L respectively.

Up to the third stage, the values of slope are similar for the elements of each pair (with the exception of *E1* in the S slabs). Nevertheless, at the third stage some differences appear between the slopes of slabs M_A and M_B or between L_A and L_B. These differences are probably caused by variations in the fibre distribution in the matrix. Such influence becomes more noticeable as the cracks increase and the fibres are more active. Despite that, the analysis of the average values shows a clear tendency for all slopes. In this case, the highest values are always observed for the slab S, followed by the ones of the M and the slab L in this order.

It is noteworthy that the 33% difference in the width of the slabs M and L leads to a *E4* 56% higher in the former. However, the width difference of only 25% between slabs S and M produce a much higher *E4* for the slabs S if compared to the slabs M (118%). These results suggest that, at stage four, the effect of the geometry on the response of the slabs S is more significant than for the slabs M and L, which will be further studied in the subsequent section.

4.3.3. Load-rotation angle curves

In the previous section, the results were presented in terms of the estimated deflection at the centre of the slab. With the aim of deepening in the study of the response of the slabs, the evolution of the load during the test is now presented in Figure 4.13 in terms of rotation angle, which is calculated by dividing the deflection at this point by the half width of the slab.

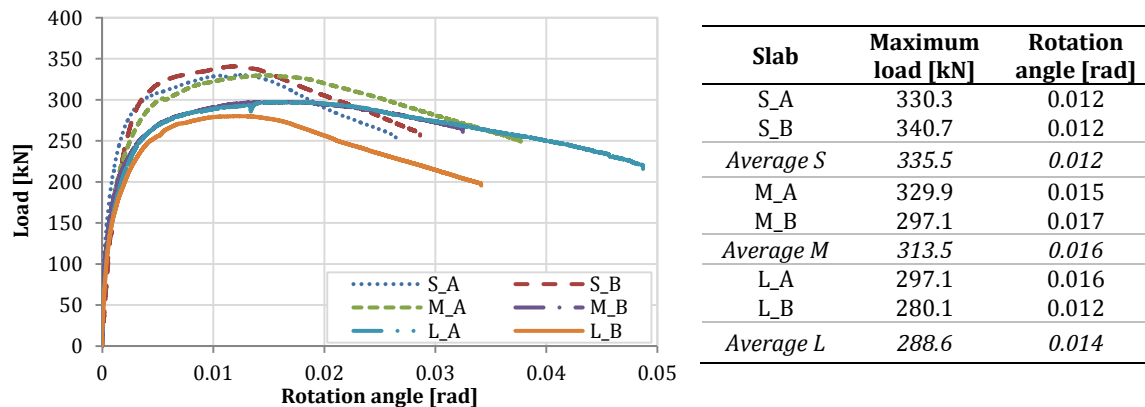


Figure 4.13 Load-rotation angle curves and maximum loads.

The slabs S and the slab M_A exhibit similar responses. On the other hand, the behaviour of the slab M_B is closer to the observed for the slabs L, particularly L_A. Furthermore, contrarily to what was observed in the load-deflection results (see Figure 4.12), the curves of all the slabs present similar slopes after the maximum load.

The table in Figure 4.13 summarizes the rotation angles corresponding to the maximum load of each slab. While the values of rotation angle for the pair of slabs S and slabs M are very close, the values for the pair of slabs L are not so similar. In fact, the slab L_B exhibits its maximum load at a rotation angle very similar to that of the slabs S.

4.3.4. Energy absorption capacity

The energy absorption capacity was analysed by calculating the area enclosed by the load-deflection curves presented in section 4.3.2. In Figure 4.14, the results of absorbed energy are plotted against the rotation angle for each slab. Additionally, the load-rotation angle curves are also included in the graphs.

As expected, the highest values of energy absorption for analogous deformations (in terms of rotation angle) correspond to the slabs L, whereas the lowest values are associated with slabs S. Such outcome may be attributed to the ductile response exhibited by the larger slabs and described in section 4.3.2. Furthermore, the rate at which the energy absorbed by the slabs L increases is higher than that of slabs M and, particularly, slabs S.

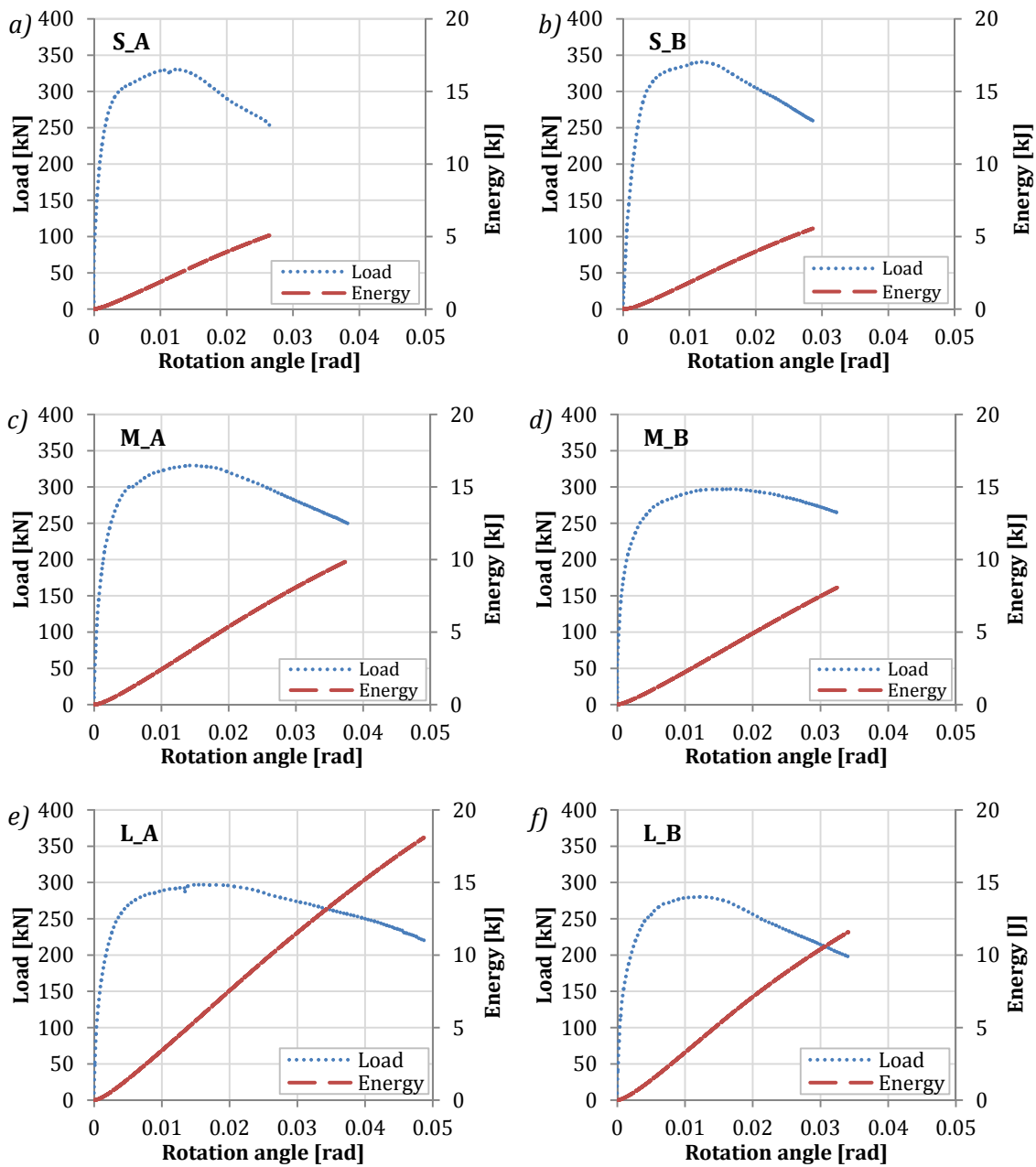


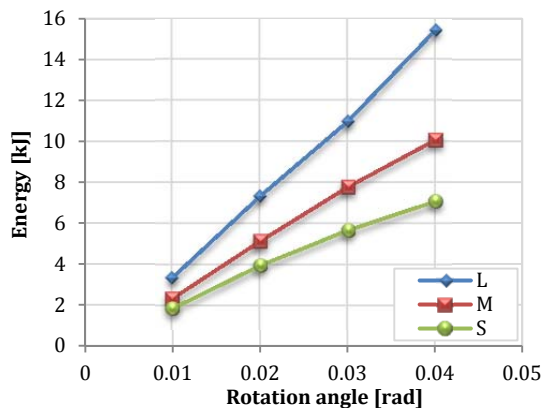
Figure 4.14 Energy absorption and load-rotation angle curves for slabs a) S_A, b) S_B, c) M_A, d) M_B, e) L_A and f) L_B.

In Table 4.9 the values of energy absorption are presented for the following rotation angles: 0.01 rad, 0.02 rad, 0.03 rad and 0.04 rad. The shaded cells indicate the slabs that did not reach such deformations during the test. In this case the area was calculated by linearly extrapolating the fourth stage of the load-deflection curve considering the slope values of E4 from Table 4.8.

Table 4.9 Energy absorption at a given rotation angle.

Slab	Energy absorption [J]			
	0.01 rad	0.02 rad	0.03 rad	0.04 rad
S_A	1872.0	3938.5	5646.0	6978.7
S_B	1834.0	3968.3	5685.4	7181.5
<i>Average S</i>	<i>1853.0</i>	<i>3953.4</i>	<i>5665.7</i>	<i>7080.1</i>
M_A	2427.3	5367.8	8080.0	10410.5
M_B	2243.7	4905.5	7469.9	9721.5
<i>Average M</i>	<i>2335.5</i>	<i>5136.6</i>	<i>7775.0</i>	<i>10066.0</i>
L_A	3420.8	7544.2	11541.7	15211.8
L_B	3282.8	7112.7	10396.9	15617.5
<i>Average L</i>	<i>3351.8</i>	<i>7328.4</i>	<i>10969.3</i>	<i>15414.7</i>

The results presented in Table 4.9 suggest that in all cases the least energy absorption capacity corresponds to the slabs S. In fact, the average absorbed energy for 0.01 rad in slabs L is 43.5% and 80.9% higher than for slabs M and S, respectively. These differences increase to 53.1 and 117.7%, respectively, for a rotation angle of 0.04 rad. To deepen in the assessment of this behaviour, the evolution of the average energy absorption is plotted against the rotation angle in Figure 4.15. Additionally, the slopes of each stretch S1 (0.01-0.02 rad), S2 (0.02-0.03 rad) and S3 (0.03-0.04 rad) are presented in the same figure.



Slab	Slopes [kJ]		
	S1	S2	S3
S	210.0	171.2	141.4
M	280.1	263.8	229.1
L	397.7	364.1	444.5

Figure 4.15 Evolution of the energy absorption capacity with the rotation angle.

The slabs L show a higher enclosed area in the load-deflection curve as the rotation angle increases. The results also show that the behaviour of the slabs S is significantly different since the slopes in each stretch are lower and their values decrease at a higher rate. For example, the decreases in the slope for slabs S from S1 to S2 and from S2 to S3 are 17% and 18%, respectively. On the other hand, the reductions for slabs M are only 6% and 13%, whereas for the slabs L the value decreases 8% from S1 to S2 and increases 22% from S2 to S3.

This behaviour was already advanced when studying the slopes of the load-deflection curves. This difference between the slabs S and the slabs M and L is influenced by their own geometry and the setup of the test. Simply supported slabs with one

dimension at least two times longer than the other (as in the case of slabs S) work almost exclusively in the shortest direction, while the slabs M and L work in two directions. Consequently, the slabs S present limited force redistribution capacity if compared to slabs M and L, thus presenting a lower bearing capacity in the post-cracking stage.

4.4. CONCLUDING REMARKS

Chapter 4 discussed the results of an experimental program involving flexural tests of full-scale SFRC slabs. The following conclusions may be drawn from this study:

- The response of the SFRC slabs revealed the capacity of the steel fibres, as the only reinforcement, to carry stresses and provide ductility for the load levels reached during the tests.
- The slabs exhibited different flexural responses according their geometry. The highest loads were registered for slabs S; however the residual strength and ductility provided by the fibre reinforcement in the slabs M and L led them to reach load levels close to those of the slabs S.
- The crack pattern of the slabs presented, in general, four main cracks that develop from the centre to the edges where the supports were located. In the case of the bigger slabs, which reached large deflections, noticeable secondary crack was also detected.
- The results suggest that the crack pattern is significantly influenced by the distribution of the fibres in the concrete matrix. Different distributions may lead to different crack patterns, thus producing variations in the response of elements with the same geometry. Such variations are more noticeable as the crack opening increases.
- The analysis of the energy absorption capacity indicated a limited stress redistribution capacity of the slabs S, which are strongly affected by their geometry since they work almost exclusively in the shortest direction; whereas the slabs M and L exhibited a significant stress redistribution capacity provided by the fibre reinforcement.

5. FIBRE ORIENTATION IN SFRC SLABS

5.1. INTRODUCTION

As suggested by the study from Chapter 4, the effectiveness of fibre reinforcement depends on the orientation of the fibres with respect to the failure plane. Taking that into account, the Model Code 2010 (*fib* 2010) includes an orientation factor that integrates the influence of fibre orientation in the design of SFRC structures. In this case, the orientation is considered to affect the design serviceability and ultimate residual strengths when favourable or unfavourable fibre orientation effects are experimentally verified.

Although this new approach represents a paramount step forward in the integration of fibre orientation in the design, the cases in which it should be used to penalize or to improve the mechanical performance of the material are vaguely defined. In general, a certain fibre orientation may be considered advantageous if the fibres are aligned with main stresses acting in the structure, thus improving the tensile performance.

Research has provided evidence that the factors governing fibre orientation are the fresh-state properties of the concrete after mixing, the production process as well as the geometry of the formwork. Examples of advantageous preferential orientations caused by the geometry are slabs and plates in which, given their low height to width ratio, the fibres tend to align in the perpendicular plane to the filling direction, which in turn it is

perpendicular to the failure planes that develop in this type of structures. This becomes more significant as the dimension of the element increases since the fibres are subjected to the flow longer than in smaller elements. This highlights the importance of studying the preferential orientations caused by the geometry of these particular structural elements as well as its repercussion in the global structural behaviour.

In order to provide a more accurate definition of the effect of fibre orientation in the design codes and to work towards an optimal design of SFRC structures, deeper insight regarding the fibre orientation in certain types of structures is required.

5.1.1. Objectives

In light of the exposed, the objective pursued in this chapter is gaining deeper insight into the fibre orientation in the SFRC slabs described in Chapter 4. The study focuses on the determination of the fibre orientation, trying to identify patterns depending on the dimensions of the slab. For that, the following specific objectives are defined:

- Assess fibre content and fibre orientation in the SFRC slabs;
- Based on the cases studied, identify different zones of orientation in the slabs and propose a fibre orientation pattern depending on the width of the slabs and
- Assess the post-cracking behaviour of the SFRC in different points of the slabs by means of a mechanical test on cubic specimens extracted from the slabs.

5.1.2. Outline of the chapter

The experimental program performed with the specimens extracted from the slabs is outlined in section 5.2. First, the drilling process and the preparation of the specimens from the slabs is presented. Then, the tests used to assess the fibre content, the fibre orientation and the post-cracking behaviour of the specimens are described

In section 5.3, a detailed analysis of the fibre orientation detected in the slabs is performed. Based on the results and the casting procedure, a fibre orientation pattern is suggested for the slabs. The post-cracking behaviour of the SFRC at different locations of the slabs is studied in section 5.4 considering the fibre orientation observed. Finally, in section 5.5, the main conclusions of the study are highlighted.

5.2. EXPERIMENTAL PROGRAM

In order to study the influence of the geometry on fibre orientation, information regarding the actual distribution of the fibres inside the slabs is required. For that, given the methods available at the UPC to assess the fibre orientation in SFRC, an experimental program based on the study of cubic specimens extracted from the slabs is proposed.

5.2.1. Core drilling

Cylindrical cores were drilled from the slabs after the tests described in Chapter 4. One of the main concerns during the process of core drilling was to keep the cores properly marked with regards to their position in the slabs. For that, a map was prepared to indicate the exact location of each of the cores, as shown in Figure 5.1 for slab S_B. The location maps of the rest of the slabs are included in section 5.3.2.

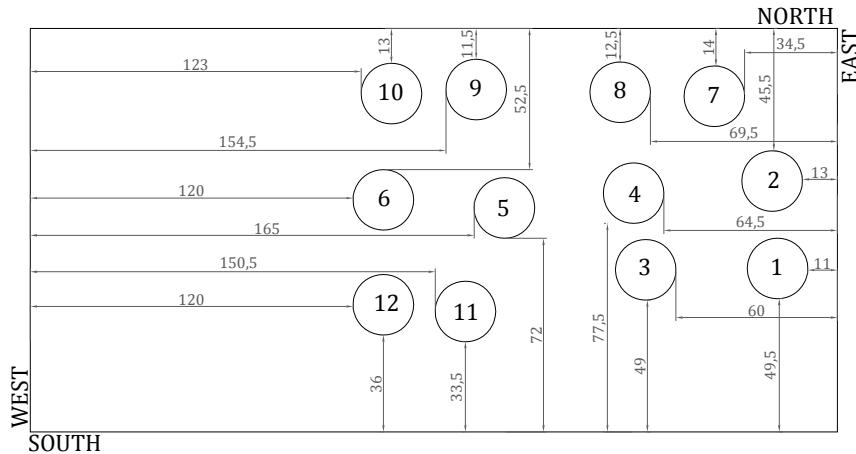


Figure 5.1 Location map of the cores in slab S_B.

Given the importance of the orientation of the cores for the study, the sides of the slabs were marked with the following: north, east, south and west (see Figure 5.1). The same criterion was used with the cores prior to extraction. In this case, the direction from east (E) to west (W) was indicated. This notation, along with the location map, allows identifying immediately the orientation of the cores in the slab. Figure 5.2 shows details of the location marks in the slabs and the drilling process of cores.

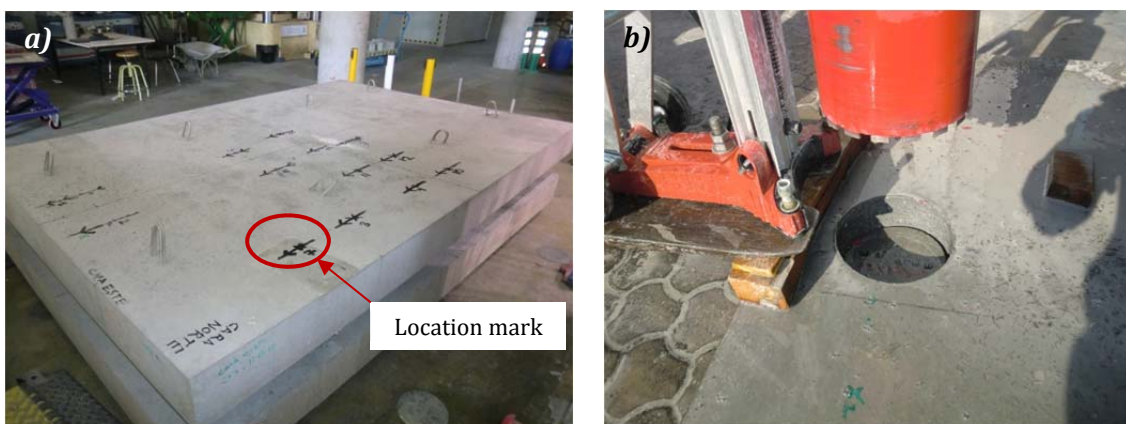


Figure 5.2 a) Slab with the core location marks before drilling and b) detail of the core drilling.

The criterion to define the position of the cores was to cover the largest surface possible and to choose points very close to each other or from symmetric locations. This last criterion intends to produce cores with similar fibre orientation whose post-cracking

behaviour could be assessed in two directions parallel to the side of the slab. The number of cores drilled from each slab is presented in Table 5.1.

Table 5.1 Number of cores drilled from each slab.

Slab	Casting date	Number of cores
L_A	09-11-10	18
L_B	11-11-10	15
M_A	09-11-10	12
M_B	11-11-10	12
S_B	23-11-10	12

Since the casting date for slabs S_A and S_B is the same and the load-deflection curves are very similar, only the former was characterized so as to reduce the number of tests. In the case of slab L_B an odd number of cores were drilled. Although the fifteenth specimen cannot be compared in terms of the mechanical test with a pair, its fibre content and orientation was assessed with the inductive method.

5.2.2. Preparation of the cubic specimens

The cylindrical cores extracted with 200 mm of height and 225 mm of diameter were cut into the 150 mm cubic samples required for the tests, as indicated in Figure 5.3a. First, the lateral edges of the cylinders were cut to obtain a 150 x 150 x 200 mm prism, as shown in Figure 5.3b. Then the 25 mm thick slices at the top and bottom of the prism were also cut (see Figure 5.3c). The cuts were made so that the sides of the resultant cubes were parallel to the sides of the slabs. The references regarding the orientation of the cubic specimen in the slab are marked in its sides (W-E and N-S) as shown in Figure 5.3c.

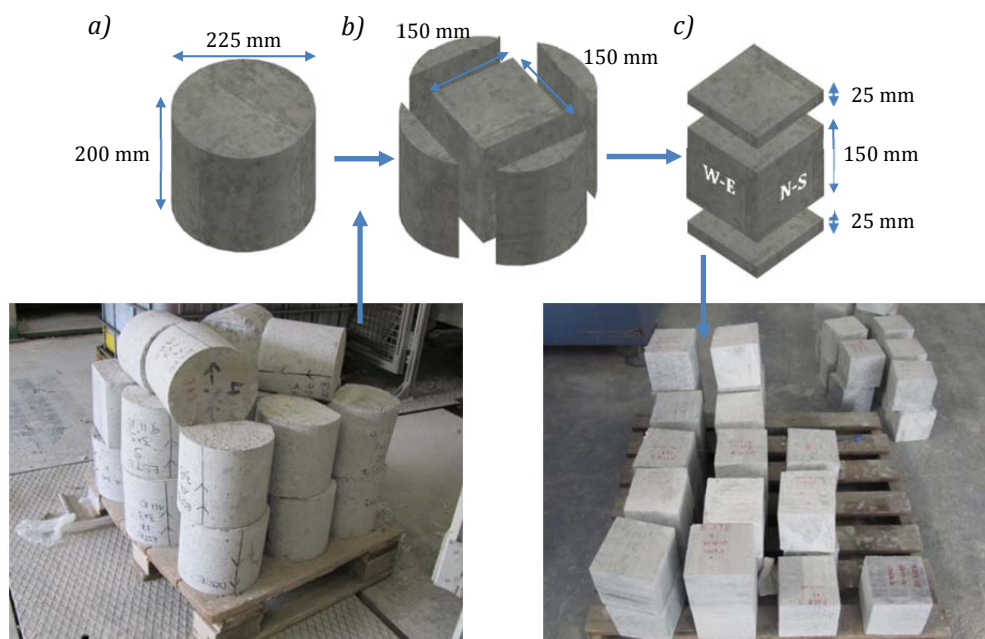


Figure 5.3 Detail of a) cylindrical cores, b) cuts in cylindrical core and c) cuts in prismatic specimens.

These cubic samples obtained underwent two different tests. First, they were tested according a non-destructive inductive method that provides information regarding fibre content and orientation in each of the three directions. Then the structural contribution of the fibres in terms of the residual strength was assessed by means of a double punch test. Both tests are described in the following sections.

5.2.3. Inductive method for assessing the amount and orientation of steel fibres

The inductive method (Juan García 2011; Torrents *et al.* 2012) allows assessing the amount and orientation of steel fibres in cubic specimens. The method is based on the ferromagnetic properties of the steel fibres that are able to alter the magnetic field around them. Therefore, if an inductive coil acting as a sensor is placed wrapping the specimen, the fibres will affect the inductance of the sensor. An increase of the inductance occurs when the fibres are located in a position parallel to the direction of the magnetic field (parallel to the axis of the coil), whereas those located in a perpendicular direction cause practically no variation. On the one hand, the average of the three measurements provides information regarding the content of fibres in the sample and, on the other hand, the differences in the measurements of the three axes give information about the orientation.

The testing procedure is very simple: the specimen is located on a non-metallic surface with the concrete-pouring face upwards (axis Z), for instance. The specimen is then wrapped by the inductance generated by a coil, as shown in Figure 5.4a, and the increase of the inductance is measured with an impedance analyser (see Figure 5.4b). The same procedure is repeated with the specimen turned towards the axes Y and X.

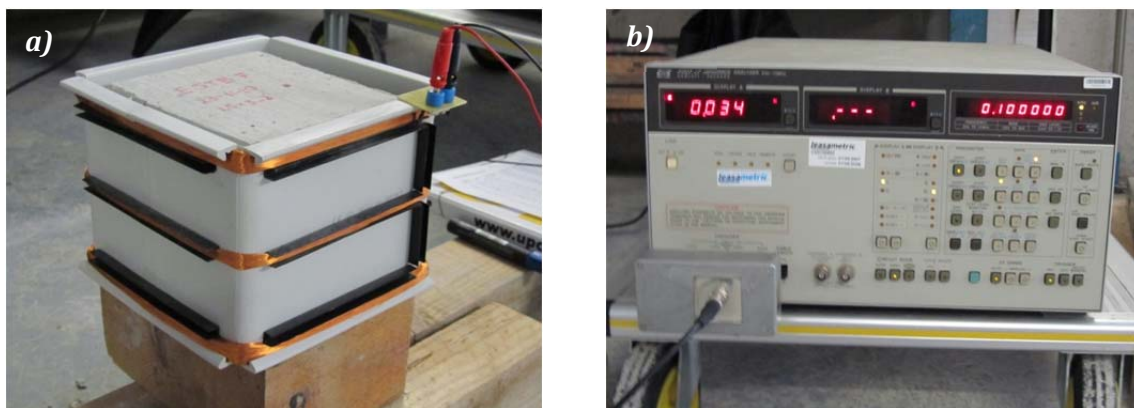


Figure 5.4 Equipment of the inductive method: a) coil and b) impedance analyser.

5.2.4. Method for the multidirectional characterization of SFRC

The multidirectional method is a new test procedure proposed by Pujadas *et al.* (2011) to assess the structural contribution of fibres in the post-cracking behaviour depending on their orientation. This method is based on the Barcelona test (Molins *et al.* 2006; Molins *et al.* 2009) and consists in a double punch test to determine the strength and toughness in the three main axes of the cube (see Figure 5.5).

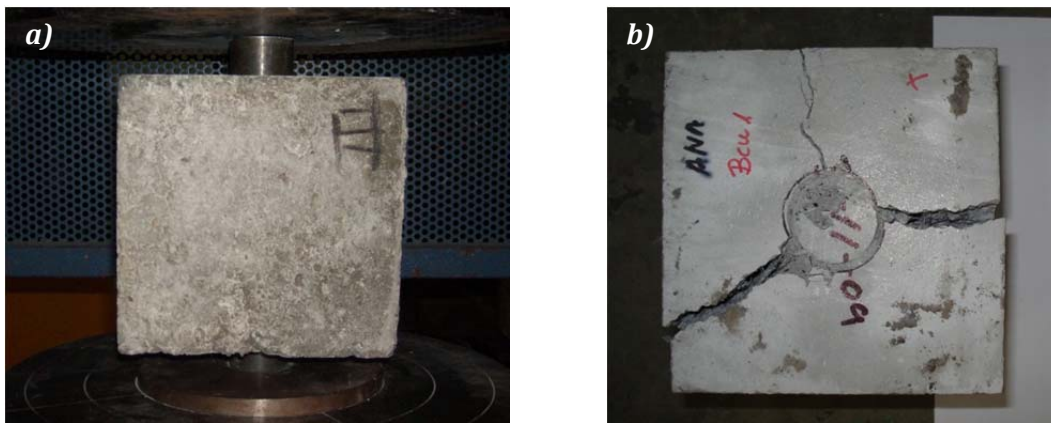


Figure 5.5 a) Multidirectional method setup and b) cubic specimen after the test.

The post-cracking strength of FRC is directly related with the amount of fibres subjected to pull-out during the test. When the load is applied, only the fibres that are not aligned with the load direction contribute to the residual strength measured. This method also allows detecting preferential planes of orientation (Stroeven and Hu 2006; Stähli 2008) since the average orientation is proportional to the post-cracking response of FRC. This was verified by conducting an experimental program on cubic specimens that may be found in Annex 1.

5.3. INDUCTIVE METHOD RESULTS

5.3.1. Fibre content

The results of fibre content of the cubic specimens are presented in Figure 5.6 for all specimens. The graph indicates that, in general, the amount of fibres in the slabs is higher than the theoretical dosage of 40 kg/m³. In most cases, the fibre content ranges from 40 to 45 kg/m³, however there are values significantly lower (31.5 kg/m³) and higher (54.1 kg/m³).

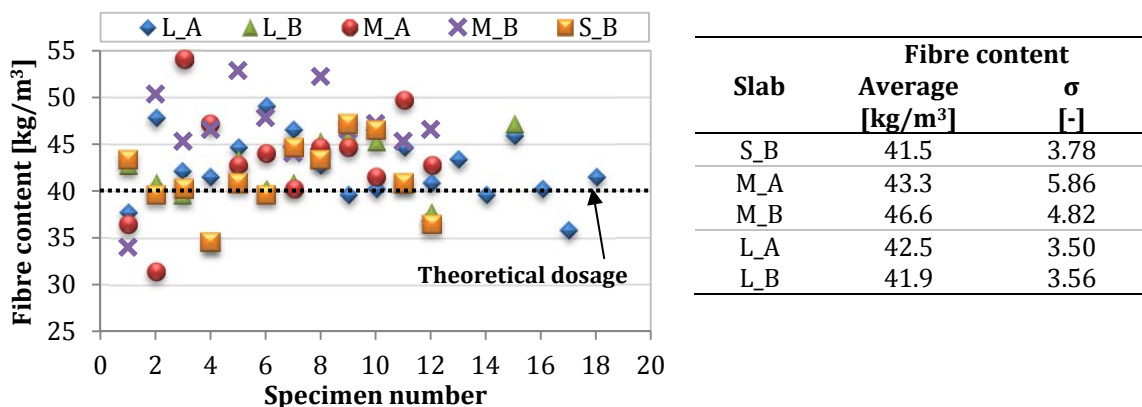


Figure 5.6 Fibre content in the cubic specimens, average content in the slabs and standard deviation.

A correlation between the fibre content and the location of the cubic specimen in the slab could not be found. Fibre contents above and below the theoretical dosage can be found either in intermediate locations or near the edges of the slabs. However, the cubic specimens obtained near the centre of the slabs (from where the concrete was poured in the casting) rarely present a fibre content lower than the theoretical dosage. These differences in fibre content could have a significant influence in the post-cracking behaviour of the SFRC in the multidirectional test, as the specimens with higher fibre content will obtain higher residual strength.

5.3.2. Fibre orientation

The results of the inductive method regarding fibre orientation are presented out in two stages. First, the orientation results of the specimens are included in a map with the location of each specimen in the slab. The annotations are represented by arrows pointing the closest edge. The orientation is expressed in terms of percentage of fibres aligned along either X or Y axes and are represented with different colours to facilitate the comprehension (blue for the alignment along X axis and red for the Y axis).

In the second stage, the specimens are distributed into several series along the two axes and are represented in a map of the slab. The specimens assigned to each series are also specified in a table. Then, the results of fibre orientation for each series are plotted in terms of alignment along X or Y axis versus position along X or Y axis so that the tendency of fibres to align along the two axes can be easily visualized and assessed in detail.

This way of presenting the results in two stages is conducted for each slab so that all the results of the same slab are presented together. Afterwards, the tendencies observed are analysed considering the casting procedure described in Chapter 4.

Small slab

The fibre orientation for slab S_B is presented in Figure 5.7. This figure shows a map with the location of each specimen in the slab. The annotations are represented by arrows that indicate the distance to the closest edge. The orientation is expressed in terms of percentage of fibres aligned along either X or Y axes, which are marked with different colours in order to facilitate the comprehension (blue for the alignment along X axis and red for the alignment along Y axis).

The results suggest a preferential orientation of the fibres in the horizontal plane (perpendicular to the pouring direction) as expected due to the geometry of the element and casting procedure. Furthermore, other preferential orientations are detected near the edges of the slab where the fibres are aligned parallel to the boundaries. Such outcome is related with the wall-effect caused by the walls of the formwork. This effect is clear in specimens 1, 2 and 7-10, which present most of the fibres parallel to the side of the mould. It may also be seen that the fibres change orientation as the analysed specimen approaches the edges (see specimens 6, 5, 4 and 2).

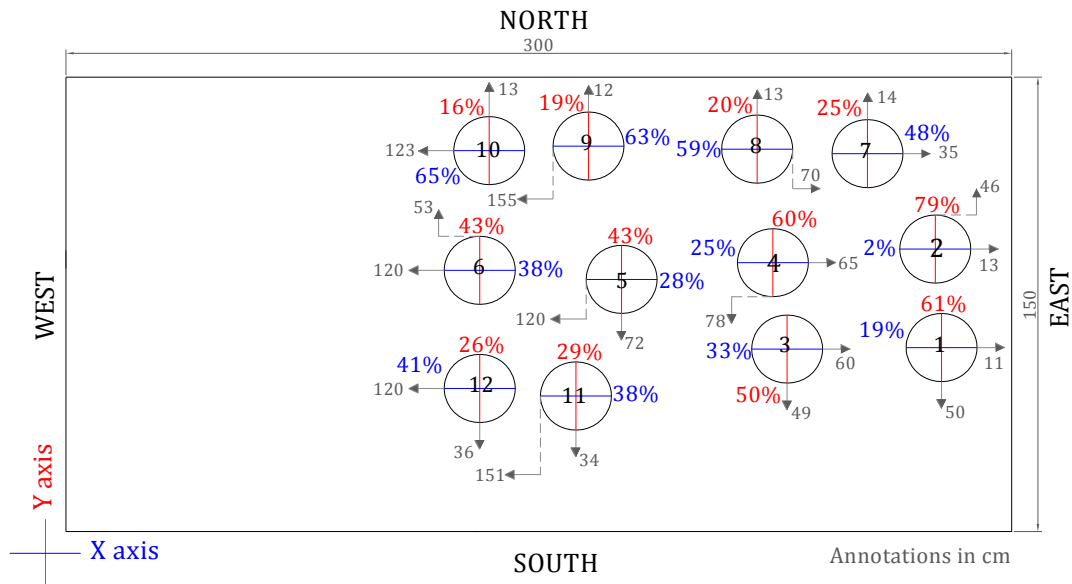


Figure 5.7 Fibre orientation in specimens of slab S_B.

The tendency of fibres to align along the two axes may be easily visualized if the specimens are grouped depending on their location. The lines marking the specimens included in each group are presented in Figure 5.8. For example, series 1 includes the specimens 7, 8, 9 and 10.

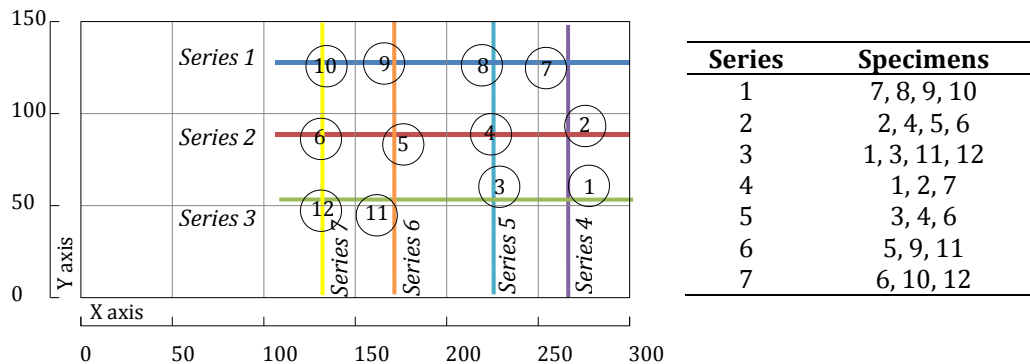


Figure 5.8 Distribution of specimens in slab S_B.

Figures 5.9a and 5.9b indicate the fibre alignment for series parallel to the X axis (1, 2 and 3). The shaded areas of the graphs represent the general tendency observed. The results from Figure 5.9a show that the fibre alignment along X axis is higher at the centre and lower at the edges of the slab. The opposite occurs for the fibre alignment along the Y axis, which is lower at the centre and higher at the edges, as shown in Figure 5.9b. Figures 5.9c and 5.9d indicate the fibre alignment for the series 4, 5, 6 and 7 that are parallel to the Y axis. In this case, the alignment of fibres along the X axis is lower at the centre and higher at the edges (see Figure 5.9c). Again, the contrary tendency is observed when the fibre alignment along the Y axis is analysed, as represented in Figure 5.9d.

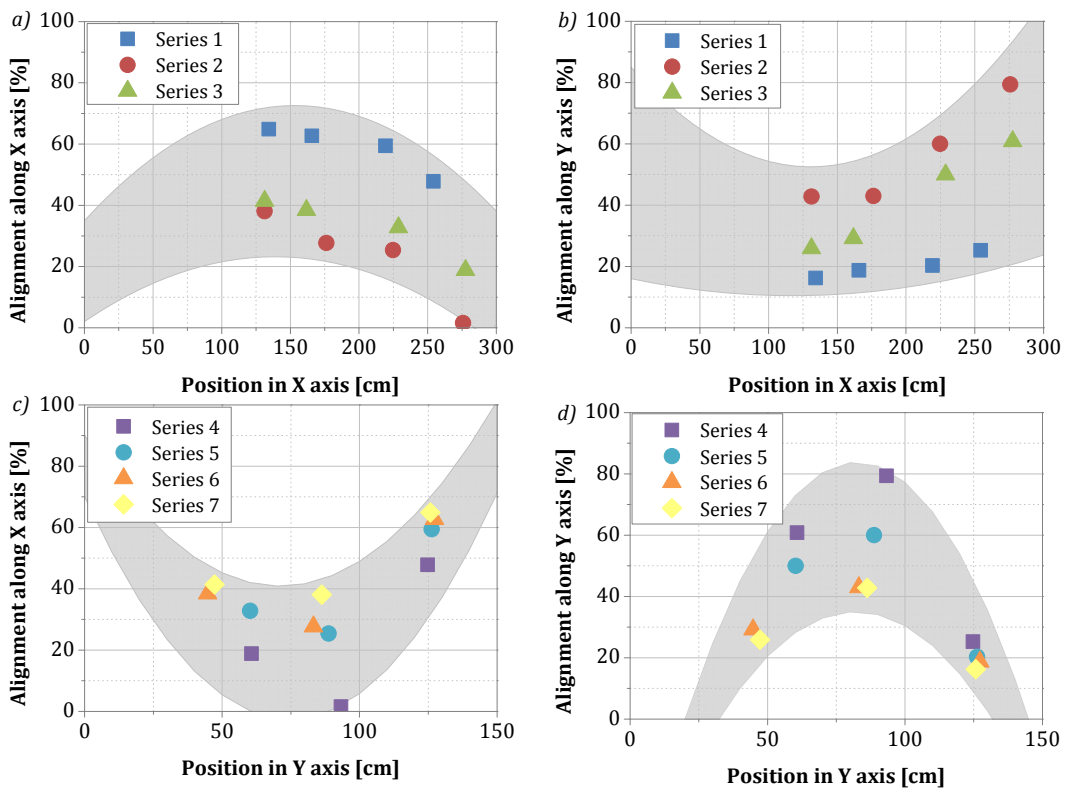


Figure 5.9 Alignment of fibres along X and Y axes for series a) 1-3 and b) 4-7 in slab S_B.

Medium slabs

The fibre orientation measured for slab M_A are presented in Figure 5.10. These results are similar to the observed in slab S_B.

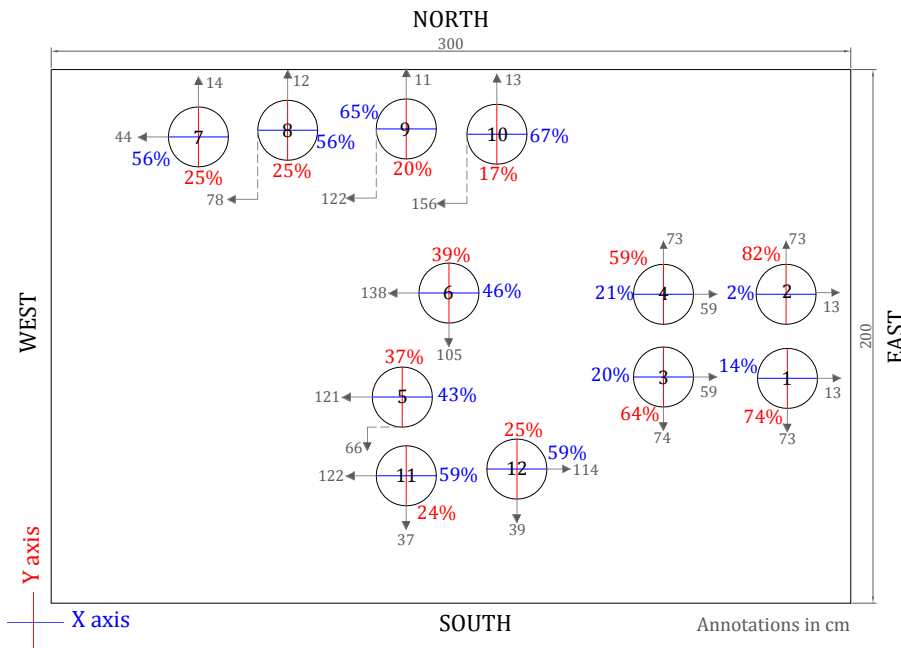


Figure 5.10 Fibre orientation in specimens of slab M_A.

In this case, the wall-effect may be detected in specimens 1, 2 and 7-10. Furthermore, it is verified that fibres tend to align parallel to the sides of the mould as they approach the edges. To expand the analysis of fibre orientation, specimens are grouped in five series according to the lines from Figure 5.11.

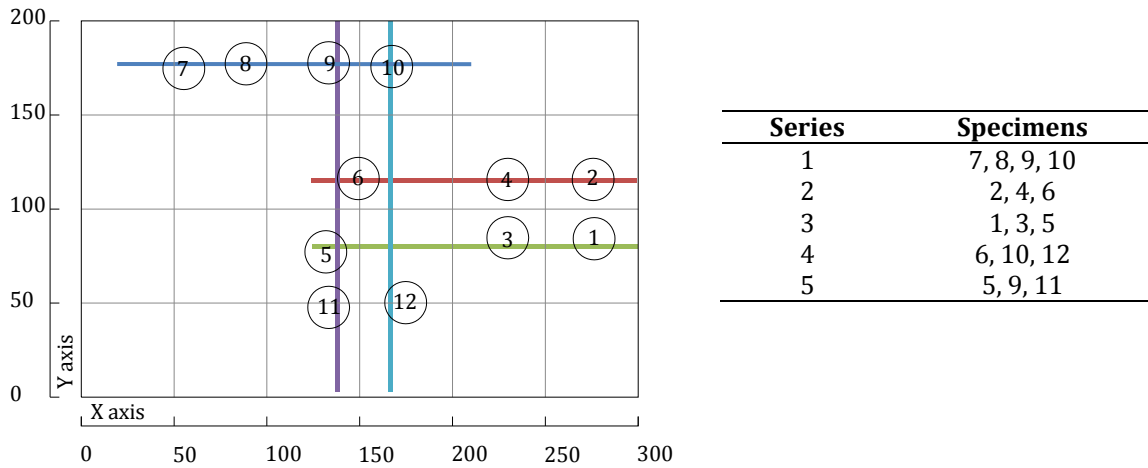


Figure 5.11 Distribution of specimens in slab M_A.

Figures 5.12a and 5.12b show the results of the series along X axis, which indicate that the fibre alignment parallel to X decreases from the centre to the edges. The opposite is observed in the alignment along Y that increases from the centre to the edges of the slab.

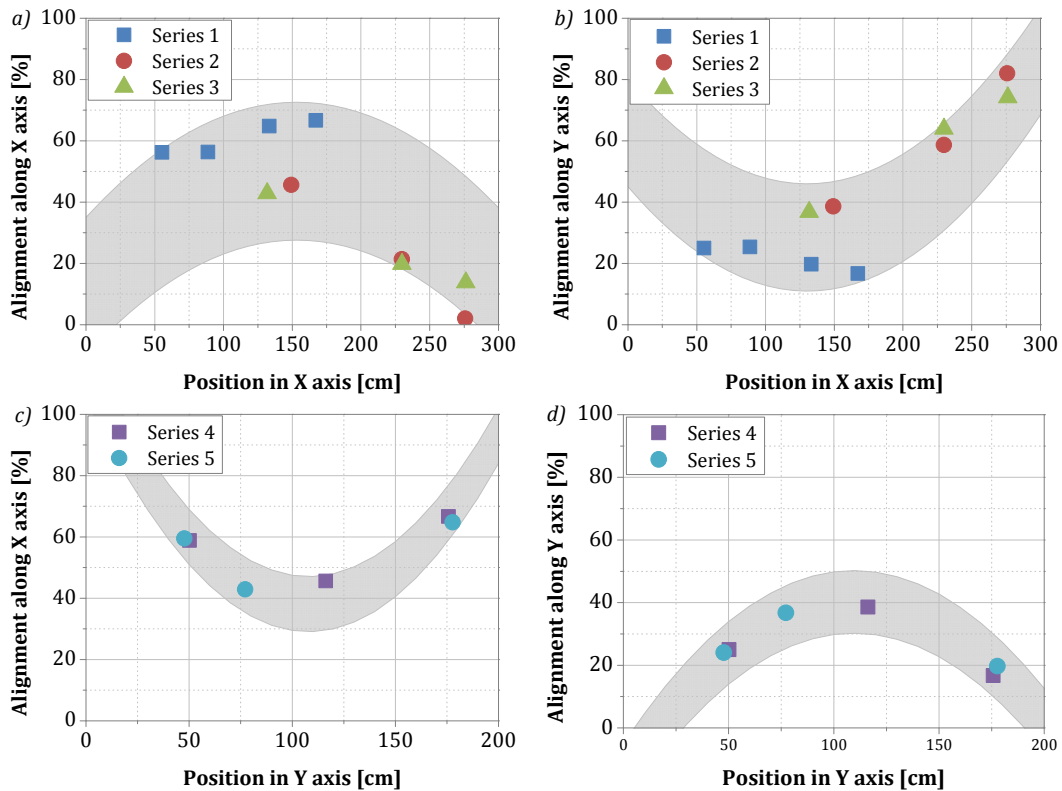


Figure 5.12 Alignment of fibres along X and Y axes for series a) 1-3 and b) 4-5 in slab M_A.

For the series defined along Y axis (see Figures 5.12c and 5.125.11d), the alignment along X increases at the edges while the alignment along Y axis decreases. Besides these tendencies, it can also be observed for the series located near the symmetry axis (series 2, 3, 4 and 5) that at central locations (around 150 cm and 100 cm for series 2 and 3 and for series 4 and 5 respectively) the percentage of fibres aligned along X and Y is very similar. However, as the specimens are farther from the symmetry axes the difference between the alignments increases.

In the results of slab M_B (see Figure 5.13), a preferential orientation in the horizontal plane (perpendicular to the casting direction, Z axis) is detected. The preferential orientations caused by the walls of the formwork are evident in the results of specimens 1, 2 and 7-10, which tend to present more fibres parallel to the edge.

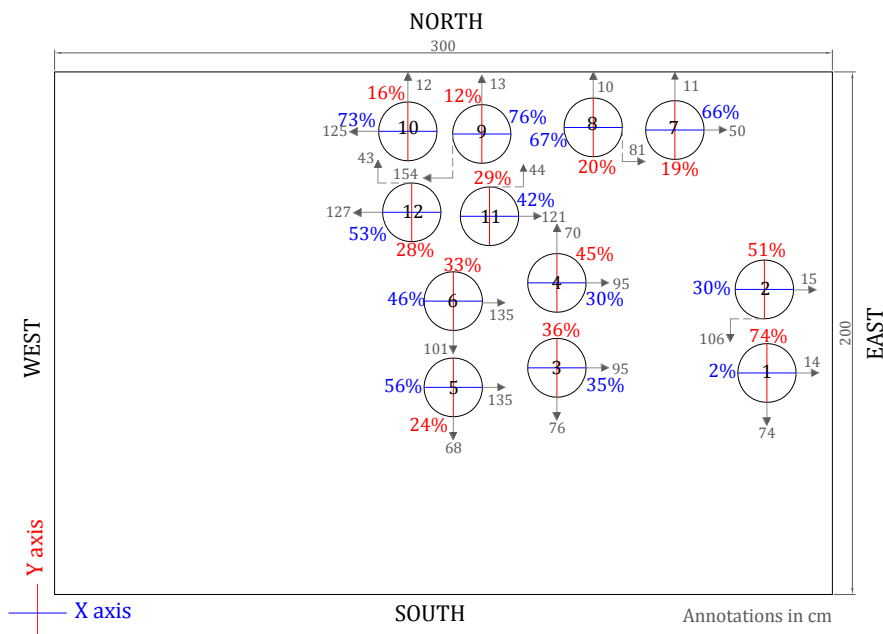


Figure 5.13 Fibre orientation in specimens of slab M_B.

As a general trend, specimens located near the centre of the slab present similar orientations in both axes (except for specimen 5 that showed a bigger difference than in other cases). A significant differences in orientation along X and Y occurs in specimens located near the edges due to the side effect introduced by the formwork.

The specimens of slab M_B are grouped in 3 series along X axis and 3 series along Y axis as represented in Figure 5.14. The results of Figure 5.15 reveal that the behaviour of series 2 and 3 (along X axis) and series 5 and 6 (along Y axis) agree with the described previously, presenting similar fibre alignments in both directions at the centre of the slab. Series 1 and 4 do not follow the same tendency since they are very close to the edges and thus influenced by the wall-effect.

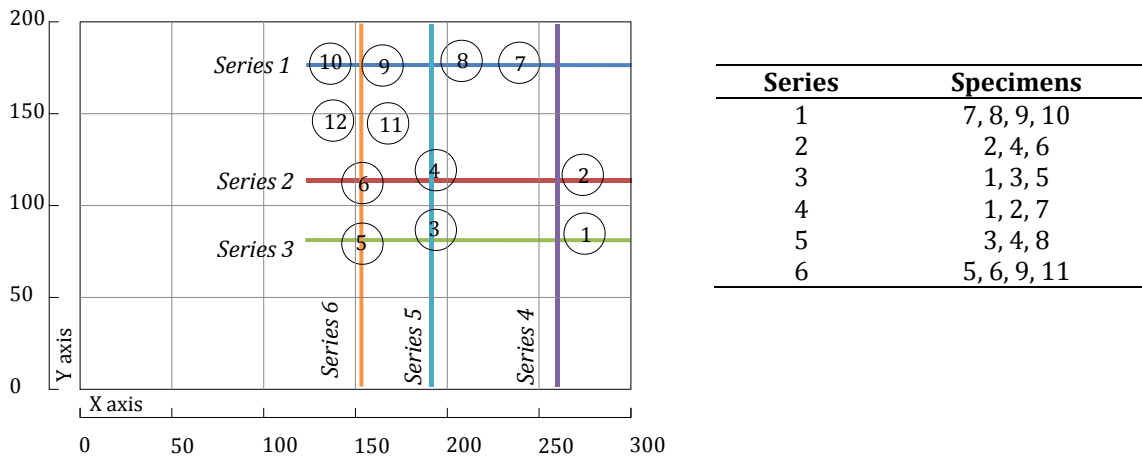


Figure 5.14 Distribution of specimens in slab M_B.

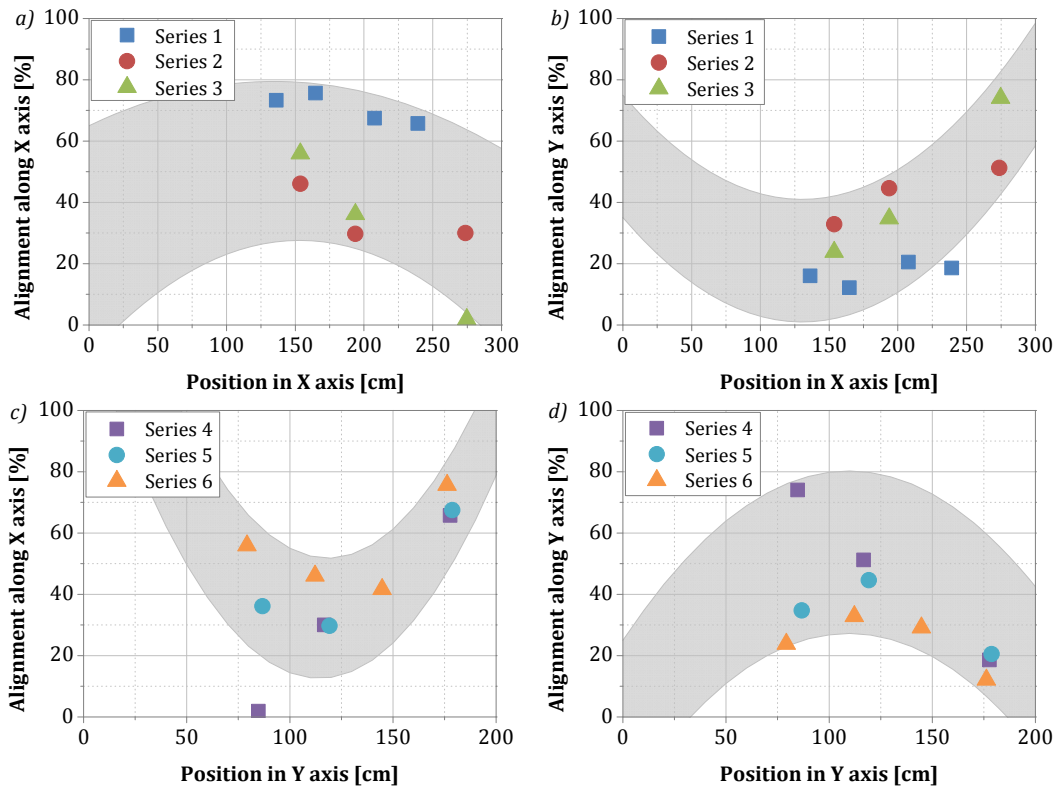


Figure 5.15 Alignment of fibres along X and Y axes for series a) 1-3 and b) 4-6 in slab M_B.

Large slabs

Two types of preferential orientations are detected in slab L_A. For once, fibres tend to be disposed on the plane perpendicular to the casting direction (X-Y plane). In addition to that, fibres close to the edges tend to be parallel to the sides of the mould due to the wall effect (observed especially in specimens 1, 2, 9-12, 15 and 16 in Figure 5.16). Figure 5.17 indicates the series of specimens used to extend the study of fibre orientation.

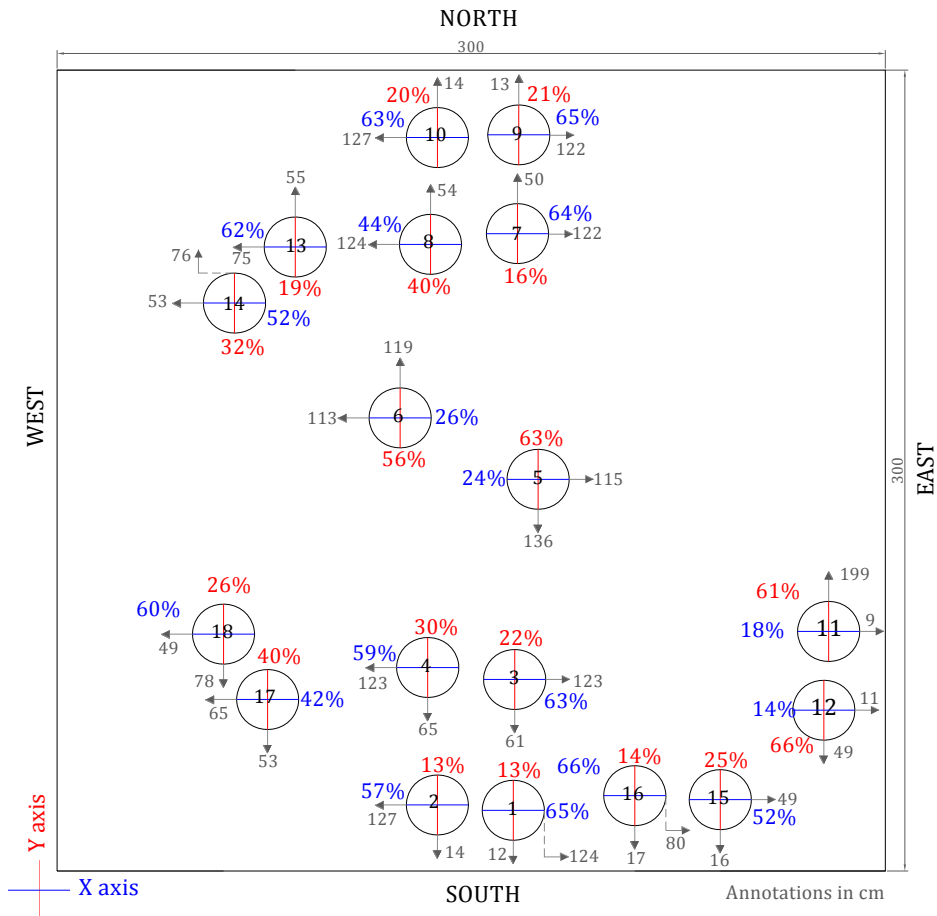
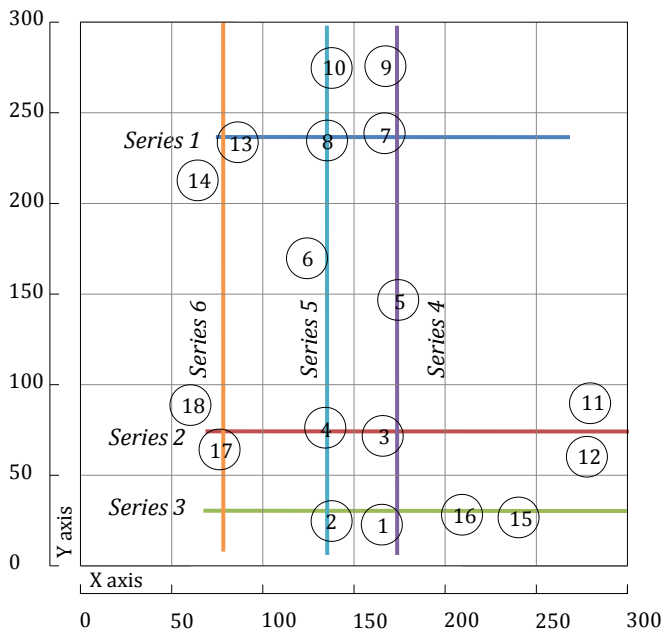


Figure 5.16 Fibre orientation in specimens of slab L_A.



Series	Specimens
1	7, 8, 13
2	3, 4, 12, 17
3	1, 2, 15, 16
4	1, 3, 5, 7, 9
5	2, 4, 6, 8, 10
6	13, 14, 17, 18

Figure 5.17 Distribution of specimens in slab L_A.

The results of the series along X axis presented in Figures 5.18a and 5.18b, indicate that the fibres tend to align along Y axis as the specimens approach the edge of the slab, becoming more parallel to the side of the mould. Consequently the amount of fibres aligned along X reduces at the edges. The series along Y axis (see Figures 5.18c and 5.18d) present the opposite behaviour.

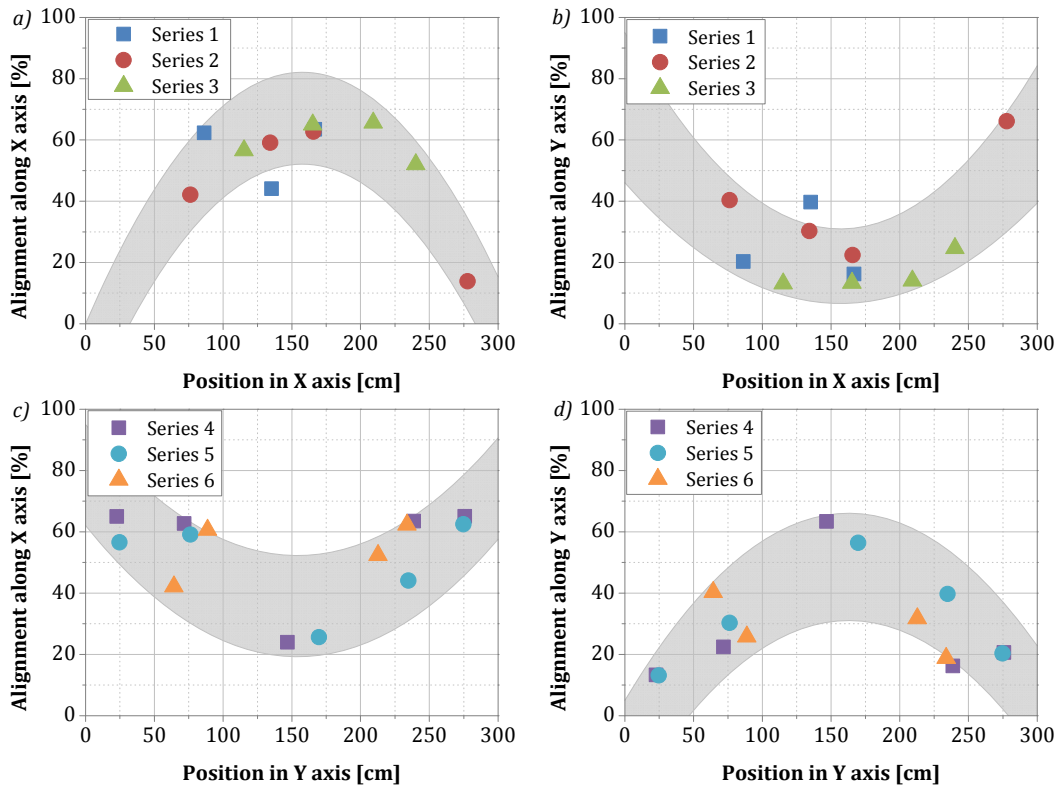


Figure 5.18 Alignment of fibres along X and Y axes for series a) 1-3 and b) 4- 6 in slab L_A.

The difference in orientation between both axes is highest at the edges whereas the specimens at central locations present a similar orientation along X and Y. It should be remarked that the described tendency of orientation applies especially to the series located near the symmetry axes of the slab. Other effects might interfere in the orientation near the edges, thus making this tendency less evident.

The results for slab L_B (see Figure 5.19) reveal two preferential orientations: in the perpendicular plane to the casting direction (Z axis) and parallel to the sides of the slab at the edges due to the wall-effect caused by the walls of the formwork. Besides, a variation on the fibre orientation is observed as the location of the specimens approach the edges, indicating that the fibres are disposed parallel to the side of the slab. Note that, although no data regarding fibre orientation is available for specimen 13, the mechanical test was performed. Figure 5.20 indicates the series of specimens for the slab L_B.

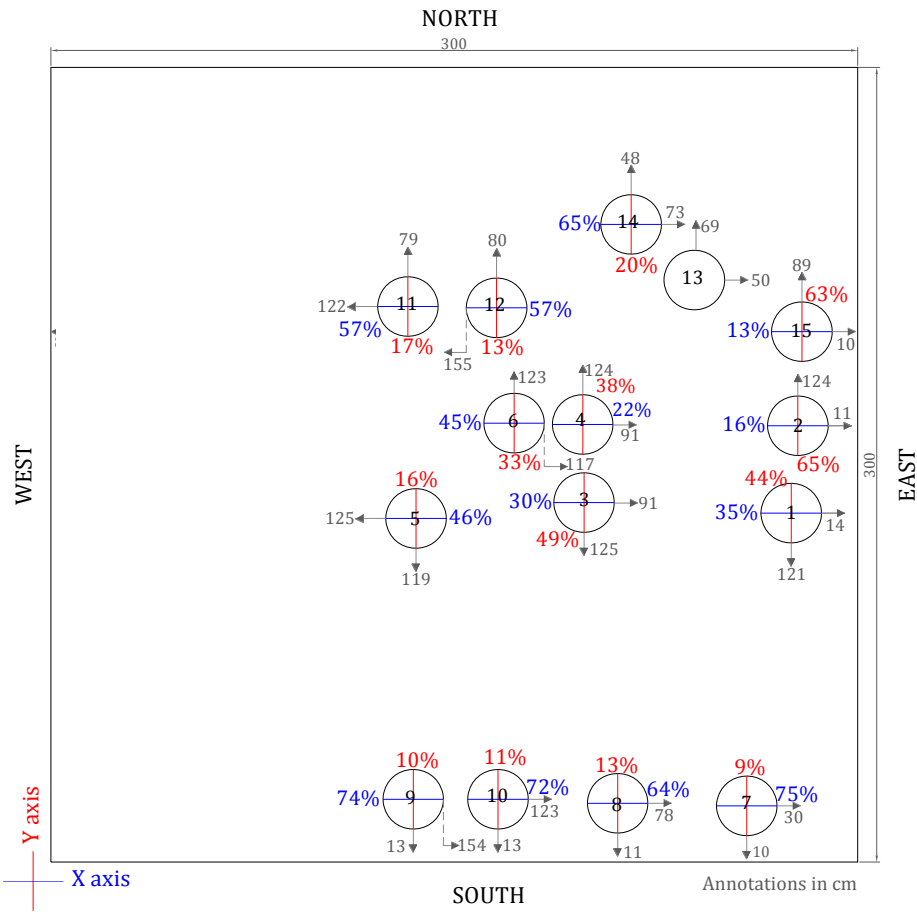


Figure 5.19 Fibre orientation in specimens of slab L_B.

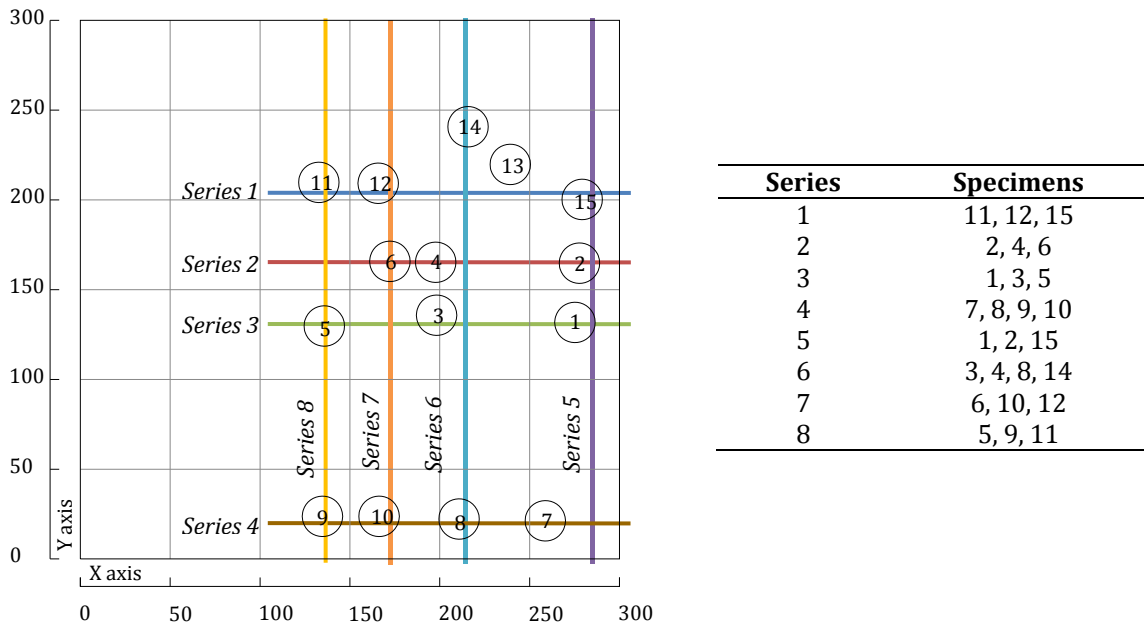


Figure 5.20 Distribution of specimens in slab L_B.

The series along X axis (Figures 5.21a and 5.21b) confirm the tendency of fibres to align along Y axis at the edges, which is clearly detected for series 1 and 2. Nevertheless, for series 3 this tendency is not so evident and it does not apply for series 4. This result is logical since series 4 is closest to the edge, being highly influenced by the wall-effect. An opposite tendency is expected in series parallel to the Y axis. This behaviour is observed in series 6 and 8 whereas series 7 does not present a clear trend (see Figures 5.21c and 5.21d) since it is located near the edges and is subjected to the wall-effect.

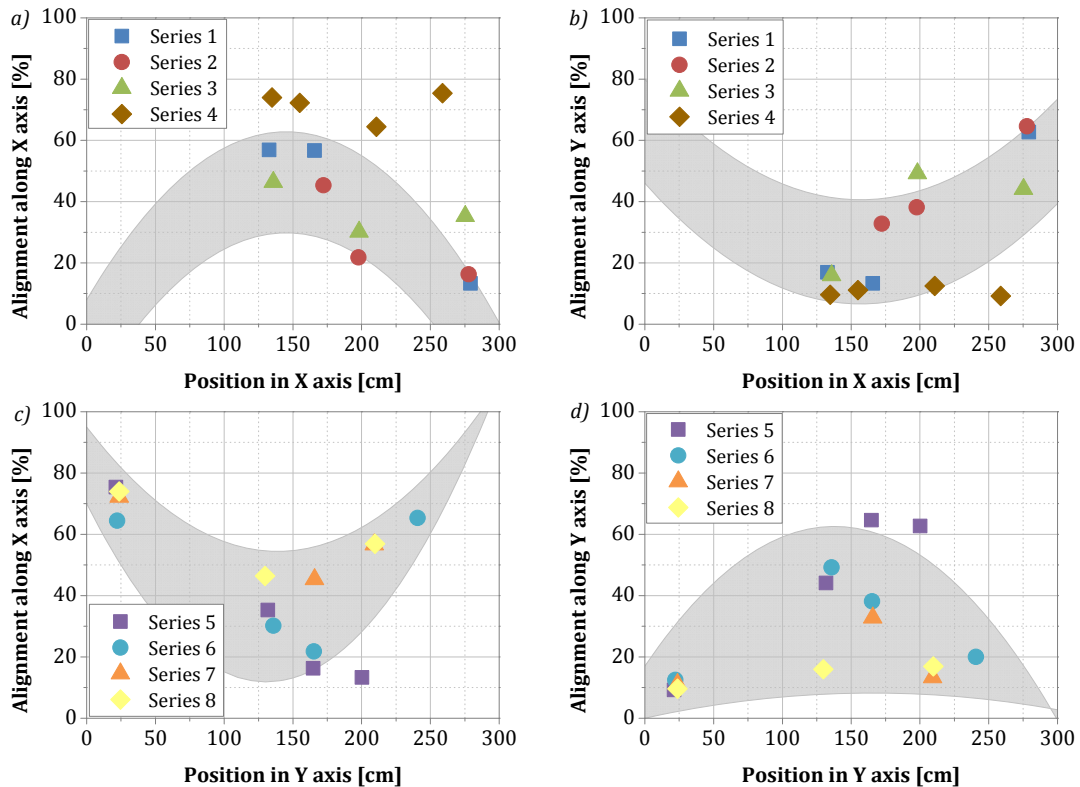


Figure 5.21 Alignment of fibres along X and Y axes for series a) 1- 4 and b) 5-8 in slab L_B.

Analysis of the orientation tendency observed in the slabs

The results show a common tendency in the orientation of the fibres that is clearly governed by two phenomena: the wall effect of the formwork (extensively discussed in previous section) and the flow of concrete. According to the latter, the fibres are exposed to the forces and the velocity profile exerted by the movement of concrete, which cause them to drift, rotate and align perpendicular to the direction of the flow. Consequently the fibres tend to change their orientation from the location they are poured, at the centre of the slab, as they advance towards the edges of the slab, as shown in Figure 5.22. This becomes more evident with the increase on the distance covered by the FRC.

This orientation is in accordance with other experimental studies, in which the flow is governed by extensional stresses (Grünwald 2004; Barnett *et al.* 2010; Boulekbache *et al.* 2010). These studies were previously introduced in Chapter 2.

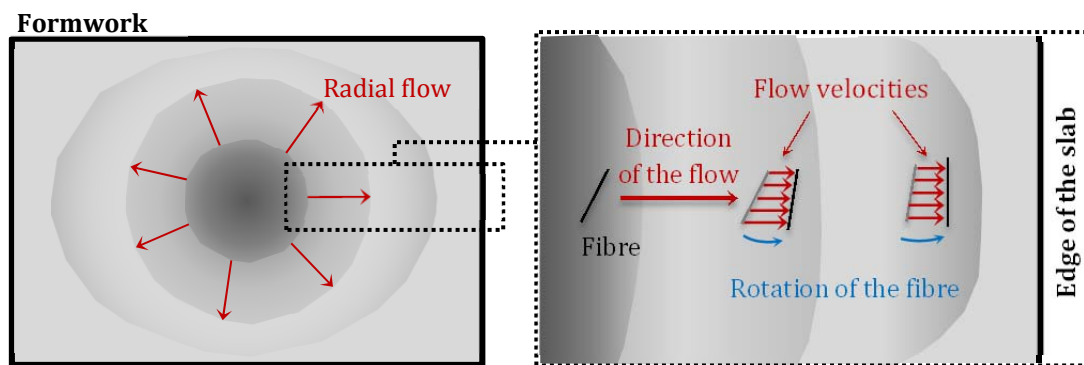


Figure 5.22 Rotation of fibres while moving from the centre of the slabs to the edges.

As a consequence of the orientation described, it was detected that the specimens located near the pouring zone have a similar percentage of alignment of the fibres along X and Y axes (with some exceptions). Conversely, specimens located further from the centre exhibit a significant difference between both axes. In such cases, the fibres tend to orientate perpendicular to the concrete flow.

In order to visualize the described behaviour, three main zones of orientation may be defined in each slab: central zone, transition zone and external zone (see Figure 5.23). In the first of them a similar alignment of fibres occurs along both axes, whereas in the external zone a tendency of preferential orientation parallel to the edges is observed. The transition zone marks a change between the other two.

In Figure 5.23, a random slab is presented with the characteristic orientation in each zone indicated by a range of values corresponding to the fibre alignment. The range is defined by the second quartile (the lowest value) and the 95th percentile (the highest value) of the results of the specimens from all slabs located in the same zone.

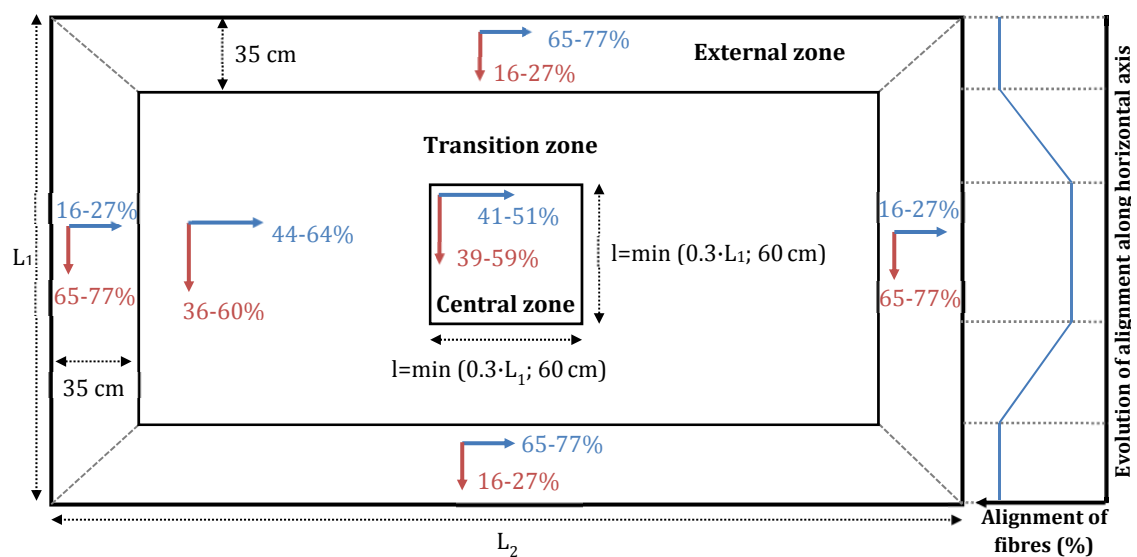


Figure 5.23 Division of slabs in zones depending on fibre orientation.

The length of the external zone is the average of the distances containing the cores from the edge (usually between 32 and 36 cm as can be observed in Chapter 4). In the central zone a double condition depending on the length L_1 (where $L_1 \leq L_2$) of the slab is considered. This double condition takes into account that in a narrow slab the distance covered by the concrete flow is shorter in one direction. In such cases, the concrete flow would reach the edges in one direction much earlier than in the other direction, raising the level of the concrete and affecting the upcoming concrete flow. This creates a new wall effect that would change the orientation of the fibres, thus reducing the extent of the central zone. Therefore, the length of the central zone is the minimum value between $0.3 \cdot L_1$ and 60 cm.

In the right side of the slab from Figure 5.23, a simplification of the alignment along the blue axis in a cross section is presented. This evolution corresponds to the described tendency of the fibres to orientate perpendicular to the flow of concrete as they advance from the centre to the edges. Notice that the proposed division of the slabs in zones responds to the analysis of the results obtained for a limited number of geometries studied in this case. Further research, including other geometries, could improve the annotation of the zones proposed.

5.4. MULTIDIRECTIONAL METHOD RESULTS

5.4.1. General methodology

The results of the multidirectional method are obtained in terms of load and displacement of the piston of the press used in the test of each direction (see Figure 5.24a). In the analysis of the results, the focus is set on the post-cracking stage since at this point the fibres are activated. For this reason, two transformations are made: the displacement is moved so that the origin corresponds to the cracking of the specimens and the load is transformed into a normalized load as presented in Figure 5.24b. Even though some results will be presented in absolute terms, the normalized load is considered to avoid distortions due to the differences in the concrete matrix and to allow a better comparison of the results obtained for the pair of specimens extracted from equivalent locations.

The normalization is performed through the division of the load measured during the test and the load corresponding to the piston displacement of 6 mm after cracking. The reason for choosing this value instead of the peak load is that it corresponds to the moment during the test when the contribution of the fibres reaches stability. Besides, notice that the some specimens could present imperceptible cracking in the matrix since the cores were drilled from the slabs after the test. In such cases, a noticeable difference in the peak load should be expected, thus making the peak value less representative and unsuitable for the normalization.

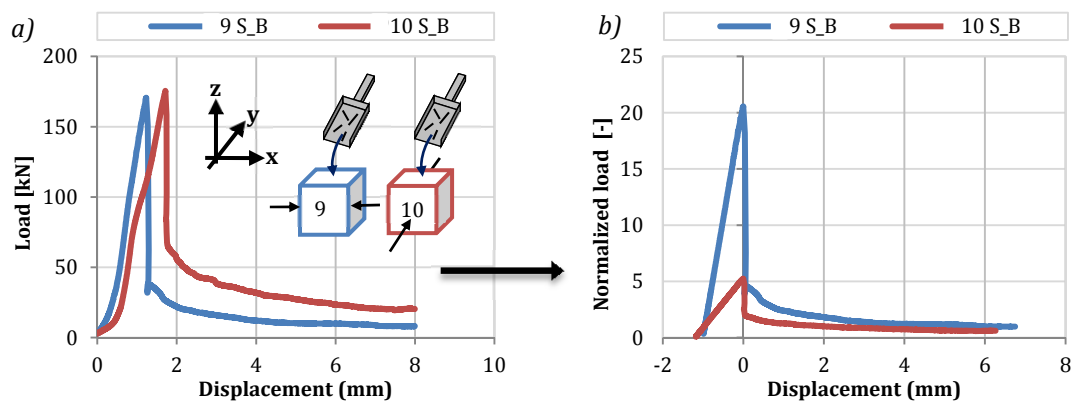


Figure 5.24 a) Results from multidirectional method and b) transformed curves for the analysis.

In this section, the fibre content and orientation assessed with the multidirectional test are compared with the obtained with the inductive method since the latter will facilitate the interpretation of the former. Consequently, the available data for each pair of specimens is: the fibre content, the fibre orientation on the three axes and the response in the post-cracking behaviour (measured in the multidirectional test).

These data are gathered in subsequent tables, in which the fibre content, the percentage of fibres aligned along the testing direction, the residual load and the normalized residual load is presented for each slab. The residual loads, both absolute and normalized, have been obtained for a displacement of 4 mm after cracking, point at which the post-cracking response is stabilized (see Figure 5.24). A few remarks on the results must be made before analysing the data.

- The specimens designated with an odd number were tested with the load applied along the X axis while the specimens labelled with an even number were tested along the Y axis.
- The results of each pair of specimens are grouped in the tables, for e.g. 1-2, 3-4, etc.
- The pairs correspond to the specimens obtained from close or symmetrically equivalent locations in the slabs (see Figures 5.9, 5.12, 5.15, 5.18, 5.21).
- As mentioned before, some specimens might present cracks since they were drilled from slabs previously tested.
- If a pair of specimens is not presented it might be due to two reasons: either the fibre orientation of one specimen is not available or the multidirectional method failed (the testing machine stopped).
- The results of the multidirectional method depend on the fibre orientation and content determined with the inductive method. The expected behaviour would be to have low values of residual load if a high percentage of fibres are aligned along the loading direction.

5.4.2. Small slab

Table 5.2 summarizes the results for slab S_B in terms of fibre content, percentage of fibres aligned along the testing direction, residual load and the normalized residual load are gathered in the subsequent tables for each slab.

Table 5.2 Residual load and normalized residual load for slab S_B.

Specimen	Fibre content [kg/m ³]	Alignment along testing direction [%]	Residual load [kN]	Normalized residual load [%]
1	43	19	22.9	163.6
2	40	79	16.3	119.2
3	40	33	30.3	127.2
4	35	60	18.8	111.8
7	45	48	10.1	110.0
8	43	21	24.8	144.1
9	47	63	10.1	62.4
10	47	16	24.8	115.5

The table confirms that the specimens with a higher percentage of fibres aligned along the testing direction present lower absolute and relative residual load if compared with their corresponding pair tested in the other direction. Regarding the fibre content, the highest variation is detected in the pair 3-4 with 5 kg/m³ of difference. However, the difference in content between the specimens forming a pair rarely reaches this value.

5.4.3. Medium slabs

In the case of slab M_A (see Table 5.3), the results indicate low values of residual load if a high percentage of fibres are aligned along the loading direction. In fact, in terms of absolute residual load only pairs 1-2 and 3-4 behave as described.

Table 5.3 Residual load and normalized residual load for slab M_A.

Specimen	Fibre content [kg/m ³]	Alignment along testing direction [%]	Residual load [kN]	Normalized residual load [%]
1	37	14	5.1	163.6
2	31	82	5.0	119.2
3	54	20	5.3	127.2
4	47	59	4.7	111.8
5	43	43	5.3	110.0
6	44	39	4.8	144.1
7	40	56	5.8	62.4
8	45	25	5.7	115.5
9	45	65	5.0	186.6
10	42	17	5.0	189.4
11	50	59	6.3	132.3
12	43	25	5.1	124.9

In the case of pair 9-10 and especially pair 11-12, the reversed performance is observed as the highest absolute load occurs for the specimen with the highest fibre

alignment along the testing direction. Since the post-cracking behaviour depends on the amount of fibres subjected to pull-out, this inverse trend may be caused by the differences in fibre content between the specimens of each pair (3 kg/m³ and 7 kg/m³, respectively).

Another plausible explanation for such performance could be the existence of undetected cracks as a result of the large-scale tests. The presence of such cracks would predefine the failure mode in the weak planes of the cracks instead of in the planes containing fewer fibres. Nevertheless, if the results are assessed in terms of normalized residual load, only pair the 11-12 presents a reversed behaviour. In this case, the reason is the higher fibre content in specimen 11 (7 kg/m³) if compared to specimen 12.

The results of slab M_B (see Table 5.4) show the expected behaviour, except for the residual load measured in pair 3-4. Specimen 4 should have a lower residual load, however, the difference in fibre content and the similarity in the percentage of fibres aligned along the testing direction of both specimens would explain the proximity of the residual load values.

In terms of normalized residual load, pairs 9-10 (located near the edges) and 11-12 do not behave as expected. In these cases, the difference in fibre content does not explain such behaviour, which might be attributed to the presence of undetected cracking of the specimens. In this case the presence of a weak plane could predefine the failure mode through these planes instead of in the planes containing fewer fibres.

Table 5.4 Residual load and normalized residual load for slab M_B.

Specimen	Fibre content [kg/m ³]	Alignment along testing direction [%]	Residual load [kN]	Normalized residual load [%]
1	34	2	31.8	132.2
2	50	51	12.7	108.9
3	45	36	25.3	118.9
4	47	45	29.1	19.5
5	53	56	14.2	85.1
6	48	33	17.0	133.1
9	47	76	10.2	169.1
10	47	16	13.6	114.6
11	45	42	20.8	176.5
12	47	28	31.9	139.9

5.4.4. Large slabs

The results of slab L_A (see Table 5.5) indicate that the pairs 11-12 and 13-14 do not present the expected behaviour. However, in terms of normalized residual load only pair 13-14 do not follow the expected trend. The difference in fibre content (3 kg/m³) could be the reason for such performance.

Table 5.5 Residual load and normalized residual load for slab L_A.

Specimen	Fibre content [kg/m ³]	Alignment along testing direction [%]	Residual load [kN]	Normalized residual load [%]
1	38	65	10.9	127.5
2	48	13	11.0	142.2
3	42	63	12.0	126.8
4	42	30	27.8	147.6
5	45	24	13.1	138.9
6	49	56	17.5	126.7
7	47	64	13.8	113.9
8	43	40	16.0	147.0
9	40	65	6.2	130.3
10	40	20	17.9	151.8
11	45	18	18.1	124.9
12	41	66	33.8	120.4
13	43	62	12.7	123.8
14	40	32	19.6	114.8
15	46	52	14.2	114.1
16	40	14	9.9	142.6
17	36	42	11.1	101.8
18	42	26	16.8	132.4

The results of slab L_B (see Table 5.6) indicate that the specimens with a higher percentage of fibres aligned along the testing direction present a lower value of relative load, except for pair 11-12. The reversed performance in this case may be explained by the difference in fibre content (3 kg/m³) between the specimens.

Table 5.6 Residual load and normalized residual load for slab L_B.

Specimen	Fibre content [kg/m ³]	Alignment along testing direction [%]	Residual load [kN]	Normalized residual load [%]
1	43	35	23.3	139.6
2	41	65	6.0	100.8
3	40	30	23.9	134.1
4	35	38	12.8	111.0
5	43	46	10.8	124.9
6	40	33	23.8	132.7
9	46	74	10.7	116.1
10	45	11	20.8	145.3
11	41	57	20.5	169.4
12	38	13	13.6	112.8

5.5. CONCLUDING REMARKS

Chapter 5 discussed the results of fibre orientation in real scale SFRC slabs and its influence in the post-cracking behaviour. The experimental program involved performing two types of tests: a non-destructive inductive method to characterize the orientation and amount of fibres and a multidirectional test envisaged to assess the post-cracking behaviour of the SFRC. The following conclusions may be derived from the results of the tests performed.

- In radial flows (or extensional flows), the fibres tend to rotate and align perpendicular to the flow as they advance from where the concrete is poured to the edges of the formwork. This becomes more noticeable as the fibres are subjected to the concrete flow for a longer period of time.
- Based on the results, the division of a random slab in three main zones of orientation was suggested. The central zone presents a similar percentage of fibres aligned along X and Y axes, whereas the external zone is characterized by a significant difference in the alignment of fibres along both axes due to the flow and the wall effects. The transition zone marks the change between the other two.
- The multidirectional test presents low values of residual loads if a high percentage of fibres are aligned along the testing direction. Differences in the fibre content and the presence of cracks in the specimens extracted from the tested slabs may prevent the abovementioned behaviour. The presence of a weak cracked plane in the specimen could predefine the failure not necessarily through the planes containing fewer amounts of fibres. On the other hand, the differences in the fibre content could affect the results since the post-cracking behaviour depends on the amount of fibres subjected to pull-out.

6. MODELLING THE FLEXURAL BEHAVIOUR OF SFRC SLABS

6.1. INTRODUCTION

The study from Chapter 5 reveals a fibre alignment in the slabs that is considerably different from the orientation found in small beams. In this context, the extrapolation of the results obtained from small scale tests that are not geometrically characteristic of the real structure could have adverse consequences both on the overall safety of the structure and on the efficient use of the SFRC.

Taking that into account, the MC2010 suggests the use of specimens which are more representative of the material in the real structural elements. Moreover, it defines partial safety factors to obtain the design strengths and an orientation factor that allows considering favourable or unfavourable effects of the distribution of fibres. It is evident that this orientation factor is a step forward to account for the lack of representativeness of the small beams in terms of fibre orientation if compared to other typologies of SFRC structures. Despite that, the MC2010 includes no factors that consider aspects related with the geometry or the hyperstatic behaviour of the element.

In fact, it was shown in Chapter 4 that the flexural response of slabs under an hyperstatic configuration exhibits a significant force redistribution capacity provided by the fibre reinforcement. Such redistribution is also not observed in most established methods for the characterization of SFRC, which consist of isostatic flexural tests of small elements (e.g. EN 14651:2005 (CEN 2005) or NBN B 15-238 (IBN 1992)).

Therefore, further research on the suitability of the constitutive models based on the performance of small beams to predict the behaviour of SFRC is required. Moreover, studies on how these models could be adapted to the design of particular structural applications (different from beams) should be conducted.

6.1.1. Objectives

The main goals pursued in this chapter is to evaluate the suitability of the current constitutive models (based on the flexural performance of small beams) to predict the behaviour of SFRC slabs and to propose geometry factors that could be considered in the design. In order to achieve these goals, the following specific objectives are defined:

- Simulate the flexural response of the real scale SFRC slabs with two constitutive models in European codes using a finite element software;
- Compare the predictions with the experimental data and analyse the suitability of the three constitutive models to design SFRC slabs;
- Perform a parametric study to determine the influence of the parameters defining the constitutive diagram in the response of the slabs;
- Determine the value of the parameters that better fit the experimental results in Chapter 4 and
- Propose geometry factors that could be introduced in the design of specific elements.

6.1.2. Outline of the chapter

Initially, in section 6.2, the finite element model used to simulate the flexural behaviour of the SFRC slabs is presented and the model type, the geometry, the boundary conditions and the material properties are described. In section 6.3, the results provided by the model are compared with the experimental data included in Chapter 4 in terms of the maximum load, the slopes and the absorbed energy of the elements. At this point the suitability of the current constitutive models to predict the response of the SFRC slabs is analysed.

Subsequently, in section 6.4, the parametric study conducted to determine the influence of the parameters defining the tensile stress-strain law is described. In this section, the variables considered in the study are defined and, lastly, the results are presented and analysed. In section 6.5, the numerical fit of the parameters of the constitutive diagram are proposed. Then, in section 6.6 the phenomenon named fibre network effect is described and geometric factors are proposed based on the numerical fit presented in the previous section. Finally, in section 6.7, the main conclusions of the study are highlighted.

6.2. FINITE ELEMENT MODEL

6.2.1. Model type

The finite element software ATENA 4.3.1g (Cervenka 2000) was used to model the tests described in Chapter 4 and address the issues mentioned in the previous section. ATENA was chosen over other finite element software since it is specialized for structural concrete (including FRC structures) and provides specific material models for 3D analysis. The tensile behaviour of concrete is modelled by nonlinear fracture mechanisms combined with the crack band method and the smeared crack approach. In the case of FRC, specific material stress-strain diagrams can be defined for compression and tension. The crack band size is automatically calculated by ATENA and the characteristic size used to estimate the strain is introduced as fraction of the specimen size (half of the height of the notched beam).

The test configuration was designed to allow redistribution of moments and the contribution of fibres in more than one direction by means of a hyperstatic support configuration and central loading (see section 4.2.3 in Chapter 4). Hence, a 3D analysis with solid elements was required. In this case, tetrahedral solid elements were selected for the meshing of the slabs.

6.2.2. Geometry and boundary conditions

Given the symmetry of the elements, only a quarter of each slab was modelled to favour the efficiency of the analysis (reduction of computation time) and a more refined mesh discretization. The neoprene sheets placed at the loading point and at the support were also modelled to reproduce the exact conditions of the real test described in Chapter 4. The nomenclature used to refer to each part of the model is indicated in Figure 6.1.

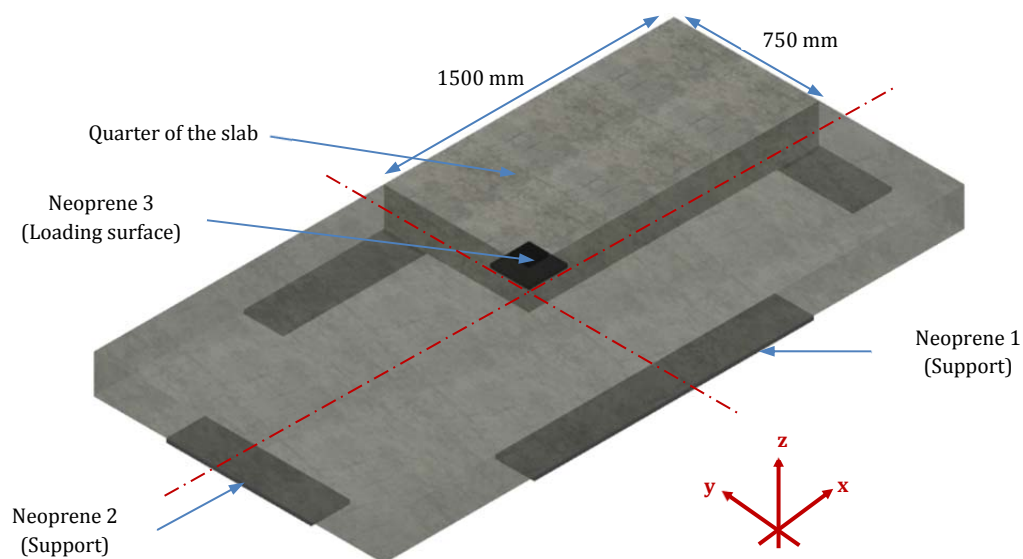


Figure 6.1 Geometry of the model of slab S.

Notice that in all models the dimensions of the neoprene 2 and 3 present the same presented in Figure 6.2. On the other hand the size of neoprene 1 varies depending on the size of the slab as indicated in Table 6.1.

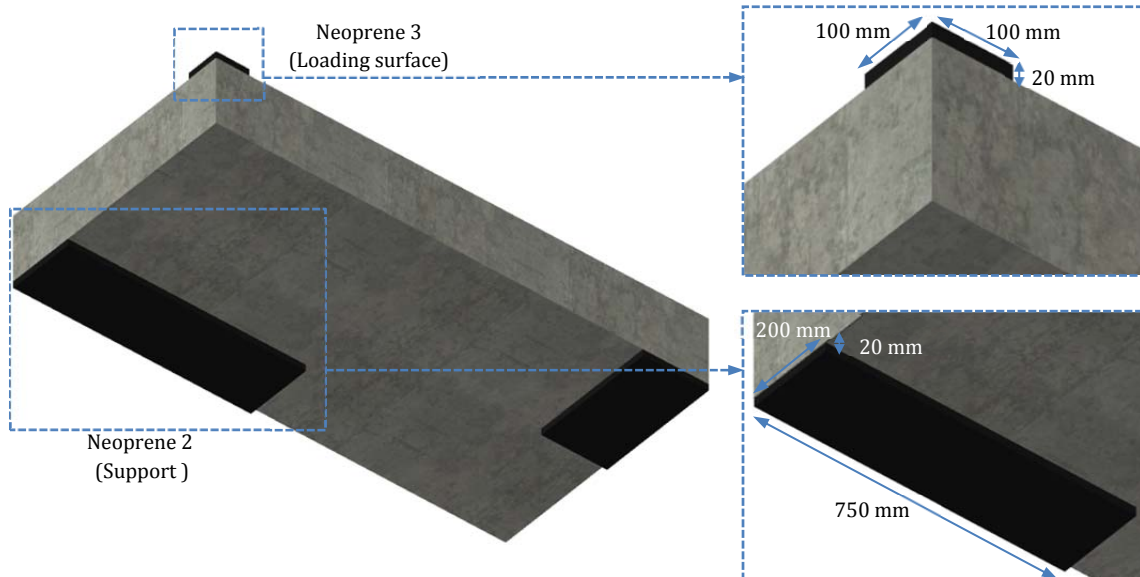


Figure 6.2 Detail of the geometry of model of slab S: neoprene 2 and neoprene 3.

Table 6.1 Dimensions of the elements in the model.

Model	Element	Length [mm]	Width [mm]	Height [mm]
Slab S	Quarter of slab	1500	750	200
	Support 1	375	200	20
Slab M	Quarter of slab	1500	1000	200
	Support 1	500	200	20
Slab L	Quarter of slab	1500	1500	200
	Support 1	750	200	20

Interface elements were added between the slab and the neoprene in order to model the contact. Furthermore, simply supported conditions were imposed by restraining the vertical displacement of the bottom face of supports 1 and 2. The displacement perpendicular to the symmetry planes is also restrained.

The load case consisted of a vertical displacement acting simultaneously at all nodes on top face of neoprene 3. Each load step was equivalent to a vertical displacement of 0.13 mm for the model S, 0.20 mm for the model M and 0.40 mm for the model L. This variation was defined in order to reproduce the load applied during the test of each slab and to assure that all models present the maximum displacement after the same number of steps.

6.2.3. Material properties

The selection of the shape of the σ - ε curve in tension is fundamental for modelling SFRC. In Chapter 2 of this thesis, several σ - ε diagrams included in European codes were presented and classified according to its shape as rectangular, bilinear, trilinear and multilinear (see Table 2.1). The rectangular and bilinear diagrams are simplified models used, as a general rule, for the ULS calculations. In this case, a higher level of accuracy was required and, therefore, the rectangular and bilinear diagrams were discarded. Given that the trilinear and multilinear diagrams present similar levels of accuracy (as observed in the results in Chapter 3), the former was chosen since less parameters were required.

A fracture energy based on total strain rotating crack model (Burguers et al. 2007) was used for the SFRC of the slabs assuming a trilinear stress-strain (σ - ε) curve in tension as shown in Figure 6.3a. General characteristics and the parameters of this model were established in accordance with Eurocode 2 (CEN 1992) and specific guidelines for SFRC (RILEM and EHE-08).

The simulations were performed using two different trilinear constitutive models: the diagram proposed by the RILEM - a reference for many years despite overestimating the post-cracking response of SFRC (Barros *et al.* 2005; Tlemat *et al.* 2006) - and the diagram defined in the EHE-08 - the most recent trilinear model in European codes.

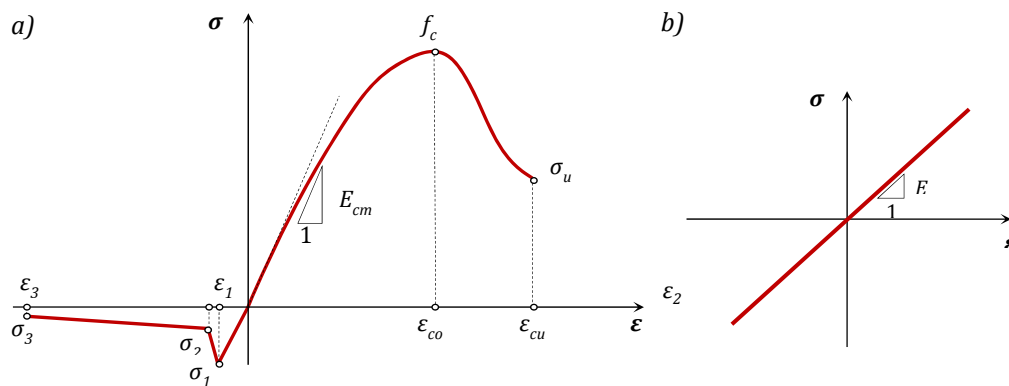


Figure 6.3. Stress-strain (σ - ε) curve used to model a) the SFRC and b) the neoprene.

The neoprene sheets of the supports and the loading surface were modelled assuming an elastic material with a linear σ - ε curve as indicated in Figure 6.3b. The modulus of elasticity of the neoprene was determined experimentally according to UNE-EN 1337-3:2005 (AENOR 2005). The results of the test are presented in Appendix 1.

During the numerical simulation, the neoprene sheets are subjected to high deformations due to the low modulus of elasticity. Since ATENA does not include any rubber like finite element specific for high deformation, an alternative solution was adopted to avoid numerical inconsistencies. For that, the thickness and the modulus of

elasticity of the neoprene sheets were increased ten times so that the equivalent stiffness is the same as measured in the laboratory.

The interface material of the contact elements (between the slab and the neoprene sheets) is based on the Mohr-Coulomb criterion with tension cut off that takes into account the relative slipping. For that, a tangential stiffness, a normal stiffness, a friction coefficient, a cohesion pressure and a cut-off traction stress must be defined. Furthermore, geometrical non-linearity was considered in the modelling.

The values adopted for the main material properties are summarized in Table 6.2. The properties of the neoprene and the interface material are common for the three models. The properties of the SFRC were defined for each model according to the experimental results of its corresponding series. The parameters defining the σ - ε curve in tension were obtained by using the residual strengths of series B1 since they are almost identical to the ones of B2 and only the result of two beams were available for B3 .

Table 6.2 Material properties considered in the FEM model.

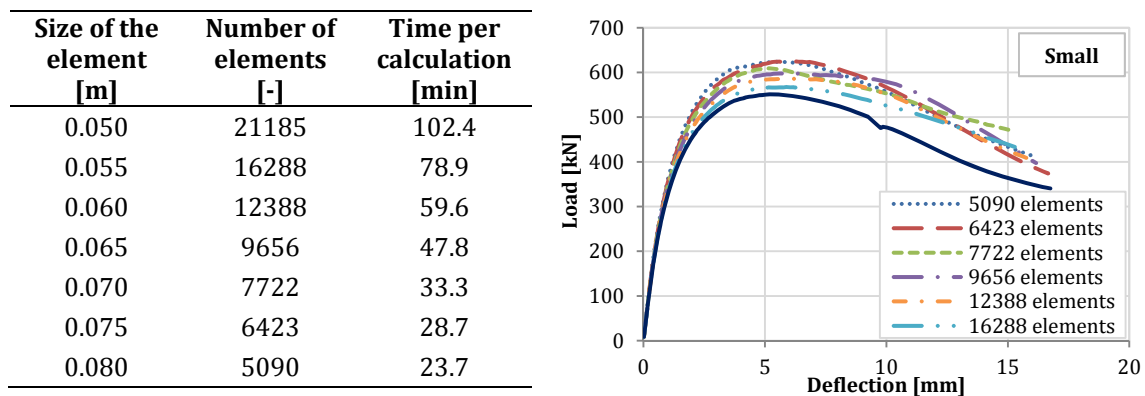
Model	Model part	Material properties	Value	Reference
Common properties for all models	Neoprene sheets	Average modulus of elasticity [MPa]	35.0	-
		Poisson ratio [-]	0.3	-
	Interface material	Normal stiffness [MN/m ³]	2.0·10 ⁸	-
		Tangential stiffness [MN/m ³]	2.0·10 ⁸	-
		Cohesion [MPa]	1.0	-
		Friction coefficient	0.1	-
		Cut-off traction stress [MPa]	0.3	-
Model S	SFRC slab	Average compressive strength [MPa]	46.8	-
		Average modulus of elasticity [GPa]	30.6	-
		Poisson ratio [-]	0.2	Eurocode 2
		Average tensile strength σ_1 [MPa]	5.6 / 2.9 / 3.7	RILEM / EHE / BCN
		Average residual strength σ_2 [MPa]	2.5 / 2.8 / 2.8	RILEM / EHE / BCN
		Average residual strength σ_3 [MPa]	2.2 / 1.7 / 1.9	RILEM / EHE / BCN
		Average residual strength σ_4 [MPa]	1.2	BCN
		Average strain ε_1 [%]	0.2 / 0.1 / 0.1	RILEM / EHE / BCN
		Average strain ε_2 [%]	0.3 / 0.2 / 0.2	RILEM / EHE / BCN
		Average strain ε_3 [%]	25.0 / 20.0 / 4.0	RILEM / EHE / BCN
		Average strain ε_4 [%]	20.0	BCN
		Tension characteristic size [m]	0.0625	ATENA Manual
Model M + Model L	SFRC slab	Average compressive strength [MPa]	46.7	-
		Average modulus of elasticity [GPa]	29.0	-
		Poisson ratio [-]	0.2	Eurocode 2
		Average tensile strength σ_1 [MPa]	5.6 / 2.9 / 3.7	RILEM / EHE / BCN
		Average residual strength σ_2 [MPa]	2.5 / 2.8 / 2.8	RILEM / EHE / BCN
		Average residual strength σ_3 [MPa]	2.2 / 1.7 / 1.9	RILEM / EHE / BCN
		Average residual strength σ_4 [MPa]	1.2	BCN
		Average strain ε_1 [%]	0.2 / 0.1 / 0.1	RILEM / EHE / BCN
		Average strain ε_2 [%]	0.3 / 0.2 / 0.2	RILEM / EHE / BCN
		Average strain ε_3 [%]	25.0 / 20.0 / 4.0	RILEM / EHE / BCN
		Average strain ε_4 [%]	20.0	BCN
		Tension characteristic size [m]	0.0625	ATENA Manual

6.2.4. Study on the influence of the mesh size

The results of a numerical simulation are affected by the size of the mesh used. Therefore, it is advisable to conduct a study to analyse how the results of the model may vary depending on the number of elements in the mesh. The study was performed only with the model S and the material data corresponding to the EHE. Seven different meshes with tetrahedral solid elements were considered in the analysis.

In Table 6.3, the size of the element, the number of elements in the mesh and the time required to complete the calculation with each of the seven meshes are presented. The most refined mesh considered contains 21185 tetrahedral solid elements and the least refined contains 5090 elements, which represents approximately four times less (see the time required for the calculation in Table 6.3).

Table 6.3 Data and results from the mesh size study.



The load-deflection ($P-\delta$) curves for slab S obtained with these meshes are presented in the figure in Table 6.3. The most refined mesh (21185 elements) certainly provides the most accurate results, nevertheless it also entails the highest calculation time. The subsequent more refined meshes (16288, 12388, 9656 and 7722 elements) provide a response that increases as the number of element reduces. In fact, the maximum load for these cases is 3.0%, 6.3%, 8.7% and 10.5% higher than for the most refined mesh, respectively. The slope in the final stretch differs slightly from the former. The meshes with 6423 elements and 5090 elements are the least refined but required a significant less amount of time to complete the calculation. Moreover, the $P-\delta$ curves obtained with these meshes present a similar shape to the most refined one, showing a slope in the final stretch almost identical.

A compromise must be found between the accuracy of the simulation and time required for the calculation. For this study, the mesh with 6423 elements was selected since the corresponding $P-\delta$ curve exhibits a similar shape to that of the most refined mesh, the time required for the calculation is low and the difference in terms of load is acceptable (the maximum load is 13.4% higher). The same size of element (0.075 m) is used for the models M and L, thus leading to a total of 8162 and 11944 elements per model, respectively.

6.3. COMPARISON BETWEEN EXPERIMENTAL AND NUMERICAL RESULTS

6.3.1. Crack patterns

The crack patterns obtained with the numerical simulations are compared in Figure 6.4 with the real crack patterns indicated in section 4.3.1 for slabs S_A, M_A and L_A considering the same deflection for each case. Since simulation was conducted only for a quarter of slab, the crack patterns also correspond to one quarter. Likewise, given that the crack patterns predicted by the RILEM and the EHE-08 models are similar, only the ones provided by the EHE-08 are shown in Figure 6.4.

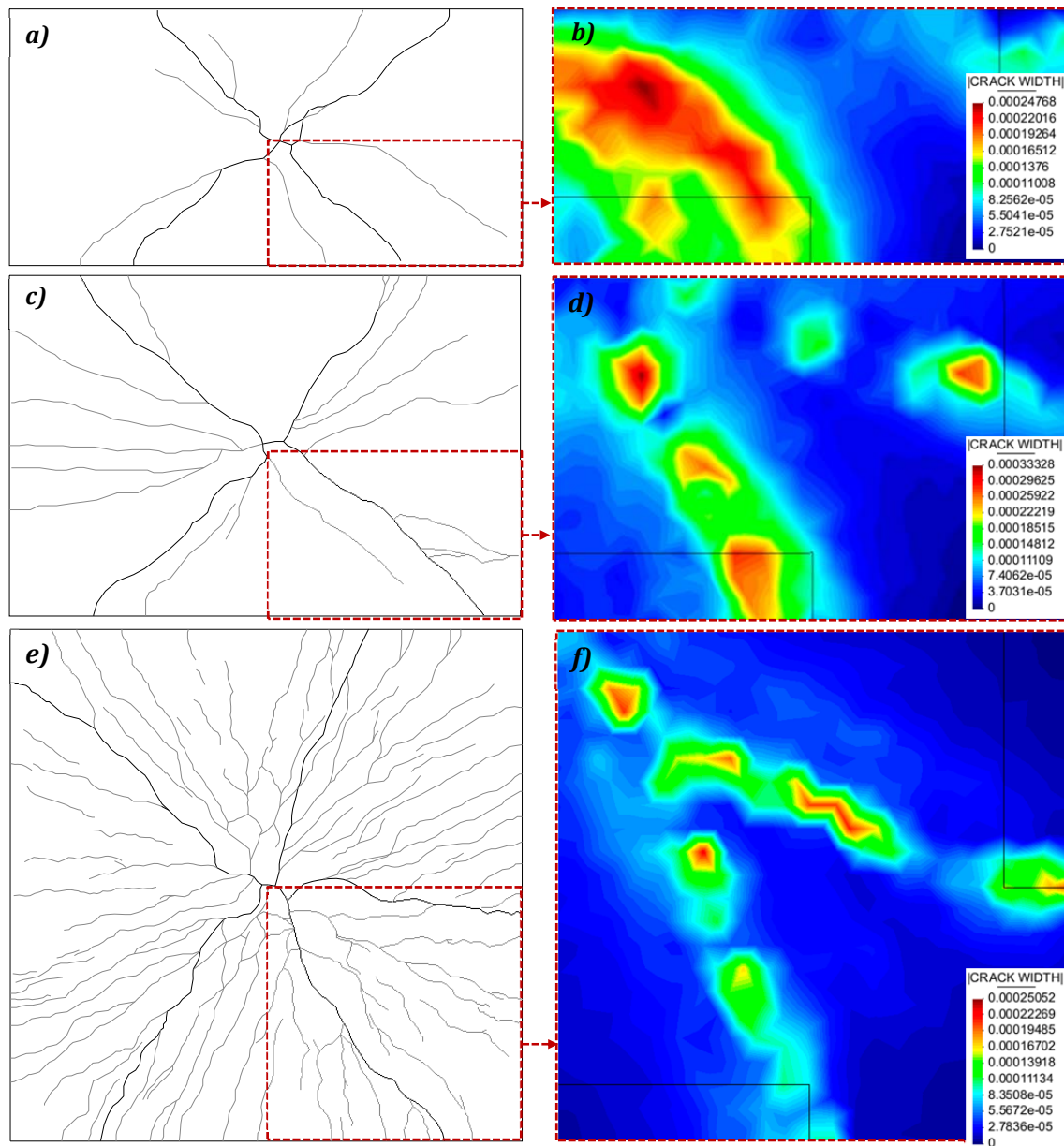


Figure 6.4 Real and predicted crack patterns: a) slab S_A; b) prediction for slab S; c) slab M_A; d) prediction for slab M; e) slab L_A and f) prediction for slab L.

The crack pattern of slab S (Figure 6.4) reveals a main crack that developed from the centre of the slab S to the edge of support 1. This crack pattern is consistent to the one observed in slab S_A (see Figure 6.4b) that presents a main crack at the approximately the same location. In the case of slab M (Figure 6.4c), a main crack is observed near support 3 while another crack starts to grow towards support 2. This result is also consistent with the crack pattern of slab M_A presented in Figure 6.4d. In the case of the slab L (see Figure 6.4e), a very similar crack pattern to the one in slab L_A (see Figure 6.4f) is observed. The consistency in the results indicates that the model proposed reproduces adequately the cracking experimentally observed. However, it is necessary to analyse whether the results in terms of load and deflections also fit the experimental data.

6.3.2. Load-deflection curves

In Figure 6.5, the load-deflection curves ($P-\delta$) obtained with the RILEM and the EHE-08 models are plotted together with the experimental results presented in Chapter 4 for each type of slabs (S, M and L).

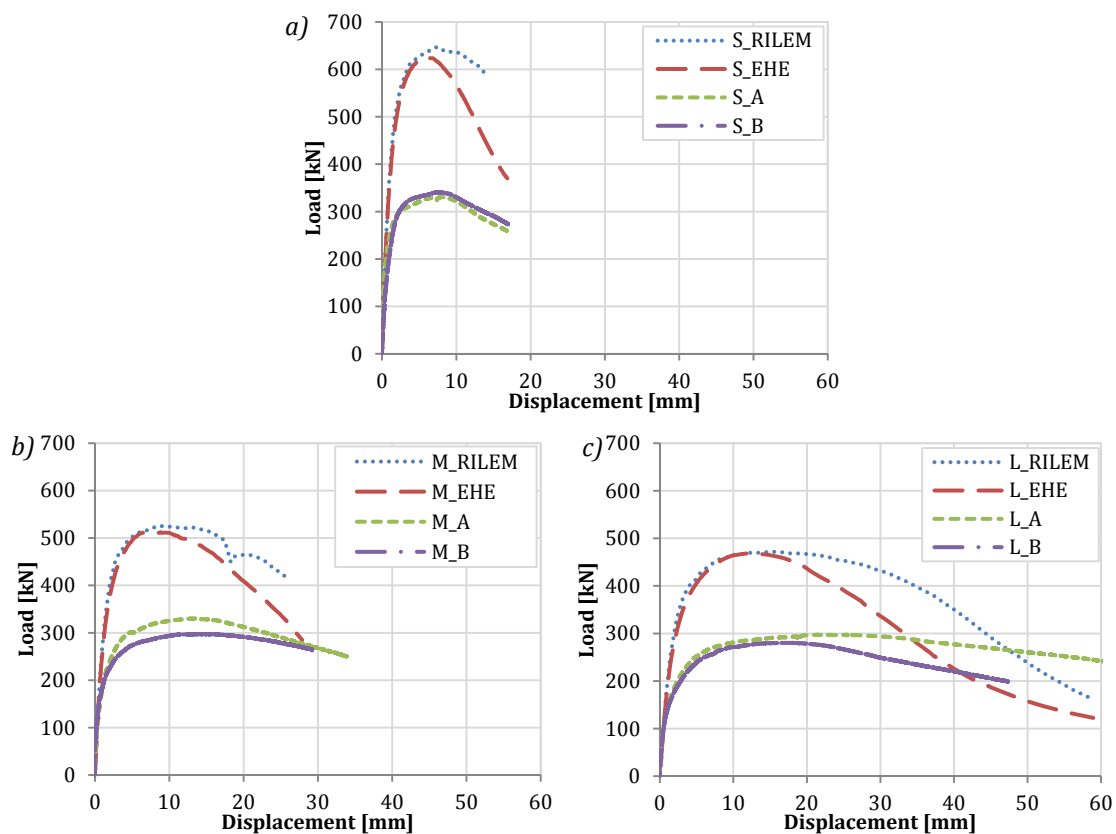


Figure 6.5 Experimental $P-\delta$ curves and simulation provided by ATENA with the RILEM and the EHE diagrams for slabs a) S, b) M and c) L.

A clear overestimation of the experimental results is observed in all cases. The prediction provided by the RILEM and the EHE-08 models are very similar until the maximum load is reached. Afterwards, the overestimation is greater for the RILEM model.

In order to analyse in detail the prediction of the RILEM and the EHE-08 diagrams for each type of slabs, some parameters derived from the P - δ curves (such as maximum deflection, deflection for certain level of load, slopes and absorbed energy) are presented in Table 6.4. Notice that the values of slope E4 (defined in section 4.3.3) of the predicted curves were calculated for the same ranges of deflections that in the case of the experimental results. Furthermore, the values of energy absorption were obtained as described in section 4.3.3 for the deflections of 15 mm, 25 mm and 45 mm for slabs S, M and L, respectively.

Table 6.4 Results of the prediction with the RILEM and the EHE and average results of slabs S, M and L.

Cases	Max. load [kN]	Deflection max. load [mm]	Load for $\delta=5$ mm [kN]	Load for $\delta=10$ mm [kN]	Slope E4 [kN/mm]	Energy absorption [J]
S_RILEM	646.7	7.3	625.1	634.7	-11.5	8158.1
S_EHE	625.0	6.1	618.5	572.2	-29.7	7844.0
Exper. S	335.5	7.8	325.9	326.0	-8.5	4532.6
M_RILEM	525.3	8.9	500.7	524.3	-9.2	11668.8
M_EHE	511.9	8.9	492.0	511.3	-15.7	10897.8
Exper. M	313.5	14.2	287.0	309.3	-3.9	7213.1
L_RILEM	471.6	15.3	410.4	464.5	-11.0	18448.1
L_EHE	468.4	12.0	402.8	464.1	-7.7	15858.4
Exper. L	288.6	19.6	245.2	276.0	-2.5	11692.1

In terms of maximum load, the prediction provided by the RILEM and the EHE diagrams are closer to the experimental data as the width of the slabs increases, in other words, the overestimation is highest for the slabs S and lowest for the slabs L. The overestimation of beam models the slabs M and L is slightly over 60%, whereas in the case of the slabs S this value is around 90%.

This tendency regarding the overestimation in the load is also observed in Table 6.4 for the values of load for a deflection of 5 mm and 10 mm. For instance, in the case of a deflection of 10 mm, the overestimation of the slabs S is 94.7% and 75.5% with the RILEM and the EHE diagrams, respectively. These values are reduced to 69.5% and 65.3% in the case of the M slabs and to 68.3% and 68.2% in the case of the slabs L, for the RILEM and the EHE diagrams respectively.

Regarding the deflection corresponding to the maximum load, the RILEM and the EHE tend to provide a lower value than the ones registered during the tests. The underestimations of the value of deflection for the slabs S are 6.6% and 22.8% for the slabs M are 37.2% and 37.5% for the slabs L are 22.1% and 38.8% for the RILEM and the EHE diagrams, respectively.

The curves predicted with the RILEM and the EHE diagrams present, in general, a steeper slope in stage E4 than the experimental results. The differences with the experimental results reach values of 36.3% and 250.6% in the case of slab S, 137.0% and 303.9% in the case of slab M and 341.9% and 209.6% in the case of slab L, for the RILEM

and the EHE-08 models respectively. The errors in the prediction of energy absorption capacity present an equivalent tendency to those of the maximum load since the overestimation is highest for the slabs S and lowest for the slabs L. The errors are 80.0% and 73.1% in the case of slab S, 61.8% and 51.1% in the case of slab M and 57.8% and 35.6% in the case of the slab L for the RILEM and the EHE-08 diagrams, respectively.

In view of the P - δ curves in Figure 6.5 and the results presented in Table 6.4, it may be concluded that the constitutive models based on the performance of small beams, such as the ones included in the RILEM and the EHE-08 may not be suitable for the design of SFRC slabs. In order to determine the values of the parameters in a trilinear diagram that fit better the experimental results of the SFRC slabs, a parametric study is conducted in the following section.

6.4. PARAMETRIC STUDY

6.4.1. Preliminary analysis

The main parameters of the trilinear constitutive model used to simulate the SFRC slabs are σ_1 , ε_1 , σ_2 , ε_2 , σ_3 and ε_3 (see Figure 6.6). With the aim of simplifying the study and minimizing the number of parameters, it was decided that the parameters σ_1 and ε_1 would remain constant and would take the values of the trilinear diagram proposed in the EHE-08. In addition to that, a preliminary analysis was performed with the slabs S prior to the parametric study in order to determine which of the other parameters have more influence in the structural response of the elements.

Two extreme limit values were defined for each of the four parameters. These limits are presented in the table in Figure 6.6. It is important to remark that σ_2 was defined as a fraction of σ_1 while σ_3 was defined as a fraction of σ_2 . This approach intends to avoid the analysis of stress-strain curves that are unreasonable for typical SFRC.

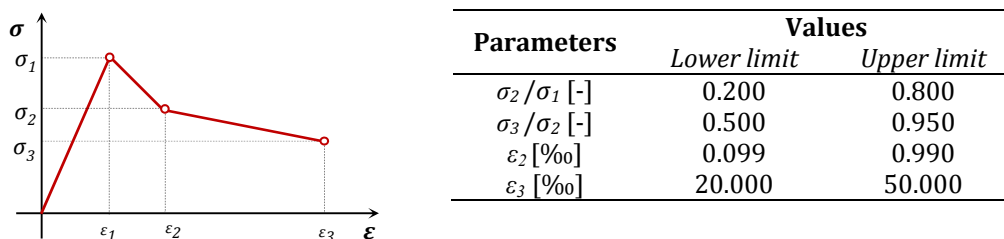


Figure 6.6 Trilinear diagram for SFRC and parameters considered in the preliminary study.

In Figure 6.7, some of the P - δ curves obtained in the preliminary study are presented to illustrate the influence of each of the parameters considered.

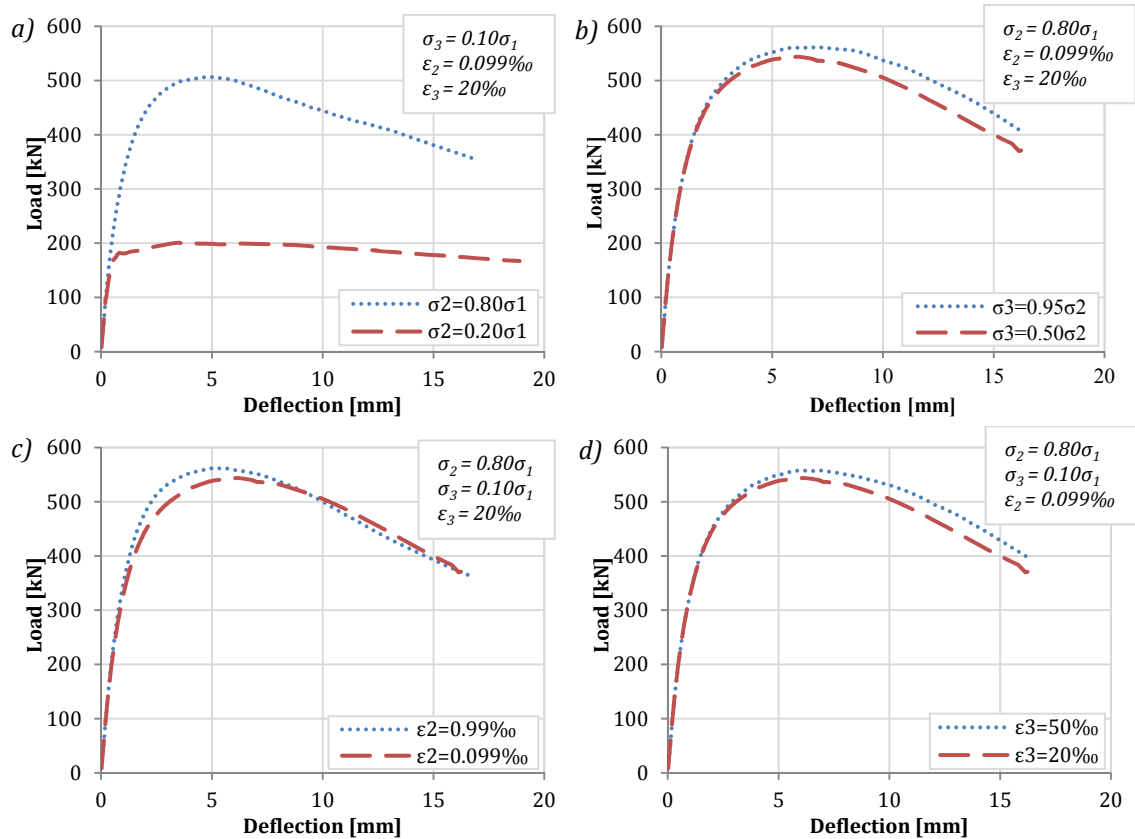


Figure 6.7 Influence of the parameters a) σ_2 , b) σ_3 , c) ε_2 and d) ε_3 .

The two curves in Figure 6.7a correspond to the study of σ_2 equal to 80% and 20% of the value of σ_1 . In order to clearly visualize the influence of the parameter σ_2 , the other parameters are kept the same (in this case σ_3 is defined in terms of percentage of σ_1 and the value is the same for both curves). The results reveal that σ_2 has a major influence on the response of the slabs, particularly in the case of the maximum load which is 171.0% higher for $\sigma_2 = 0.80\sigma_1$ than for $\sigma_2 = 0.20\sigma_1$. Figure 6.7b shows the influence of σ_3 , when the other parameters are kept the same. The increase of σ_3 from $0.50\sigma_2$ to $0.95\sigma_2$ causes a slight increase of the load, more noticeable in the last stretch of the curve. In fact, in the case of $\sigma_3 = 0.50\sigma_2$ the maximum load is 3.2% higher than for $\sigma_3 = 0.95\sigma_2$ (the maximum load occurs at 6.1 mm and at 6.8 mm respectively), whereas the difference is of 8.6% for larger deflections such as 12 mm.

The results in Figure 6.7c indicate that increasing the value of ε_2 ten times does not affect significantly the response of the slabs. However, a slight difference in the value of the maximum load and its corresponding deflection is observed. The maximum load is 3.3% higher for $\varepsilon_2 = 10\varepsilon_1$ than it is for $\varepsilon_2 = \varepsilon_1$ and the deflection at which the maximum load is registered is 15.1% bigger for $\varepsilon_2 = 10\varepsilon_1$. The results in Figure 6.7d correspond to the study of ε_3 . An increase of the latter produces a slight increase of the load, particularly in the final stretch of the curve. The maximum load in the case of $\varepsilon_3 = 50\%$ is only 2.6% higher than in the case of $\varepsilon_3 = 20\%$. This difference reaches 6.2% for a deflection of 12 mm.

6.4.2. Variables considered

The preliminary study reveals that σ_2 has a remarkable influence on the structural behaviour of the slabs. Such influence is much smaller in the case of σ_3 , ε_2 and ε_3 . From the preliminary study it was detected that σ_3 and ε_3 mainly affect the load in the final stretch of the curve. The parameter ε_2 affects the response in terms of the maximum load (for smaller deflections).

Following this philosophy of design guidelines such as CNR-DT 204, the MC2010 and the EHE-08, the value of the parameter ε_3 is set in 20‰, which corresponds to the ultimate strain for elements subjected to bending. Therefore, the parameters of the constitutive diagram that remain constant are σ_1 , ε_1 and ε_3 . Their values, specified in Table 6.5, are defined according to the EHE-08 and are based on the experimental data of batch B1 (see Chapter 4).

Table 6.5 Values of σ_1 , ε_1 and ε_3 for slabs S, M and L.

Parameters	Values
σ_1 [MPa]	2.879
ε_1 [‰]	0.099
ε_3 [‰]	20.000

Table 6.6 shows the values of the variables analysed in the parametric study (σ_2 , σ_3 and ε_2). In order to obtain comparable results, the same values were considered in the three slabs. The combination of these values led to 150 cases for each type of slab (450 in total). Notice that one of the values selected for ε_2 is 0.099‰, which corresponds to ε_1 . However, for notation purposes it is presented as 0.1‰.

Table 6.6 Variables of the parametric study for slabs S, M and L.

Variables	Units	Values						Cases
σ_2/σ_1	[-]	0.30	0.40	0.50	0.60	0.70	0.80	
σ_3/σ_2	[-]	0.50	0.65	0.80	0.95	1.10	-	150
ε_2	[‰]	0.10	0.30	0.50	0.70	0.90	-	

The decision of analysing more values for σ_2 than for σ_3 and ε_2 was made based on the results of the preliminary study, which indicated that σ_2 has a major influence in the response of the slabs.

6.4.3. Analysis of the influence of σ_2

Load-deflection curves

In Figure 6.8, the P - δ curves obtained for the six different values of σ_2 are presented for the slabs S, M and L. In order to avoid repetitions, given that the tendencies are similar, only the curves corresponding to $\sigma_3=0.50\sigma_2$ and $\varepsilon_2=0.3$ ‰ are herein presented.

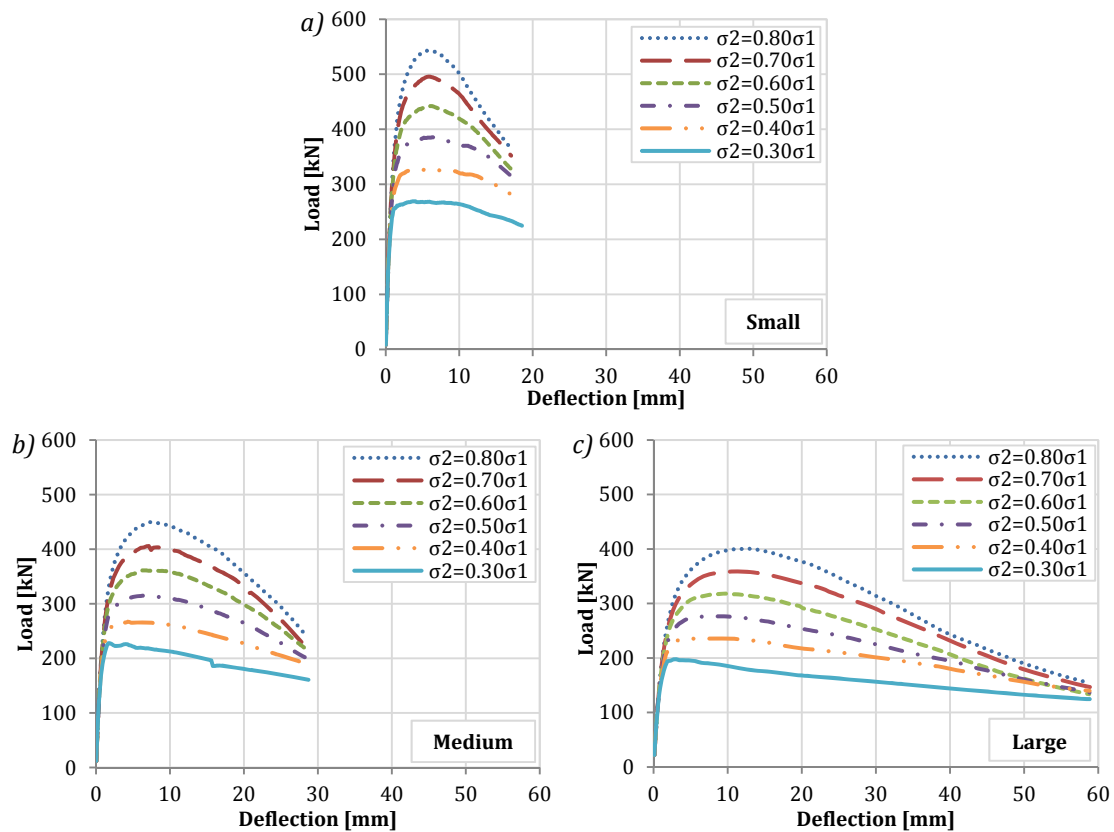


Figure 6.8 Influence of σ_2 in the P - δ curves for slabs a) S, b) M and c) L.

A general overview of the curves reveals that the maximum load increases with the value of σ_2 for all types of slabs. From these curves, additional information regarding the slope of the final stretch and the energy absorption may be obtained. This information is analysed in detail in subsequent sections, identifying the tendency in the variation of the results depending on the parameter σ_2 .

In such detailed analysis, the results are presented for all values of ε_2 considered in the study but only for one value of the parameter σ_3 (in this case $\sigma_3=0.50\sigma_2$). This procedure of selective presentation intends to avoid the repetitive description of all the results obtained in the parametric study, which showed similar tendencies.

Maximum load

In Figure 6.9, the influence of σ_2 in the P - δ curves is analysed in terms of the maximum load for each type of slab. Additionally, the tendency of how the maximum load varies with σ_2 is shown for different values of ε_2 . In this case, the results in Figure 6.9 correspond to $\sigma_3=0.50\sigma_2$. The results reveal an approximately linear tendency of the maximum load, that increases with σ_2 , as expected from the P - δ curves in Figure 6.8. Given that the curves exhibit an approximately linear behaviour, the slopes of the curves were determined and are presented in Table 6.7 for slabs S, M and L.

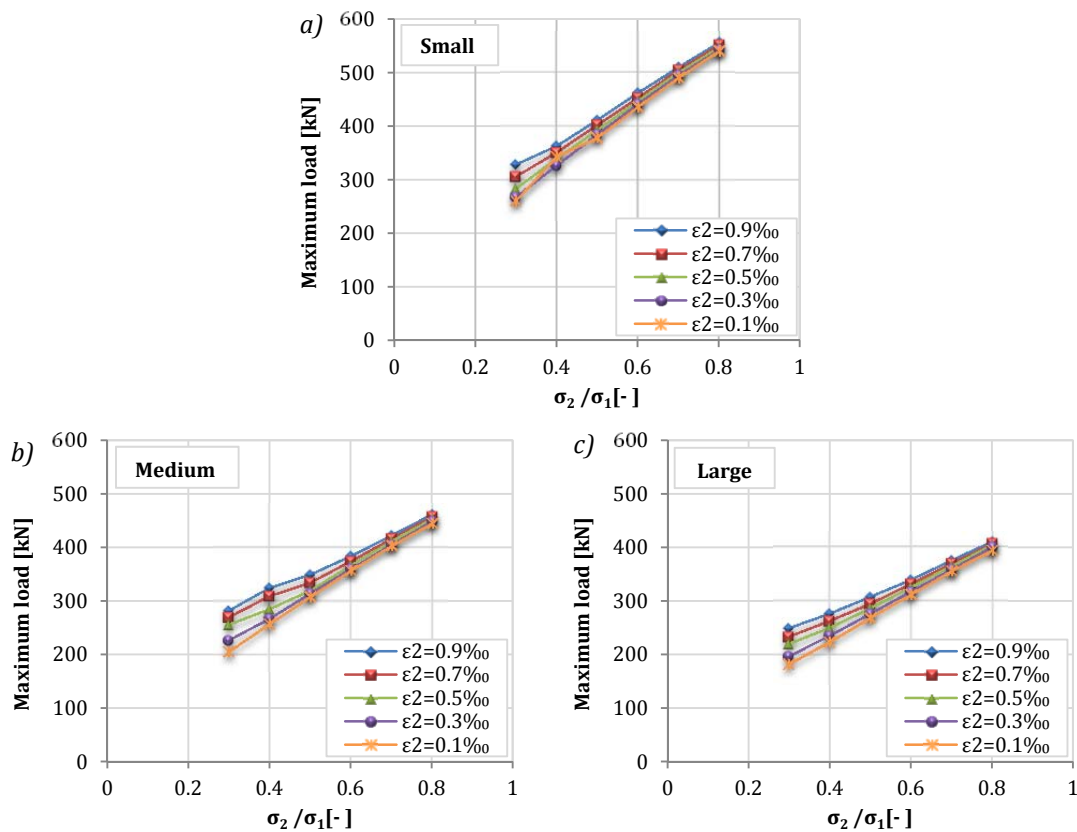


Figure 6.9 Influence of σ_2 in the maximum load for slabs a) S, b) M and c) L.

Table 6.7 Slope of the tendencies in Figure 6.9.

Strain ϵ_2 [‰]	Slopes [kN]		
	Small	Medium	Large
0.1	540.7	481.1	426.5
0.3	550.8	449.0	407.3
0.5	528.0	404.4	370.8
0.7	495.5	371.8	349.1
0.9	464.6	350.3	323.2
Average	515.9	411.3	375.4

These results indicate that the influence of σ_2 in the maximum load is greater as the slabs are smaller, in other words, the average rate at which the maximum load increases with the value of σ_2 is 25.4% and 37.4% higher for the slabs S than for the slabs M and L, respectively. Additionally, in general, this rate increases as the value of ϵ_2 decreases. If the increments of maximum load are compared in terms of percentage, for example, for the P - δ curves with $\sigma_2=0.30\sigma_1$ and $\sigma_2=0.80\sigma_1$ (considering $\sigma_3=0.50\sigma_2$ and $\epsilon_2=0.3\text{‰}$) the values are 91.0% for S, 98.8% for M and 100.5% for L.

From the results in Figure 6.9, it can be concluded that the parameter σ_2 of the constitutive diagram has a significant influence in the value of maximum load. In fact, this parameter is an indicator of the post-cracking strength of the material provided by the

fibre reinforcement since after the cracking occurs, when the tensile strength of concrete (σ_1) is reached, it is the fibres that contribute to the bearing of stresses. Hence, the higher is the value of σ_2 , the higher is the post-cracking strength provided by the fibre reinforcement and the higher is the maximum load.

Slope $E4$

Figure 6.10 shows the influence of σ_2 in the P - δ curves in terms of the slope $E4$ for the slabs S, M and L. The variation of $E4$ due to σ_2 is presented for different values of ε_2 and for $\sigma_3=0.50\sigma_2$. The tendencies of the results indicate a strong influence of σ_2 in the slopes of the slabs S and M, whereas for slab L the variation of slope is not as significant as in the other slabs. In all cases, the absolute value of the slope $E4$ increases with σ_2 . From this, it can be concluded that the influence of σ_2 in the slope $E4$ is greater for the stiffer slabs which are slabs M and, particularly, S. By comparing the curves with $\sigma_2=0.30\sigma_1$ and $\sigma_2=0.50\sigma_1$ (considering $\sigma_3=0.50\sigma_2$ and $\varepsilon_2=0.5\text{‰}$), the increases of slope in terms of percentage are 308.5% for slab S, 178.1% for slab M and 97.4% for slab L.

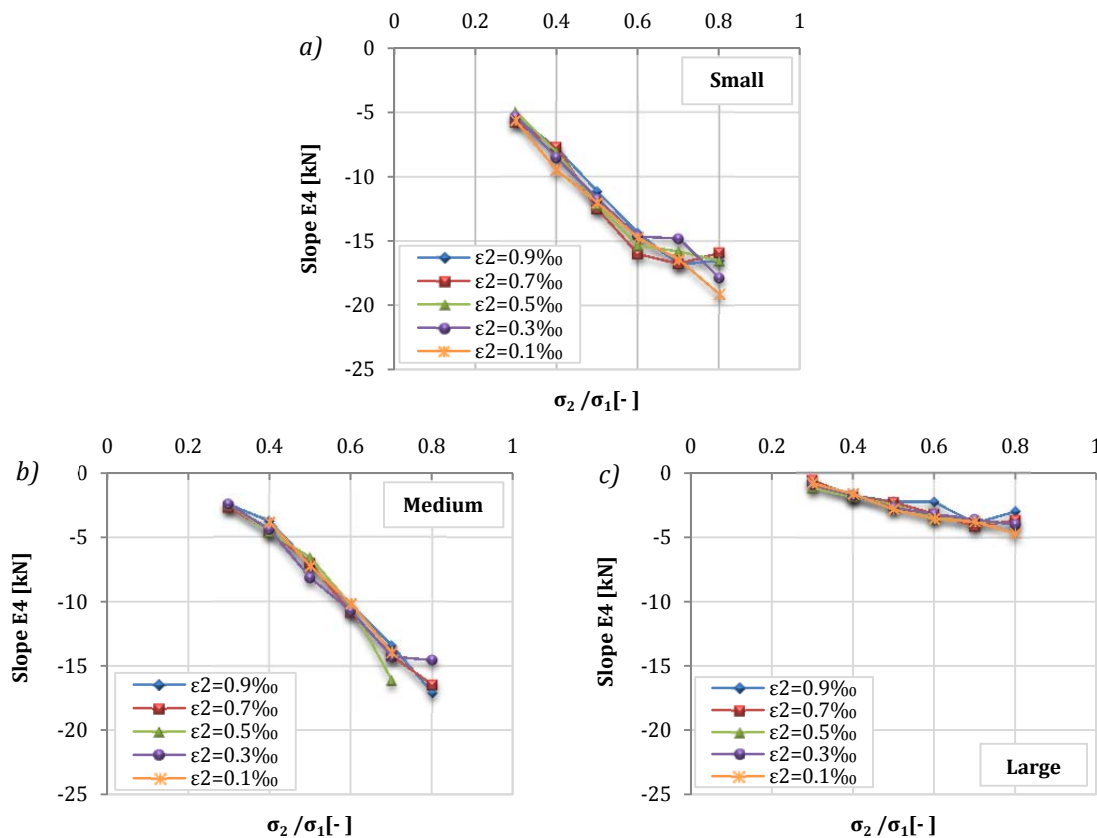


Figure 6.10 Influence of σ_2 in the slope $E4$ for slabs a) S, b) M and c) L.

The results reveal that the influence of σ_2 in the slope $E4$ is particularly significant in the slab S. Given the test setup and its geometry, the slab S has a limited force redistribution capacity and exhibits a less ductile behaviour which results in a steep slope in the last stretch of the P - δ curve. Therefore, it seems natural that an increase in σ_2 , which

leads to an increase of the maximum load, also results in steeper slopes. In contrast to this behaviour, the slab L presents a gentle slope given its ductile behaviour and greater force redistribution capacity. Therefore, the influence of σ_2 in the slope $E4$ of the slab L is minor.

Absorbed energy

In the graphs in Figure 6.21, the influence of σ_2 in the energy absorption for a deflection of 15 mm is studied for the slabs S, M and L. The variation of the energy absorption due to σ_2 is plotted for different values of ϵ_2 and for $\sigma_3=0.50\sigma_2$. The results show an increase of the absorbed energy with σ_2 . As in the case of the maximum load, the curves present approximately linear tendencies (see values of slopes in Table 6.8).

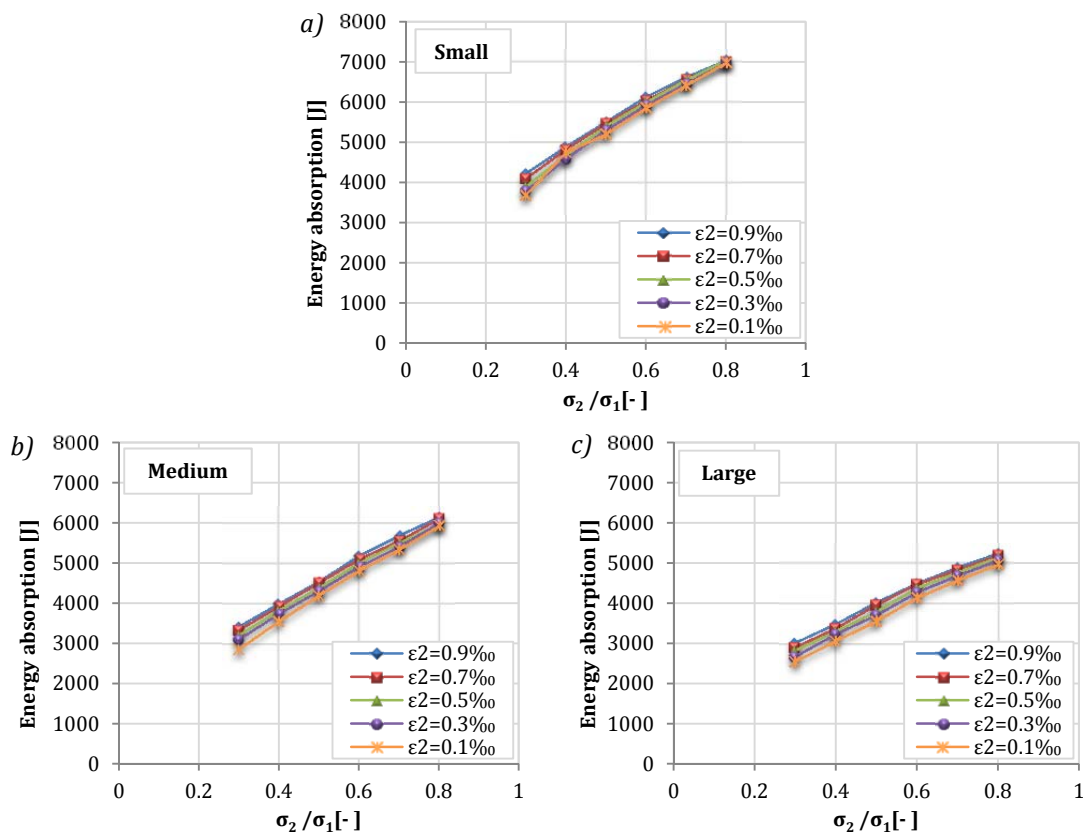


Figure 6.11 Influence of σ_2 in the energy absorption for slabs a) S, b) M and c) L.

Table 6.8 Slope of the tendencies in Figure 6.11.

Strain ϵ_2 [‰]	Slopes [J]		
	Small	Medium	Large
0.1	6321.7	5527.7	4885.3
0.3	6349.1	5520.8	4808.8
0.5	6258.5	5556.1	4698.5
0.7	5800.1	5738.6	4636.3
0.9	5677.7	6090.6	4499.7
Average	6081.4	5686.8	4705.7

The slopes reveal that the influence of σ_2 in the energy absorption is greater for slab S, which is the stiffest one. In fact, the rate at which this property increases for slab S is 6.9% and 29.2% higher for slabs M and L, respectively. Notice that these tendencies may change if, instead of the energy absorption at 15 mm, the total energy absorption was considered. In such case, the greatest increase would be for slab L. In terms of percentage, the increments of energy absorption at 15 mm between the curves with $\sigma_2=30\%\sigma_1$ and $\sigma_2=80\%\sigma_1$ (for $\varepsilon_2=0.3\text{‰}$) are 79.2% for slab S, 89.5% for slab M and 88.3% for slab L.

From the results in Figure 6.11 it can be concluded that σ_2 has a major influence in the variation of the energy absorption capacity. This phenomenon was expected since an increase of σ_2 implies a greater contribution of the fibre reinforcement and, therefore, a larger area enclosed by the P - δ curve, which defines the energy absorption capacity.

6.4.4. Analysis of the influence of σ_3

Load-deflection curves

The P - δ curves obtained for different values of σ_3 are presented in Figure 6.12. The results correspond to $\sigma_2=0.50\sigma_1$ and $\varepsilon_2=0.3\text{‰}$. The influence of the parameter σ_3 is not as significant as in the case of σ_2 . However, an increase of σ_3 leads to a higher maximum load that occurs for larger deflections.

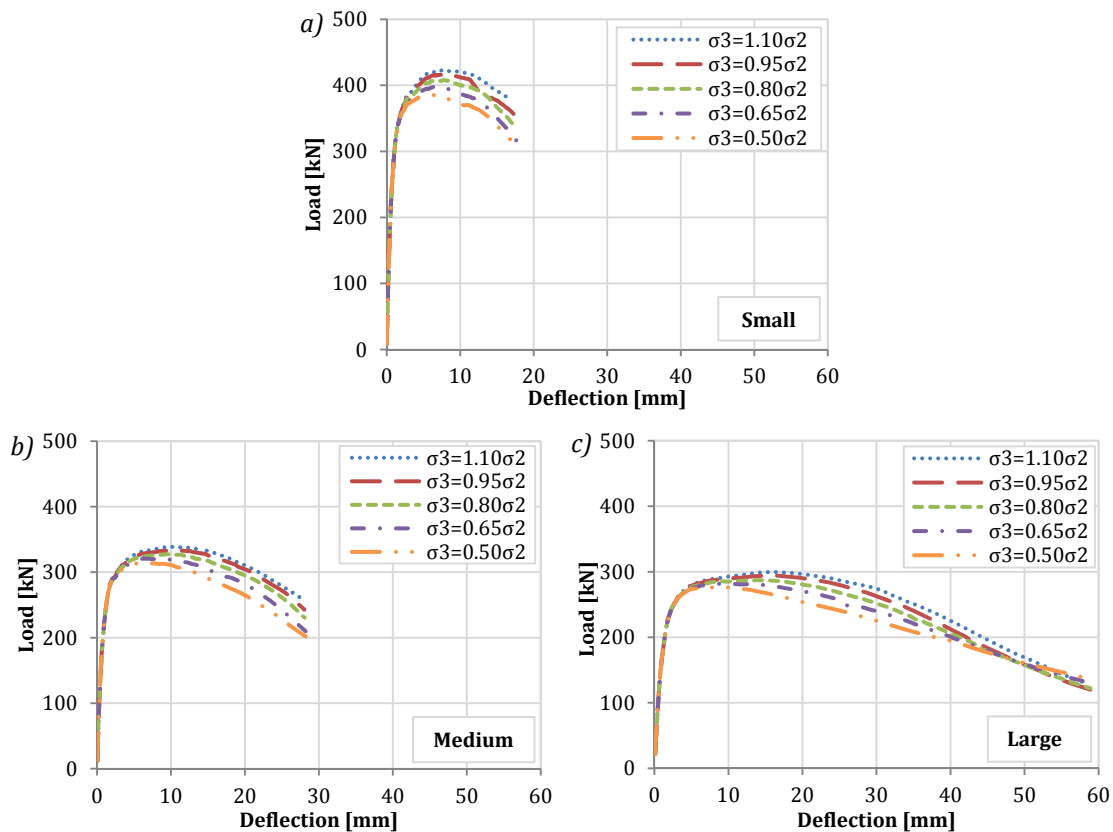


Figure 6.12 Influence of σ_3 in the P - δ curves for slabs a) S, b) M and c) L.

Maximum load

The maximum loads of the $P-\delta$ curves are plotted in Figure 6.13 against the σ_3 for the slabs S, M and L. These results correspond to $\sigma_2=0.50\sigma_1$, which is representative of the obtained with other values. The results indicate an increase of the maximum load with σ_3 , even though it is not as significant as in the case of σ_2 . Likewise, the curves exhibit an approximate linear behaviour with values of slopes that included in Table 6.9.

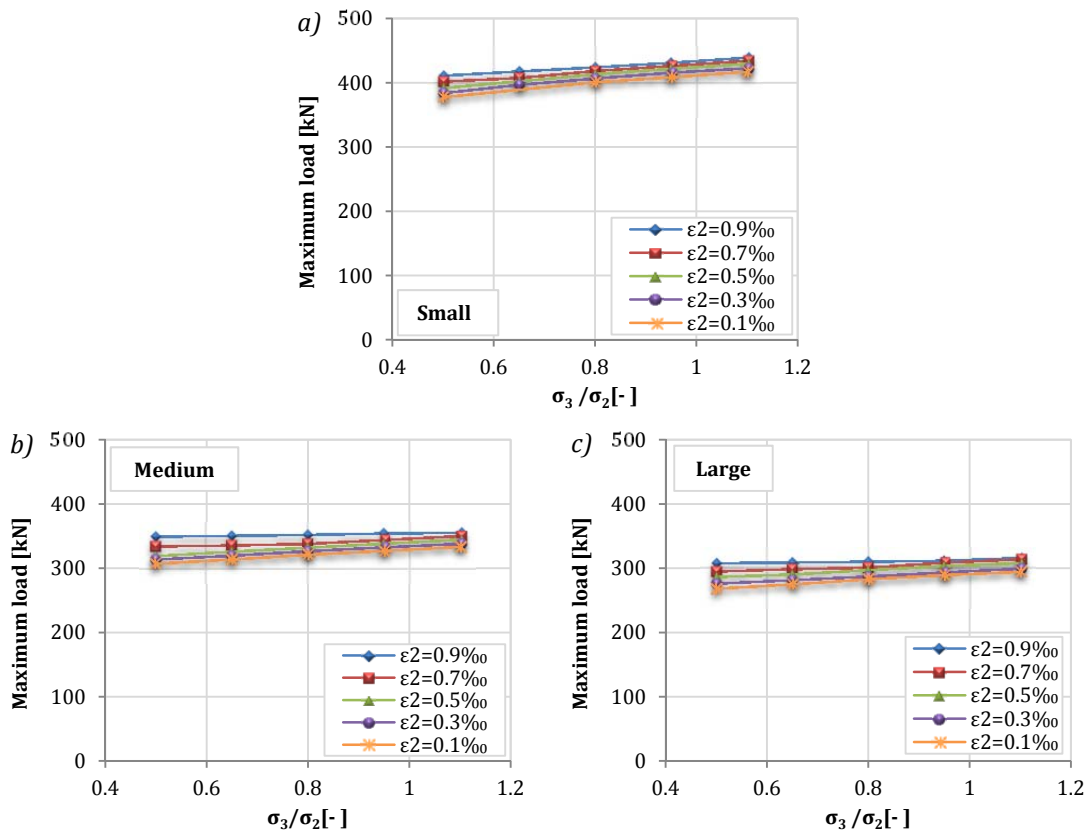


Figure 6.13 Influence of σ_3 in the maximum load for slabs a) S, b) M and c) L.

Table 6.9 Slope of the tendencies in Figure 6.13.

Strain ϵ_2 [‰]	Slopes [kN]		
	Small	Medium	Large
0.1	64.9	43.1	44.0
0.3	62.6	40.9	38.8
0.5	62.3	42.2	36.6
0.7	54.5	26.7	31.7
0.9	45.3	10.3	12.4
Average	57.9	32.6	32.7

From slopes it is observed that the slabs M and L present very similar tendencies with an increase rate of the maximum load almost identical. The influence of σ_3 on the response of slab S is more significant than for the other slabs since the average slope is

77.6% and 77.1% higher for slabs M and L, respectively. However, the increase is less evident than the observed in the analysis of σ_2 . This phenomenon was expected since σ_3 is not related with the maximum contribution of the fibre but rather with the gradual decrease in the post-cracking strength due to the intensification of the debonding between the fibre and the concrete matrix. Therefore, the higher is the value of σ_3 the higher will be the stresses that can be endured when the pull-out mechanisms are activated.

Slope $E4$

Figure 6.14 shows the slopes $E4$ against σ_3 to determine its influence in the response of the slabs S, M and L. These results correspond to $\sigma_2 = 0.50\sigma_1$. In contrast to what was observed in the case of σ_2 , a clear tendency of how σ_3 affects the slope $E4$ cannot be identified. The curves in Figure 6.14c indicate that the slope $E4$ of slab L increases (in terms of absolute value) with σ_3 . In fact, an increase of 59.5% of $E4$ is observed between limit values of σ_3 ($\sigma_3 = 0.50\sigma_2$ and $\sigma_3 = 0.95\sigma_2$) and $\varepsilon_2 = 0.3\text{‰}$. However, the curves in Figures 6.14a for slabs S and M exhibit a diffuse tendency in comparison with slabs L.

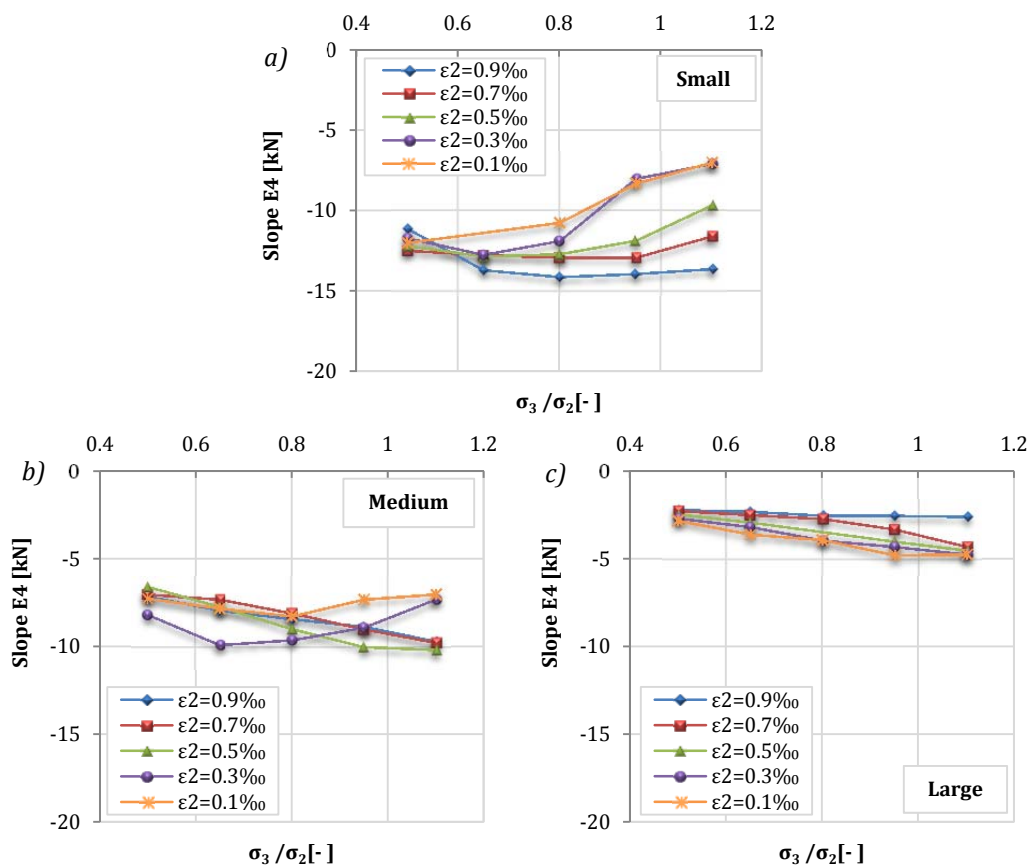


Figure 6.14 Influence of σ_3 in the slope $E4$ for slabs a) S, b) M and c) L.

The curves in Figure 6.14 reveal that the influence of the parameter σ_3 in the value of slope $E4$ is minor, compared to the case of σ_2 (see section 6.4.4). Nevertheless, it was expected that an increase of σ_3 would lead to less steep slopes and smaller $E4$ values.

Absorbed energy

The variation of the energy absorption depending on σ_3 for a deflection of 15 mm is plotted for different values of ε_2 and for $\sigma_3=0.50\sigma_2$ in Figure 6.15. The curves in Figure 6.15 suggest a slight increment in the energy absorption capacity of all slabs as σ_3 increases (if compared to the influence of σ_2). Furthermore, the curves in in Figure 6.15 exhibit approximately linear behaviour with slopes that are presented in Table 6.10.

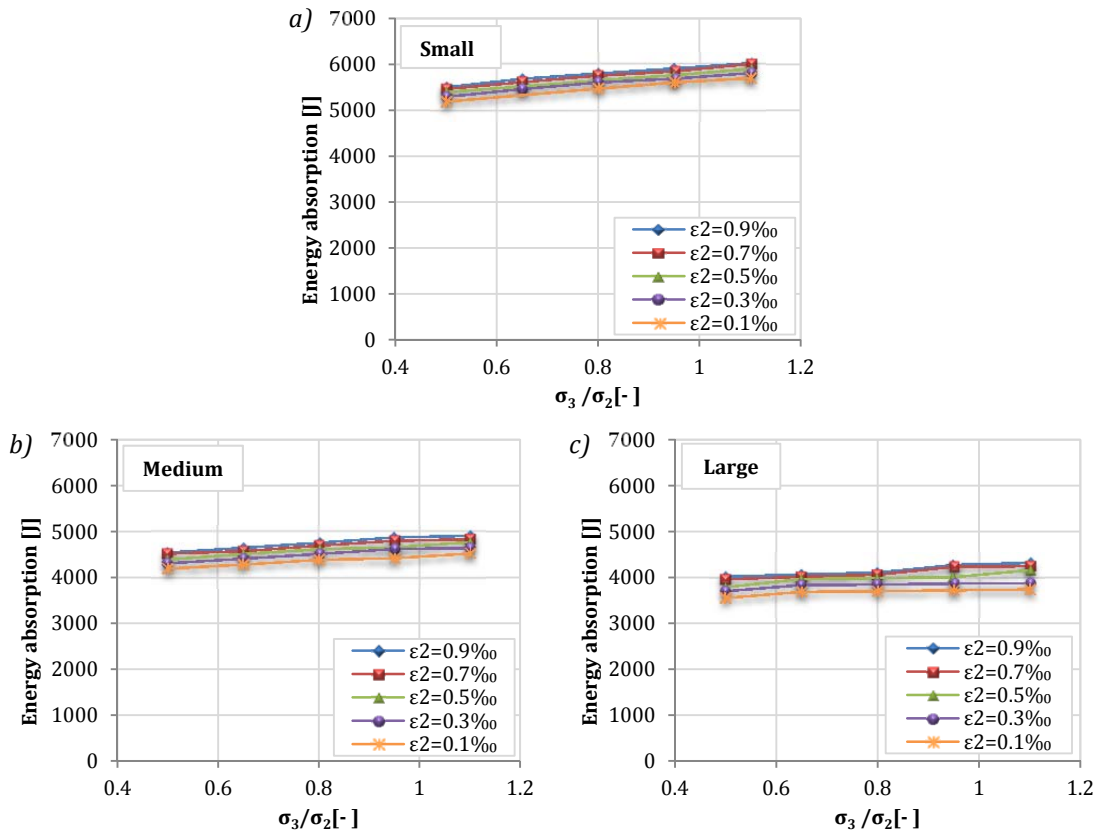


Figure 6.15 Influence of σ_3 in the energy absorption for slabs a) S, b) M and c) L.

Table 6.10 Slope of the tendencies in Figure 6.15.

Strain ε_2 [‰]	Slopes [J]		
	Small	Medium	Large
0.1	849.8	527.1	270.0
0.3	822.0	575.4	252.0
0.5	819.4	596.3	522.3
0.7	863.3	565	521.0
0.9	827.4	630.4	531.9
Average	836.4	578.8	419.4

The average slope for slab S is 44.5% and 99.4% higher than slabs M and L, respectively. The comparison of curves with limit values of σ_3 ($\sigma_3=50\sigma_2$ and $\sigma_3=95\sigma_2$) and $\varepsilon_2=0.3\text{‰}$ shows increments of 7.2%, 7.1% and 4.4% for slabs S, M and L, respectively.

When the debonding between the fibres and the concrete matrix starts, a gradual decrease in the post-cracking strength occurs. In this phenomenon, the value of σ_3 will determine the shape of the curve. If high values of σ_3 are considered, the last stretch of the P - δ curves will be higher as observed in Figure 6.12. Since the energy absorption in this case is measured by the area enclosed by the P - δ curves, the higher σ_3 the greater the energy absorption.

6.4.5. Analysis of the influence of ε_2

Load-deflection curves

The P - δ curves obtained for the values of ε_2 are presented for the slabs S, M and L in Figure 6.16, taking into account $\sigma_2=0.70\sigma_1$ and $\sigma_3=0.95\sigma_2$. As expected, ε_2 shows a minor influence on the values and on the shape of the curves regardless of the size of the slab.

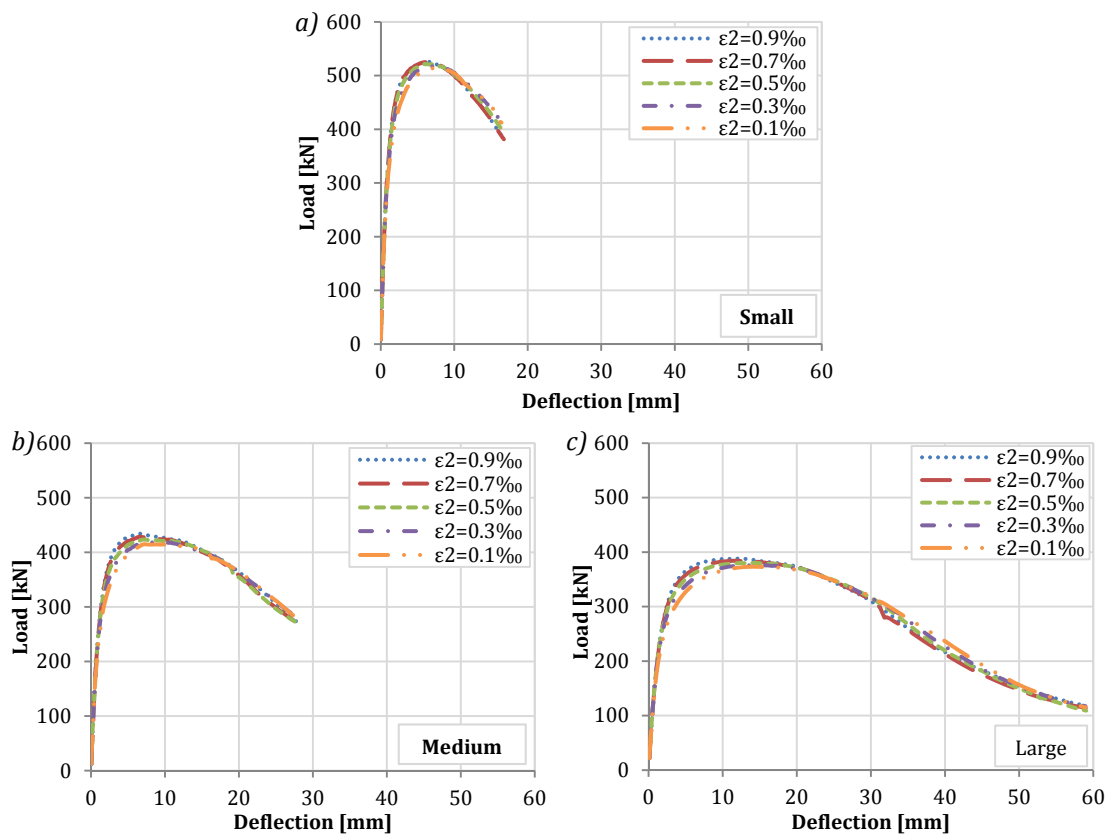


Figure 6.16 Influence of ε_2 in the P - δ curves ($\sigma_2=0.70\sigma_1$ and $\sigma_3=0.95\sigma_2$) for: a) S, b) M and c) L.

Maximum load

In Figure 6.17, the influence of the value of ε_2 in the P - δ curves is analysed in terms of the maximum load. In this case, the results correspond to $\sigma_3=0.95\sigma_2$ and are presented for different values of σ_2 . The curves show a slight increase in the maximum load with ε_2 . Even though, the tendencies of the three slabs are very similar, the results suggest that an

increase in ϵ_2 leads to a greater increase in the maximum load for slab L than for the slabs S and M. Furthermore, the increase is higher for low values of σ_2 (see $\sigma_2=0.30\sigma_1$). Such outcome may be easily identified by the slope of the curves, presented in Table 6.11.

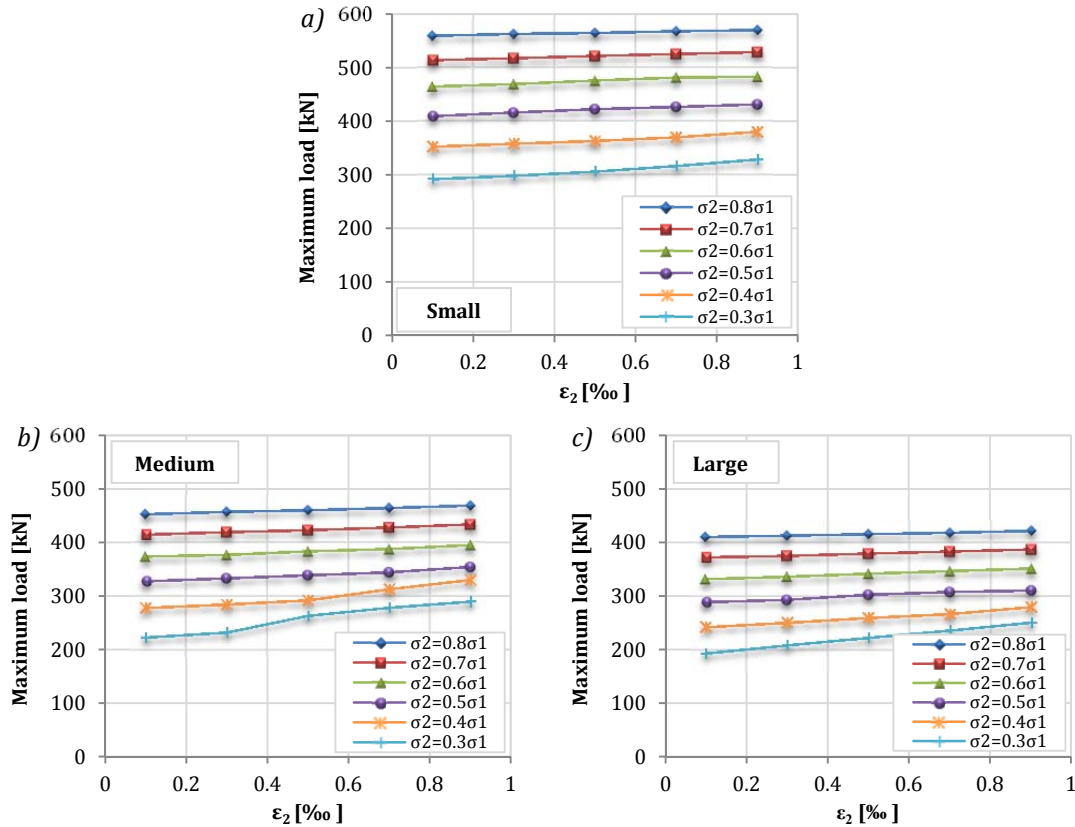


Figure 6.17 Influence of ϵ_2 in the maximum load for slabs a) S, b) M and c) L.

Table 6.11 Slope of the tendencies in Figure 6.17.

Stress σ_2 [σ_2/σ_1]	Slopes [kN]		
	Small	Medium	Large
0.3	45.7	89.8	71.3
0.4	33.6	66.3	45.6
0.5	27.2	32.4	29.1
0.6	24.4	26.8	24.8
0.7	19.3	23.3	18.6
0.8	13.4	19.6	14.4
Average	27.3	43.0	34.0

In this case, the slopes do not reveal a clear tendency regarding the influence of ϵ_2 . In fact, slabs S and L present average slopes that are 36.5% and 20.9% lower than for slab M. Nevertheless, the small slopes in all $P-\delta$ curves confirm that the influence of ϵ_2 in the maximum load is minor if compared to that observed with σ_2 and σ_3 .

Slope E4

In Figure 6.18, the influence of ε_2 in the response of slabs S, M and L is analysed in terms of the slopes $E4$. These results of slope correspond to $\sigma_3=0.95\sigma_2$ and are presented for different values of σ_2 . In general, the results for slabs S and M (see Figures 6.18a and 6.18b) indicate that the absolute value of $E4$ increases with the ε_2 . The increase of ε_2 from 0.1‰ to 0.9‰ produces an average increment of slope equal to 46.5% and 44.4% for slabs S and M, respectively. On the other hand, the tendency of slab L seems constant.

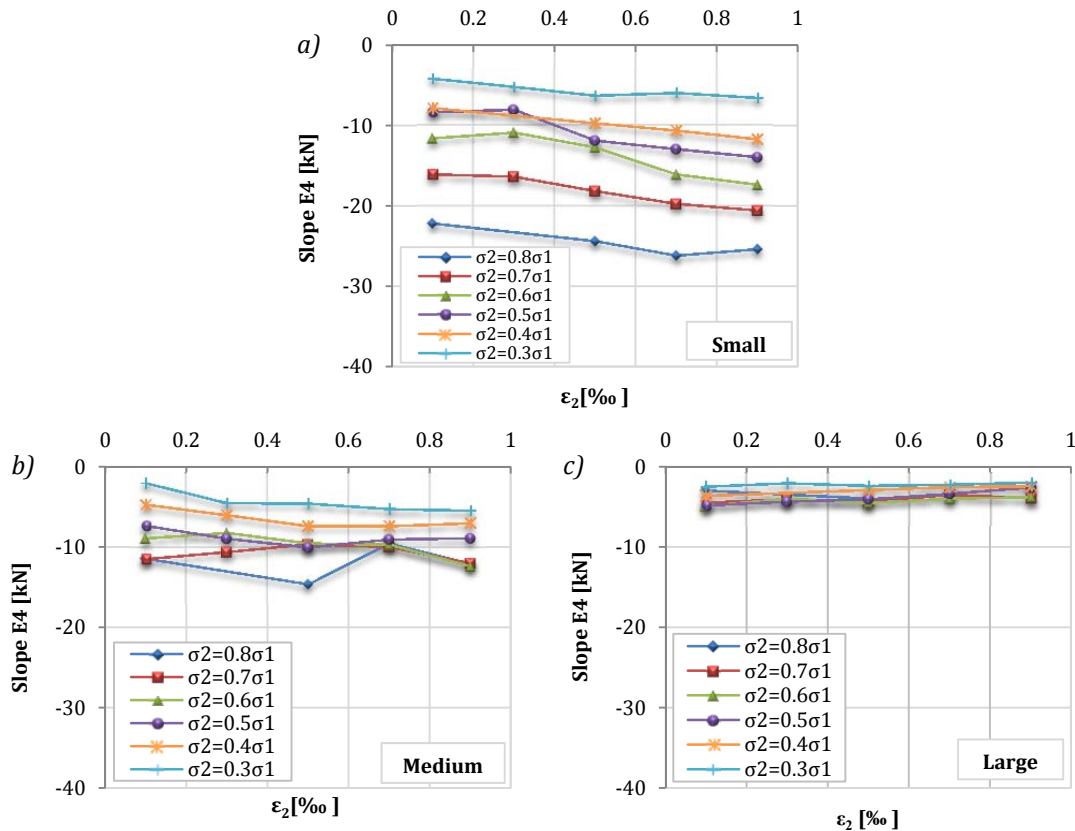


Figure 6.18 Influence of ε_2 in the slope $E4$ for slabs a) S, b) M and c) L.

The $P-\delta$ curves from Figure 6.16 indicate that a clear tendency on the influence of the parameter ε_2 in the value of slope $E4$ cannot be identified. Furthermore, from the calculated percentages it seems that this parameter has a minor influence if compared to the σ_2 and σ_3 (previously studied in this section).

Absorbed energy

Figure 6.19 shows the influence of ε_2 in the energy absorption capacity for a deflection of 15 mm. In this case, the results correspond to $\sigma_3=0.95\sigma_2$ and are presented for different values of σ_2 . The curves reveal a slight increase in the absorbed energy with ε_2 . The tendencies observed for the slabs S, M and L are almost identical, with an

approximately linear behaviour in all cases. In order to study in detail these tendencies, the slopes of the curves are presented in Table 6.12.

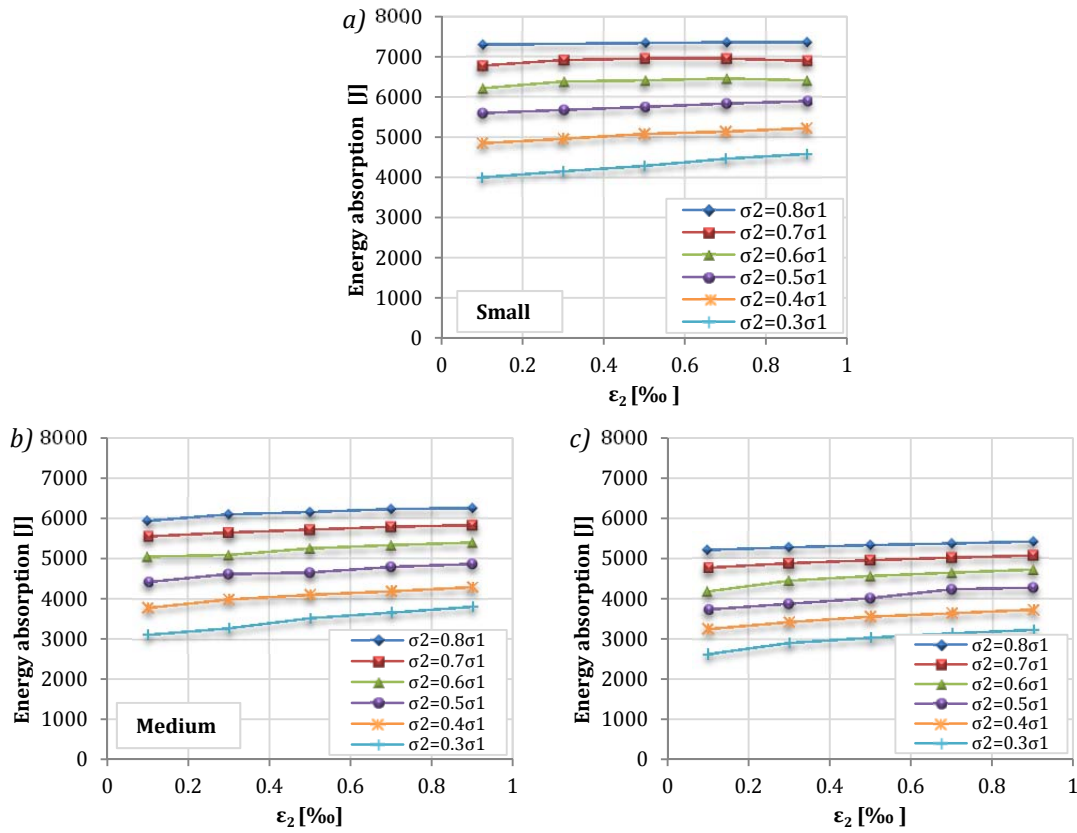


Figure 6.19 Influence of ϵ_2 in the energy absorption for slabs a) S, b) M and c) L.

Table 6.12 Slope of the tendencies in Figure 6.19.

Stress σ_2 [σ_2/σ_1]	Slopes [J]		
	Small	Medium	Large
0.3	736.9	891.9	721.3
0.4	464.9	613.4	590.2
0.5	376.9	536.1	724.6
0.6	233.1	472.5	639.1
0.7	140.5	349.2	378.5
0.8	74.8	381.0	252.7
Average	337.9	540.7	551.1

The average slopes of the curves indicate that the rates at which the energy absorption capacity increases in slab L is 38.7% and 1.9% higher than that for slabs S and M, respectively. The fact that this property increases with ϵ_2 was expected since it causes an increase of the maximum load. Even though this increment is small, it is sufficient to enlarge the area enclosed by the P - δ curve and, therefore, the energy absorption capacity.

6.5. NUMERICAL FIT OF THE PARAMETERS

Based on the study conducted in section 6.4, an iterative process was performed to find the parameters σ_2 , σ_3 and ε_2 that yield a good fit between the experimental and the numerical results. Given the minor influence of ε_2 in the structural response of the slabs, its value was set constant. It was defined as $\varepsilon_2 = \varepsilon_1 + 0.1\%$, according to the European codes and guidelines (in particular, the trilinear models of the DBV, the RILEM and the EHE-08). Consequently, only the values of stress σ_2 and σ_3 were subjected to the fitting process. The values finally obtained are presented in Table 6.13. Notice that the parameters σ_1 and ε_1 were defined according to EHE-08.

Table 6.13 Values of the parameters σ_2 , σ_3 and ε_2 for slabs S, M and L.

Slab	Batch	$\sigma_2/\sigma_{1(EHE)}$	σ_3/σ_2	ε_2 [‰]
S	B3	0.40	0.50	$\varepsilon_1 + 0.1$
M	B1	0.47	0.95	$\varepsilon_1 + 0.1$
L	B1	0.57	1.00	$\varepsilon_1 + 0.1$

The P - δ curves predicted with the values from Table 6.13 are compared with the experimental results in the graphs in Figure 6.20.

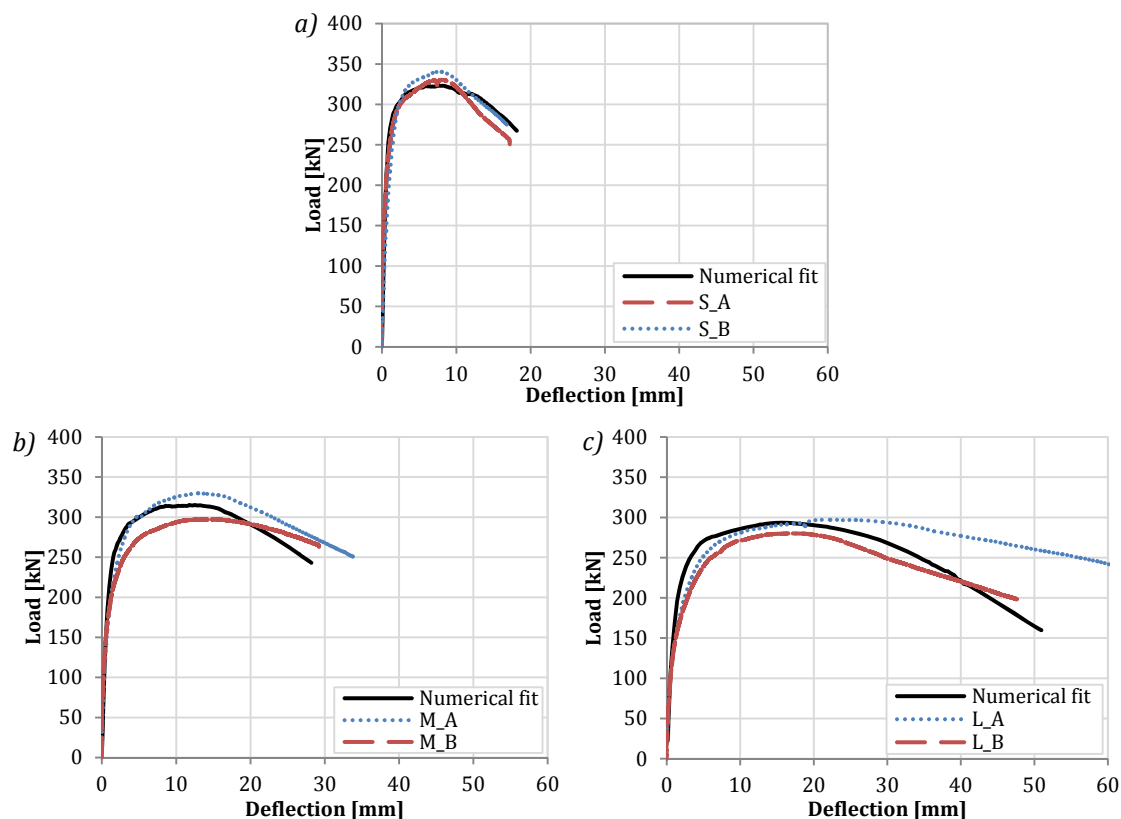


Figure 6.20 P - δ curves resulting from the numerical fit of the parameters for slabs a) S, b) M and c) L.

The graphs show that, particularly for the slabs S and M, the numerical fit curve remains between the experimental ones, whereas the prediction of slab L presents larger

differences. In order to analyse in detail the fit of the experimental curves, some of the results that can be derived from the P - δ curves are presented in Table 6.14. Notice that the energy absorption correspond to deflections of 15 mm, 25 mm and 45 mm for slabs the S, M and L, respectively.

Table 6.14 Average experimental results and results of the numerical fit.

Cases	Max. load [kN]	Deflection max. load [mm]	Load for $\delta=5$ mm [kN]	Load for $\delta=10$ mm [kN]	Slope $E4$ [kN/mm]	Energy absorption [J]
Exper. S	335.5	7.8	325.9	326.0	-8.5	4532.6
Numerical fit S	323.6	8.2	319.9	318.0	-8.5	4516.0
Exper. M	313.5	14.2	287.0	309.3	-3.9	7213.1
Numerical fit M	315.1	11.8	299.6	313.3	-6.4	7220.5
Exper. L	288.6	19.6	245.2	276.0	-2.5	11692.1
Numerical fit L	293.3	15.5	268.1	285.1	-5.8	11590.8

The numerical result of slab S fits very well the experimental results measured in the laboratory. Furthermore, the values in Table 6.14 indicate that the prediction remains on the safe side, exhibiting load values slightly lower than the experimentally registered. For example, an underestimation of 3.5% is observed for the maximum load. This load occurs at a predicted deflection of 8.2 mm which is 5.1% higher than the average measured for the slabs S. The numerical and the experimental results fit are also good for the slope $E4$ and the energy absorption. In fact, the same value of slope $E4$ and a slight underestimation of only 1.3% of the absorbed energy are obtained.

In the case of the slab M, the numerical curve with the parameters proposed in Table 6.13 fit the curves of slab M_A and M_B remarkably well, as observed in Figure 6.20. The maximum load predicted is almost identical to the average experimental result, which is overestimated only by 0.5%. The overestimations of the loads for deflections of 5 mm and 10 mm are 4.4% and 1.3%, respectively. Bigger differences are observed in the values of the deflection for the maximum load and the slope $E4$. The former is underestimated by 16.9% and the latter is overestimated by 64.1%. Despite this difference in the value of $E4$, the energy absorption is underestimated only by 0.6%, thus indicating a satisfactory fit between experimental and numerical results.

Regarding the numerical fit of slab L, it must be pointed out that this geometry presented the greatest differences in the P - δ curves between the pair slabs L_A and L_B. Hence, the determination of the parameters of the constitutive diagrams that fit well both slabs is more complicated in this case than for slabs S_A and S_B, for example, which present an almost identical slope. However, it is considered that the P - δ curve obtained with the numerical fit of the parameters approaches the experimental curves, as shown in Figure 6.20. The maximum load of the numerical fit overestimates the average experimental value in 1.6%. The overestimation of loads increases for deflections of 5 mm and 10 mm, reaching values of 9.3% and 3.3%, respectively. The maximum load in the numerical fit occurs at 15.5 mm, which is 20.9% lower than the average of the experimentally registered.

At this point, it is worthwhile highlighting that one of the most difficult parameters of the P - δ curves to simulate as experimentally observed was the value of slope $E4$. This was particularly problematic as the dimensions of the slab increased. Despite the differences between experimental and numerical values of slopes $E4$ in slabs M and L, it was considered that the overall curves presented a good fit if the other results, such as the ones presented in Table 6.14 and, especially, the maximum load and energy absorption exhibited acceptable differences. In fact, the energy absorbed at 45 mm is only 0.9% lower than the average determined from the experimental results. Moreover, with the values adopted, the prediction remains on the safe side for the post-cracking regime.

Based on the results presented in Figure 6.20 and Table 6.14 it is clear that the proper simulation of the flexural response of the SFRC slabs presented in Chapter 4 is possible and requires the definition of specific values for the parameters σ_2 , σ_3 and ε_2 . The next section extends the analysis on these parameters, comparing them with the ones proposed according with the RILEM and the EHE for each slab.

6.6. FIBRE NETWORK EFFECT AND PROPOSAL OF GEOMETRY FACTORS

6.6.1. Introduction

In section 6.3 of this chapter it was confirmed that the constitutive models proposed by the RILEM and the EHE-08 are not suitable for the design of SFRC slabs since they overestimate by far the real structural response. In order to determine the differences between these models and the constitutive curves obtained through the numerical fit, the values of all models are presented in Table 6.15.

Table 6.15 Average results of slabs S, M and L and results of the prediction of the RILEM and the EHE.

Slab	σ - ε diagram	σ_1 [MPa]	σ_2 [MPa]	σ_3 [MPa]	ε_1 [‰]	ε_2 [‰]	ε_3 [‰]
S	RILEM	5.616	2.545	2.219	0.186	0.286	25.000
	EHE-08	2.888	2.811	1.698	0.096	0.196	20.000
	Numerical fit S	2.888	1.155	0.578	0.096	0.196	20.000
M + L	RILEM	5.606	2.545	2.219	0.193	0.293	25.000
	EHE-08	2.879	2.811	1.698	0.099	0.199	20.000
	Numerical fit M	2.879	1.353	1.285	0.099	0.199	20.000
	Numerical fit L	2.879	1.641	1.641	0.099	0.199	20.000

The values of stress σ_2 presented in Table 6.15 for slabs M and L are 17.1% and 42.1% higher than that for slab S. In the case of σ_3 , the values increase 122.3% and 184.0%, respectively. Although the greatest differences among the diagrams are detected for σ_3 , the parametric study conducted in section 6.4 allowed identifying σ_2 as the parameter that has the major influence in the flexural response of the slabs.

Table 6.15 also shows that reductions of 58.9% and 66.0% in the values of σ_2 and σ_3 , respectively, proposed by the EHE-08 are required in order to obtain a good prediction

of the flexural response of the slab S. If the comparison is made with the values of the RILEM, the reductions in the stress are 54.6% and 74.0% for σ_2 and σ_3 , respectively.

For slab M, the values of stress σ_2 and σ_3 proposed by the EHE-08 are reduced 51.9% and 24.3% in the numerical fit, while a reduction of respectively 46.8% and 42.1% is required in the case of the RILEM. The σ_2 and σ_3 obtained in the numerical fit for slab L represent a 41.6% decrease for σ_2 and a 3.4% increase for σ_3 from the EHE-08. In the case of the values of RILEM, a reduction of 35.5% and 26.0% is observed, respectively.

The σ - ε diagrams obtained for slabs S, M and L from the numerical fit of the parameters are plotted in Figure 6.21. Notice that the numerical fit was based on the values of σ_1 , ε_1 and ε_3 proposed by the EHE-08.

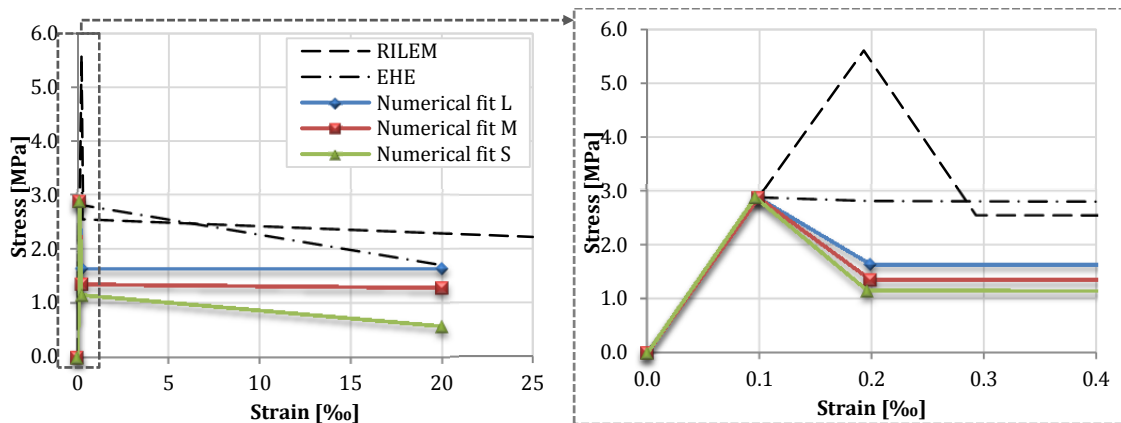


Figure 6.21 Constitutive models from RILEM, EHE and from the numerical fit of the parameters for slabs a) S, b) M and c) L.

It is obvious that the main differences between the RILEM or the EHE-08 models and the curves obtained in this chapter are verified for σ_2 and σ_3 , which tend to be overestimated in the design codes. Such difference seems to decrease as the width of the slab increases. In fact, the highest and lowest values of σ_2 and σ_3 are observed for slabs L and S, respectively.

6.6.2. Fibre network effect

In view of the analysis conducted in the previous section, the question that may be posed at this point is why larger slabs present higher values of stress in the σ - ε diagram than that of smaller slabs? According to the literature (Kooiman 2000; Laranjeira 2010), different responses of FRC may be caused by the properties of the concrete matrix affecting the fibre-matrix interface, the fibre orientation and the fibre type and content.

In this case, the properties of the SFRC are practically the same for all slabs as described in Chapter 4. The only difference detected is the orientation of the fibres due to the dimensions of the slabs (analysed in detail in Chapter 5) and the hyperstatic behaviour

of the real structure. One of the main conclusions of the study conducted in Chapter 5 was that in radial flows (or extensional flows) the fibres tend to rotate and align perpendicular to the flow as they advance from where the concrete is poured to the edges of the formwork. Likewise, the influence of the walls of the formwork in the orientation of the fibres was also identified close to the edges.

On the basis of this study, a division of the slabs in three main zones of orientation (central, transition and external zones) was outlined (see Figure 5.23). These results are very useful to justify the differences in the stress-strain curve depending on the size of the slabs. In this sense, the reason herein proposed to explain such behaviour is that in slab L there are more fibres advantageously aligned, providing a greater crack bridging capacity.

Figure 6.22 illustrates schematically the evolution of the concrete radial flow in a smaller rectangular slab (see Figure 6.22a), such as slab S, and in a larger square slab (see Figure 6.22b), such as slab L. In the case of the latter, the concrete flows more or less regularly in all directions and the fibres align perpendicularly to the direction of the flow. On the contrary, in the smaller slab the way the concrete flows is not regular since it is affected by the shorter size, flowing more along the longest dimension. The area in the slab where the fibre orientation is not affected by the walls of the formwork is smaller in the case of the slab in Figure 6.22b and, therefore, there are fewer fibres that are not affected by the wall-effect.

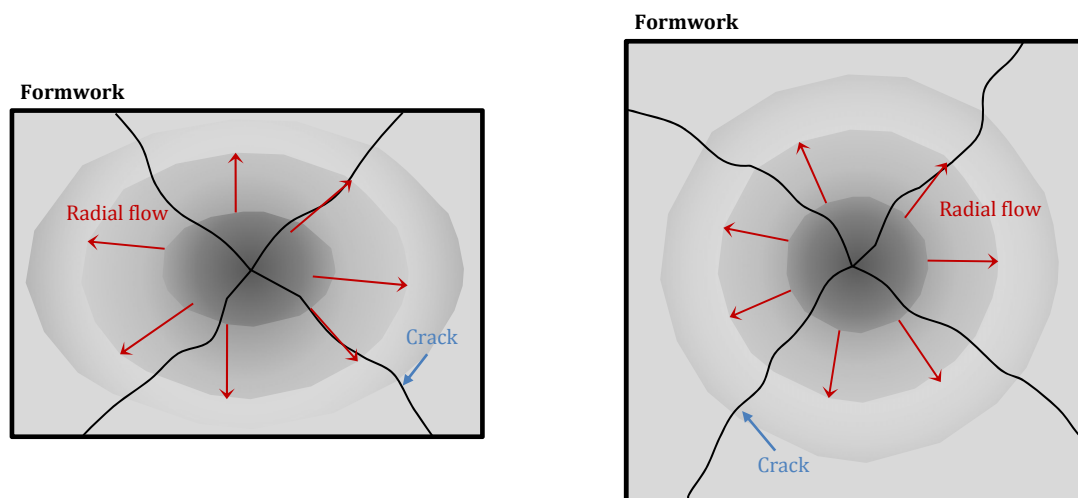


Figure 6.22 Fibre orientation in a) a smaller rectangular slab and b) a larger square slab.

Considering the development of the cracks in Figure 6.22 (depicted according to what was observed in Chapter 4), the way fibres align (perpendicularly to the flow) is more advantageous in the case of Figure 6.22b since fibres are more likely to be disposed perpendicularly to the cracks. Therefore, a higher stress bearing capacity is observed in the sectional level for the largest slabs. The quantification of this effect of the fibre reinforcement would be of great interest for the design of this type of structure. Hereinafter, this effect will be referred to as fibre network effect.

Given that the main differences among the numerical fits of each slab correspond to the values of σ_2 and σ_3 , the fibre network effect is assessed through these two parameters. The values of σ_2 and σ_3 for slabs M and L are compared with the values of σ_2 and σ_3 for slab S in terms of their ratio as indicated in the expressions (6.1) and (6.2).

$$\eta_{f\sigma_2} = \frac{\sigma_{2i}}{\sigma_{2S}} \text{ for } i = M, L \quad (6.1)$$

$$\eta_{f\sigma_3} = \frac{\sigma_{3i}}{\sigma_{3S}} \text{ for } i = M, L \quad (6.2)$$

In this context, the ratios $\eta_{f\sigma_2}$ and $\eta_{f\sigma_3}$ represent the increase on load bearing capacity observed at the sectional level as a result of the slab geometry, thus representing the amount fibre network effect generated, taking as a reference slab S. The values of these factors are presented in Table 6.16.

Table 6.16 Fibre network effect factors for the slabs S, M and L.

Slab	Width [m]	Width/Length [-]	$\eta_{f\sigma_2}$ [-]	$\eta_{f\sigma_3}$ [-]
S	1.5	0.50	1.00	1.00
M	2.0	0.67	1.17	2.23
L	3.0	1.00	1.42	2.84

Based on the values presented in Table 6.16, the Lab Fit Curve Fitting Software was used to find the functions that fit the evolution of the fibre network effect factors depending on the width to length ratio (b/a) of the slab. The expressions (6.3) and (6.4) represent the function obtained for $\eta_{f\sigma_2}$ and $\eta_{f\sigma_3}$, respectively. Notice that the minimum value of the ratio b/a considered in this study is 0.5.

$$\eta_{f\sigma_2} = 1.733(1 - e^{-1.703 \cdot b/a}) \quad (6.3)$$

$$\eta_{f\sigma_3} = -\frac{0.619}{(b/a)^2} + 3.514 \quad (6.4)$$

The curves obtained with expressions (6.3) and (6.4) are plotted in Figure 6.23 with the $\eta_{f\sigma_2}$ and $\eta_{f\sigma_3}$ factors obtained experimentally for different b/a ratio. The correlation coefficients (R^2) of the curves are also indicated in the same figure.

The curves show that the increase in the fibre network effect is more pronounced in the case of σ_3 . Again, it is necessary to emphasize that the parametric study conducted in this chapter points to the parameter σ_2 as the more influential in the flexural response of the slabs. Hence, despite the curves in Figure 6.23 reveal a more moderate increase, the parameter governing the fibre network effect is σ_2 . Furthermore, the tendencies of the curves suggest that the fibre network effect for both values of stress increases up to a b/a ratio equal to 1. In this regard, further experimental validation is required in order to corroborate this trend.

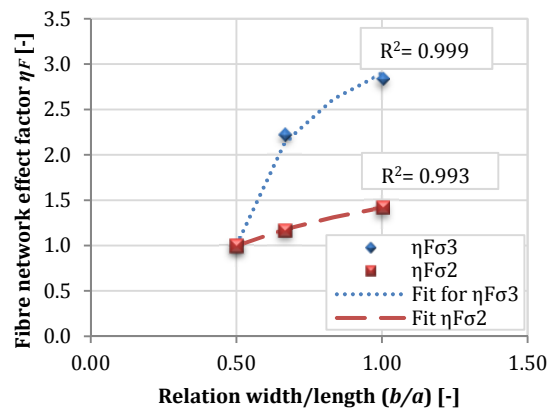


Figure 6.23 Evolution of the values of $\eta_{F\sigma 2}$ and $\eta_{F\sigma 3}$ with the b/a ratio of the slab.

It should be pointed out that, despite the expressions (6.3) and (6.4) are defined as a function of b/a , the results herein presented were only experimentally verified for a length (a) of 3.0 m as described in Chapter 4. In order to generalize the expressions to other dimensions, the experimental program must be extended in the future.

6.6.3. Proposal of geometry factors

This section aims at proposing a simple methodology to obtain σ - ε diagrams that are more representative of the structural behaviour of the slabs and, therefore, suitable for their design. The philosophy behind this proposal is to provide geometry factors that could be applied to the current constitutive models (to the values of σ_2 and σ_3) in order to improve the prediction of the flexural response of the SFRC slabs, integrating the fibre network effect described in 6.6.2.

The method developed to obtain suitable σ - ε diagrams to simulate the response of SFRC slabs is presented in Figure 6.24. Notice that the method proposed takes as a reference the methodology established in the EHE-08 and the factors are based on the values of the parameters of the constitutive model proposed in this thesis.

First the σ - ε diagram is obtained using the results of flexural test of beams following the standard procedure defined in the existing codes. Then, base factors (ζ_B) are applied to the stress values of the original diagram in order to account for the differences between the resistant mechanisms observed in the small beam and in an equivalent slab. Given that the variations observed in σ_2 and σ_3 are different, the former should be affected by the base factor $\zeta_{B\sigma 2}$ and the latter should be affected by $\zeta_{B\sigma 3}$. The resulting σ - ε diagram corresponds to the numerical fit obtained for slab S which is the slab of reference in the method herein presented.

Afterwards, in order to determine the suitable σ - ε diagram to predict the response of a slab with a certain width (b), the fibre network effect factors need to be applied to the values of σ_2 and σ_3 of the reference slab. These factors, as previously described, take into

account the internal redistribution of stresses due to the presence of fibres in a slab depending on the width.

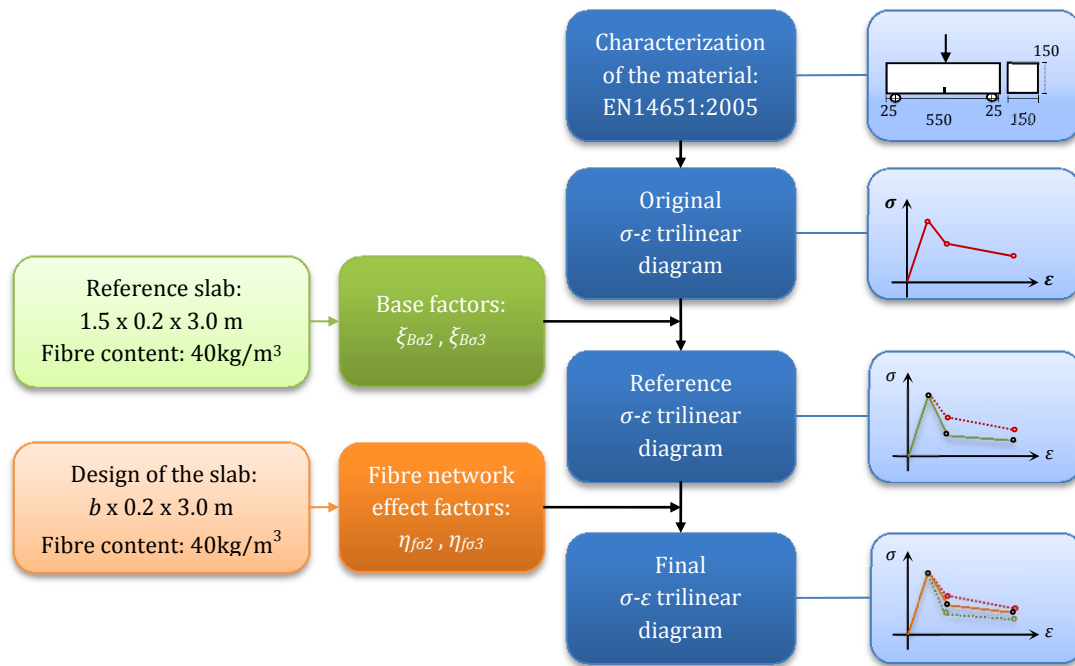


Figure 6.24 Method developed to obtain σ - ϵ diagrams for the design of SFRC slabs.

Considering the abovementioned, the base factors ($\xi_{B\sigma_2}$ and $\xi_{B\sigma_3}$) are defined as the stress ratio between the numerical fit of the reference slab (slab S) and the original value obtained from the EHE. Notice that these base factors are proposed for a reference slab with the same dimensions and fibre content as the slab S. The values of these factors are presented in Table 6.17.

Table 6.17 Base factors associated with the reference slab.

Base factor	Value
$\xi_{B\sigma_2}$	0.41
$\xi_{B\sigma_3}$	0.34

The fibre network effect factors ($\eta_{f\sigma_2}$ and $\eta_{f\sigma_3}$) were already defined in the previous section according with expressions (6.3) and (6.4). In order to simplify this method, a single factor that integrates the base factor and the fibre network effect factor is proposed for the values of stress σ_2 and σ_3 in expressions (6.5) and (6.6), respectively. Hereinafter, this factor will be referred as geometry factor (ξ_{σ_i}).

$$\xi_{\sigma_2} = \xi_{B\sigma_2} \cdot \eta_{f\sigma_2} \leq 1 \tag{6.5}$$

$$\xi_{\sigma_3} = \xi_{B\sigma_3} \cdot \eta_{f\sigma_3} \leq 1 \tag{6.6}$$

The geometry factor is proposed to correct the overestimation in the response of the slabs provided by the current σ - ϵ diagrams. According to this, the value of the

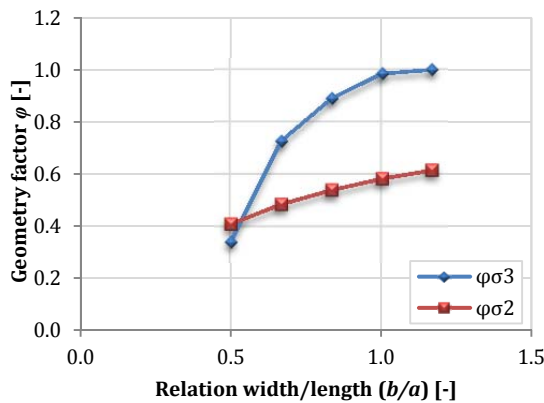
geometry factor must not be bigger than 1. The expressions in (6.5) and (6.6) are general and could be extrapolated to other dimensions of slabs and fibre contents if the base factors and fibre network effect factors were determined and experimentally validated.

For the particular case studied in this chapter, considering the values of the base factors and the expressions (6.3) and (6.4), the expressions (6.5) and (6.6) may be rewritten as (6.7) and (6.8).

$$\xi_{\sigma_2} = 0.711(1 - e^{-1.703 \cdot b/a}) \leq 1 \quad (6.7)$$

$$\xi_{\sigma_3} = -\frac{0.254}{(b/a)^2} + 1.195 \leq 1 \quad (6.8)$$

The curves and the values obtained with expressions (6.7) and (6.8) for slabs with different b/a ratios are presented in Figure 6.25.



b/a	ξ_{σ_2}	ξ_{σ_3}
0.50	0.41	0.34
0.67	0.48	0.72
0.83	0.54	0.89
1.00	0.58	0.99
1.17	0.61	1.00

Figure 6.25 Evolution of the values of ξ_{σ_2} and ξ_{σ_3} with the b/a ratio of the slab.

Notice that the geometry factor applied to σ_2 ($\xi_{B\sigma_2}$) increases from 0.41 to 0.58 as the b/a ratio ranges from 0.5 to 1.0. For the same range of b/a , the geometry factor for σ_3 ($\xi_{B\sigma_3}$) varies from 0.34 to 1.00.

6.7. CONCLUDING REMARKS

Chapter 6 discussed the results of the numerical modelling of the flexural tests of full-scale SFRC slabs. The following conclusions can be drawn from the study conducted.

- The current constitutive models from RILEM and EHE-08 for the design of FRC based on the performance of small beams overestimate the results of the flexural response of the slabs and, therefore, are not suitable to predict the behaviour of this type of element.
- According to the parametric study, the stress σ_2 is the parameter that has the biggest influence over the structural response of the slabs, particularly in the

maximum load and the energy absorption capacity (σ_1 , ε_1 and ε_3 are kept constant). The stress σ_3 and the strain ε_2 lead to minor changes in the response of the slabs if compared to σ_2 .

- The numerical fit of the parameters a trilinear σ - ε diagram for the slabs S, M and L allowed obtaining a close response to the experimental results. In this procedure, the slope of the final stretch of the P - δ curves was the most difficult characteristic to simulate.
- The comparison of the σ - ε diagrams proposed with the numerical fit for each type of slab allowed identifying a fibre network effect. This phenomenon is associated with a favourable fibre orientation regarding the cracking planes, which may lead to a different sectional response depending on the width of the slab. This effect was quantified by means of a fibre network effect factor that presents higher values as the length to width ratio increases.
- A simple method to obtain suitable σ - ε diagrams for the design of SFRC slabs was proposed. This method is based on the estimation of geometry factors that take into account the fibre network effect and, indirectly, the internal hyperstaticity of the structure.

7. CONSTITUTIVE MODEL BASED ON THE BARCELONA TEST

7.1. INTRODUCTION

The current design codes and guidelines for SFRC propose different constitutive models with a common characteristic: the parameters of the models are obtained by means of flexural tests on small beams, as introduced in Chapter 2. These models are known to provide satisfactory predictions of the behaviour of beams, as confirmed from the results in Chapter 3. However, their suitability for other typologies of structures is arguable as demonstrated in Part III of this thesis for the case of slabs.

Although bending tests are currently the most applied to characterize the tensile properties of SFRC, a large scatter in their results has been reported in the literature, often reaching values of 20% (Parmentier *et al.* 2008; Molins *et al.* 2009) in contrast to that of the compression test which is lower than 10% (Bencardino *et al.* 2008). These large scatters indicate that the beam test may not be the most suitable to systematically control the material quality. Alternatively, the most recent design codes and guidelines accept other types of test. The CNR-DT 204 proposes the use of tension tests and the EHE-08 and the MC2010 specify that other tests may be accepted if correlation factors with the parameters of the bending test are proven.

Thus, a new testing method was presented by Molins *et al.* (2007) to overcome the abovementioned drawbacks: the Barcelona test (UNE 83515:2010 (AENOR 2010)), which

was already introduced in Chapter 2. This is a simple and reliable test to systematically control the tensile properties of FRC, based on DPT formerly presented by Chen (1970) to characterize the tensile strength of plain concrete. Some of the advantages of using the Barcelona test are: the material saving and lighter specimens, the simplicity in execution, a reduced scatter if compared with other testing methods and the possibility of testing cores drilled from real FRC structures.

Even though there are analytical expressions of the tensile strength in the literature, there is no formulation that allows obtaining the stress-strain (σ - ε) relation directly from the Barcelona test. Instead, correlations factors with the bending test are used (Molins *et al.* 2009). In order to establish the Barcelona test as an alternative testing method on which codes and guidelines could base their design procedure for SFRC structures, a formulation to obtain the σ - ε relation directly from the test is required.

7.1.1. Objectives

In the light of the exposed, the objective of this chapter is to propose a model whose parameters are assessed from the Barcelona test. To achieve this goal, the following specific objectives are defined:

- Review the analytical expressions in the literature to determine the tensile strength in the double punch test;
- Develop an analytical formulation to obtain a σ - ε constitutive model based on the Barcelona test;
- Validate the proposed formulation by conducting an experimental program and a numerical simulation;
- Propose a simplification of the model that may be easily adopted by the professionals and
- Compare the constitutive model based on the Barcelona test with the constitutive models in European codes and guidelines, which are based on beam tests.

7.1.2. Outline of the chapter

Initially, in section 7.2 a study of the current analytical expressions for determining the tensile strength is performed. Subsequently, in section 7.3, a brief description of the failure mechanism of the test is introduced, setting the basis for the deduction of the model which is presented afterwards. In section 0, the predictions of the tensile strength provided by the expression in the literature and the new formulation herein proposed are analysed on the basis of experimental data from the literature. Subsequently, a simplified version of the model is proposed in section 7.5.

Then, an experimental program involving Barcelona tests and beam tests is presented in section 0. This section includes the description of the specimens, the materials and the concrete mix and a brief analysis of the results. The aim of this experimental program is to provide experimental data so as to validate the formulation proposed and to compare it with the constitutive models based on beam tests in subsequent sections.

The fit between the simplified and the complete models is presented in section 7.7 based on the experimental data. In section 7.8, the Barcelona test is simulated and the numerical results are compared with the experimental data from section 0. After the validation, in section 7.9, the simplified version of the constitutive model proposed is compared to the constitutive models based on beam tests. Finally, in section 7.10, the main conclusions of the study are highlighted.

7.2. ANALYTICAL EXPRESSIONS FOR THE TENSILE STRENGTH

Several analytical expressions were reported in the literature for determining the tensile strength (f_{ct}) of the DPT (Chen 1970; Chen and Yuan 1980; Bortolotti 1988; Marti 1989; Wei and Chau 2000; Molins *et al.* 2007). In Table 7.1, a summary of the closed-form expressions is presented. The main parameters defining these expressions are: the maximum load (P), the diameter and the height of the specimen (d and h , respectively) and the diameter of the plate (d').

Table 7.1 Analytical expressions for the tensile strength.

Study	Hypothesis / Approach	Expression
Chen (1970) ¹	Limit analysis of perfect elasto-plastic material	$f_{ct} = \frac{P}{\pi \left(1.2 \frac{d}{2} h - \left(\frac{d'}{2} \right)^2 \right)}$
Chen and Yuan (1980) ²	Concrete as an elasto-plastic strain-hardening and fracture material (FEM analysis)	$f_{ct} = \frac{0.75P}{\pi \left(1.2 \frac{d}{2} h - \left(\frac{d'}{2} \right)^2 \right)}$
Bortolotti (1988) ³	Modification of the Coulomb failure criterion for concrete	$f_{ct} = \frac{P}{\pi \left(\frac{d}{2} h - \left(\frac{d'}{2} \right)^2 \cot \beta \right)}$
Marti (1989) ⁴	Non-linear fracture mechanics	$f_{ct} = 0.4 \frac{P}{4 \left(\frac{d}{2} \right)^2} \sqrt{1 + \frac{d}{\lambda d_a}}$
Molins <i>et al.</i> (2007)	Strut-and-tie model	$f_{ct} = \frac{P}{9\pi h \frac{d'}{2}}$

1, 2: Both expressions are proposed in Chen and Yuan (1980).

3: where $\beta = \frac{\pi}{2} - \frac{\varphi}{2}$ is the failure angle and φ is the internal friction angle.

4: where d_a is the maximum aggregate size and λ is an experimental parameter depending on the material.

The first expression by Chen (1970) is based on a limit analysis, assuming a perfect elasto-plastic material and is dependant of the geometry, the internal friction angle (φ) and the failure angle (β). In order to simplify the expression, several assumptions were made regarding the size of the element ($h/d = 1$ and $h/d' = 4$) and the values of the angles ($\varphi = 30^\circ$ and $\beta = 10^\circ$). Given the discrepancies with the experimental data, a subsequent study by Chen and Yuan (1980) proposed a reduction factor that provides a value of tensile strength 25% lower. This reduction factor was determined by performing a FEM analysis and assuming strain-hardening and cracking of the material.

Bortolotti (1988) considered a particular modified Coulomb-like failure criterion. Failure is reached through two consecutive limit states (in which the sample is represented by a concrete cube): the first corresponds to the f_{ct} reached in the splitting surface and the second is the failure of the conical surfaces under the plates, reached after a constant loading redistribution process (with softening in the tensile failure surfaces). This approach considers φ and β as variables depending on the type of concrete. Marti (1989) conducted a study on the size effect in the DPT for a h/d ratio equal to 1 and proposed an expression based on non-linear fracture mechanics that depends on the maximum aggregate size (d_a) and an empirical constant dependant on the material (λ).

The previous expressions were proposed to estimate f_t of plain concrete as an approximation. Nevertheless, there was no exact solution for the elastic tensile stress within a solid circular cylinder under the DPT. The study by Wei and Chau (2000) presents a new solution method for the analysis of stresses in the DPT in which the equilibrium equations are decoupled by introducing two displacement functions. The adaptation of the DPT as a method for the control de tensile properties of FRC required an expression to determine the post-cracking strengths. With that purpose, Molins *et al.* (2007) suggest a strut-and-tie model for specimens with $h/d = 1$ from which a formulation valid for both f_{ct} and the residual post-cracking strength was proposed.

Some of the hypothesis regarding the geometry and the parameters that influence the f_t assumed in each of the described expressions are listed in Table 7.2.

Table 7.2 Summary of the hypothesis assumed.

Assumptions of the expressions	Chen (1970)	Chen (1980)	Bortolotti (1988)	Marti (1989)	Wei (2000)	Molins (2007)
Particularized for $h/d = 1$ and $h/d' = 4$	•	•	•	•		•
Poisson ratio as a variable					•	
Constant value for φ and β	30°/10°	30°/10°		36.9°		
φ and α are variables depending on f_c			•			
Maximum size of the aggregate (d_a)				•		
Uniform increase of tension along the planes containing the axis of the cylinder			•	•	•	
Valid for FRC (residual strength)						•

The previous expressions allow determining the f_{ct} for plain concrete and, in the case of the expression by Molins *et al.* (2007), the residual strengths in the post-cracking stage. However, there is no formulation that provides the σ - ε relation and that is valid for both the linear-elastic and post-cracking stages. This chapter provides expressions to obtain both the stress and the strain from the Barcelona test. Such expressions are based on an innovative approach that uses the principle of virtual work to provide a more realistic representation of the kinematic mechanism observed on the post-cracking stage.

7.3. FORMULATION TO PREDICT THE TENSILE BEHAVIOUR OF FRC

7.3.1. Failure mechanism of the Barcelona test

In the Barcelona test, the applied load produces a tensile stress field with cylindrical symmetry. In this first stage, the resistant mechanism is characterized by the concrete matrix bearing the stresses. When the tensile strength of concrete is reached, there is a transition stage in which radial cracks open perpendicularly to the stress field and two wedges are formed under the cylindrical plates where the load is applied. These wedges can be idealized as cones with the same diameter of cylindrical plates (Chen 1970; Bortolotti 1988; Molins *et al.* 2009; AENOR 2010; Carmona *et al.* 2012).

After the cracks stabilize, a kinematic mechanism occurs in which the conical wedges slide inside the specimen a certain displacement (δ_p) causing the lateral displacement (δ_L) of the concrete segments divided by the radial cracks (see Figure 7.1). Further detail on the failure mechanism may be found in Pujadas *et al.* (2012).

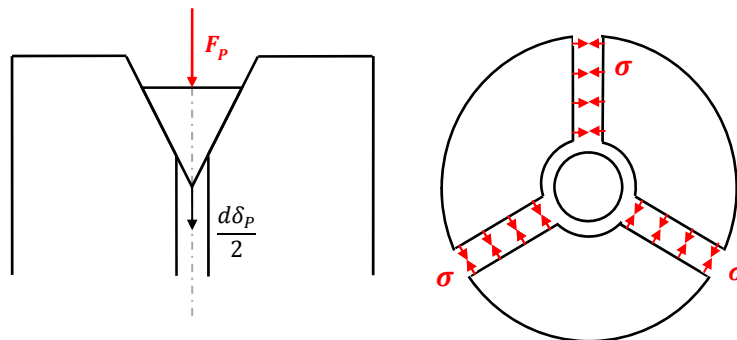


Figure 7.1 Barcelona test specimen after cracking (frontal and top view).

7.3.2. Formulation to estimate the stress (σ)

All deductions are performed considering a cylindrical coordinate system with the longitudinal axis coinciding with the axis of the Barcelona test sample. Furthermore, only half of the sample is analysed in order to simplify the visualization of the phenomenon.

The cracking surface of the conical wedge is determined by the failure angle of the material (β), which in turn depends of the interlocking effect between the aggregates and

the fibres crossing the contact surface. After the cracking, the force applied by the metallic plate (F_P) generates at the surface of the conical wedge a friction force (F_{fr}) and a normal force (F_N), as shown in Figure 7.2a. To simplify the 2D representation, F_{fr} and F_N are positioned at one side even though in reality they are distributed all around surface.

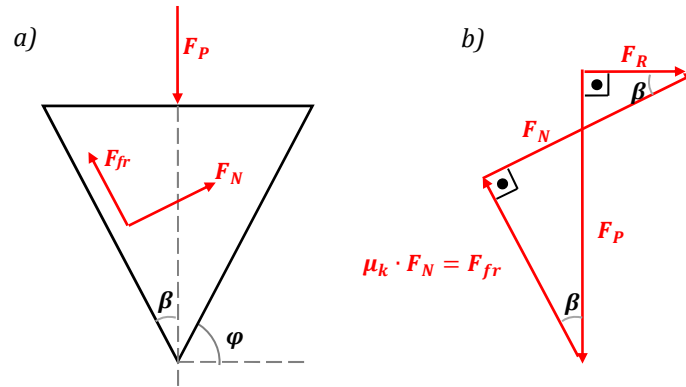


Figure 7.2 Detail of a) interplay of forces and b) balance of forces at the conical wedge.

Figure 7.2b shows the balance of forces acting. Notice that the force F_P is completely balanced by the vertical components of F_{fr} and F_N . However, a horizontal resulting radial force named F_R appears. Such force is not out of balance since it is distributed all around the lateral surface pointing towards the center of the conical wedge, thus cancelling itself.

The force F_{fr} may be represented according with equation (7.1) as the product of a kinetic friction coefficient (μ_k) and the normal force (F_N). It is important to remark that the kinetic friction coefficient should be used in this case since the conical wedge is constantly moving during the test. By applying equation (7.1) and simple trigonometry in Figure 7.2b, equations (7.2) and (7.3) may be deduced to estimate F_P and F_R , respectively.

$$F_{fr} = \mu_k \cdot F_N \quad (7.1)$$

$$F_P = F_N \cdot \text{sen } \beta + F_{fr} \cdot \text{cos } \beta = F_N \cdot (\text{sen } \beta + \mu_k \cdot \text{cos } \beta) \quad (7.2)$$

$$F_R = F_N \cdot \text{cos } \beta + F_{fr} \cdot \text{sen } \beta = F_N \cdot (\text{cos } \beta - \mu_k \cdot \text{sen } \beta) \quad (7.3)$$

After combining equations (7.2) and (7.3), equation (7.4) is obtained to estimate F_R depending on the value of F_P .

$$F_R = F_P \cdot \frac{\text{cos } \beta - \mu_k \cdot \text{sen } \beta}{\text{sen } \beta + \mu_k \cdot \text{cos } \beta} \quad (7.4)$$

By the principle of action and reaction, the forces applied to the conical wedge should also be applied with the same magnitude and opposite direction to the rest of the specimen. This is represented in Figure 7.3 along with the balance of forces. Again a

resulting radial force appears with a magnitude that could be estimated through equation (7.4). However, due to the presence of radial cracks, in this case F_R must be generated by the contribution of the fibres.

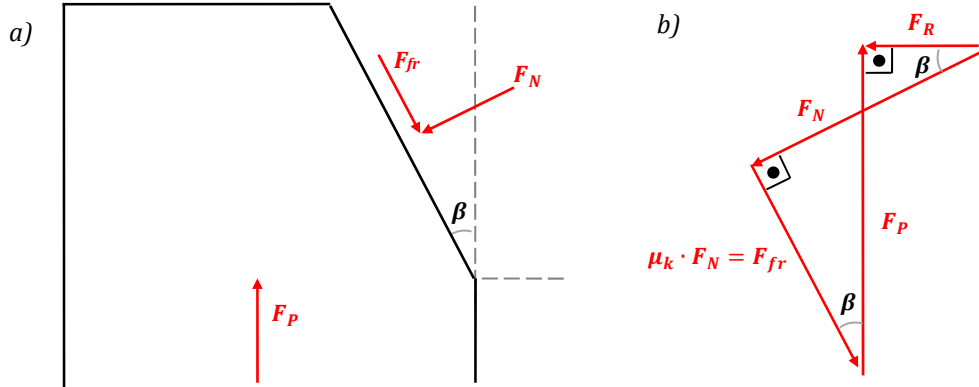


Figure 7.3 Detail of a) interplay of forces and b) balance of forces at the conical wedge.

This contribution is estimated using the infinitesimal slice from Figure 7.4. This slice receives a normal stress that balances the infinitesimal radial force dF_r . In order to simplify the deduction it is assumed that an average normal stress (σ) is uniformly distributed over the whole area of the cracked radial surface (A). Consequently, the resulting force acting at the cracks must equal $\sigma \cdot A$ (see Figure 7.4c).

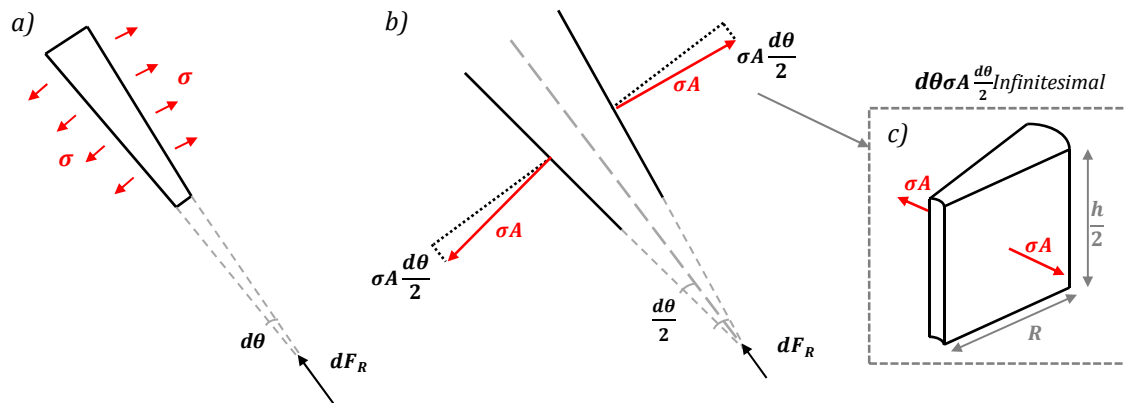


Figure 7.4 Infinitesimal slice of a concrete segment.

In this context, the equilibrium of forces in the infinitesimal slice may be represented through equation (7.5), which considers that for small values $\sin d\theta \approx d\theta$. The total value of F_R in cylindrical coordinates may be obtained by integrating equation (7.5) around the complete circumferential angular section, leading to equation (7.6).

$$dF_R = 2 \cdot \sigma \cdot A \cdot \frac{d\theta}{2} = \sigma \cdot A \cdot d\theta \tag{7.5}$$

$$F_R = \int_0^{2\pi} dF_R = 2 \cdot \pi \cdot \sigma \cdot A \tag{7.6}$$

Substituting equation 4.2 in 4.6 gives equation 4.7, which allows the estimation of the tensile stress (σ) resisted by the FRC depending of the load applied by the press (F_p). In this case, the area of the cracked radial surface (A) should be obtained in equation (4.8) as the area of the sectional cut of one quarter of the specimen subtracted by the sectional area of half of one conical wedge, which is not part of the cracked surface.

$$\sigma = \frac{F_p}{2 \cdot \pi \cdot A} \cdot \frac{\cos \beta - \mu_k \cdot \sin \beta}{\sin \beta + \mu_k \cdot \cos \beta} \quad (7.7)$$

$$A = \frac{d \cdot h}{4} - \frac{d'^2}{4 \cdot \tan \beta} \quad (7.8)$$

7.3.3. Formulation to estimate the strain (ε)

During the test, the specimen is divided in a number of segments that equals the total number n of cracks formed. In order to simplify the deduction it is assumed that all concrete segments have the same size with an internal angle $2\pi/n$. When the kinematic mechanism starts, each conical wedge slide $d\delta_p/2$ into the specimen leading to the lateral displacement ($d\delta_L$) of the concrete segments, which is depicted in Figure 7.5a.

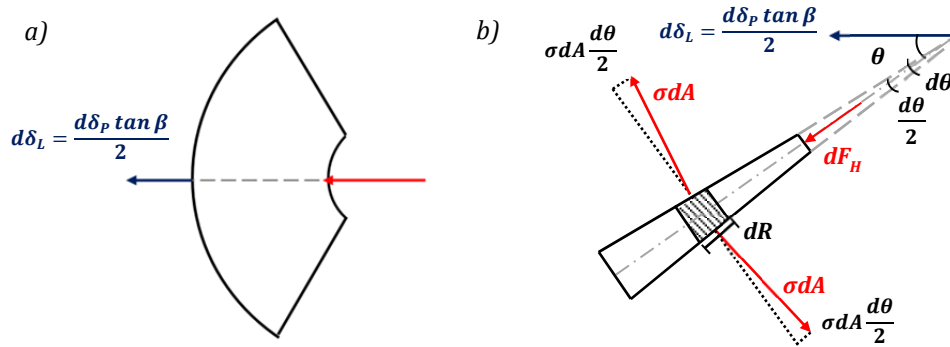


Figure 7.5 a) Lateral displacement of concrete segment and b) infinitesimal section of segment.

Both displacements are related with the angle β of the conical wedge according to equation (7.9). Consider an infinitesimal element in a slice of the concrete segment (see Figure 7.5b) with a lateral area dA that equals $dR \cdot dh$. The differential work ($d\tau$) done by the tensile stress in this element may be expressed as shown in equation (7.10). Notice that the lateral displacement occurs with the same direction and magnitude in all infinitesimal elements since it may be assumed that the concrete segments move as independent bodies.

$$d\delta_L = \frac{d\delta_p}{2} \tan \beta \quad (7.9)$$

$$d\tau = \left(2\sigma dA \frac{d\theta}{2} \right) d\delta_L \cos \theta = \sigma dh dR \left(\frac{d\delta_p}{2} \tan \beta \right) \cos \theta d\theta \quad (7.10)$$

In this context, the work produced at each segment may be calculated through the sum of $d\tau$ for all infinitesimal elements included in the segment. This is equivalent to a triple integration of $d\tau$ in the interval $(-\pi/n, \pi/n)$, for a radius ranging from 0 to the radius of the specimen (R) and for a height varying from 0 to half the height of the specimen ($h/2$), as shown in equation (7.11). The latter may be multiplied by the number of segments (n) to obtain the total work of the specimen, which is shown in equation (7.12).

$$\tau_n = \int_0^{h/2} \int_0^R \int_{-\pi/n}^{\pi/n} d\tau = \sigma \frac{h}{2} R d\delta_p \tan \beta \sin\left(\frac{\pi}{n}\right) \quad (7.11)$$

$$\tau = n \cdot \tau_n = n \cdot \sigma \cdot \frac{h}{2} \cdot R \cdot d\delta_p \cdot \tan \beta \cdot \sin\left(\frac{\pi}{n}\right) \quad (7.12)$$

Suppose now an equivalent specimen subjected to the same kinematic mechanism but that was not allowed to have radial cracks. In this case, the lateral displacement δ_L experienced would be caused by a circumferential deformation due to the tensile stresses (Figure 7.6).

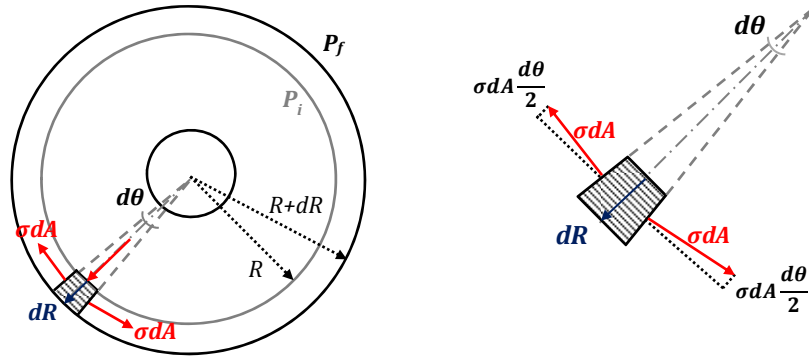


Figure 7.6 Circumferential deformation of the specimen.

The circumferential deformation may be written according with equation (7.13). The latter is the used in equation to estimate the work done by the tensile stress in an infinitesimal element with a lateral area dA .

$$\varepsilon = \frac{dR}{R} \quad (7.13)$$

$$d\tau = 2 \cdot \sigma \cdot dA \cdot \frac{d\theta}{2} \cdot dR = \sigma \cdot dA \cdot d\theta \cdot (R \cdot \varepsilon) \quad (7.14)$$

Following the same procedure described previously, the total work of the specimen is estimated through the triple integration of $d\tau$ in the interval $(-\pi, \pi)$, for a radius ranging from 0 to the radius of the specimen (R) and for a height varying from 0 to half the height of the specimen ($h/2$), as shown in equation (7.15).

$$\tau = \int_0^{h/2} \int_0^R \int_{-\pi}^{\pi} d\tau = \frac{2\pi\sigma h \varepsilon R^2}{4} = \pi\sigma \frac{h}{2} \varepsilon R^2 \quad (7.15)$$

Assuming that the circumferential deformation of the specimen is equivalent to the lateral displacement of the concrete section, the increments of work in (7.11) and (7.12) may be considered equal, as shown in expression (7.16) and in (7.17).

$$n \sigma \frac{h}{2} R d\delta_p \tan \beta \sin\left(\frac{\pi}{n}\right) = \pi \sigma \frac{h}{2} \varepsilon R^2 \quad (7.16)$$

$$n d\delta_p \tan \beta \sin\left(\frac{\pi}{n}\right) = \pi \varepsilon R \quad (7.17)$$

Finally, the strain in the specimen may be written as in expression (7.18) or in terms of increments as in equation (7.19).

$$\varepsilon = \frac{n\delta_p}{\pi R} \tan \beta \sin\left(\frac{\pi}{n}\right) \quad (7.18)$$

$$\Delta\varepsilon = \frac{n\Delta\delta_p}{\pi R} \tan \beta \sin\left(\frac{\pi}{n}\right) \quad (7.19)$$

7.3.4. Values of failure angle (β) and friction coefficient (μ)

In the formulation proposed in the previous section, the values of the failure angle (β) and the kinetic friction coefficient (μ_k) are required. The value of β is usually defined in the literature by means of the internal friction angle of the material (φ) since it determines the cracking surface of the conical wedge. A review on the different values for φ proposed by several authors during the past 50 years may be found in Carmona *et al.* (2012).

The actual length of the conical wedge was measured in the experiences conducted at the Laboratory of Structure Technology Luis Agulló. Figure 7.7a shows the procedure of opening the specimen, which was performed avoiding any damage of the conical wedge.

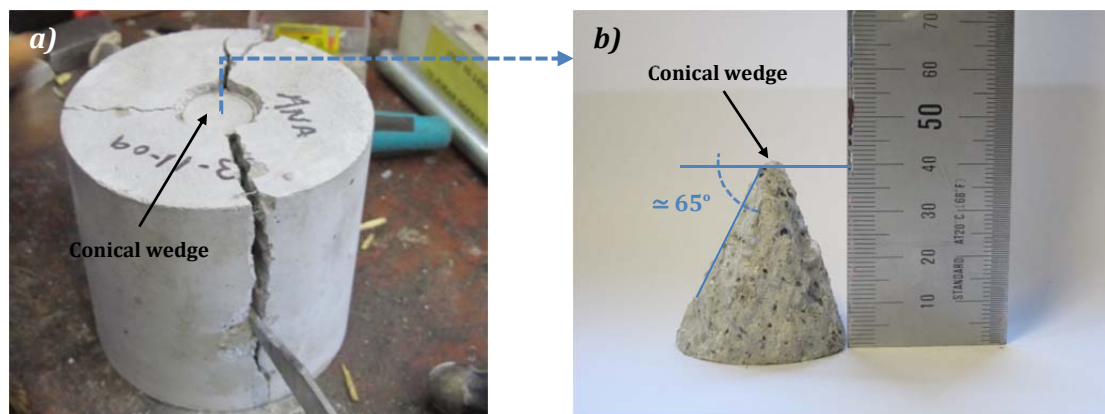


Figure 7.7 a) Opening of the specimen and b) measurements of the length of the conical wedge.

After the conical wedge was separated from the concrete segments, its length was measured as observed in Figure 7.7b. The measurements revealed that the length of the

conical wedge (l) is approximately 40 mm. Taking into account the dimensions of the steel punch ($d' = 37.5$ mm) and using expression (7.20), the internal friction angle is 65° . Hence, the values are $\varphi=65^\circ$ and $\beta=25^\circ$.

$$l = \frac{d'}{2} \tan \varphi \quad (7.20)$$

Regarding the friction coefficient, the values presented in the literature usually cover the static friction coefficient of concrete (μ_s). Nevertheless, very limited information is available for the kinetic friction coefficient (μ_k). It is known that the value of μ_k for the same surface tends to be smaller than μ_s . This should be especially true for two cracked concrete surfaces subjected to considerable relative displacement, such as observed in the Barcelona test. As the surfaces start moving, the roughness is smoothened due to the cracking of their irregularities, thus reducing the values of the friction coefficient. Furthermore, the small cracked parts should remain between the two surfaces, leading to an additional reduction. Figure 7.7b confirms that a rather smooth conical wedge is observed after the test.

In the absence of reliable values of μ_k , the μ_s proposed in the MC2010 and summarized in Table 7.3 is used as a reference. Considering the aspect of the conical wedge after the test, it is assumed that the μ_s should be around 0.7 or 0.8, characteristic of rough surfaces. These values should be reduced to take into account the differences between μ_k and μ_s as well as the mechanism observed during the test. Then, a μ_k equal to 0.5 is considered a reasonable initial approximation. It is important to remark that more studies are necessary to characterize μ_k and the variables affecting this parameter.

Table 7.3 Friction coefficient for plain concrete according to the MC2010.

Interface roughness	Friction coefficient μ [-]
Smooth interface	0.5 - 0.7
Rough interface	0.7 - 1.0
Very rough interface	1.0 - 1.4

7.4. PREDICTION OF THE TENSILE STRENGTH

The values of tensile strength (f_{ct}) estimated by the different closed-form expressions presented are compared by using experimental data from the study by Guàrdia (2008). This study entailed the testing of several series of SCSFRC and high-performance self-compacting steel fibre reinforced concrete (HPSCSFRC). For this analysis, two series were chosen: A40 that corresponds to a SCSFRC with 40 kg/m^3 of fibres and B40 that is a HPSCSFRC with also 40 kg/m^3 of fibres. Both series used Dramix® RC80/60BP, which present circular cross-section and hooked ends gathered into bundles by water-soluble glue. The main properties from series A40 and B40 are presented in Table 7.4. Further information regarding the experimental program may be found in Guàrdia (2008).

Table 7.4 Main data from the study of Guàrdia (2008).

	Compression		Modulus of elasticity		Slump flow	
	f_{cm} [MPa]	CV [%]	E_{cm} [MPa]	CV [%]	D_f [mm]	T_{50} [s]
A40	45.7	0.7	32300.0	2.5	745.0	1.7
B40	76.1	2.2	36300.0	1.1	720.0	3.2

Five closed-formed expressions will be analysed: Chen (1970), Chen and Yuan (1980), Bortolotti (1988), Molins *et al.* (2007) and the expression herein proposed (referred as Blanco). The main parameters of these expressions are presented in Table 7.5.

Table 7.5 Main parameters defining the expressions for tensile strength.

Expression	Parameters	A40	B40
Common parameters	h [mm]	150.00	150.00
	d [mm]	150.00	150.00
	d' [mm]	37.50	37.50
Bortolotti	φ [rad]	1.00	1.08
	β [rad]	0.29	0.25
Blanco	β [rad]	0.436	0.436
	μ_k [-]	0.50	0.50

The common geometrical parameters in Table 7.5 are associated to the size of the specimens, in this case with a diameter and a height equal to 150 mm and a diameter of the steel punch of 37.5 mm. Bortolotti deduces the internal friction angle (φ) from the cubic compressive strength by means of an expression that is a function of the compressive-tensile strengths ratio. To obtain the values in Table 7.5, the average compressive strength (f_{cm}) of each series was considered (see Table 7.4). The determination of the failure angle (β) is immediate once φ is known. According to the author, experimental measurements should not be considered due to their dispersion.

For the expression herein proposed, the parameters β and μ are defined according to what was exposed in the section since no information is provided in Guàrdia (2008) regarding the conical wedge. Hence, $\beta=0.438$ rad, corresponding to a cone length of 40 mm, and $\mu_k=0.5$ are assumed.

In Table 7.6, the predicted values of f_t are presented together the maximum load registered during the Barcelona test. From the expressions studied in this section, only the expressions by Chen (1970), Chen and Yuan (1980) and Molins *et al.* (2007) are dependent just from geometric parameters. Other parameters are implicitly assumed during the deduction. On the contrary, Bortolotti (1988) introduces the friction angle (φ) and failure angle (β) as variables depending on the type of concrete. The new formulation herein proposed also introduces two variables: the failure angle (β) and the kinetic friction coefficient (μ_k). Although recommended values are suggested for β and μ_k , other values may be assumed based on experimental results.

Table 7.6 Comparison of the tensile strength estimated by the expressions in the literature.

Specimen	Max load [kN]	Tensile strength [MPa]				
		Chen (1970)	Chen (1980)	Bortolotti (1988)	Molins (2007)	Blanco (2013)
A40_1	155.59	3.77	2.83	4.93	1.96	3.73
A40_2	144.46	3.50	2.62	4.57	1.82	3.46
A40_3	151.21	3.66	2.75	4.79	1.90	3.63
A40_4	139.59	3.38	2.53	4.42	1.76	3.35
A40_5	162.5	3.93	2.95	5.15	2.04	3.90
A40_6	156.23	3.78	2.84	4.95	1.96	3.75
A40_7	161.29	3.90	2.93	5.11	2.03	3.87
A40_8	165.21	4.00	3.00	5.23	2.08	3.96
A40_9	157.32	3.81	2.86	4.98	1.98	3.77
A40_10	158.94	3.85	2.89	5.03	2.00	3.81
B40_1	160.02	3.87	2.91	5.17	2.01	3.84
B40_2	134.87	3.27	2.45	4.36	1.70	3.23
B40_3	146.51	3.55	2.66	4.73	1.84	3.51
B40_4	148.19	3.59	2.69	4.79	1.86	3.55
B40_5	178.56	4.32	3.24	5.77	2.25	4.28
B40_6	191.05	4.63	3.47	6.17	2.40	4.58

The results indicate that the highest values of f_{ct} are provided by the formulation by Bortolotti; whereas the values obtained with the expression by Molins *et al.* (2007) are the lowest. The results also reveal that f_{ct} estimated with the Bortolotti formulation is 152% and 157% higher than the value provided by the Molins formulation, for A40 and B40, respectively. This is a significant difference when trying to predict the f_{ct} of concrete. The results from the new formulation are almost identical to those obtained with the formulation of Chen (1970) and approximately 25% smaller than those from Bortolotti.

Even though the new formulation was deduced for the post-cracking response of FRC, its results are very similar to those obtained with formulations deduced by other authors to predict the maximum tensile strength of plain concrete. Therefore, to simplify the number of equations needed to characterize the complete behaviour of FRC, the new formulation proposed is considered for the prediction of both the pre-cracked and the post-cracked tensile strength.

7.5. SIMPLIFIED MODEL

With the equations deduced in previous section it is possible to estimate the complete σ - ε based on the Barcelona test. However, the current European design codes and guidelines for FRC include simplified constitutive models. A simplified constitutive model is characterized by continuous non-differentiable σ - ε diagrams that may take the shape of a rectangular, bilinear, trilinear or even multilinear diagram, as indicated in

Chapter 2 (see Table 2.1). This type of diagram is easier to implement in the design tools and to be adopted by professionals. Hence, the interest of simplifying the formulation presented in section 7.3. The simplification herein proposed takes the shape of a multilinear σ - ε diagram, as indicated in Figure 7.8.

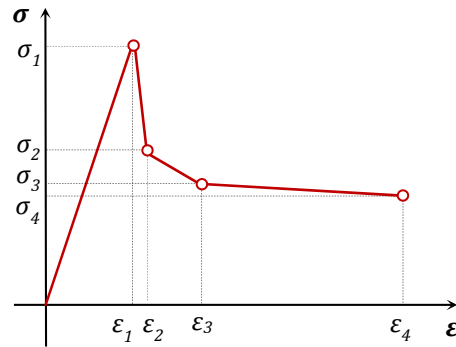


Figure 7.8 Simplified σ - ε diagram.

The first stage of the curve corresponds to the linear-elastic stage prior to cracking, where the concrete matrix bears the tensile stresses. The tensile strength (σ_1) and its corresponding strain (ε_1) can be calculated as indicated in expressions (7.21) and (7.22).

$$\sigma_1 = \frac{F_{Pmax}}{2 \cdot \pi \cdot A} \cdot \frac{\cos \beta - \mu_k \cdot \sin \beta}{\sin \beta + \mu_k \cdot \cos \beta} \quad (7.21)$$

$$\varepsilon_1 = \frac{\sigma_1}{E_{cm}} \quad (7.22)$$

The value of σ_1 can be easily determined by knowing the maximum load registered during the test (F_{Pmax}) and the values of the failure angle (β) and the kinetic friction coefficient (μ_k). When the value of σ_1 is known, the strain ε_1 may be obtained using the modulus of elasticity (E_{cm}).

Once the tensile strength of the concrete matrix is reached, cracking occurs and there is a drop of stress until the fibres start their bridging capacity, characterized by σ_2 and ε_2 . The value of ε_2 is established following the philosophy in most European codes and guidelines which define this parameter as in equation (7.23).

$$\varepsilon_2 = \varepsilon_1 + 0.1\%_0 \quad (7.23)$$

In order to determine the value of σ_2 , the load associated with the value of ε_2 must be known. For that, the displacement equivalent to the strain ε_2 must be calculated isolating $\Delta\delta_p$ in equation (7.19), which gives equation (7.24). If a number of cracks equal 3, a β equal to 0.438 rad and a $\Delta\varepsilon$ equal to 0.1 ‰ ($\varepsilon_2 - \varepsilon_1$ from equation (7.23)) are assumed, the value 0.02 mm of displacement equivalent to the strain ε_2 is obtained. Notice that the 0.02 mm is measured from the displacement corresponding to F_{Pmax} onwards.

$$\Delta\delta_p = \frac{\Delta\varepsilon\pi R}{n \tan\beta \sin\left(\frac{\pi}{n}\right)} = \frac{0.0001 \cdot \pi \cdot 75 \text{ mm}}{3 \cdot \tan(0.436) \cdot \sin\left(\frac{\pi}{3}\right)} = 0.02 \text{ mm} \quad (7.24)$$

The stress of σ_2 may be determined as shown in (7.25) for the value of load corresponding to a displacement of 0.02 mm ($F_{P0.02mm}$).

$$\sigma_2 = \frac{F_{P0.02mm}}{2 \cdot \pi \cdot A} \cdot \frac{\cos \beta - \mu_k \cdot \text{sen } \beta}{\text{sen } \beta + \mu_k \cdot \cos \beta} \quad (7.25)$$

The same procedure was used to estimate the values of σ_3 related with the strain ε_3 . After analysing several experimental results, a ε_3 equal to 4.0‰ was chosen in order to obtain a good fit with the complete constitutive curve. This corresponds to a $\Delta\varepsilon$ of 3.9‰ ($\varepsilon_3 - \varepsilon_1 = 4.0‰ - 0.1‰$), assuming that for typical concrete ε_1 should be close to 0.1‰. Substituting this value in equation (7.24) gives a relative displacement $\Delta\delta_p$ of approximately 0.8 mm. Therefore, the value stress σ_3 may be calculated as indicated in expression (7.26).

$$\sigma_3 = \frac{F_{P0.75mm}}{2 \cdot \pi \cdot A} \cdot \frac{\cos \beta - \mu_k \cdot \text{sen } \beta}{\text{sen } \beta + \mu_k \cdot \cos \beta} \quad (7.26)$$

The value of ε_4 is assumed as 20‰, following the tendency observed in several instruction and codes regarding the maximum strain for the constitutive curves of FRC. Considering the same assumptions as for ε_3 , the displacement associated to 20‰ estimated in equation (7.24) is approximately 3.9 mm and, therefore, the value of σ_4 may be determined as indicated in expression (7.27).

$$\sigma_4 = \frac{F_{P4.00mm}}{2 \cdot \pi \cdot A} \cdot \frac{\cos \beta - \mu_k \cdot \text{sen } \beta}{\text{sen } \beta + \mu_k \cdot \cos \beta} \quad (7.27)$$

Table 7.7 summarizes the parameters defining the simplified σ - ε diagram derived from the Barcelona test. Notice that the values stresses may be expressed as function of the load associated to a certain displacement, considering the constant (ω).

Table 7.7 Summary of the parameters defining the simplified σ - ε diagram.

Strain [‰]	Stress [MPa]
$\varepsilon_1 = \frac{\sigma_1}{E_{cm}}$	$\sigma_1 = \frac{F_{Pmax}}{2 \cdot \pi \cdot A} \cdot \frac{\cos \beta - \mu_k \cdot \text{sen } \beta}{\text{sen } \beta + \mu_k \cdot \cos \beta} = \omega F_{Pmax}$
$\varepsilon_2 = \varepsilon_1 + 0.1‰$	$\sigma_2 = \frac{F_{P0.02mm}}{2 \cdot \pi \cdot A} \cdot \frac{\cos \beta - \mu_k \cdot \text{sen } \beta}{\text{sen } \beta + \mu_k \cdot \cos \beta} = \omega F_{p0.02mm}$
$\varepsilon_3 = 4.0‰$	$\sigma_3 = \frac{F_{P0.75mm}}{2 \cdot \pi \cdot A} \cdot \frac{\cos \beta - \mu_k \cdot \text{sen } \beta}{\text{sen } \beta + \mu_k \cdot \cos \beta} = \omega F_{p0.8mm}$
$\varepsilon_4 = 20‰$	$\sigma_4 = \frac{F_{P4.00mm}}{2 \cdot \pi \cdot A} \cdot \frac{\cos \beta - \mu_k \cdot \text{sen } \beta}{\text{sen } \beta + \mu_k \cdot \cos \beta} = \omega F_{p3.9mm}$

7.6. EXPERIMENTAL PROGRAM

An experimental program involving Barcelona tests and 3-point bending tests of SFRC specimens with two different fibre contents was conducted. The results of both tests are compared in terms of scatter. In addition to the two series of SFRC corresponding to the experimental program herein presented, the main data of two other series of SFRC and two series of PFRC included in Monsó (2011) and Pujadas (2013), respectively, are presented.

The results of these studies, together with the results of the present experimental program, are used in subsequent sections to validate the formulation proposed (see section 7.8) and to compare the new formulation with the constitutive models from European codes and guidelines based on flexural tests (see section 7.9). Thus, a total of six series of FRC, including three types of fibres and six different fibre contents, were considered in the analysis.

7.6.1. Specimens

The specimens of the Barcelona test and the bending test are listed in Table 7.8 and were produced according to UNE 83515:2010 (AENOR 2010) and EN 14651:2005 (CEN 2005), respectively. According to the notation adopted, the letters A, B and C identify a different type of fibre and the number following the letter corresponds to the fibre content (in kg/m³). The letters B and C, appended at the end, differentiate the cylindrical specimens from the beams, followed by a number identifying the specimens of the series.

Table 7.8 Series of FRC beams and cylinders.

Series	Reference	Cylinders (C)	Beams (B)	Notation
A40	Blanco 2013	5	6	A40_C1 or A40_B2
A60	Blanco 2013	2	1	A60_C2 or A60_B3
B30	Monsó 2011	10	8	B30_C3 or B30_B4
B50	Monsó 2011	10	10	B50_C4 or B50_B5
C5	Pujadas 2013	6	3	C5_C5 or C5_B6
C7	Pujadas 2013	5	3	C7_C6 or C7_B1

7.6.2. Materials and concrete mix

The concrete from series A40 and A60 was produced in a 750 litres vertical axis mixer with the following mixing process: initially the dried components were mixed during one minute. Afterwards, the water was added and the paste was mixed during two minutes before the superplasticizer was included. Finally, the steel fibres were included and the concrete was mixed for two additional minutes. The total time of production ranged approximately from five to seven minutes. Notice that the mixing procedure for the others series may be found in Monsó (2011) and Pujadas (2013).

The details of the concrete mix for series A40 and A60 are presented in Table 7.9. As indicated in the notation presented in Table 7.8, the fibre contents used for series B and C are: 30 kg/m³ and 50 kg/m³ in the case of the former and 5 kg/m³, 7 kg/m³ in the case of the latter. These values represent in terms of percentage of the total volume: 0.38% and 0.64% for the SF of series B and 0.55 % and 0.77 % for the PF of series C. The fibres contents of series A represent 0.51% (40 kg/m³) and 0.76% (60 kg/m³) in volume.

Table 7.9 Concrete mix.

Materials	Characteristics	Quantities [kg/m ³]	
		A40	A60
Gravel (6/15 mm)	Granite	520	520
Gravel (2.5/6 mm)	Granite	400	400
Sand (0/3 mm)	Granite	510	500
Cement	CEM I 52,5 R	350	400
Filler	Marble dust	300	260
Water	-	178	170
Superplasticizer	Adva® Flow 400	12	12
Fibres	-	40	60

The steel fibres used in A40 and A60 were Dramix® RC80/50BN with circular cross-section and hooked ends. These fibres are made of low carbon steel and are gathered into bundles by water-soluble glue. Additional characteristics of this fibre are summarized in Table 7.10. The main characteristics of the SF used in the series B30 and B50 and the PF used in series C5 and C7 are also included in Table 7.10. Further detail on these fibres may be found in in Monsó (2011) and Pujadas (2013), respectively.

Table 7.10 Characteristics of the fibres (provided by the manufacturer).

Characteristic	Unit	A	B	C
Length (L)	[mm]	50	50	48
Diameter (d)	[mm]	0.62	1.05	-
Aspect ratio (L/d)	[-]	83	48	-
Tensile strength (f_y)	[MPa]	1270	1115	550
Modulus of elasticity (E)	[GPa]	210	210	10
Number of fibres per kg	[-]	8100	2800	35000

The specimens were vibrated externally by means of a vibrating table at 3000 rev/min during 10 seconds approximately (see Figure 7.9). Within 24 hours of casting, they were removed from the moulds and were moist cured under a plastic sheet during 7 days approximately. Subsequently, they were transported from the ESCOFET S.A facilities to the Laboratory of Structure Technology Luis Agulló at the UPC, where they were stored in a curing room at 20±2 Celsius degrees and 95% of relative humidity until the performance of the tests, at the age of 28 days.

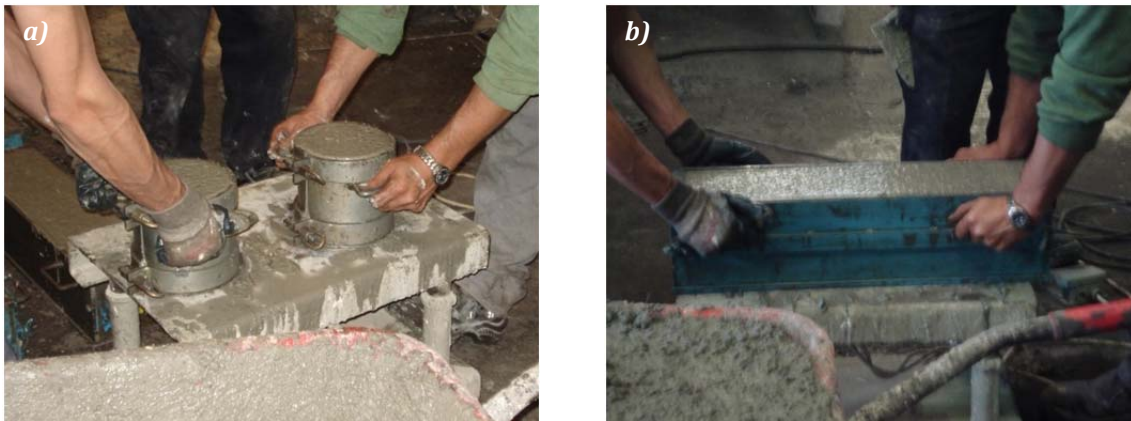


Figure 7.9 Vibration of the specimens: a) cylinders and c) beams.

7.6.3. Results

The average results at 28 days of the compressive strength (f_{cm}) and the modulus of elasticity (E_{cm}) of each series are presented in Table 7.11 as well as their corresponding coefficients of variation (CV). The compression test and the modulus of elasticity test were performed according to UNE 83507:2004 (AENOR 2004b) and UNE 83316:1996 (AENOR 1996), respectively. In addition to series A40 and A60, the results for series B30, B50, C5 and C7 are also included in Table 7.11.

Table 7.11 Compressive strength and modulus of elasticity at 28 days.

Series	Compressive strength		Modulus of elasticity	
	f_{cm} [MPa]	CV [%]	E_{cm} [GPa]	CV [%]
A40	46.73	0.77	29029	0.96
A60	54.30	1.51	31597	1.10
B30	44.85	1.8	30200	-
B50	43.97	4.8	30000	-
C5	52.15	1.58	31312	0.96
C7	54.64	0.83	32095	2.14

It should be remarked that the study by Monsó (2011) does not provide any results regarding the modulus of elasticity and, therefore, the values were estimated from the average compressive strength according to the formulation provided by the EHE-08.

The main results of the Barcelona tests and the flexural tests performed at 28 days are presented in Table 7.12. For the Barcelona test, the results are the average values of the tensile strength (f_{ct}) and the residual tensile strengths (f_{ctR2} , f_{ctR4} and f_{ctR6}) corresponding to the TCOD of 2 mm, 4 mm and 6 mm, respectively. The results of the flexural test correspond to the average values of the limit of proportionality (f_l) and the residual flexural tensile strengths f_{R1} , f_{R2} , f_{R3} and f_{R4} associated to crack mouth opening CMOD of 0.05 mm, 0.50 mm, 1.50 mm, 2.50 mm and 3.50 mm, respectively.

Table 7.12 Main results of the Barcelona test and the flexural test for series A40 and A60.

Test	Parameters	A40		A60	
		Average [MPa]	CV [%]	Average [MPa]	CV [%]
Barcelona test	f_{ct}	3.80	4.29	4.50	1.14
	$f_{ctR,2}$	1.84	21.36	2.65	9.18
	$f_{ctR,4}$	1.43	22.14	1.79	5.07
	$f_{ctR,6}$	1.08	29.80	1.38	3.18
Flexural test	f_L	5.29	2.23	3.72	-
	f_{R1}	6.13	13.71	6.40	-
	f_{R2}	7.04	15.77	6.12	-
	f_{R3}	7.08	15.05	6.24	-
	f_{R4}	6.62	12.08	6.47	-

In general, the scatter of the Barcelona test is lower than that of the flexural test since the failure plane are bigger in the case of the former. This was observed experimentally in several studies (Guàrdia 2008; Molins *et al.* 2009; Blanco *et al.* 2012). In case of series A40, the coefficients of variation for the Barcelona test are over the average expected for the test. On the other hand, the results of series A60 present low scatter. Regarding the flexural test, the coefficients of variation for series A40 are lower than some of the reported by other authors (Parmentier *et al.* 2008 and Molins *et al.* 2009). The curves obtained from the Barcelona test and the flexural test for series A40 are presented in Figure 7.10.

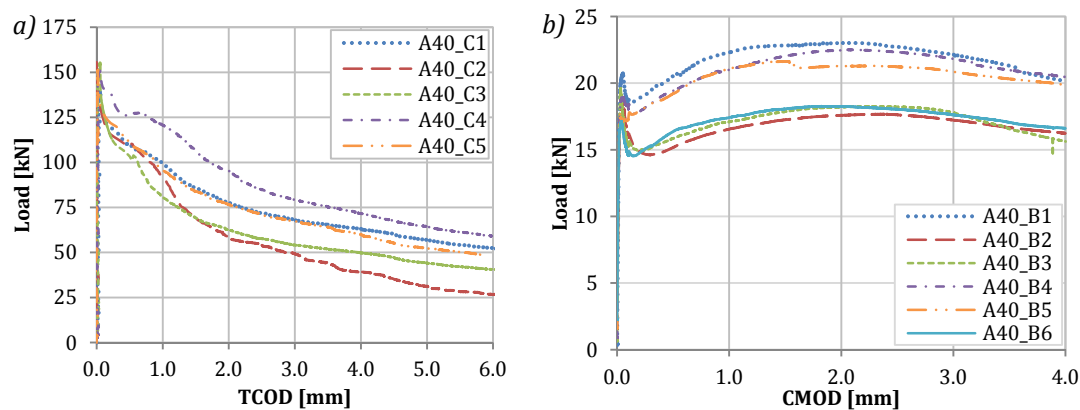


Figure 7.10 Results of series A40: a) Barcelona test and b) flexural test (EN14651:2005).

7.7. FIT BETWEEN SIMPLIFIED AND COMPLETE MODELS

Figure 7.11 shows the comparison between the simplified and the complete σ - ε models deduced in this study. The resulting curves for one specimen of series A40, A60, B30, B50, C5 and C7. The curves reveal a good fit and the validity for steel and plastic fibres as well as for different fibre contents of the simplified model which represents with good accuracy the shape of the curve.

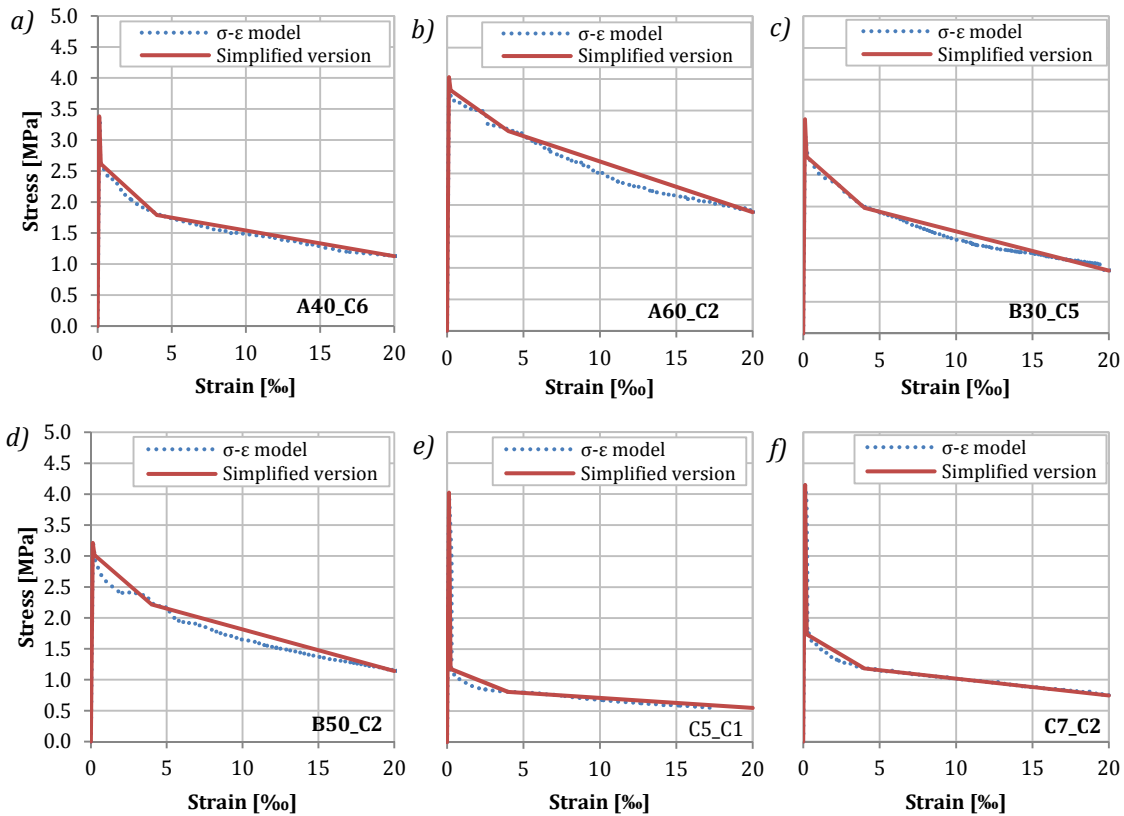


Figure 7.11 Comparison of the σ - ϵ model with the simplified version for a) A40_C6, b) A60_C2, c) B30_C5, d) B50_C2, e) C5_C1 and f) C7_C2.

7.8. NUMERICAL VALIDATION

In order to validate the formulation, the Barcelona tests performed in the experimental program are modelled with finite element software. For that, the tensile response of the FRC is defined with the σ - ϵ model resulting from the simplified formulation proposed in this chapter. The numerical results obtained in the finite element software are compared to the experimental ones, thus providing valuable information about the accuracy of the formulation proposed.

7.8.1. Model type

The finite element software DIANA 9.4 was chosen to model the Barcelona test over other finite element software given its extensive material library and analysis capabilities. The setup of the Barcelona test required a 3D analysis, using solid and interface elements to simulate the behaviour of the specimen during the test.

The FRC was meshed with a six-node isoparametric solid wedge element (TP18L) based on linear area interpolation in the triangular domain and a linear isoparametric interpolation in the orthogonal direction. By default DIANA applies a 1-point integration

scheme in the triangular domain and a 2-point integration scheme in the orthogonal direction to the triangular surfaces. The interface was meshed with a plane quadrilateral solid (Q24IF) based on a linear interpolation. In this case, DIANA applies a 3x3 Newton-Cotes integration scheme.

7.8.2. Geometry and boundary conditions

Given the symmetry of the test, only half of the specimen was modelled to favour the efficiency of the analysis (reduction of computation time) and a more refined mesh discretization (see Figures 7.12a, 7.12b and 7.12c). Furthermore, the steel punch used in the Barcelona test to transmit the load to the specimen was not modelled. Instead, the load was directly applied in an equivalent area on the top surface of the FRC specimen.

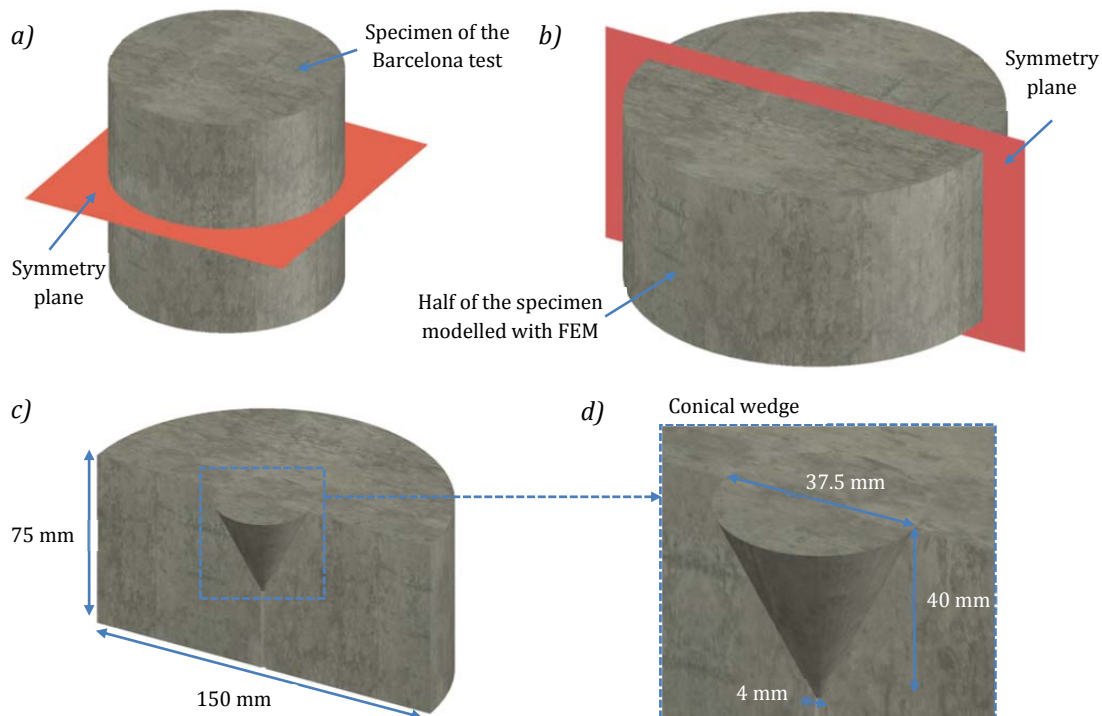


Figure.12 a) Specimen of the Barcelona test, b) half of the specimen modelled with FEM, c) definition of the conical wedge in the model and d) detail of the conical wedge.

The fracture process observed during the test leads to a change of the resistant mechanism. This change is difficult to reproduce with a single mesh for all the volume since it entails localized large displacements at certain locations (particularly in the formation of the cone) that may cause divergences and a different response from the real one. For this reason, the specimen was not addressed as a single volume but as the summation of the cone and the rest of the specimen. Likewise, to avoid concentrated loads in the vertex, the cone was approximated as an inverted truncated cone with a top diameter equal to that of the steel punch; a bottom diameter of 4 mm and a height of 40

mm (see Figure.12d). An interface element was defined between the lateral surface of the cone and the the specimen to allow the displacement of the cone and the cracking.

Symmetry conditions were imposed by restraining the vertical displacement of the bottom face of the half specimen. The load case consisted of a vertical displacement acting simultaneously at all nodes on the loading surface. Each load step was equivalent to a vertical displacement of 0.025 mm.

The meshes of each of the 4 parts of the specimen were radially generated so as to reduce the influence that the discretization adopted may have on the mesh and the results. This meshing strategy allowed obtaining uniform angular divisions. Two different density meshes were considered to conduct the simulation (with 1800 elements and 3600 elements approximately). Nevertheless, since both of them provided similar results, the less refined mesh was selected to reduce the computation time.

7.8.3. Material properties

A fracture energy based on total strain rotating crack model (Burguers et al. 2007) was used for the FRC of the specimens assuming the multilinear (σ - ϵ) curve in tension proposed in section 7.5 (as shown in Figure 7.13). General characteristics and the parameters of this model were established in accordance with Eurocode 2 (CEN 1992).

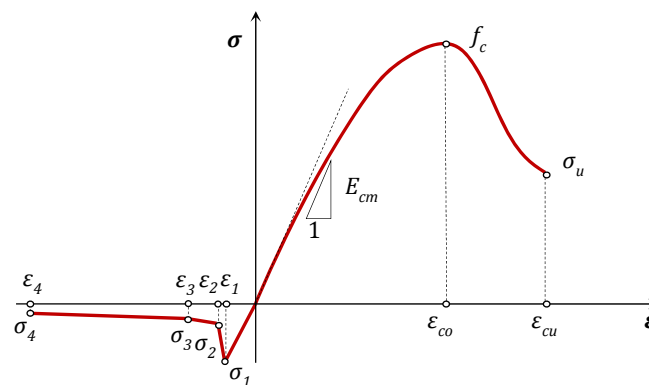


Figure 7.13 . Stress-strain (σ - ϵ) curve to model the FRC.

The interface material between the cone and the rest of the specimen is characterized by a linear normal and linear tangential stiffness and a frictional behaviour simulated using a Coulomb friction model with a brittle gapping criterion.

Table 7.13 includes a summary of the main properties of the materials. Notice that for the validation of the formulation six types of FRC were considered: four series of SFRC (A40, A60, B30 and B50) and two series of PFRC (C5 and C7). Consequently, the main properties of the FRC are classified according to series A, B and C. Despite modelling all the specimens of each series, only two specimens of each series are presented in order to avoid repetitions since the tendencies are very similar. For this reason, the values of tensile strengths and residual strengths corresponding to two specimens of each series are

presented in Table 7.13. These values were determined by considering the $\beta=0.438$ rad, $\mu_s=0.8$ and $n=3$. The properties of the interface material are common for all cases.

Table 7.13 Material properties considered in the FEM model.

Model part	Material properties	Value	Reference
Interface material	Normal stiffness [MN/m ³]	1.0·10 ⁵	
	Tangential stiffness [MN/m ³]	1.0·10 ⁵	
	Tangent friction angle [rad]	0.8	
	Tangent of dilatancy angle [rad]	0.0	
SFRC (Series A)	Average compressive strength [MPa]	46.7 / 54.3	A40 / A60
	Average modulus of elasticity [GPa]	29.0 / 31.6	A40 / A60
	Poisson ratio [-]	0.2	Eurocode 2
	Tensile strength σ_1 [MPa]	3.4 / 3.4 / 3.9 / 4.0	A40_C5 / _C6 / A60_C1 / _C2
	Residual strength σ_2 [MPa]	2.9 / 2.6 / 3.8 / 3.8	A40_C5 / _C6 / A60_C1 / _C2
	Residual strength σ_3 [MPa]	2.3 / 1.8 / 3.4 / 3.2	A40_C5 / _C6 / A60_C1 / _C2
	Residual strength σ_4 [MPa]	1.5 / 1.1 / 2.2 / 1.9	A40_C5 / _C6 / A60_C1 / _C2
	Strain ε_1 [‰]	0.1	A40_C5 / _C6 / A60_C1 / _C2
	Strain ε_2 [‰]	0.2	A40_C5 / _C6 / A60_C1 / _C2
	Strain ε_3 [‰]	4.0	A40_C5 / _C6 / A60_C1 / _C2
Strain ε_4 [‰]	20.0	A40_C5 / _C6 / A60_C1 / _C2	
SFRC (Series B)	Average compressive strength [MPa]	44.9 / 44.0	B30 / B50
	Average modulus of elasticity [GPa]	30.2 / 30.0	B30 / B50
	Poisson ratio [-]	0.2	Eurocode 2
	Tensile strength σ_1 [MPa]	3.4 / 2.9 / 3.2 / 3.3	B30_C5 / _C8 / B50_C2 / _C8
	Residual strength σ_2 [MPa]	2.8 / 2.3 / 3.0 / 2.7	B30_C5 / _C8 / B50_C2 / _C8
	Residual strength σ_3 [MPa]	2.0 / 1.9 / 2.2 / 1.7	B30_C5 / _C8 / B50_C2 / _C8
	Residual strength σ_4 [MPa]	1.0 / 1.0 / 1.1 / 1.0	B30_C5 / _C8 / B50_C2 / _C8
	Strain ε_1 [‰]	0.1	B30_C5 / _C8 / B50_C2 / _C8
	Strain ε_2 [‰]	0.2	B30_C5 / _C8 / B50_C2 / _C8
	Strain ε_3 [‰]	4.0	B30_C5 / _C8 / B50_C2 / _C8
Strain ε_4 [‰]	20.0	B30_C5 / _C8 / B50_C2 / _C8	
PFRC	Average compressive strength [MPa]	52.2 / 54.6	C5 / C7
	Average modulus of elasticity [GPa]	31.3 / 32.1	C5 / C7
	Poisson ratio [-]	0.2	Eurocode 2
	Tensile strength σ_1 [MPa]	4.0 / 3.7 / 4.1 / 3.9	C5_C2 / _C5 / C7_C2 / _C5
	Residual strength σ_2 [MPa]	1.7 / 2.1 / 1.7 / 2.1	C5_C2 / _C5 / C7_C2 / _C5
	Residual strength σ_3 [MPa]	0.9 / 1.1 / 1.2 / 1.0	C5_C2 / _C5 / C7_C2 / _C5
	Residual strength σ_4 [MPa]	0.5 / 0.7 / 0.7 / 0.8	C5_C2 / _C5 / C7_C2 / _C5
	Strain ε_1 [‰]	0.1	C5_C2 / _C5 / C7_C2 / _C5
	Strain ε_2 [‰]	0.2	C5_C2 / _C5 / C7_C2 / _C5
	Strain ε_3 [‰]	4.0	C5_C2 / _C5 / C7_C2 / _C5
Strain ε_4 [‰]	20.0	C5_C2 / _C5 / C7_C2 / _C5	

7.8.4. Results

In Figure 7.15, the experimental and the predicted curves are compared for two specimens of each series. It must be remarked that in the experimental results there is an accommodation effect between the surfaces of the piston and the specimen (due to irregularities of the surface of the specimen) that leads to larger displacements in the early stages. This effect was not observed in the simulation with the finite element software since the contact is perfect from the beginning of the test. For this reason, the maximum load of the experimental curve was moved to match the peak of the simulated curve.

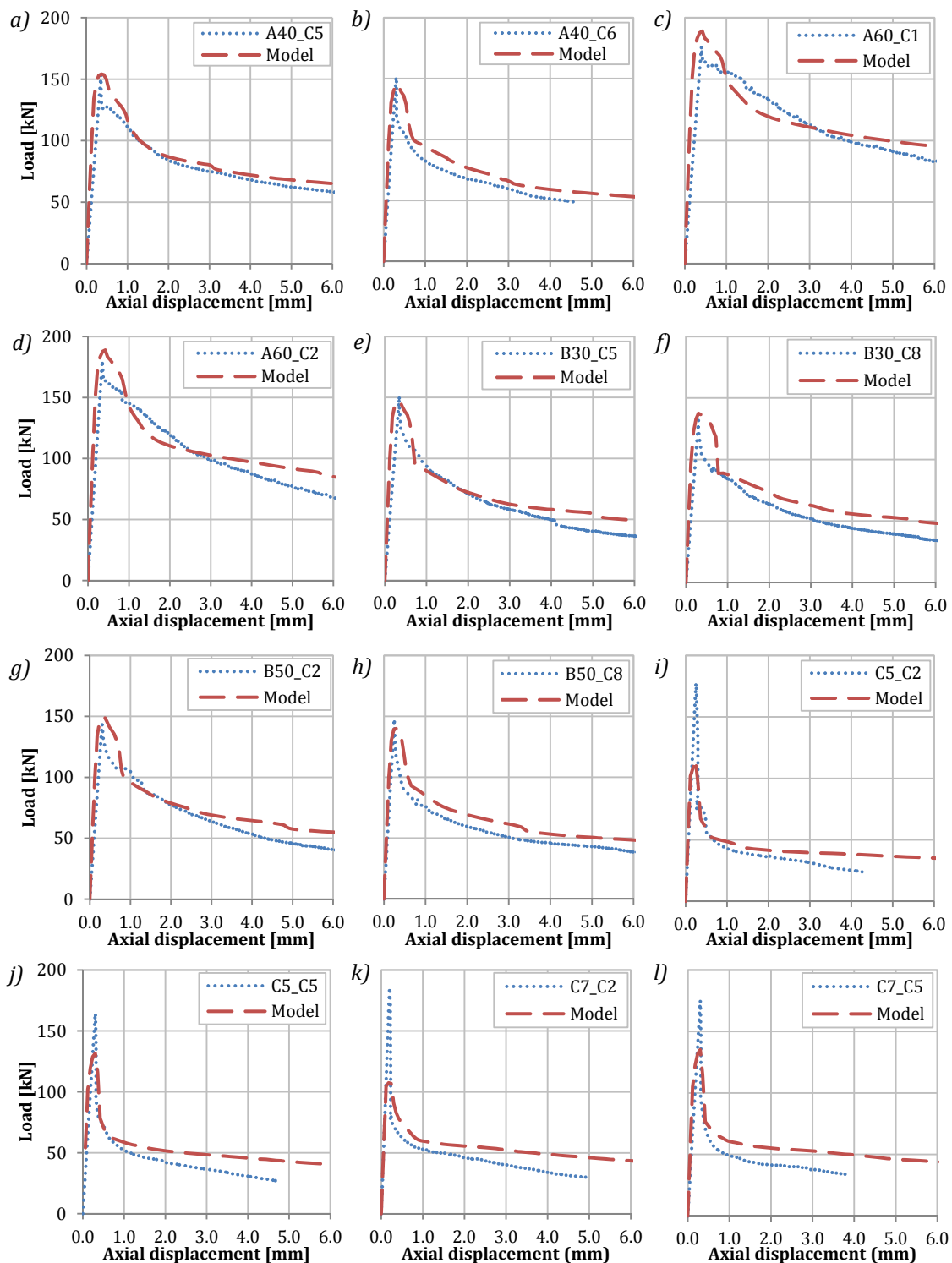


Figure 7.14 Experimental and numerical P - δ curves for: a) A40_C5, b) A40_C6, c) A60_C1, d) A60_C2, e) B30_C5, f) B30_C8, g) B50_C2, h) B50_C8, i) C5_C2, j) C5_C5, k) C7_C2 and l) C7_C5.

A general overview of the curves reveals that, although the model is not able to predict the sudden drop of load after the cracking occurs, it provides a satisfactory prediction of the the post-cracking stage. In general, the model provides a tensile strength

very close to the experimentally obtained for series A and B, whereas the predicted value for series C is lower than the experimental value. Regarding the post-cracking stage, the predicted curves exhibit a similar tendency to the one experimentally observed in all series analysed, especially in the stretch between 1.0 mm and the end of the test. However, a growing difference between the experimental and the predicted curves is detected as the displacement increases. This is particularly true for displacements bigger than 3.0 mm.

In order to further analyse this behaviour, the differences in the values of load for displacements of 1.0 mm, 3.0 mm and 5.0 mm are included in Table 7.14. Notice that a positive value indicates that the prediction overestimates the value of load, whereas a negative number corresponds to an underestimation of the experimental value.

Table 7.14 Differences between experimental and predicted load values for displacements of 1.0 mm, 3.0 mm and 5.0 mm.

Series	Specimen	Differences between experimental data and model [%]		
		1.0 mm	3.0 mm	5.0 mm
A (SFRC)	A40_C5	9.3	7.5	9.3
	A40_C6	14.9	13.0	15.0
	A60_C1	-0.1	-1.2	9.2
	A60_C2	0.6	4.8	19.2
B (SFRC)	B30_C5	-4.1	7.9	36.5
	B30_C8	4.7	21.8	34.0
	B50_C2	-7.4	8.8	26.5
	B50_C8	14.5	22.3	17.4
C (PFRC)	C5_C2	14.3	26.4	-
	C5_C5	13.5	33.2	-
	C7_C2	13.2	32.1	55.7
	C7_C5	24.2	41.7	-

From the values, it may be observed that the difference between both curves is increases with the displacement. However, while the difference at 5.0 mm remains under 20% for series A, the overestimations of the values of load for series B and C are higher. It should be remarked that, at such advanced stage of the test, the influence of the type of fibre and the fibre content may be significant. Notice that the average difference for series B50 is lower than for series B30, which has lower fibre content than the former. This behaviour may also be observed for series C, since the average difference is lower for C7 than for C5.

Despite some differences, the model yields results with a tendency and an absolute value similar to those from the experimental test. Taking into account the particularities in the response of FRC and the numerical difficulty to simulate the Barcelona test in a finite element model, the results indicate that the simplified constitutive equation from this work provides satisfactory results.

7.9. COMPARATIVE ANALYSIS WITH THE MODELS IN EUROPEAN CODES

In this section the formulation based on the Barcelona test is compared with the constitutive models in the European codes and recommendations for the design of FRC. For that purpose, the trilinear/multilinear models from DBV, the RILEM, the EHE-08 and the MC2010 were selected since they reproduce more accurately the contribution of the fibres after cracking. In the case of the CNR-DT 204, the bilinear model was considered.

7.9.1. Steel fibres

The values of the parameters defining each of the constitutive models for series A40, A60, B30 and B50 are presented in Table 7.15. Notice that the tensile strength is σ_1 for all models except the M2010, in which the tensile strength is represented by σ_2 due to the shape of the diagram (see Chapter 2 and Chapter 3). Additionally, it should be pointed out that partial safety factors were not used to obtain any values of stress and strain. The notation used in this section to refer the models in the codes is DBV, RILEM, CNR-DT, EHE and MC (or beam models as a group); while for the formulation proposed it is BCN.

Table 7.15 Parameters defining the constitutive models of series A40, A60, B30 and B50.

Series	Models	σ_1	ϵ_1	σ_2	ϵ_2	σ_3	ϵ_3	σ_4	ϵ_4
		[MPa]	[‰]	[MPa]	[‰]	[MPa]	[‰]	[MPa]	[‰]
A40	DBV	2.536	0.104	0.642	0.204	-	-	0.522	10.000
	RILEM	5.907	0.203	2.811	0.303	-	-	2.451	25.000
	CNR-DT	2.811	0.097	-	-	-	-	1.916	20.000
	EHE	3.038	0.105	2.811	0.205	-	-	2.120	20.000
	MC	3.106	0.107	3.451	0.150	2.940	0.158	2.274	20.000
	BCN	3.376	0.116	2.595	0.216	1.714	4.000	1.074	20.000
A60	DBV	3.395	0.107	1.200	0.207	-	-	0.996	10.000
	RILEM	6.657	0.211	2.879	0.311	-	-	2.394	25.000
	CNR-DT	2.879	0.091	-	-	-	-	1.146	20.000
	EHE	3.423	0.091	2.879	0.208	-	-	1.895	20.000
	MC	3.500	0.111	3.889	0.150	3.129	0.160	1.839	20.000
	BCN	3.988	0.126	3.788	0.226	3.296	4.000	2.018	20.000
B30	DBV	2.918	0.097	0.040	0.197	-	-	0.000	6.300
	RILEM	5.722	0.189	1.677	0.289	-	-	1.338	25.000
	CNR-DT	1.677	0.056	-	-	-	-	0.884	20.000
	EHE	2.943	0.097	1.677	0.197	-	-	1.164	20.000
	MC	3.009	0.100	3.343	0.150	1.791	0.175	1.201	20.000
	BCN	3.011	0.111	2.434	0.211	1.678	4.000	0.815	20.000
B50	DBV	2.871	0.096	0.332	0.196	-	-	0.175	10.000
	RILEM	5.629	0.188	3.860	0.288	-	-	3.284	25.000
	CNR-DT	3.860	0.129	-	-	-	-	2.312	20.000
	EHE	2.895	0.109	3.860	0.196	-	-	2.753	20.000
	MC	2.960	0.099	3.288	0.196	4.083	0.150	2.931	20.000
	BCN	3.225	0.108	2.887	0.208	1.928	4.000	0.951	20.000

The results regarding the tensile strength (σ_1) reveal that the lowest values always correspond to the DBV and the highest to the RILEM. In this analysis, the value of the CNR-

DT model is not considered since it is a simplified bilinear model which cannot be compared to a trilinear model.

The values provided by the BCN model remain between those two limit values. In fact, the value of σ_1 of the DBV is 24.9%, 14.9%, 3.1% and 11.0% lower than the value of the BCN for series A40, A60, B30 and B50, respectively; whereas the value of the RILEM is 75.0%, 66.9%, 90.1% and 74.5% higher than the value of BCN for A40, A60, B30 and B50, respectively. In general, the beam model that presents the closest values to the BCN is the MC (note that the tensile strength of the MC corresponds to σ_2).

The other parameters in Table 7.15, particularly the values of stress, may be more easily identified and analysed if plotted. In Figure 7.15, the constitutive models obtained from the average results of the beam tests are compared to the models determined by means of the average results of the Barcelona test for each series. In general, the highest values of correspond to the RILEM, the EHE or the MC. The BCN model ranges between the ones presenting the lowest and the highest values of residual strengths (except for series A60). The curves of series A40 are an example of such behaviour.

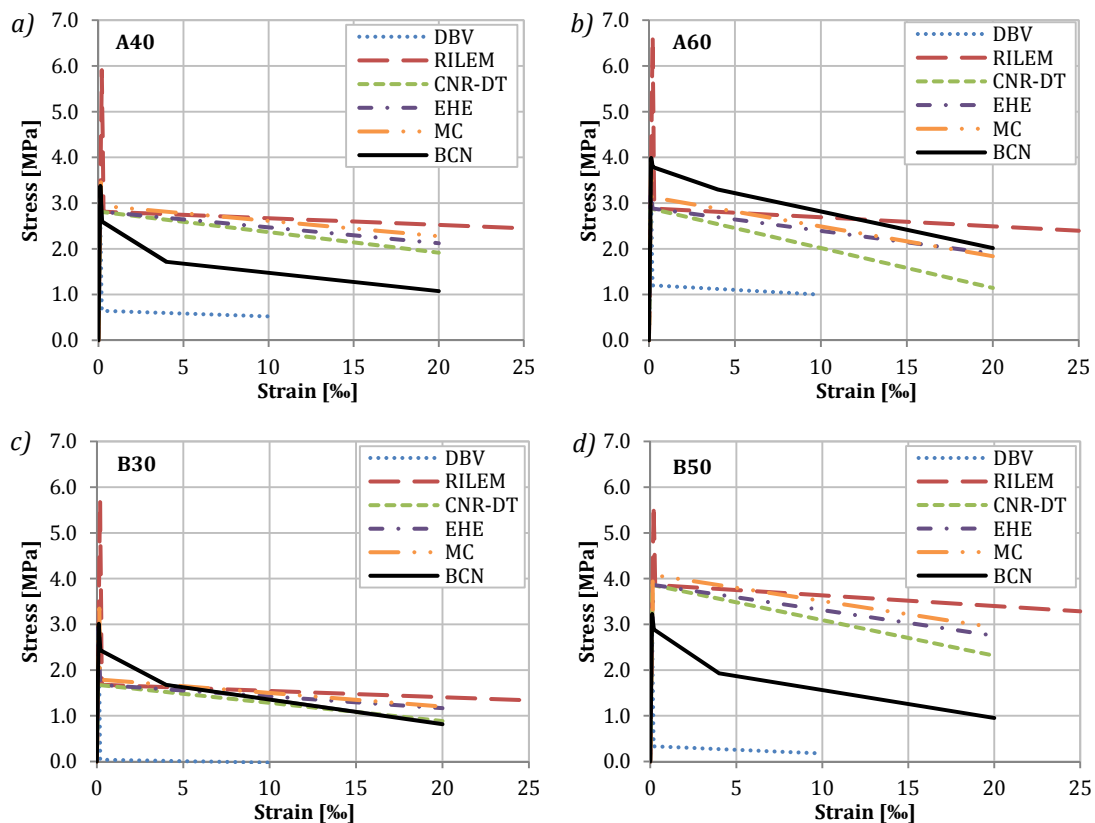


Figure 7.15 Comparison of the formulation based on the Barcelona test with the constitutive models based on beam tests for the series with SF: a) A40, b) A60, c) B30 and d) B50.

Figures 7.15a and 7.15b correspond to the same type of steel fibre with a high aspect ratio ($L/d = 83$) for fibre contents of 40 kg/m³ and 60 kg/m³, respectively. An

increase of 20 kg/m³ in the fibre content leads to a significant increment in the values of stress, which is observed if the curves obtained with the BCN model for A40 and A60 are compared. In fact, the values of σ_2 , σ_3 and σ_4 for A60 are 46.0%, 92.3% and 87.9% higher than for A40. It is reasonable that the lowest increment corresponds to σ_2 since after the cracking the reinforcement capacity of the fibres is not fully developed until higher values of strain, which correspond to σ_3 . Likewise, it could be expected that the increment in the value of the ultimate stress (σ_4) should be lower than for σ_3 due to the debonding-slipping mechanisms.

However, this phenomenon does not occur in the case of the beam models (as indicated in the previous paragraph) which might be due to the fact that the characterization of series A60 according to EN14651:2005 was performed with only one beam (see section 7.6). Therefore, conclusive remarks cannot be made from comparing the beam models of series A40 and A60; even though a significant increase in the response should be expected if more beams had been tested.

Regarding 7.15c and 7.15d, corresponding to series B30 and B50, a noticeable increase in the response is observed in the beam models when the amount of fibres increases from 30 kg/m³ to 50 kg/m³. The increase in the case of the BCN model is more subtle than for series A40 and A60; being the values of σ_2 , σ_3 and σ_4 for B50 only 18.6%, 15.0% and 16.8% higher than for B30. The reason for this difference between series A and B may be attributed to the type of fibre. Despite having the same length, the SF of series B has a smaller aspect ratio than the SF of series A and, consequently, the number of fibres in the concrete matrix is lower. Therefore, despite increasing the fibre content in 20 kg/m³ in both cases, the number of fibres is higher for series A, thus leading to a higher restriction of the crack opening and higher values of stress.

From the behaviour observed in Figures 7.15c and 7.15d a question regarding the differences between the beam models and the BCN test may be raised. Why the increase in fibre content leads to bigger increments in the stresses for the beam models? This is probably related to the amount of energy dissipated at the moment the main cracks appear and during the whole test. The study by Guàrdia (2008) revealed that the energy dissipated in the Barcelona test is around 4 to 5 times bigger than in the beam test. Such difference in the amount of energy released may be attributed to the bigger crack surface in the case of the Barcelona test. Hence, an equivalent increment in the values of stress in the BCN model would require a bigger increase of the fibre content.

7.9.2. Plastic fibres

The values of the parameters that define each of the constitutive models for series C5 and C7 are included in Table 7.16. The notation used to refer the models is the same as for the series with steel fibres. Again, no partial safety factors were used to obtain any values of stress and strain.

Table 7.16 Parameters defining the constitutive models of series C5 and C7.

Series	Models	σ_1	ϵ_1	σ_2	ϵ_2	σ_3	ϵ_3	σ_u	ϵ_u
		[MPa]	[‰]	[MPa]	[‰]	[MPa]	[‰]	[MPa]	[‰]
C5	DBV	3.289	0.105	0.303	0.205	-	-	0.244	10.000
	RILEM	6.449	0.206	0.818	0.306	-	-	0.769	25.000
	CNR-DT	0.818	0.026	-	-	-	-	0.608	20.000
	EHE	3.748	0.120	0.818	0.220	-	-	0.653	20.000
	MC	3.391	0.108	3.768	0.150	0.848	0.189	0.692	20.000
	BCN	3.905	0.125	1.631	0.225	0.961	4.000	0.606	20.000
C7	DBV	3.409	0.106	0.594	0.206	-	-	0.655	10.000
	RILEM	6.685	0.208	1.561	0.308	-	-	1.931	25.000
	CNR-DT	1.561	0.049	-	-	-	-	2.074	20.000
	EHE	3.438	0.121	1.561	0.207	-	-	1.645	20.000
	MC	3.515	0.110	3.906	0.150	1.487	0.180	1.868	20.000
	BCN	4.064	0.127	1.760	0.227	1.077	4.000	0.723	20.000

The values in Table 7.16. indicate that the DBV is the model that presents, once more, the lowest value of tensile strength (with exception of the bilinear model of the CNR-DT). The highest value corresponds to the RILEM. The values provided by the BCN model remain between these two limits since σ_1 of the DBV is 15.8% and 16.1% lower than the value of the BCN for series C5 and C7, respectively. On the other hand, the value of the RILEM is 65.1% and 64.5% higher than those of BCN for C5 and C7, respectively. The closest values to the tensile strength provided by the BCN model are the ones from the MC (note that the tensile strength of the MC corresponds to σ_2).

Similarly to the analysis of the steel fibres, the other parameters are analysed by means of the curves in Figure 7.16. The methodology followed in this case is the same as for series A and B.

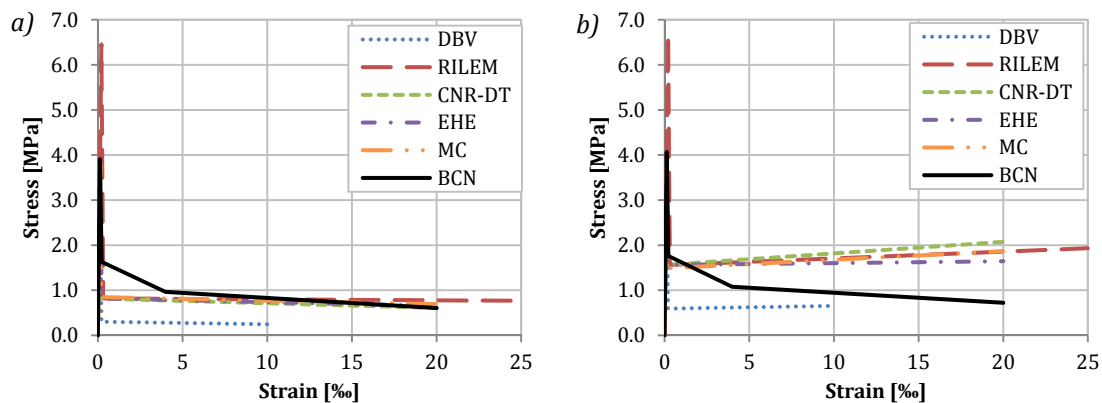


Figure 7.16 Comparison of the formulation based on the Barcelona test with the constitutive models based on beam tests for the series with PF: a) C5 and b) C7.

A general overview of Figures 7.16a and 7.16b indicates that an increase in the fibre content of 2 kg/m³ (from 0.55 % to 0.77 % in volume) does not result in a significant increase of the values of stress for neither the beam models nor the BCN model. However,

a significant difference in the response of the beam models is observed between series C5 and C7 since the latter exhibits hardening behaviour. This phenomenon does not appear in the case of the BCN model and the reason may be found in the failure mechanism of the Barcelona test.

Failure in the Barcelona test occurs when the stress in the specimens reaches the tensile strength of concrete. At this point, two scenarios are possible: a softening behaviour or a hardening behaviour. The softening behaviour is the most common response and usually takes place for low or moderate fibre contents since the restriction to the opening of the radial cracks is small. In such case, the conical wedge would slide inside the specimen leading to a sudden reduction of the load (and energy dissipation) until the main cracks open and the fibres start their bridging mechanism. If, however, the amount of fibres is big enough, a higher restriction to the crack opening would occur as the fibres restrict the slide of the conical wedge into the specimen. This is particularly true for short fibres since their bridging capacity is activated for smaller crack openings. In this case, an increase in the load value and a hardening behaviour of the material are expected.

The same argument could be valid for the beam test. However why is it that for the same amount and type of fibres the hardening behaviour only occurs in the beam models? This is, again, related to the amount of energy dissipated when the main cracks appear and during the whole test. Given that the energy dissipated in the beam test is smaller and less abrupt than in the Barcelona test, it is possible that for the same fibre content this is high enough to result in a hardening behaviour in the bending test but still not enough to generate such response in the Barcelona test. In fact, hardening in the Barcelona test would only occur if the amount of fibres was very high and after the formation of the conical wedge the fibres did not break.

7.10. CONCLUDING REMARKS

The main conclusions derived from the study conducted in this Chapter are presented below.

- The analytical formulation proposed to estimate the constitutive model for FRC was simplified in the form of a multilinear σ - ε diagram in which the values of strain are predefined. The simplified model may be easily implemented in the current design tools.
- The numerical simulation of the Barcelona test with the simplified version of the model provided satisfactory predictions of the experimental curves, despite overestimating the post-cracking response. The numerical results revealed that the model is valid for concrete reinforced with either steel or plastic fibres.
- The comparison of the BCN model with the constitutive models in European codes and guidelines revealed that, in average, the BCN model remains between the

model with the lowest values of stress (DBV) and the one with the highest values (RILEM).

8. POST-CRACKING CREEP BEHAVIOUR OF SFRC

8.1. INTRODUCTION

The deformation of a concrete specimen under sustained load increases gradually with time and may be from two to three times greater than its initial value (Neville *et al.* 1983). In addition, important creep deformations might lead to serviceability problems but also to stress redistribution and even affect the strength of the material (MacKay and Trottier 2004; Fernández Ruiz *et al.* 2007). Extensive research was performed over the years regarding the creep of plain and reinforced concrete, particularly in the field of the mechanisms causing creep (Bažant and Prasanna 1989; Bažant *et al.* 1997) and the models for its prediction (Trost 1967; Bažant and Osman 1976; Bažant and Baweja 1995). In order to satisfy the serviceability requirements, the prediction of the long-term performance of concrete structures is integrated in the structural design of reinforced concrete structures.

The statement regarding the effects of severe creep deformations holds true for SFRC structures. However, in Chapter 2 of this thesis, the long-term performance of SFRC was identified as one of the topics still to be discussed and included in the design codes and guidelines. In fact, despite the expansion of steel fibres as a concrete reinforcement, only a few studies are found in the literature regarding the long-term performance of SFRC and the studies concerning its modelling are even scarcer.

Consequently, further research on the post-cracking creep behaviour of SFRC needs to be conducted. Moreover, reliable models to predict creep deformations are necessary to satisfy the serviceability requirements in the design of SFRC structures.

8.1.1. Objectives

The main goal pursued in this chapter is to evaluate the post-cracking creep flexural behaviour of SFRC beams. For that, the following specific objectives are defined:

- Assess the post-cracking creep flexural behaviour of SFRC beams with different pre-cracking widths and load levels in terms of crack width and creep coefficient;
- Evaluate applicability of the formulations to predict the creep coefficient in current codes and guidelines to the response of SFRC under sustained loads in the post-cracking stage and
- Propose a simple model that could reproduce the creep deformations of SFRC in the post-cracking stage in terms of creep coefficient.

8.1.2. Outline of the chapter

Initially, in section 8.2, an experimental program is proposed to study the post-cracking creep behaviour of SFRC. A detailed description of the specimens, the material properties, the long-term test setup, the long-term test procedure, the environment conditions is provided in this section. Subsequently, in section 8.3, the results of the long-term test in terms of crack width and creep coefficient are analysed in detail. Likewise, in section 8.4, the results of the failure tests are evaluated.

In section 8.5, the formulations included in current codes and guidelines to determinate the evolution of the creep coefficient are applied and their prediction is compared with the experimental data. Then, a simplified model to obtain the performance curves of the post-cracking creep behaviour of SFRC beams is proposed in section 8.6. Furthermore, the curves provided by this model are compared to the experimental curves. Finally, in section 8.7, the main conclusions of the study are highlighted.

8.2. EXPERIMENTAL PROGRAM

8.2.1. Specimens and research parameters

In order to study the creep of SFRC in the post-cracking stage, a total of 15 small beams with 600 mm of length, 150 mm of width and 150 mm of height were cast. The beams were tested following a 4-point bending test in two stages; in the first one (S1) the creep test was performed on 9 beams and, in the second one (S2), this number was reduced to 6. Furthermore, in S1, the long-term test was performed in ambient conditions, while in S2 the long-term test was conducted in a climate controlled room.

The main parameters of the research are the pre-cracking width and the load level. Other properties such as the type of concrete, the type of fibre and the fibre content were not considered as variables in this study. The pre-cracking widths and load levels defined for the creep test are presented in Table 8.1.

Table 8.1 Research parameters.

Research parameters	Values
Pre-cracking width [mm]	0.25
	1.50
	2.50
Load level [%]	50
	60

In general, the study of the creep behaviour in the post-cracking stage is conducted for crack widths that are representative of the SLS. For this reason, some of the beams were pre-cracked at 0.25 mm. Nevertheless, in order to assess the capacity of the steel fibre as controller of deformations due to creep, crack widths of 1.50 mm and 2.50 mm were also considered. Given that the tests conducted in do not correspond to any standard, the criterion to define the load applied during the long-term tests was a percentage of the load registered for the pre-cracking width. The two load levels in Table 8.1 correspond to serviceability loads and were defined after reviewing other studies (see Chapter 2).

8.2.2. Materials and concrete mix

The concrete of the two series of beams (S1 and S2) was produced at ESCOFET S.A facilities in a 750 litres vertical axis mixer following the same mixing procedure: initially the dried components were mixed during one minute, subsequently the water was added and the paste was mixed during two minutes. Then, the superplasticizer was added and the steel fibres were included. Afterwards, the concrete was mixed for two additional minutes. Considering this, the total time of mixing was around 5-7 minutes. The details of the concrete mix for both series are presented in Table 8.2.

Table 8.2 Concrete mix.

Materials	Characteristics	Quantities [kg/m ³]	
		S1	S2
Gravel (6/15 mm)	Granite	520	520
Gravel (2.5/6 mm)	Granite	400	400
Sand (0/3 mm)	Granite	500	510
Cement	CEM I 52,5 R	400	350
Filler	Marble dust	260	300
Water	-	168	178
Superplasticizer	Adva® Flow 400	12	12
Fibres	Steel fibres	40	40


It should be remarked that the change in the mix composition of S2 with respect to S1 aimed at reducing the average compressive strength (f_{cm}) of the series. As indicated

later, in Table 8.4 the f_{cm} of S1 is over 50 MPa and, therefore, this SFRC is classified as a high-performance concrete according to the EHE-08. Since the aim of the research was to study conventional concrete, the mix composition was modified in S2.

The steel fibres used were of type Dramix® RC80/50BN with circular cross-section and hooked ends. These fibres are made of low carbon steel and are gathered into bundles by water-soluble glue. Further properties are presented in Table 8.3.

Table 8.3 Characteristics of the fibres used (provided by the manufacturer).

Characteristic	Unit	Value
Length (L)	[mm]	50
Diameter (d)	[mm]	0.62
Aspect ratio (L/d)	[-]	83
Tensile strength (f_y)	[MPa]	1270
Modulus of elasticity (E)	[GPa]	210
Number of fibres per kg	[-]	8100



In order to characterize each concrete series, the following specimens were cast: three prismatic beams (150 x 150 x 600 mm) for the flexural strength (EN 14651:2005 (CEN2005)), three cylindrical samples (150 x 300 mm) for the compressive strength (UNE 83507:2004 (AENOR 2004b)) and three cylindrical samples (150 x 300 mm) for the modulus of elasticity (UNE 83316:1996 (AENOR 1996)).

All specimens were vibrated externally by means of a vibrating table at 3000 rpm during 10 seconds approximately. The elements were removed from the moulds within 24 hours of casting and were moist cured under a plastic sheet for approximately one week (see later Table 8.5), after which they were transported from the ESCOFET S.A. facilities to the Laboratory of Structure Technology Luis Agulló at the UPC. Then, the specimens were kept in a curing room at 20 ± 2 Celsius degrees and 95% of relative humidity.

Table 8.4 shows the average compressive strength (f_{cm}), average modulus of elasticity (E_{cm}), limit of proportionality (f_L) and the residual flexural tensile strengths (f_{R1} , f_{R2} , f_{R3} and f_{R4}) corresponding to CMODs of 0.05 mm, 0.50 mm, 1.50 mm, 2.50 mm and 3.50 mm, respectively.

Table 8.4 Modulus of elasticity, compressive and residual flexural strengths at 28 days.

Property		S1		S2	
		Average [MPa]	CV [%]	Average [MPa]	CV [%]
Modulus of elasticity	E_{cm}	31597	1.08	30160	2.20
Compressive strength	f_{cm}	54.30	1.51	46.77	2.54
	f_L	3.73	8.57	3.76	7.96
Residual flexural strengths	f_{R1}	4.62	12.15	3.75	22.29
	f_{R2}	5.09	13.77	4.24	17.91
	f_{R3}	5.10	15.91	4.30	15.88
	f_{R4}	4.87	14.08	4.17	15.68

The results in Table 8.4 reveal that the values of f_{Ri} are higher than f_L . Regarding the scattering, the CV is high but in the same order of magnitude as reported by Parmentier *et al.* (2008) and Molins *et al.* (2009).

8.2.3. Preparation and pre-cracking of the beams

Several activities are conducted in order to prepare the beams for the creep test, some of which were already described in the previous section, such as the demoulding and the curing. In Figure 8.5, a summary of these activities and their duration is presented (only if the activity took more than a day).

Table 8.5 Activities for the preparation of the beams.

Activities	S1		S2	
	Date	Duration [days]	Date	Duration [days]
Casting	03/11/2009	-	23/11/2010	-
Demoulding	04/11/2009	-	24/11/2010	-
Moist curing	04/11/2009	5	24/11/2010	9
Storage in curing room	09/11/2009	18	03/12/2010	11
Notching at 21 days	24/11/2009	-	14/12/2010	-
Storage in curing room	24/11/2009	63	14/12/2010	134
Pre-cracking of beams	27/01/2010	-	28/04/2010	-

The beams were notched 21 days after the casting in the centre of the beams on the face originally in contact with the base of the moulds. The depth of the notch is 25 mm. Afterwards, they were stored in the curing room at 20 ± 2 Celsius degrees and 95% of relative humidity until they were pre-cracked.

The beams were pre-cracked according to the long-term test setup which corresponds to a 4-point bending test with a span of 450 mm and a load span of 150 mm (one third of the span) as shown in Figure 8.1a. The pre-cracking consisted in loading the notched beams up to the value of pre-crack specified for the long-term test. While the loading took place, CMOD was measured as well as the crack width at 15 mm above the bottom surface of the beam (w_{15}) as indicated in Figure 8.1a.

The CMOD was used to control the test and it was measured with a displacement transducer placed at the crack mouth, while the crack width at 15 mm was measured with the same LVDT transducer used afterwards during the long-term test (see Figure 8.1b). The reason for measuring the crack width during the long-term test 15 mm above the bottom surface instead of the CMOD was the lack of enough space in the test setup (see section 8.2.3) to measure the CMOD with the equipment available in the laboratory. However, if necessary, the relation between the crack width measured and the CMOD may be obtained geometrically.

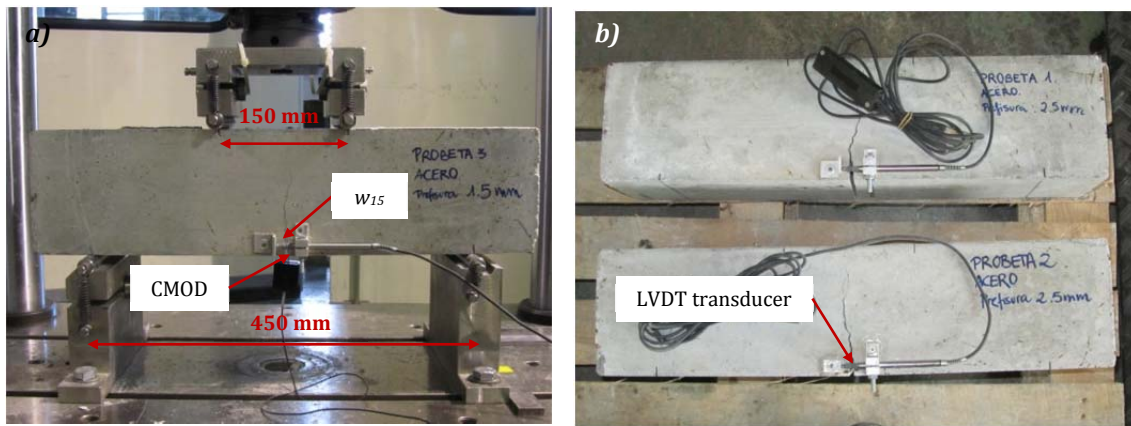


Figure 8.1 a) Pre-cracking test and b) beams with LVDT transducer for long-term test.

In the second stage of the experimental program, the deflection of one beam was measured to correlate the deflection and the crack width in the long term-test. For that, a device consisting of a steel frame with a mechanism on the sides to place the LVDT transducer vertically was set on the beam (see Figures 8.2a and 8.2b). After the pre-cracking, the steel frame remained on the beam for the long-term test, thus enabling registering the deflection as well as the crack width.

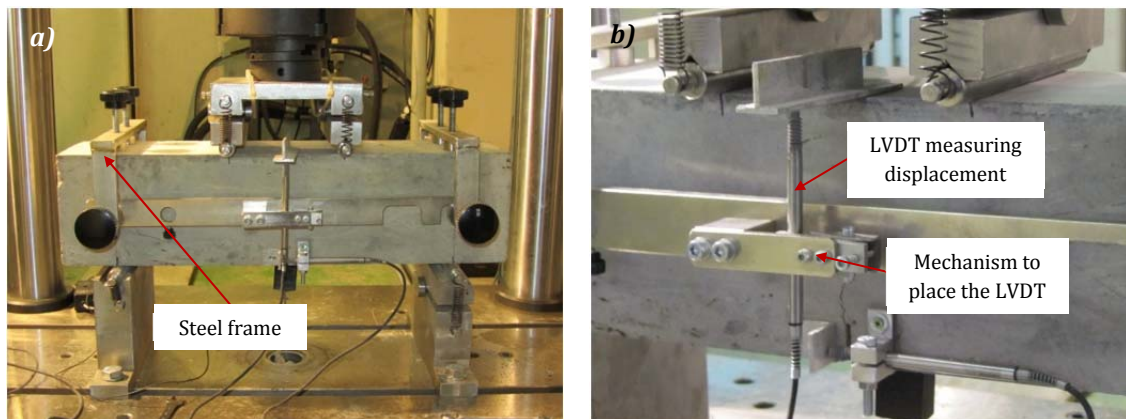


Figure 8.2 a) Device to measure deflection and b) detail of the LVDT transducer.

The main data regarding the pre-cracking of the beams is presented in Table 8.6. The table includes the load corresponding to the limit of proportionality (F_L) as defined in EN14651:2005, the pre-cracking width (w_p) measured 15 mm above the bottom surface, the load for which w_p occurred (F_p) and the residual pre-cracking width (w_{pr}) after the unloading. The pre-cracking deflection (δ_p) and the residual pre-cracking deflection (δ_{pr}) are also included for the beam of the second stage in which this variable was measured.

It should be remarked that the values of w_{pr} were only registered in the second stage of the experimental program. Notice that the notation used for the beams in this case indicates the stage of the experimental program (S1 or S2) followed by a number that

indicates the beam. This notation will be updated in section 8.2.3 to include the pre-cracking width and the load level in the long-term test.

Table 8.6 Main data of the pre-cracking of the beams.

Beam	F_L [kN]	w_p [mm]	δ_p [mm]	F_p [kN]	w_{pr} [mm]	δ_{pr} [mm]
S1_1	21.2	0.257	-	19.3	-	-
S1_2	21.0	0.252	-	16.7	-	-
S1_3	20.3	0.202	-	20.0	-	-
S1_4	20.6	0.253	-	20.0	-	-
S1_5	16.7	0.251	-	15.3	-	-
S1_6	15.8	0.252	-	13.2	-	-
S1_7	20.9	2.501	-	24.3	-	-
S1_8	16.3	1.502	-	15.2	-	-
S1_9	17.8	1.500	-	19.0	-	-
S2_1	27.9	2.746	-	32.8	2.351	-
S2_2	29.0	1.578	-	30.8	1.224	-
S2_3	23.4	0.336	-	27.0	0.181	-
S2_4	25.1	0.332	-	23.7	0.190	-
S2_5	24.6	0.363	-	20.9	0.200	-
S2_6	28.3	2.825	2.259	34.1	2.384	1.848

The values of w_p for S1 correspond to the research parameters defined in section 8.2.1, however for S2 they are slightly higher to those defined in the research parameters. This increase in the values of w_p were due to problems with the control device while the pre-cracking procedure occurred.

8.2.4. Long-term test

Test setup

The setup for the long-term test was composed by a steel frame, measurement devices (LVDT transducers and sensors) and a data acquisition system. Each frame was prepared to work with a column of three beams. Between the beams in the column, elements to guarantee the support and the load transmission were placed to achieve a 4-point bending test setup, as shown in Figure 8.3 where main components of the test equipment are indicated.

The loading mechanism was based on the lever principle: applying a force in one edge of a rigid object used with an appropriate fulcrum or pivot point can multiply the mechanical force (effort) applied to another object. In this case, a weight was applied in one end of the lever (see “Force edge” in Figure 8.3) which has the fulcrum or pivot point in the other end (see “Fulcrum” in Figure 8.3). The effort applied to the object (in this case the column of beams) was placed in an intermediate point of the lever between the fulcrum and the force edge (see “Effort point” in Figure 8.3). The lever mechanism allowed loading the beams with the desired low requiring less weight than if the loading was carried out directly on the beams.

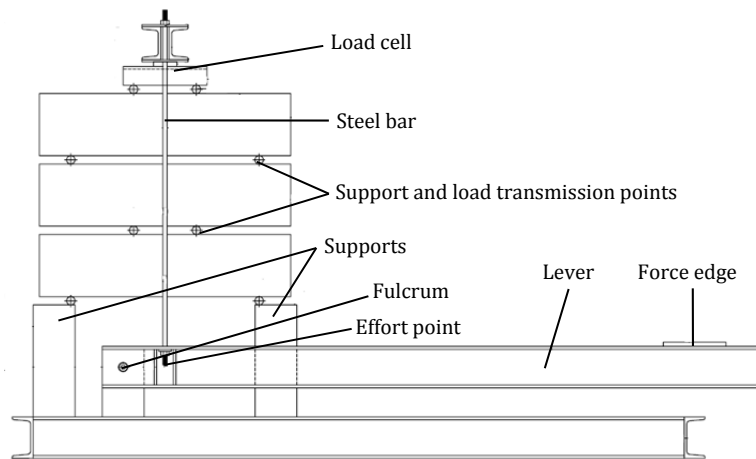


Figure 8.3 Side view of the frame for the creep test.

The effort or load resulting in the effort point from placing weight in the edge force was transmitted to the loading plate at the top of the column by means of the vertical steel bars at both sides of the column of beams (see “Steel bar” in Figure 8.3). When these bars were fixed the load was immediately transferred to the loading plate and, consequently, to the beams through the load transmission points. Further detail on the equipment may be found in Arango *et al.* (2012).

The variables registered during the test were the load, the crack width measured 15 mm above the bottom surface, the displacement at midspan (in one beam of series S2), the temperature and the humidity. Load cells, displacement transducers and sensors for the temperature and humidity were used to measure these variables throughout the test.

Given that the increase in the values of these variables is expected to stabilize with time, the frequency with which these were registered decreased as the long-term progressed. During at least the first 2 hours and 30 minutes the variables were registered every 5 seconds. This time increased up to 10 minutes in S1 and to 5 minutes in S2 after approximately 24 hours and to 30 minutes almost 4 months after the test started for both stages. This time remained constant until the unloading procedure, point at which the time was reduced to capture the recovery of the beams.

Test procedure

The test procedure was divided in two stages: the loaded stage and the unloaded stage. Before the loading starts, the lever of the steel frame was lifted (Figure 8.4a). Then, the support elements were placed and above them the first beam, connecting the displacement transducer to check that the measures were in range. Afterwards, the second element of support and load transmission was placed on the top surface of the first beam and above it the second beam (Figure 8.4b). This procedure was repeated until the column of three beams was assembled (see Figure 8.4c). Then, the bars on both sides of the column were attached but not fixed (no load was transmitted to the beams at this point).

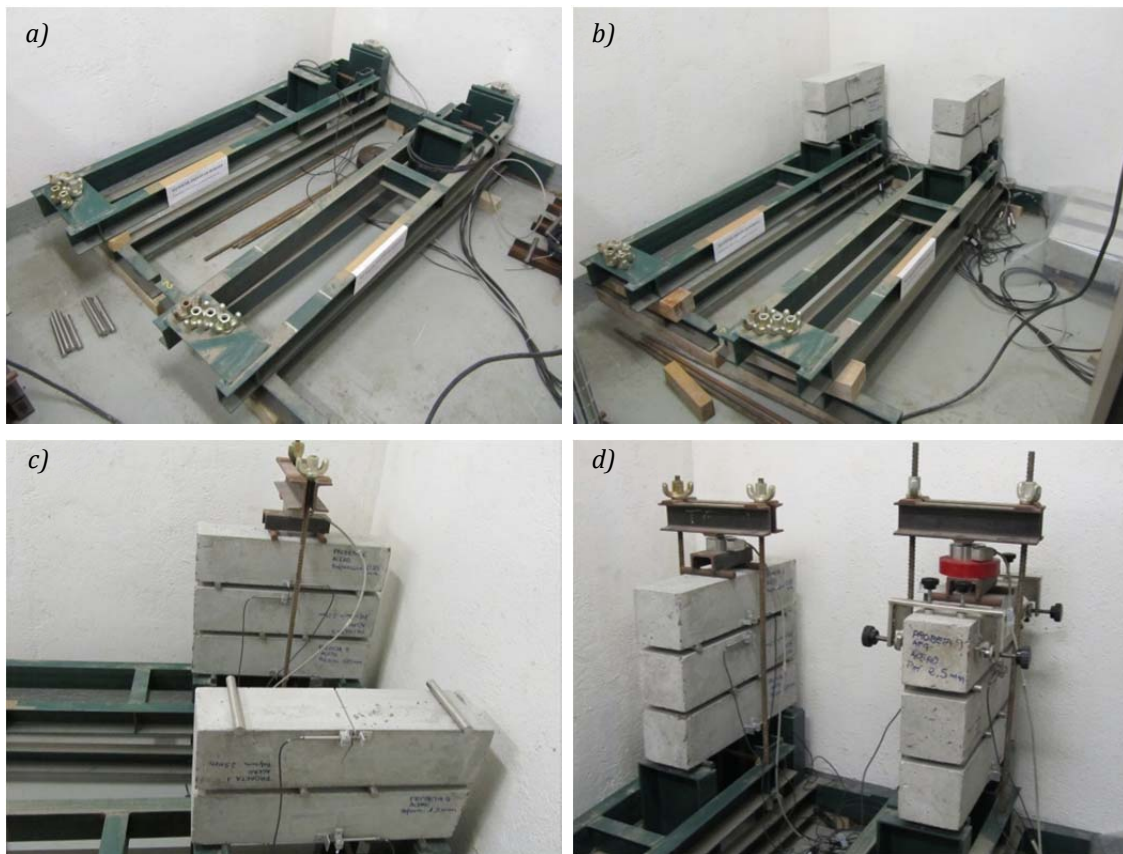


Figure 8.4 Preparation of the test before loading.

Once the measure of all displacement transducers were checked, the bars on both sides of the column were fixed, the lever of the steel frame was liberated (a small preload was applied at that moment) and, finally, the load specified for the test was then applied. The test setup during the long-term test is shown in Figure 8.4.

The main data of each beam is presented in Table 8.7. This table includes the average load applied during the long-term test (F_c) and the load level applied, which is the ratio F_c/F_p in terms of percentage (the values of F_p were already included in Table 8.6). The values of w_p are included again in this table since, together with the values of the load level, they are used to define the notation of the beams that will be used hereinafter. This is defined firstly by the series (S1 or S2) which indicates the type of concrete of the beam, followed by the value of w_p (e.g. 0.25 or 1.50) and finally the notation ends with the load level to which the beams are subjected.

The theoretical load levels considered for the study were 50% and 60% of the P_p registered during the pre-cracking test as described in section 8.2.1. However, it should be remarked that the average F_c applied is the same in the three beams of a column and, given the natural differences between the F_p of each beam, the real load level is slightly difference from the theoretical. Particularly, in S1 the load levels were lower than the defined in section 8.2.1.

Table 8.7 Main data of the beams.

Beam	Frame	w_p [mm]	F_c [kN]	Load level [%]	Notation
S1_1	3	0.257	9.1	47.0	S1_0.25_47.0%
S1_2	2	0.252	10.4	62.2	S1_0.25_62.2%
S1_3	2	0.202	10.5	52.3	S1_0.20_52.3%
S1_4	2	0.253	10.4	52.3	S1_0.25_52.3%
S1_5	1	0.251	7.1	46.5	S1_0.25_46.5%
S1_6	1	0.252	7.1	53.7	S1_0.25_53.7%
S1_7	3	2.501	9.0	37.1	S1_2.50_37.1%
S1_8	1	1.502	7.1	46.8	S1_1.50_46.8%
S1_9	3	1.500	9.1	48.0	S1_1.50_48.0%
S2_1	2	2.746	16.2	49.5	S2_2.75_49.5%
S2_2	2	1.578	16.3	52.9	S2_1.58_52.9%
S2_3	1	0.336	14.5	53.9	S2_0.34_53.9%
S2_4	1	0.332	14.6	61.6	S2_0.33_61.6%
S2_5	1	0.363	14.6	69.8	S2_0.36_69.8%
S2_6	2	2.825	16.2	47.5	S2_2.83_47.5%

Furthermore, the weight of the beams placed on top of the others was also considered, which accentuates the differences in the load levels among the beams of a column. The weight of the device placed for measuring deflection in one beam of S2 is also considered. Hence, the values of F_c in correspond to the average load registered during the long-term test plus the additional weight on top of each beam.

Figure 8.5 shows a scheme of the location of the beams in the frames and their position in the columns. Furthermore, the load applied in each of the frame is also indicated. Notice that this load may be different from the real load applied in each of the beams due to the additional weight previously mentioned.

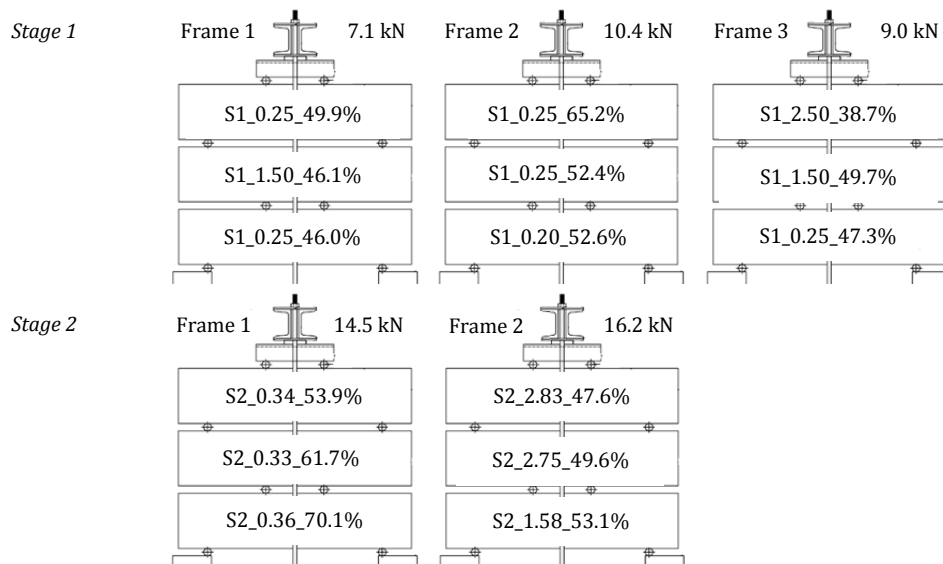


Figure 8.5 Location of the beams in the frames.

Control of the humidity and temperature

The conditions of humidity and temperature in S1 and S2 of the experimental program were different since, as previously mentioned, in the former the beams were in in the Laboratory of Structure Technology Luis Agulló exposed to ambient conditions whereas in the latter in a climate-controlled room (see Figure 8.6). During the long-term tests of both stages, the humidity and the temperature were registered.

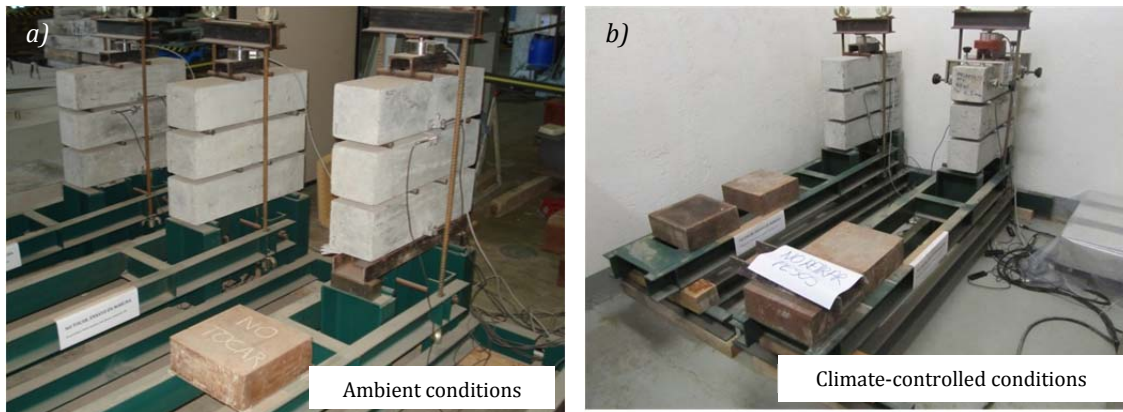


Figure 8.6 Long-term test in a) ambient conditions and b) climate-controlled room conditions.

The curves in Figures 8.7a and 8.7b correspond to the evolution of humidity and temperature with time, respectively, in S1 (in ambient conditions).

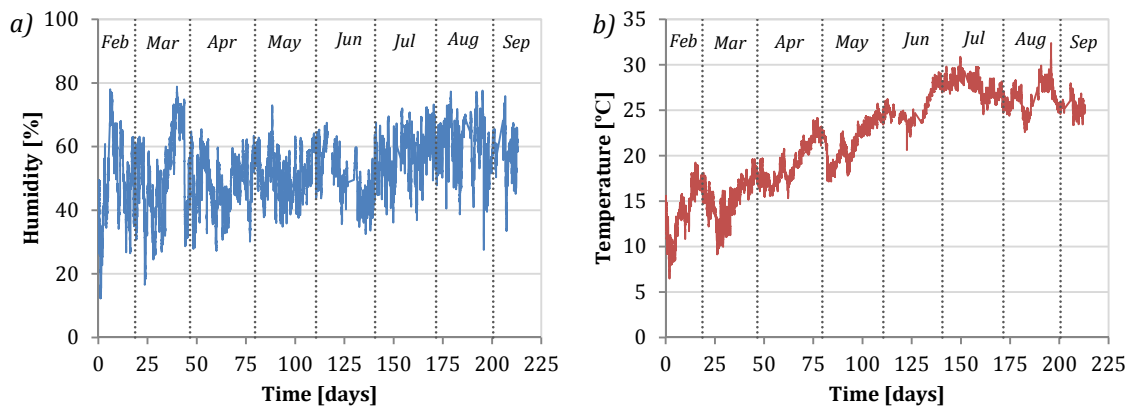


Figure 8.7 Evolution of a) humidity and b) temperature in stage 1 (ambient conditions).

Given the differences in the values of humidity and temperature observed in Figure 8.7, a more detailed analysis of the maximum, minimum and average values registered each month is conducted subsequently. These data are presented in Table 8.8. The results reveal that the lowest value of humidity registered was 12.3% (in February), while the highest value was 78.8% (in March). In the case of the temperature, the lowest value, also registered in February, was 6.5°C, whereas the highest was 32.4°C measured in August. This represents a difference of 25.9°C, almost five times higher. These variations are significant and, therefore, must be considered in the analysis of the results.

Table 8.8 Maximum, minimum and average data of humidity and temperature in stage 1.

Climate conditions		Feb	Mar	Apr	May	Jun	Jul	Aug	Sep
Humidity [%]	Max.	78.0	78.8	65.5	73.0	67.5	72.4	77.6	75.9
	Min.	12.3	16.5	27.3	34.8	32.5	33.6	27.5	33.5
	Average	36.9	49.9	48.8	50.3	54.4	56.4	60.5	57.9
Temperature [°C]	Max.	19.2	19.7	24.1	25.7	28.9	30.9	32.4	28.0
	Min.	6.5	9.1	15.3	17.1	20.6	24.5	22.6	23.4
	Average	12.7	15.3	19.2	21.3	24.7	27.9	26.5	25.4

The humidity and the temperature registered during S2, in climate-controlled conditions, are presented in Figure 8.8.

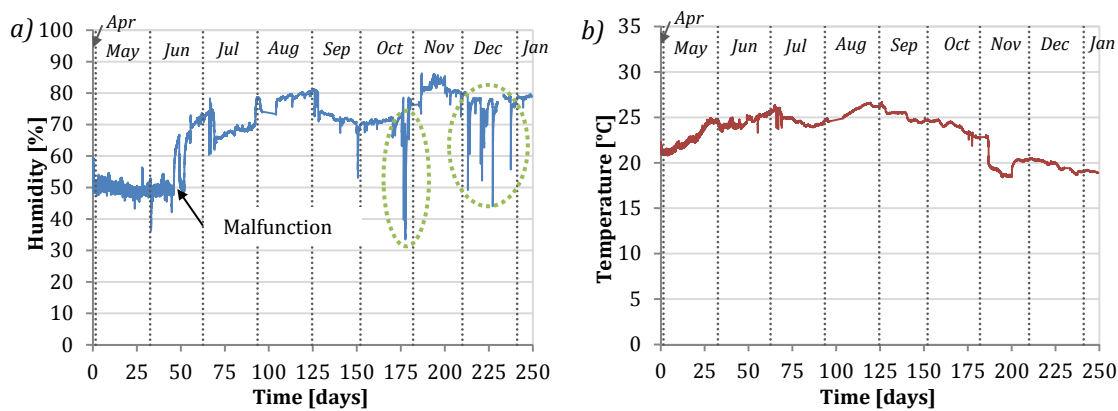


Figure 8.8 Evolution of a) humidity and b) temperature in stage 2 (controlled conditions).

The graphs indicate that the variations for S2 are significantly smaller than in S1. However, it must be remarked that the system controlling the humidity in the room presented a malfunctioning from mid-June and was only repaired after the completion of the test. Additionally, at the end of October and in December significant decreases of humidity were detected (circled in Figure 8.8a). The cause is unknown, even though the performance of other tests in the climate-controlled room suggests that the door may have been left opened during a long time. In Table 8.9, detailed data regarding the evolution of the temperature and humidity during S2 are presented.

Table 8.9 Maximum, minimum and average data of humidity and temperature in stage 2.

Climate conditions		Apr	May	Jun	Jul	Aug	Sep	Nov	Dec	Jan
Humidity [%]	Max.	59.6	56.4	73.7	78.7	80.7	81.3	78.6	86.3	80.4
	Min.	48.2	43.2	36.3	60.3	73.1	53.1	33.5	73.4	44.0
	Average	52.7	50.4	57.9	69.1	78.3	73.3	70.2	77.8	75.9
Temperature [°C]	Max.	22.3	24.9	25.7	26.4	26.6	26.7	24.8	23.0	20.5
	Min.	20.8	20.8	23.3	23.7	24.5	24.3	21.8	18.4	18.6
	Average	21.3	21.8	24.5	24.7	25.5	25.8	23.8	22.2	19.8

The lowest humidity corresponds to the month of May with a value of 50.4% and the highest was measured in December and its value was 86.3%. This difference is due to the malfunctioning of the system controlling the humidity. In terms of temperature, the lowest value was 18.4°C (in December), whereas the highest was 26.7°C (in September). This is a difference of 8.3°C, which is remarkably smaller than in S1.

The average values of humidity and temperature are now plotted in Figure 8.9. The curves reveal that the climate-controlled conditions helped reducing the variation in the average temperature in S2. However, the malfunctioning of the system entailed similar variations of humidity in both stages, even though the difference between the minimum and the maximum values are significantly bigger in S1 (see Tables 8.8 and 8.9).

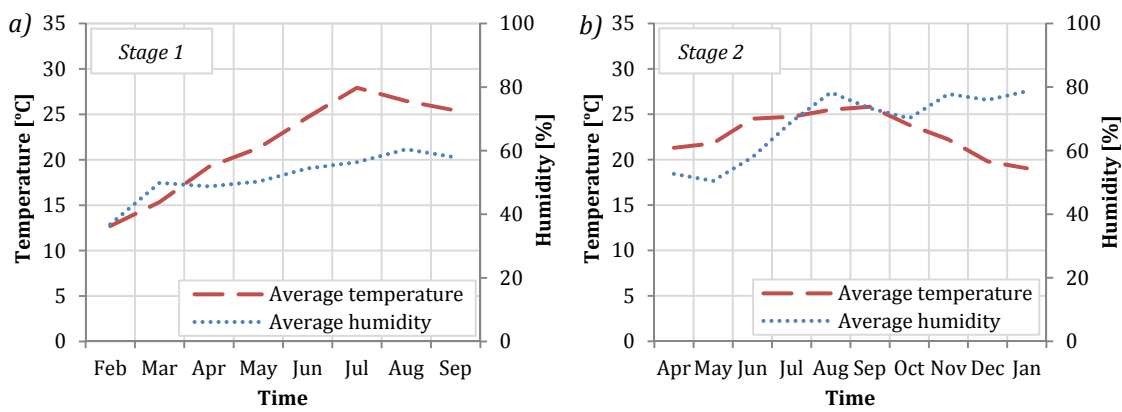


Figure 8.9 Average humidity and temperature in a) stage 1 and b) stage 2.

From the analysis of the humidity and temperature conditions, it may be assumed that the beams of S1 were subjected to drying creep since they were exposed to ambient conditions with alternating humidity and temperature (as observed in Figure 8.7). For the beams of S2, given that the malfunctioning of the system controlling the climate conditions of the room and that the humidity was lower than in the curing room, assuming basic creep may not be correct but the variations of humidity are small if compared to S1.

Therefore, considering that the beams of both stages were moist-cured, the drying concrete of S1 is expected to creep at a higher rate and exhibit bigger creep deformations than the concrete of S2 that remains more wet. Furthermore, the beams of S1 are subjected to alternating conditions between two limits which lead to greater creep deformations. In terms of the temperature, the ratio of creep deformations increases when the temperature rises.

Control of the load during the loaded stage

The load applied during the long-term test was controlled by means of load cells which registered its value. Figure 8.10 shows the evolution of the load in the frames of each stage. The empty spaces in the curves correspond to periods in which the data acquisition system failed due to electricity outages.

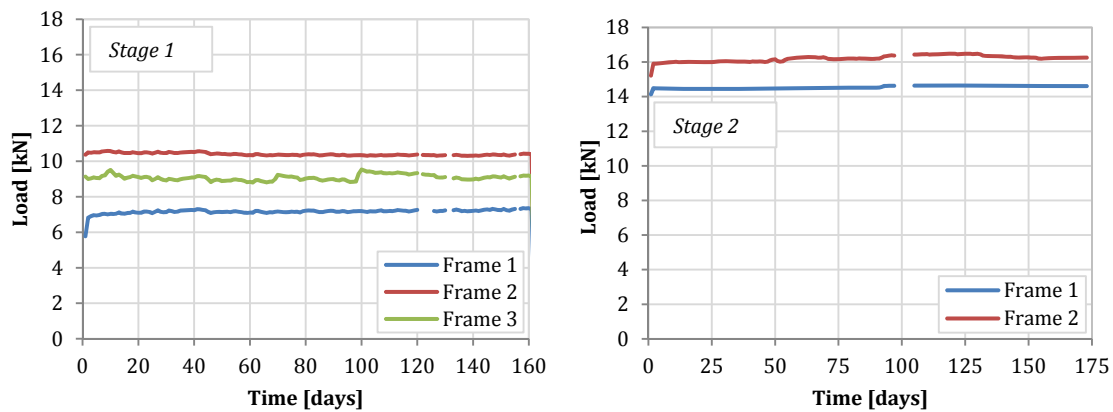


Figure 8.10 Variation of the load during a) stage 1 and b) stage 2.

The results reveal that there was no significant variation in the value of load during the tests that could affect the results. The average values of load registered for frame 1, frame 2 and frame 3 in S1 are 7.1 kN, 10.4 kN and 9.0 kN, respectively. The highest and lowest values for each of them vary 3.4% and 11.8% respectively for frame 1, 2.4% and 1.1% respectively for frame 2 and 7.1% and 4.3% respectively for frame 3. Regarding results for S2, the average load applied in frame 1 is 14.5 kN and in frame 2 is 16.2 kN. In the case of frame 1, the highest and the lowest values of load registered during the loaded stage only differ in 0.8% and 2.2% with respect to the average value; while for frame 2 the highest and lowest value vary in 1.8% and 2.1% with respect to the average.

The loaded stage lasted approximately 5 months for S1 and almost 6 months for S2, after which the beams were unloaded. The unloading procedure consisted in lifting the free edge of the lever (see Figure 8.3) and liberating the steel bars that transmit the load. In this precise moment, the beams are unloaded and the deflection recovery starts. The beams remained unloaded in the test setup nearly eight weeks in the case of S1 and ten weeks in the case of S2. The duration of both stages and other significant dates of the long-term test are detailed in Table 8.10. Notice that for S1, 14 days passed between the pre-cracking and the loading, during which the beams remained in ambient conditions.

Table 8.10 Significant dates of the long-term test.

Data	S1	S2
Age of concrete at time of loading [days]	99	157
Start date of the loaded stage	10/02/2010	29/04/2011
Duration of the loaded stage [days]	158	172
Start date of the unloaded stage [days]	21/07/2010	19/10/2011
Duration of the unloaded stage [days]	54	81

Notice that the beams of S2 were 58 days older than the beams of S1 at the time of the loading. However, Neville *et al.* (1983) reports that for ages greater than 28 days, the influence of the age at the application of load is negligible.

8.2.5. Failure test and loading history

After the long-term test, the beams were reloaded up to failure in a 4-point bending test setup (the same setup of the pre-cracking and the long-term test, see Figure 8.1a). Therefore, the loading history of the beams is composed by three stages that correspond to the pre-cracking, the long-term test and the failure test. An example of the loading history of a beam is presented in Figure 8.11.

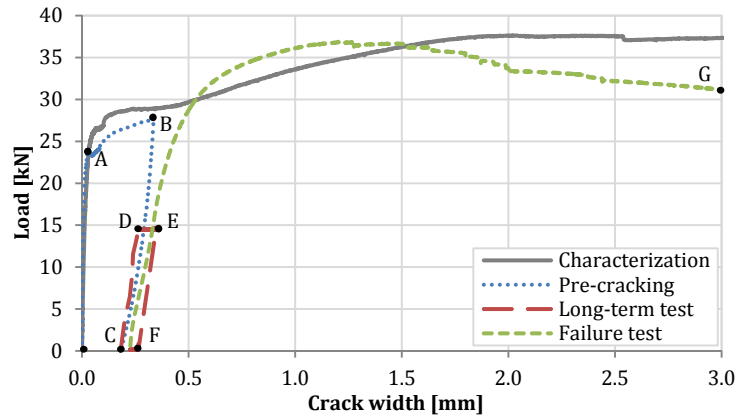


Figure 8.11 Loading history of a beam.

The first part of the curve corresponds to the pre-cracking of the beam (from point O to point C), where a linear elastic behaviour is identified in the stretch OA. After the cracking (A), the loading procedure continues up to the pre-cracking width specified for the beam (B). Then, the beam is unloaded registering the recovery. The second part of the curve (from point C to point F) corresponds to the long-term test. The loading procedure and the resulting initial crack width may be identified in the first stretch of this part of the curve (CD). The stretch DE corresponds to the development of the creep deformations which ended when the beams were unloaded. The stretch EF reveals the capacity of the material to recover the deformations. Finally, part three of the curve (stretch FG) corresponds to the failure test.

8.3. RESULTS OF THE LONG-TERM TEST

8.3.1. Evolution of the crack width

Initial crack width

During the long-term test, an initial crack width (w_i) occurs due to the loading of the beams and the crack width due to creep at (w_c^j) starts from that point onwards. Therefore, the total crack width at a time j (w_t^j) may be expressed as indicated in the expression (8.1). Figure 8.12 shows the evolution of the total crack width with time and the initial crack width and the crack width due to creep at $j=150$ days are indicated.

$$w_t^j = w_i + w_c^j \quad (8.1)$$

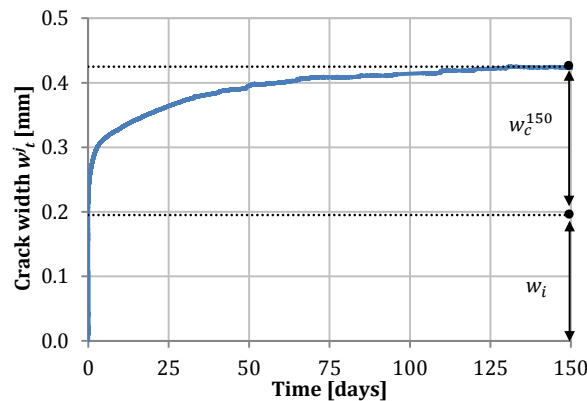


Figure 8.12 Definition of initial crack width, crack width due to creep and total crack width.

Considering the abovementioned, the values of initial crack width are presented in Table 8.11. From the results, it is observed that for S1 the bigger values of w_i do not correspond to the beams with the bigger w_p (pre-cracking width); instead, the beams with a higher load level present such values. It must be remarked that in S1, the beams with $w_p=0.25$ mm present a higher load. However, in the case of S2, the bigger values of w_i correspond to those beams with a bigger values of w_p such as S2_2.75_49.5% and S2_2.83_47.4%. For the beams with close values of w_p such as S2_0.34_53.9%, S2_0.33_61.6% and S2_0.36_69.8%, it is the load level which defines the beam with the bigger values of w_i .

Table 8.11 Initial crack width.

Beams of S1	w_i [mm]	Beams of S2	w_i [mm]
S1_0.20_52.3%	0.072	S2_0.33_61.6%	0.107
S1_0.25_46.5%	0.057	S2_0.34_53.9%	0.096
S1_0.25_47.0%	0.031	S2_0.36_69.8%	0.124
S1_0.25_52.3%	0.087	S2_1.58_52.9%	0.183
S1_0.25_53.7%	0.153	S2_2.75_49.5%	0.195
S1_0.25_62.2%	0.125	S2_2.83_47.5%	0.180
S1_1.50_46.8%	0.057	-	-
S1_1.50_48.0%	0.077	-	-
S1_2.50_37.1%	0.070	-	-

In order to deepen in the analysis of the results regarding w_i , the values for all beams were plotted against the pre-cracking width w_p in Figure 8.13a and against the load level in Figure 8.13b (the values of crack width due to creep and total crack width at 150 days presented in Table 8.11 are analysed later in the chapter).

The results of S1 in Figure 8.13a do not show a clear tendency regarding the values of w_i , however it should be remarked that the load level applied to the beams with bigger w_p was lower, particularly for beam S1_2.50_37.1%, than the beams with $w_p=0.25$ mm. Despite that, if the values of w_i are plotted as a function of the load level (see Figure 8.13b)

a tendency may be identified since w_i increases with the load level regardless of the value of w_p , suggesting that w_i may be more influenced by the load level applied than w_p .

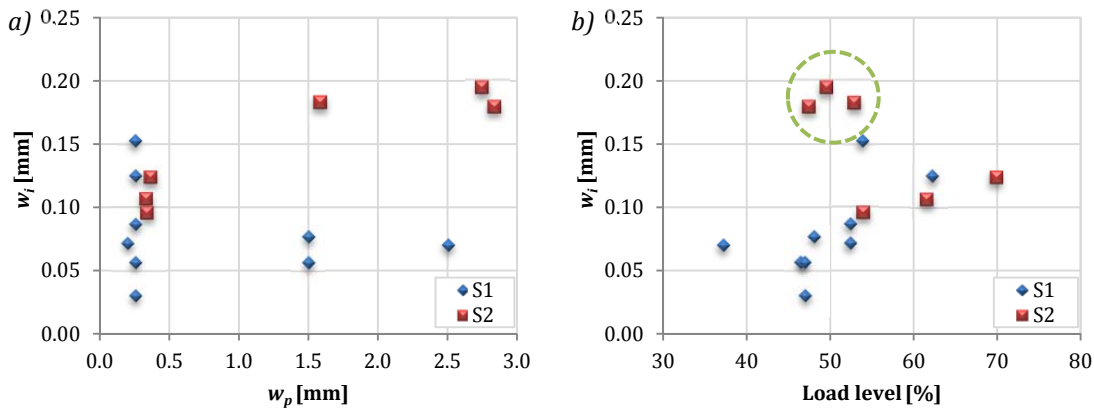


Figure 8.13 Initial crack width as a function of a) w_p and b) the load level.

In the case of S2, Figures 8.13a and 8.13b show that, in general, w_i increases with w_p and the load level. This behaviour was already reported by Arango (2010). Nevertheless, in Figure 8.13b, three beams do not follow this tendency since despite a lower load level they exhibit a bigger value of w_i (see green circle). These beams (S2_1.58_52.9%, S2_2.75_49.5% and S2_2.83_47.5%) present bigger values of w_p , which may explain why with a lower load level present bigger values than the other beams of S2.

Crack width due to creep

In the analysis of the crack width due to creep, average values per day were considered. This criterion was taken after verifying that the variations of the maximum and the lowest values with respect to the average value of the day were admissible. In fact, the average variations of the maximum and lowest values with respect to the average values in S1 were around 1.5% for most of the beams. The largest variations were for 4.3% and 3.9% for the maximum and lowest values, respectively and correspond to beam S1_0.25_46.5%. In case of S2, these average variations are even smaller, being around 0.5% for most beams. Only beam S2_0.34_53.9% presents bigger variations, reaching values of 0.7% and 0.6% for the maximum and the lowest values, respectively.

Hence, the evolution of w_c^j during the long-term test is presented in Figure 8.14 for each beam in terms of average values per day. The curves are grouped by stages (S1 or S2) and by w_p , plotting together the values of 1.50 mm and 2.50 mm.

Figures 8.14a and 8.14b reveal that, for beams with $w_p=0.25$ mm, the crack width due to creep is bigger for the beams with a higher load level. This is true for all beams with the exception of beam S1_0.25_53.7% that, despite having a lower load level than other beams, exhibits a bigger values of w_c^j . The characteristic variability of the material in the

number of fibres crossing the crack (Buratti *et al.* 2011; Kanstad and Zirgulis 2012) may explain these results.

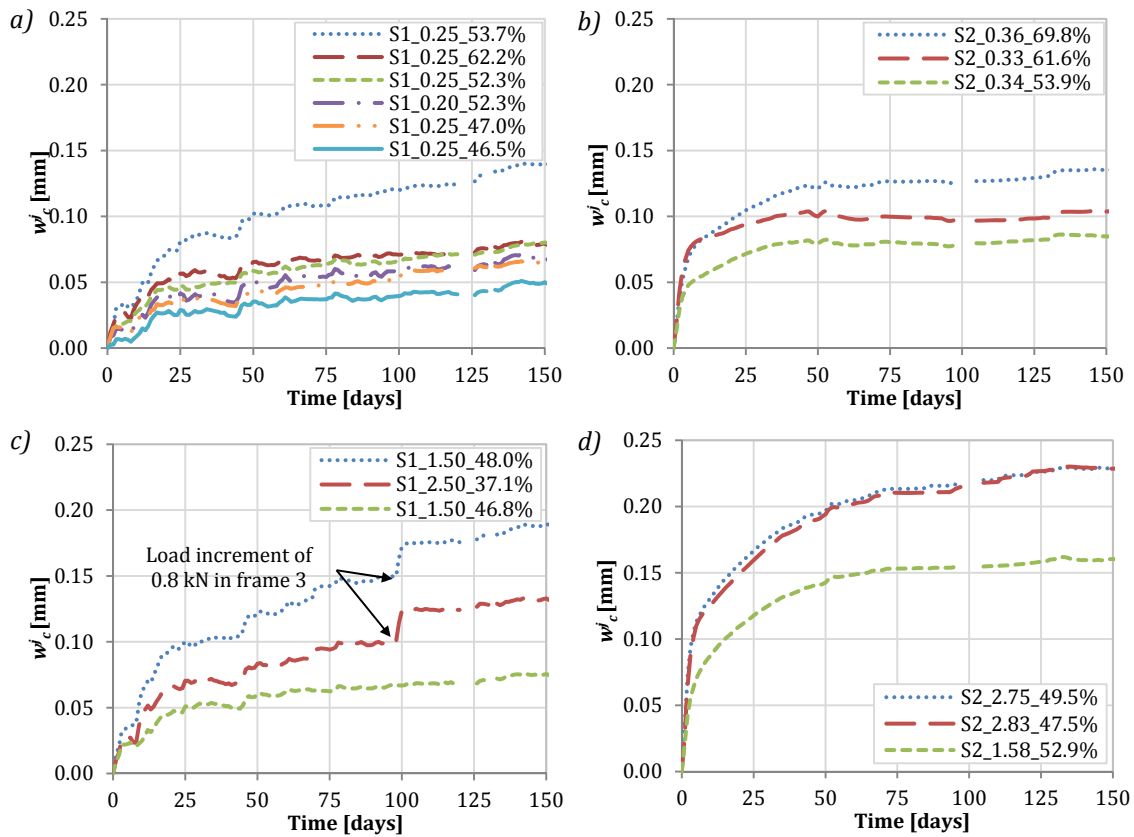


Figure 8.14 Crack width due to creep for S1 - a) $w_p=0.25$ mm, b) $w_p=1.50$ mm and $w_p=2.50$ mm - and for S2 - c) $w_p \approx 0.34$ mm, d) $w_p=1.58$ mm and $w_p \approx 2.80$ mm -.

Figure 8.14c indicates that for $w_p=1.50$ mm, the beam with a higher load level also presents bigger values of w_c^j . Regarding the beam with $w_p=2.50$ mm, it seems that the value of w_p is not always decisive in the value of w_c^j since the beam S1_1.50_48.0% presents bigger values of w_c^j . This result may be attributed to the relatively low load level of beam S1_2.50_37.1% and to the intrinsic variability of the material in the number of fibres crossing the crack. Furthermore, a sudden increase of the w_c^j is detected around day 100 for the beams S1_1.50_48.0% and S1_2.50_37.1%, which were placed in frame 3, as shown in Figure 8.5. This increase was due to an increment in the load applied in that frame of 0.8 kN which, however, did not seem to affect significantly the third beam in the frame (S1_0.25_47.0%) since no significant variation is observed in Figure 8.14a.

Figure 8.14d shows that beams with values of $w_p \approx 2.80$ mm (S2_2.75_49.5% and S2_2.83_47.5%) exhibit almost identical curves with bigger values of w_c^j than for the beam with $w_p=1.58$ mm, despite having the latter a slightly higher load level.

If the evolution of the crack width due to creep is plotted in logarithmic scale a change in the slope of the curve is detected in the results of S1 that is not identified in the results of S2. These curves are presented in Figure 8.15a for $w_p=0.25$ mm and in Figure 8.15b for $w_p=1.50$ mm and $w_p=2.50$ mm.

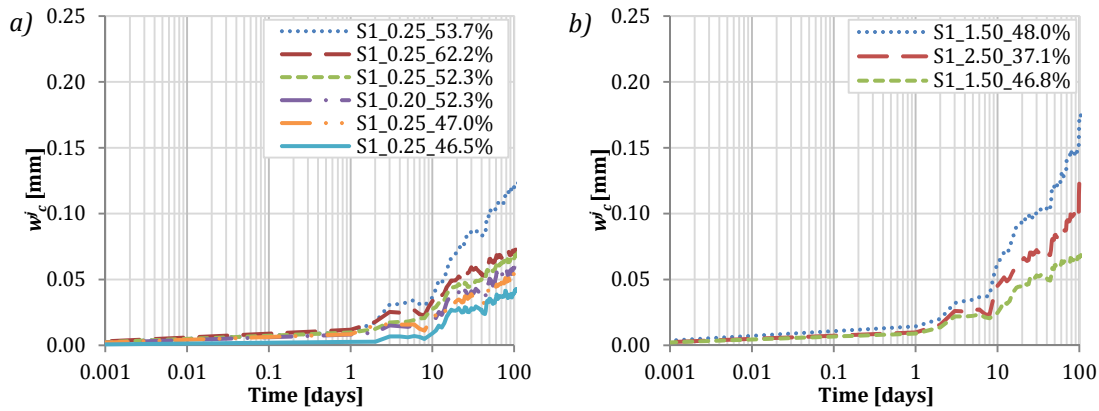


Figure 8.15 Evolution of w_c for S1 - a) $w_p=0.25$ mm, b) $w_p=1.50$ mm and $w_p=2.50$ mm -.

This change in the tendency of the crack width due to creep may be explained by the differences in the humidity and temperature conditions between the time the beams were stored (in controlled conditions) and the long-term test, which was in ambient conditions. Consequently, in addition to the effects of the sustained load, the beams were subjected to a drying procedure. This situation may lead to the change in the tendency observed in Figure 8.15.

With the aim of analysing in detail the crack width due to creep measured in the test, the values of the crack width due to creep at 90 days (w_c^{90}) and 150 days (w_c^{150}) and the total crack width at 90 days (w_t^{90}) and 150 days (w_t^{150}) are presented in Table 8.12.

Table 8.12 Crack width due to creep at 30, 90 and 150 days.

Beam	w_c^{30} [mm]	w_c^{90} [mm]	w_c^{150} [mm]	Δw_c^{30-90} [%]	Δw_c^{90-150} [%]
S1_0.20_52.3%	0.041	0.055	0.069	34.1	25.5
S1_0.25_46.5%	0.028	0.037	0.050	32.1	35.1
S1_0.25_47.0%	0.038	0.048	0.066	26.3	37.5
S1_0.25_52.3%	0.047	0.065	0.080	38.3	23.1
S1_0.25_53.7%	0.087	0.116	0.140	33.3	20.7
S1_0.25_62.2%	0.059	0.069	0.080	16.9	15.9
S1_1.50_46.8%	0.053	0.065	0.076	22.6	16.9
S1_1.50_48.0%	0.101	0.147	0.190	45.5	29.3
S1_2.50_37.1%	0.072	0.098	0.133	36.1	35.7
S2_0.33_61.6%	0.096	0.099	0.104	3.1	5.1
S2_0.34_53.9%	0.075	0.079	0.085	5.3	7.6
S2_0.36_69.8%	0.110	0.127	0.135	15.5	6.3
S2_1.58_52.9%	0.125	0.154	0.160	23.2	3.9
S2_2.75_49.5%	0.176	0.216	0.229	22.7	6.0
S2_2.83_47.5%	0.170	0.211	0.229	24.1	8.5

The values presented in Table 8.12 reveal that, in general, the highest increments correspond to the time between days 30 and 90. These are particularly significant in the beams of S1. The values of Δw_c^{90-150} are considerably lower for the beams of S2 than for the beams of S1. The reason for this difference may be attributed to the humidity and temperature conditions, which were different in S1 and S2 as described in section 8.2.4. It is interesting to note that some of the highest values of Δw_c^{90-150} correspond to the three beams in frame 3 (S1_0.25_47.0%, S1_1.50_48.0% and S1_2.50_37.1%) which experienced a sudden increment of load around day 100. For that reason, in the subsequent analysis the values of w_c^{90} are considered, thus avoiding the increment of load in frame 3.

The values of crack width due to creep at 90 days (w_c^{90}) are plotted as a function of the pre-cracking width and the load level in Figures 8.16a and 8.16b, respectively. The results in Figure 8.16a indicate that w_c^{90} increases with the value of w_p , in general for both series. Nevertheless, beams S1_0.25_53.7% and S1_1.50_48.0% remain outside this tendency (see points circled in green). These results may be explained, again, by the variability in the number of fibres crossing the crack. If these results are plotted against the load level, as shown in Figure 8.16b, it is difficult to observe a clear tendency. The points circled in green in Figure 8.16b seem to follow the same trend, increasing their value of w_c^{90} with the load level. However, the rest do not present this trend either by having a bigger pre-cracking width or by the unavoidable variability in the number of fibres crossing the crack.

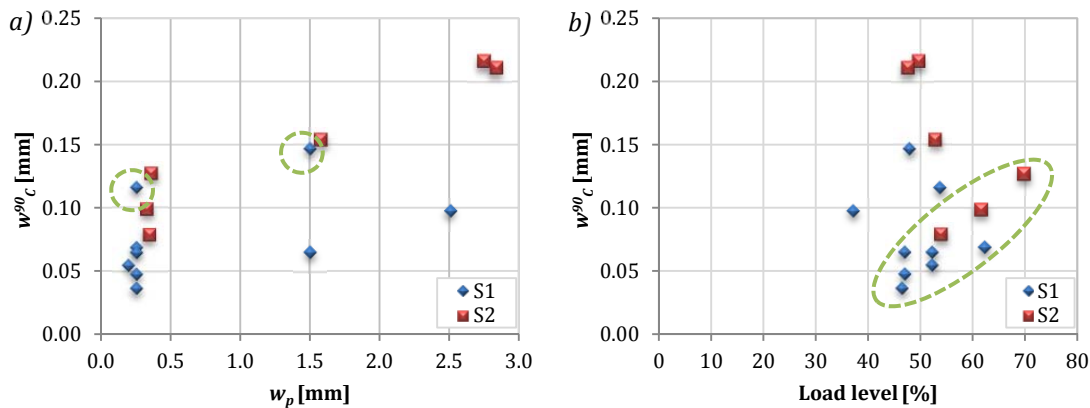


Figure 8.16 Crack width due to creep at 90 days as a function of a) w_p and b) the load level.

If the crack width due to creep w_c^j is differentiated with respect to time, the rate of creep deformation (in terms of crack width) may be obtained. This rate of crack width due to creep is plotted in Figure 8.17.

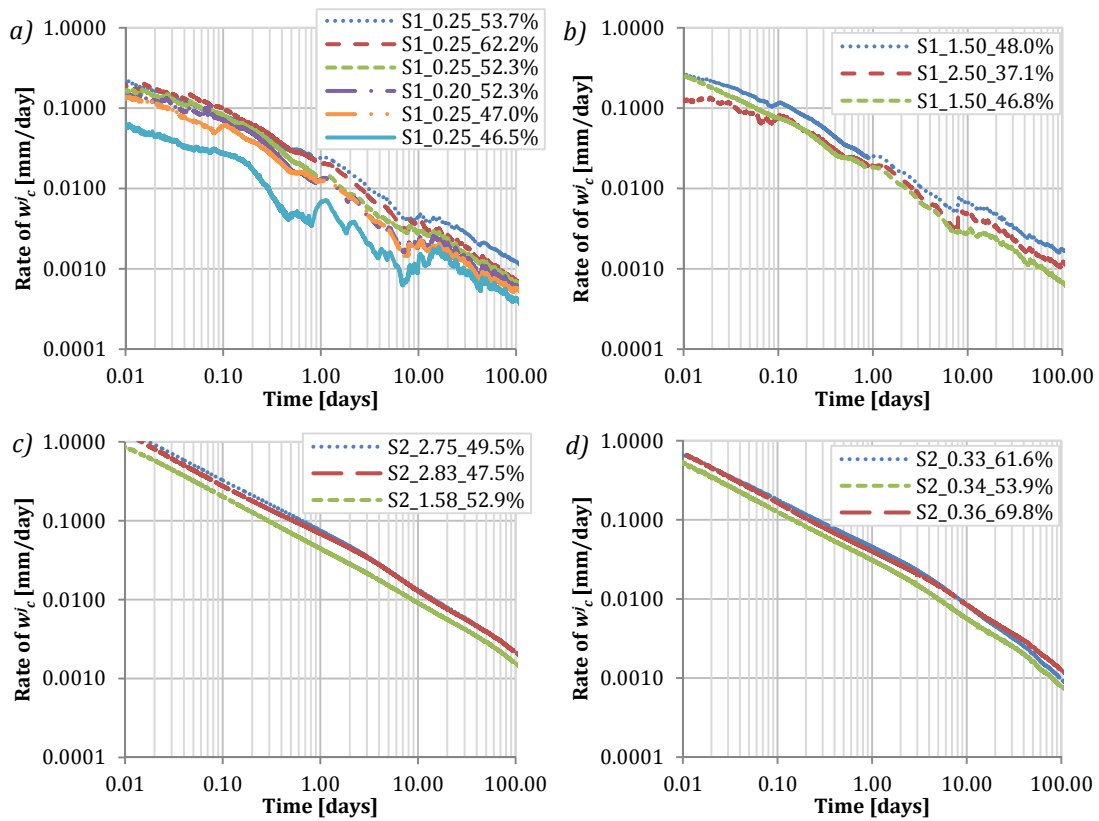


Figure 8.17 Evolution of the rate of w_c^j with time.

The curves reveal that the logarithm of the rate of w_c^j decreases with linear tendency with the logarithm of time. Additionally, it reached barely measurable levels after 100 days of loading, around 0.001 mm/day (or even smaller in some cases such as in Figure 8.17a), which represented a reduction of approximately 99%. This behaviour was already reported by Bernard (2010) regarding the creep of fibre reinforced shotcrete.

8.3.2. Evolution of the deflection

In the analysis of the deflection measured in beam S2_2.83_47.5%, the total deflection at a time j (δ_t^j) is defined as the summation of an initial deflection (δ_i) caused by the loading of the beam and a deflection due to creep (δ_c^j) that starts after the initial deflection, as indicated in expression (8.2). The values of δ_i , the deflection due to creep at 150 days (δ_c^{150}) and the total deflection at 150 days (δ_t^{150}) are presented in Table 8.13.

$$\delta_t^j = \delta_i + \delta_c^j \tag{8.2}$$

Table 8.13 Initial deflection, deflection due to creep and total deflection at 150 days.

Beam	δ_i [mm]	δ_c^{150} [mm]	δ_t^{150} [mm]
S2_2.83_47.5%	0.180	0.229	0.409

The evolution of the deflection due to creep is plotted in Figure 8.18a and its relation with the crack width due to creep is presented in Figure 8.18b. Notice that the values of deflection correspond to the average measured each day. This assumption was made since the average variations of the maximum and minimum values registered with respect to the average value measured each day are lower than 0.5%.

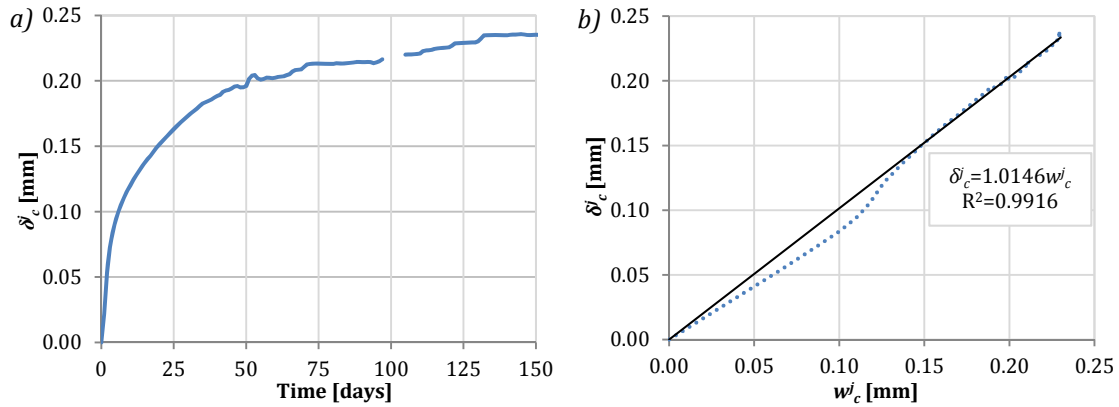


Figure 8.18 a) Deflection due to creep in beam S2_2.83_47.5% and b) relation between the crack width and the deflection due to creep in beam S2_2.83_47.5%.

The curve in Figure 8.18b reveals a linear relation between the crack width and the deflection due to creep measured in beam S2_2.83_47.5% with a correlation coefficient very close to 1.0. These results reveal that

8.3.3. Evolution of the creep coefficient

The creep coefficient for an instant t is defined as the ratio between the deformation due to creep and the elastic deformation. However, when the deformation is not directly measured, the creep coefficient may be determined by means of the crack width or the deflection as reported in several studies (Arango 2010; Buratti and Mazzotti 2012; Kanstad and Zirgulis 2012). Therefore, for the purpose of this research, the creep coefficient at a time j defined in terms of crack width (φ_w^j) is the ratio between the crack width due to creep (w_c^j) and the initial crack width (w_i), as indicated in expression (8.3).

$$\varphi_w^j = \frac{w_c^j}{w_i} \quad (8.3)$$

The evolution of the creep coefficient is presented in Figure 8.19 for each beam and the curves are grouped by stages (S1 or S2) and by the value of w_p . Notice that the values of 1.50 mm and 2.50 mm were plotted together.

The curves from Figure 8.19a reveal that the beams of S1 with a $w_p=0.25$ mm present a close values of φ_w^j , with the exception of beam S1_0.25_47.0%. In fact, this curve is closer to the evolution exhibited by beams in Figure 8.19c which also correspond to S1

but were pre-cracked up to 1.50 mm and 2.50 mm. The beams presenting the highest values of ϕ_w^j correspond to the three beams placed in frame 3 which, in addition, present three different values of w_p (beams S1_0.25_47.0%, S1_1.50_48.0% and S1_2.50_37.1%, as indicated in Figure 8.5). However, beam S1_1.50_46.8% (placed in frame 1) exhibits lower values of ϕ_w^j than beam S1_0.25_47.0%, even though it was pre-cracked up to a bigger crack width and loaded with a higher load level.

It must be remarked that the beams in frame 3 were subjected to a sudden increment of load of 0.8 kN, as previously indicated in section 8.3.1. This increment affected the curves in Figure 8.19c which otherwise would have a significant lower value of creep coefficient at 150 days, as may be observed from the tendency of the curves. Nevertheless, this statement cannot be made in the case of beam S1_0.25_47.0%.

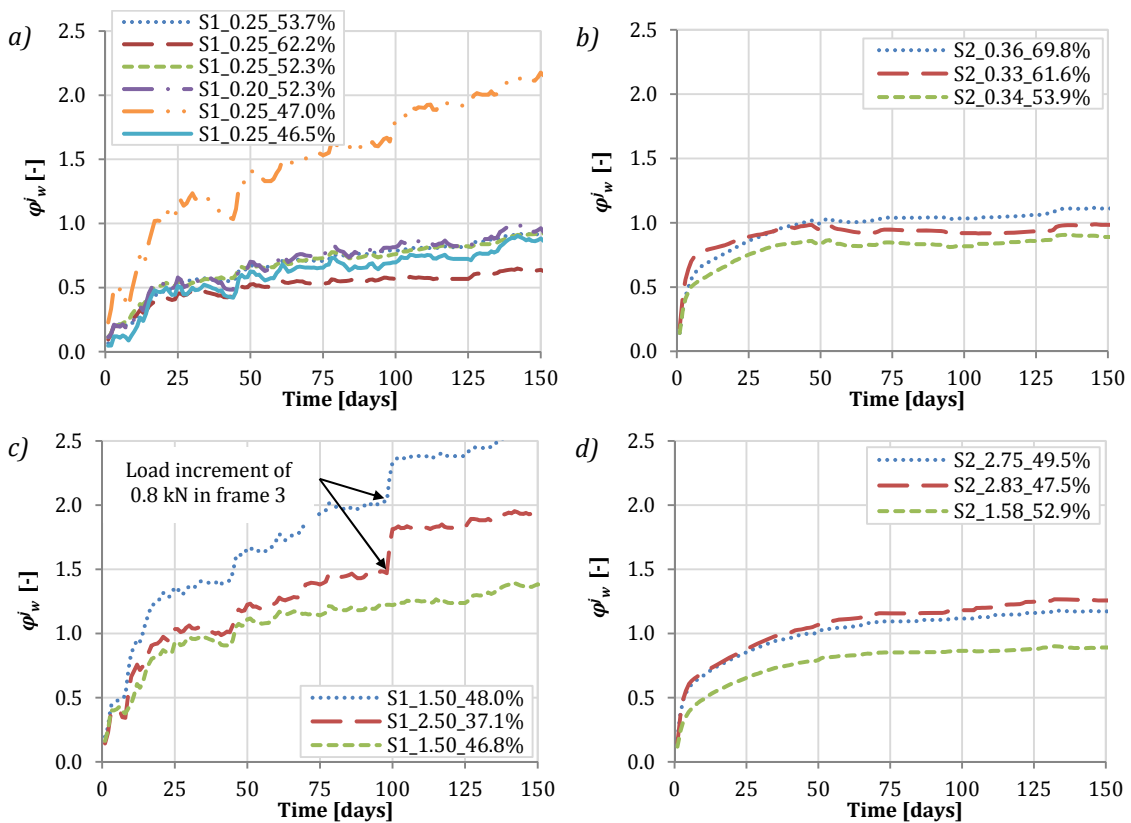


Figure 8.19 Creep coefficient for S1 - a) $w_p=0.25$ mm, b) $w_p=1.50$ mm and $w_p=2.50$ mm - and for S2 - c) $w_p \approx 0.34$ mm, d) $w_p=1.58$ mm and $w_p \approx 2.80$ mm -.

The beams of series S2 present very similar curves of the evolution of ϕ_w^j with time (see Figures 8.19c and 8.19d), stabilizing around day 75 with values close to 1.0. This similarity in the curves of S2 as opposed to the variability in the curves of S1 may be attributed to the relative humidity and temperature conditions. The variations of humidity and temperature in S2 are considerably smaller than in S1, thus confirming the influence of these two parameters in the creep deformations.

Table 8.14 shows the creep coefficient at 30 (φ_w^{30}), 90 (φ_w^{90}) and 150 days (φ_w^{150}). The results indicate that, in general, the bigger increments in the value of the creep coefficient occur between days 30 and 90. Afterwards, the curves tend to stabilize as observed in most beams in Figure 8.19 and, consequently, the increment in the value of $\Delta\varphi_w^{90-150}$ is lower. Nevertheless, a significant different behaviour is observed in the beams of S1 and S2 since the increments in S2 are much lower, 6.2% in average, whereas in the case of S2 this value reaches 26.6%. This difference may be explained by the different conditions of humidity and temperature previously mentioned. Additionally, it is also observed that some of the highest values of $\Delta\varphi_w^{90-150}$ correspond to the beams in S1 placed in frame 3, which experienced a sudden increment of load.

Table 8.14 Creep coefficient at 30, 90 and 150 days.

Beam	φ_w^{30} [-]	φ_w^{90} [-]	φ_w^{150} [-]	$\Delta\varphi_w^{30-90}$ [%]	$\Delta\varphi_w^{90-150}$ [%]
S1_0.20_52.3%	0.57	0.76	0.96	33.3	26.3
S1_0.25_46.5%	0.50	0.66	0.88	32.0	33.3
S1_0.25_47.0%	1.23	1.58	2.18	28.5	38.0
S1_0.25_52.3%	0.54	0.75	0.92	38.9	22.7
S1_0.25_53.7%	0.57	0.76	0.92	33.3	21.1
S1_0.25_62.2%	0.47	0.55	0.64	17.0	16.4
S1_1.50_46.8%	0.97	1.18	1.38	21.6	16.9
S1_1.50_48.0%	1.37	1.99	2.57	45.3	29.1
S1_2.50_37.1%	1.06	1.44	1.95	35.8	35.4
S2_0.33_61.6%	0.91	0.94	0.98	3.3	4.3
S2_0.34_53.9%	0.79	0.83	0.89	5.1	7.2
S2_0.36_69.8%	0.90	1.04	1.11	15.6	6.7
S2_1.58_52.9%	0.69	0.85	0.89	23.2	4.7
S2_2.75_49.5%	0.90	1.11	1.17	23.3	5.4
S2_2.83_47.5%	0.93	1.16	1.26	24.7	8.6

The values of creep coefficient at 90 days (φ_w^{90}) are plotted against the w_p and the load level in Figure 8.18.

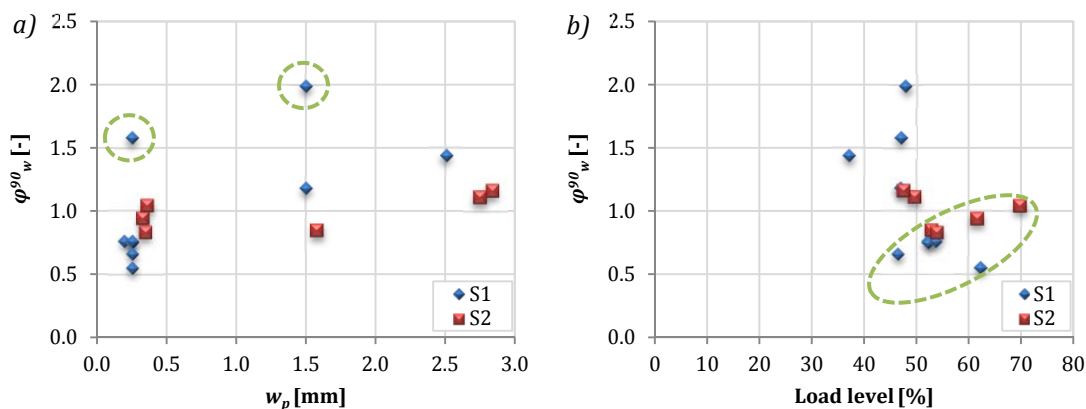


Figure 8.20 Creep coefficient for S1 -a) $w_p=0.25$ mm, b) $w_p=1.50$ mm and $w_p=2.50$ mm - and for S2: c) $w_p \approx 0.34$ mm, d) $w_p=1.58$ mm and $w_p \approx 2.80$ mm -.

The results indicate that, in general, the creep coefficient increases with the value of w_p except for the two points circled in Figure 8.18a that correspond to beams S1_0.25_47.0% and S1_1.50_48.0%. This same tendency may be observed in some of the beams in Figure 8.18b since the circled points increase their creep coefficient with the load. However, the rest of the beams remain outside this trend. This behaviour was already observed in the analysis of the crack width due to creep. The differences in the response of the beams with similar values of w_p and load levels may be attributed to the variability in the number of fibres crossing the crack or to the variations of humidity and temperature registered during S1.

8.4. RESULTS OF THE FAILURE TEST

Failure tests were performed after the long-term test as previously described in section 8.2.5. In this section, the results of such tests are presented and analysed. Figure 8.21 shows the load-crack width curves obtained in both stages. Notice that the crack width was measured with the same device used in the long-term test, placed 15 mm above the bottom surface of the beams and that the values presented correspond only to the crack width generated by the loading procedure of the failure test. It should be remarked that the results of beams S1_0.25_53.7%, S2_2.75_49.5%, S2_0.34_53.9% are not available since the tests failed due to problems with the control device.

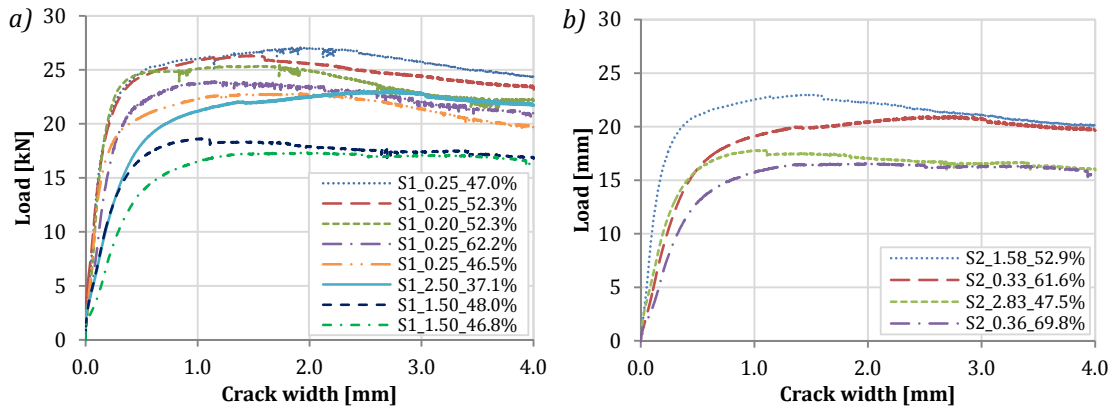


Figure 8.21 Failure tests of beams of series a) S1 and b) S2.

The curves in Figure 8.21a indicate that the beams with a better performance correspond to those pre-cracked up to 0.25 mm, while the beams with bigger values of w_p (S1_2.50_37.1% and S1_1.50_48.0%) exhibit a lower response. In the case of S2, Figure 8.21b shows that the response of the beams not only depends on the value of w_p but also of the load level (notice that the beams in S2, in general, were subjected to higher load levels than the beams in S1).

For instance, the beam which presents the best performance is S2_1.58_52.9%, that has a bigger value of w_p than beam S2_0.33_61.6%. However, the latter experienced a

higher load level during the long-term test which may explain the reason for such response. The beam with the biggest value of w_p is S2_2.83_47.5% and, despite being pre-cracked up to 2.83 mm, shows a better response than beam S2_0.36_69.8% which was subjected to a load level close to 70%.

8.5. PREDICTION OF THE CREEP COEFFICIENT

In this section, the formulations included in the EHE-08 and the MC2010 to predict the evolution of the creep coefficient with time are presented and applied to the experimental tests conducted, thus comparing the prediction provided by the formulations and the experimental curves. It should be remarked that these formulations are empirical and calibrated on the basis of creep tests in compression for plain concrete, whereas the focus of the experimental program was the flexural behaviour. Nevertheless, these are the only formulations provided in codes and recommendations to predict the creep coefficient; hence the interest in analysing how close is their prediction to the experimental results.

Furthermore, despite Bažant and Oh (1984) propose a creep coefficient in tension that is three times greater than in compression, most studies assume the same model in compression and tension (Marí 2000; Torres Llinàs 2001).

8.5.1. Formulation in the EHE-08

According to the EHE-08, the creep coefficient may be obtained by means of the expression (8.4), where φ_0 is the basic creep coefficient and $\beta_c(t-t_0)$ is the function that describes the development of creep with time.

$$\varphi(t, t_0) = \varphi_0 \beta_c(t - t_0) \quad (8.4)$$

The basic creep coefficient (φ_0) may be determined by means of expression (8.5), where: φ_{HR} is the coefficient that considers the influence of the relative humidity (HR), $\beta(f_{cm})$ is a factors that allows taking into account the strength of concrete and, finally, $\beta(t_0)$ factor that includes the influence of the age of concrete at the moment of loading (t_0).

The expressions for φ_{HR} , $\beta(f_{cm})$ and $\beta(t_0)$ are (8.6), (8.7) and (8.8), respectively.

$$\varphi_0 = \varphi_{HR} \beta(f_{cm}) \beta(t_0) \quad (8.5)$$

$$\varphi_{HR} = \left[1 + \frac{1 - \frac{HR}{100}}{0.1 \sqrt[3]{e}} \alpha_1 \right] \alpha_2 \text{ for } f_{cm} > 35 \text{ N/mm}^2 \quad (8.6)$$

$$\beta(f_{cm}) = \frac{16.8}{\sqrt{f_{ck} + 8}} \quad (8.7)$$

$$\beta(t_0) = \frac{1}{0.1 + t_0^{0.2}} \quad (8.8)$$

The function defining the evolution of creep with time ($\beta_c(t-t_0)$) is defined as shown in expression (8.9).

$$\beta_c(t - t_0) = \left[\frac{(t - t_0)}{\beta_H + (t - t_0)} \right]^{0.3} \quad (8.9)$$

The parameters β_H , α_1 , α_2 and α_3 are defined by the expressions (8.10) and (8.11). In the previous expressions, f_{cm} is the average compressive strength, HR is the relative humidity of the ambient environment in %, e is the average thickness in mm and equals the ratio between the cross section of the specimen and the effective perimeter in contact with the atmosphere.

$$\beta_H = 1.5[1 + (0.012HR)^{18}]e + 250 \leq 1500\alpha_3 \text{ for } f_{cm} > 35 \text{ N/mm}^2 \quad (8.10)$$

$$\alpha_1 = \left[\frac{35}{f_{cm}} \right]^{0.7} ; \alpha_2 = \left[\frac{35}{f_{cm}} \right]^{0.2} ; \alpha_3 = \left[\frac{35}{f_{cm}} \right]^{0.5} \quad (8.11)$$

8.5.2. Formulation in the Model Code 2010

The Model Code proposes a different approach from the EHE-08 to determine the creep coefficient. In this case, the total creep is separated into the components basic creep (φ_{bc}) and drying creep (φ_{dc}), as shown in expression (8.12). This approach assumes a linear behaviour and applies the principle of superposition. Nevertheless, given that the actual behaviour is non-linear, some prediction errors are inevitable.

$$\varphi(t, t_0) = \varphi_{bc}(t, t_0) + \varphi_{dc}(t, t_0) \quad (8.12)$$

The basic creep coefficient (φ_{bc}) may be calculated as indicated in expression (8.13). The parameters $\beta_{bc}(f_{cm})$ and $\beta_{bc}(t, t_0)$ are defined in expressions (8.14) and (8.15).

$$\varphi_{bc}(t, t_0) = \beta_{bc}(f_{cm})\beta_{bc}(t, t_0) \quad (8.13)$$

$$\beta_{bc}(f_{cm}) = \frac{1.8}{(f_{cm})^{0.7}} \quad (8.14)$$

$$\beta_{bc}(t, t_0) = \ln \left(\left(\frac{30}{t_{0,adj}} + 0.035 \right)^2 (t - t_0) + 1 \right) \quad (8.15)$$

The drying creep coefficient (φ_{dc}) may be estimated as shown in expression (8.16). The parameters $\beta_{dc}(f_{cm})$, $\beta(RH)$, $\beta_{dc}(t_0)$ and $\beta_{dc}(t, t_0)$ are defined by the expressions (8.17), (8.18), (8.19) and (8.20).

$$\varphi_{dc}(t, t_0) = \beta_{dc}(f_{cm})\beta(RH)\beta_{dc}(t_0)\beta_{dc}(t, t_0) \quad (8.16)$$

$$\beta_{dc}(f_{cm}) = \frac{412}{(f_{cm})^{1.4}} \quad (8.17)$$

$$\beta(RH) = \left[1 + \frac{1 - \frac{RH}{100}}{\sqrt[3]{0.1 \frac{h}{100}}} \right] \quad (8.18)$$

$$\beta_{dc}(t_0) = \frac{1}{0.1 + t_{0,adj}^{0.2}} \quad (8.19)$$

$$\beta_{dc}(t, t_0) = \left[\frac{(t - t_0)}{\beta_h + (t - t_0)} \right]^{\gamma(t_0)} \quad (8.20)$$

The parameters γ_{t_0} , β_h may be estimated as indicated in expressions (8.21) and (8.22). The parameter $\alpha_{f_{cm}}$ is defined by the expression (8.23).

$$\gamma(t_0) = \frac{1}{2.3 + \frac{3.5}{\sqrt{t_{0,adj}}}} \quad (8.21)$$

$$\beta_h = 1.5 h + 250\alpha_{f_{cm}} \leq 1500\alpha_{f_{cm}} \quad (8.22)$$

$$\alpha_{f_{cm}} = \left(\frac{35}{f_{cm}} \right)^{0.5} \quad (8.23)$$

In the previous expressions, f_{cm} is the average compressive strength, RH is the relative humidity of the ambient environment in %, h is the notional size of the member in mm. As in the case of the EHE, this parameter is defined by the ratio between the cross section and the semi-perimeter of the specimen in contact with the atmosphere.

8.5.3. Results

The prediction of the evolution of the creep coefficient provided by the EHE-08 and the MC2010 are compared with the evolution of the experimental creep coefficient of all beams in Figure 8.22. Notice that the value of relative humidity used in the predictions corresponds to the average of the values registered during the long-term test.

The curves reveal that, in general, the prediction provided by the EHE-08 and the MC2010 underestimate the values of the creep coefficient, particularly in the case of the

MC2010. The prediction of the EHE-08 is accurate in the first stages and the shape of the curve is very similar to the tendency observed in the experimental curves. However, the MC2010 provides a curve that becomes closer to the experimental curves with time, presenting a significant difference in the early stages.

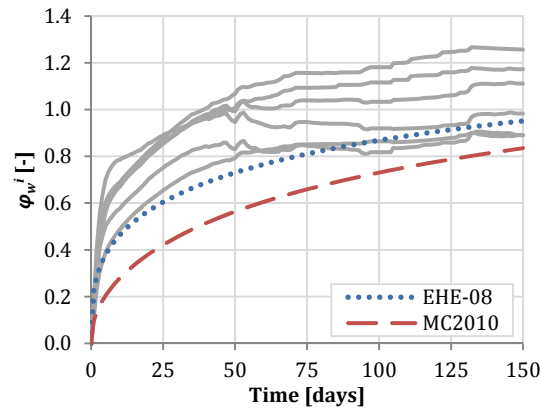


Figure 8.22 Evolution with time of the experimental and predicted creep coefficients for S2.

In order to analyse in detail these results, the creep coefficients at 30 days, 90 days and 150 days are presented in Table 8.15.

Table 8.15 Experimental and predicted creep coefficients at 30, 90 and 150 days.

Beam	φ_w^{30} [-]	φ_w^{90} [-]	φ_w^{150} [-]
EHE-08	0.64	0.85	0.95
MC2010	0.46	0.70	0.83
S2_2.75_49.5%	0.90	1.11	1.17
S2_1.58_52.9%	0.69	0.85	0.89
S2_0.34_53.9%	0.79	0.83	0.89
S2_0.33_61.6%	0.91	0.94	0.98
S2_0.36_69.8%	0.90	1.04	1.11
S2_2.83_47.5%	0.93	1.16	1.26

The results show that the difference of the predictions by the EHE-08 and the MC2010 with the closest experimental curve (corresponding to beam S2_1.58_52.9%) are 7.8%, 0.0% and 6.7% for 30, 90 and 150 days, respectively, for EHE-08 and 50.0%, 17.6% and 6.7% for 30, 90 and 150 days, respectively, for the MC2010. The prediction of both models presents the biggest differences with beam S2_2.83_47.5%. These variations are 31.2%, 26.7% and 24.6% for 30 days, 90 days and 150 days, respectively, for EHE-08. In the case of the MC2010, these percentages are 50.5%, 39.7% and 34.1% for 30 days, 90 days and 150 days, respectively.

In addition to the fact that these models were calibrated by means of compression tests, the MC2010 points out that due to the inherent scatter of creep and shrinkage deformations, the errors of the model and the general uncertainty caused by randomness of the properties of the material and the environment, a prediction on the deformation

may result in considerable error. If, additionally, the characteristic variability of the FRC properties (due to the fibre reinforcement itself) is included in the previous considerations, the error may increase significantly. Considering the aforementioned and in view of the results, it may be concluded that even though the EHE-08 provides a curve that is close to the experimental curves, these formulations do not represent satisfactorily the behaviour observed experimentally.

8.6. CREEP MODEL

In this section, a formulation based on rheological models is proposed to find performance curves that are representative of the response exhibited by the beams of S2. For the purpose of this study, only the beams of S2 are considered since they were under climate-controlled conditions and presented an average compressive strength that according to the EHE-08 corresponds to a conventional concrete.

In the study by Bernard (2010), the viscoelastic model described by Findley *et al.* (1976) was used to model the time-dependent creep behaviour of FRS panels (reinforced with either steel or synthetic fibres). It consisted in a four-element viscoelastic model with elastic elements (spring) and viscous elements (dashpot), as shown in Figure 8.23a. However, for the purpose of this study, a simplification of this model was considered and resulting in a two-element viscoelastic model (see Figure 8.23b), which may also be known as a Maxwell model (Neville *et al.* 1983).

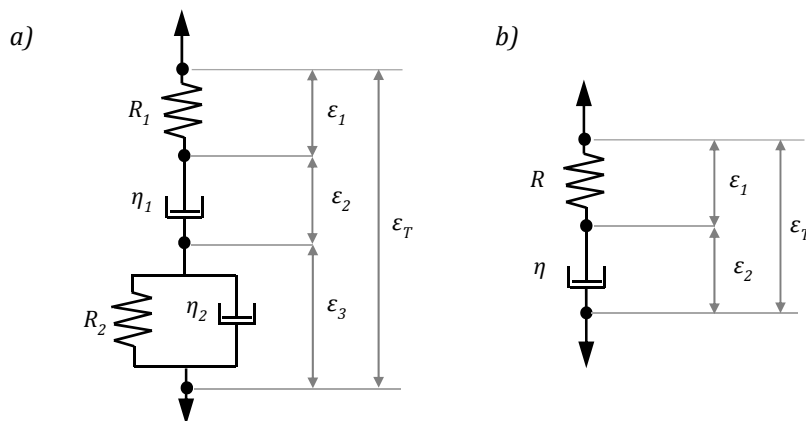


Figure 8.23 a) Four-element viscoelastic model of creep in Findley *et al.* (1979) and b) simplified version of two-element viscoelastic model of creep.

Therefore, for the simplified model applied in this study the total strain (ε_T) exhibited by the SFRC under a sustained stress (σ) may be defined as the summation of two components as indicated in expression (8.24).

$$\varepsilon_T = \varepsilon_1 + \varepsilon_2 \quad (8.24)$$

The first component (spring) corresponds to the elastic (non-linear) behaviour of the SFRC, while the second component (dashpot) represents the viscoelastic behaviour. Considering R as a resistance parameter (the spring constant) and η as a damping coefficient (related to the dashpot), the parameters ε_1 and ε_2 may be expressed as indicated in (8.25) and (8.26). Notice that t represents time and B is a constant value.

$$\varepsilon_1 = \frac{\sigma}{R} \quad (8.25)$$

$$\varepsilon_2 = \frac{\sigma}{\eta} t^B \quad (8.26)$$

In the present study, the stress to which the concrete and the fibres in the crack were subjected is unknown. However, the model herein proposed aims at predicting the performance curve of the creep coefficient that, as previously, described may be expressed as indicated in (8.27).

$$\varphi_\varepsilon = \frac{\varepsilon_T - \varepsilon_1}{\varepsilon_1} = \frac{\varepsilon_2}{\varepsilon_1} \quad (8.27)$$

If expressions (8.25) and (8.26) are considered, the expression for creep coefficient (φ_ε) may be rewritten as shown in (8.28).

$$\varphi_\varepsilon = \frac{\varepsilon_T - \varepsilon_1}{\varepsilon_1} = \frac{\varepsilon_2}{\varepsilon_1} = \frac{R}{\eta} t^B \quad (8.28)$$

Given that the deformation was not directly measured in this study, the creep coefficient was determined by means of the crack width as an approximation. Therefore, the creep coefficient in terms of crack width (φ_w) is proportional to the expression (8.28) and may be expressed as indicated in (8.29), where A is a constant value.

$$\varphi_w = At^B \quad (8.29)$$

In fact expression (8.28) was already presented by other authors, as reported by (Neville *et al.* 1983), to obtain the creep coefficient of concrete and, afterwards, it was re-advocated for basic creep. In this case, the expression is proposed for SFRC with the values A and B defined as functions of the initial crack width (w_i) and the average load applied to each beam (F_c), as indicated in expressions (8.30) and (8.31).

These parameters (w_i and F_c) were chosen as input values since they provide the best fit with the evolution of the creep coefficient (φ_w) with time. The functions A and B were obtained by means of the LabFit Curve Fitting Software and were selected due to their fit with the input parameters (w_i and F_c). The correlation with expression (8.30) is $R^2=0.899$ and with expression (8.31) is $R^2=0.702$.

$$A = \frac{w_i - 0.123}{2.179F_c - 31.743} + 1.859w_i \quad (8.30)$$

$$B = 0.539w_i^{\left(\frac{9.438}{F_c}\right)} \quad (8.31)$$

The curves of evolution of creep coefficient predicted with the model are compared with the experimental curves in Figure 8.24. A general overview reveals that the model predicts satisfactorily the evolution of the creep coefficient with time. In order to analyse in detail these results, the experimental and predicted creep coefficients at 30, 90 and 150 days are presented in Table 8.16. Likewise, the variation of the predicted value with respect to the experimentally obtained is also included.

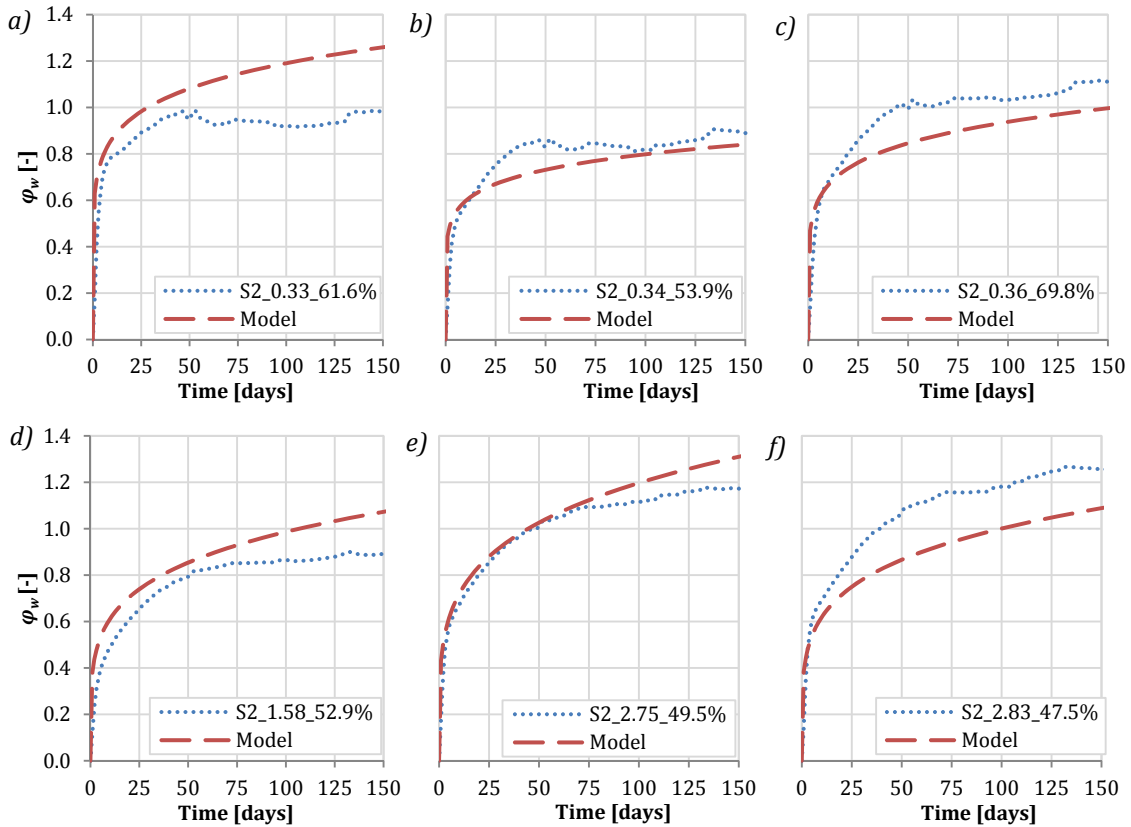


Figure 8.24 Experimental and predicted evolution of φ_w for beams of series S2.

Table 8.16 Experimental and predicted creep coefficient at 30, 90 and 150 days.

Beam	φ_w^{30} [-]		φ_w^{90} [-]		φ_w^{150} [-]		Variation [%]		
	Exp.	Model	Exp.	Model	Exp.	Model	φ_w^{30}	φ_w^{90}	φ_w^{150}
S2_2.75_49.5%	0.90	0.92	1.11	1.17	1.17	1.31	2.2	5.4	12.0
S2_1.58_52.9%	0.69	0.77	0.85	0.96	0.89	1.07	11.6	12.9	20.2
S2_0.34_53.9%	0.79	0.69	0.83	0.79	0.89	0.84	-12.7	-4.8	-5.6
S2_0.33_61.6%	0.91	1.01	0.94	1.17	0.98	1.26	11.0	24.5	28.6
S2_0.36_69.8%	0.90	0.78	1.04	0.92	1.11	1.00	-13.3	-11.5	-9.9
S2_2.83_47.5%	0.93	0.78	1.16	0.98	1.26	1.09	-16.1	-15.5	-13.5

The results indicate that, in general, the variation between the predicted and the experimental value is bigger with time. Nevertheless, there are beams that present the inverse tendency. Furthermore, from the six beams studied, the prediction overestimates the values of the creep coefficient in three of the cases, remaining on the safe side; whereas the values of the other three are underestimated. A clear trend on the accuracy of the model depending on the pre-cracking width or the load level applied cannot be identified.

It is important to remark that the model representing the performance curve of SFRC under sustained loads in post-cracking conditions is based on the experimental program conducted which entailed a small number of tests and considered a limited number of variables. In order to extrapolate this model to other conditions or to propose a creep coefficient for SFRC, further research should be performed regarding the influence of fibre content, fibre type, higher load levels, etc.

8.7. CONCLUDING REMARKS

Chapter 7 discussed the results of an experimental program undertaken to study the post-cracking creep flexural behaviour of SFRC. The following conclusions can be drawn from the study conducted.

- The rate of crack width due to creep decreased progressively, reaching very low values (0.001 mm/day) after 100 days of sustained load.
- The beams under climate-controlled conditions exhibited creep coefficients for the SFRC around 1.0 and 1.2 after 150 days of loading for the beams with smallest pre-cracking widths, whereas the beams pre-cracked up to higher crack widths exhibited creep coefficients close to 1.4. However, these values should be considered with caution due to the reduced number of tests conducted in the study.
- The beams tested in ambient conditions presented higher values of crack width due to creep and creep coefficient than the beams under climate-controlled conditions. The reason for that are the changes in relative humidity and temperature conditions registered for the beams in ambient conditions. Moreover, the variations in the behaviour among the beams exposed to ambient conditions were greater than that observed among the beams under climate-controlled conditions.
- The formulations proposed in the EHE-08 and the MC2010 to estimate the creep coefficient are not suitable to predict the long-term flexural behaviour of the SFRC. Despite that the estimation of the EHE-08 is close to some of the experimental curves, in general, both models underestimate the creep coefficient. The cause for such outcome may be attributed to the fact that the models are based on creep tests in compression for plain concrete.

- The simplified two-element viscoelastic model proposed represents satisfactorily the experimental response, considering the number of tests conducted in the experimental program.

9. CONCLUSIONS AND FUTURE PERSPECTIVES

9.1. GENERAL CONCLUSIONS

The steel fibre reinforcement technology has experienced great advances in the past 20 years. However, several aspects still require further research. For that reason, a rather generalist doctoral thesis was proposed, focusing on 4 specific issues: the adequacy of the current constitutive models to simulate the flexural performance of RC-SFRC beams; the structural response, fibre orientation and modelling of SFRC slabs with different geometry; the proposal of an alternative constitutive model based on the Barcelona test and, finally, the assessment of the post-cracking creep behaviour of SFRC. Subsequently, the general conclusion of each of the subjects is presented in response to the general objectives defined in Chapter 1. Specific conclusions will be presented in the following section.

Regarding the first subject, it is demonstrated that the current constitutive models in European codes and recommendations provide satisfactory predictions of the flexural behaviour of RC-SFRC beams. It should be remarked that if the beams were only reinforced with steel fibres, a higher difference between the prediction of the models and the experimental curves might have been observed due to predominant influence of the fibre reinforcement. Nevertheless, despite the performance of such beams is highly affected by the traditional reinforcement, a significant contribution of the two types of steel fibres is observed in the analysis of the experimental results.

The second subject represents a contribution to the comprehension of the flexural behaviour of SFRC slabs with different dimensions. In this context, the study not only focuses on the experimental behaviour of the slabs but also on the fibre orientation and on the modelling of their response. The study conducted demonstrates the influence of the geometry in the fibre orientation and, in turn, the influence of the latter in the structural response of the slabs. In this regard, the most significant contribution is the observation of a fibre network effect that leads to an enhanced sectional response as the width of the slabs increases. This phenomenon, which may be attributed to the favourable orientation of the fibres regarding the cracking plane, is quantified by means of a factor that increases with the width.

Another relevant conclusion from the study is that the existing constitutive models are not suitable for the design of SFRC slabs. The results of the numerical simulations performed with these models overestimate the structural response measured during the test. The main cause of this outcome is the low representativeness of the beam test as a method for the characterization of the flexural behaviour of the slabs. In order to compensate such phenomenon, geometry factors that take into account the fibre network effect and, indirectly, the internal hyperstaticity of the structure provided by the fibres are proposed for the cases studied. These geometry factors correct the values of the σ - ε diagram obtained from the beam test.

The third subject entails a significant advance since it presents the first formulation to estimate σ - ε relation in tension directly from the Barcelona test, thus representing an alternative to the models based on the performance of small beams. According to the study conducted, the new constitutive model is valid for concrete reinforced with either steel or plastic fibres.

In the fourth subject, it is verified that the rate of the crack width due to creep decreases progressively with time. In fact, the value of the creep coefficient stabilizes after 5 months, exhibiting almost a constant value at that time for the beams under climate-controlled conditions. The model proposed to predict the evolution of the creep coefficient reproduces satisfactorily the experimental data, even though a limited number of tests were performed.

9.2. SPECIFIC CONCLUSIONS

Several specific objectives are proposed in Chapter 1 for each of the subjects studied. In response to these specific objectives, the contributions made are described in detail in the chapters of this doctoral thesis. With the aim of providing a general overview of the contributions, the main specific conclusions of each subject addressed in the thesis are presented next.

RC-SFRC beams

- The crack spacing is reduced by the addition or the increase in the steel fibres content. Even though this statement is generally true, in certain cases such behaviour is not so clear. The expressions proposed in the guidelines (RILEM and CNR-DT 204) underestimate the crack spacing most likely due to the presence of transversal reinforcement in the RC-SFRC beams.
- The beams with fibres show a significant reduction in the crack width if compared with the control beams without fibres. This is even more evident when the fibre content increases. For example, the crack width associated to a load of 40 kN for a beam with a fibre content of 0.50% in volume is approximately 50% smaller than the measured for a beam with a content of 0.25% subjected to the same load level.
- The maximum contribution of the fibres was observed for crack widths between 0.55 mm and 0.80 mm (depending on the type and amount of fibres). Their contribution stabilizes around 1.2 mm and 1.4 mm. In addition to that, it was verified that the short fibres turn out to be more active in the first stages of the cracking, while the long fibres continue to control the cracking and provide ductility for larger deformations. The RILEM formulation to predict the average crack width provides satisfactory results once the cracking stabilizes.
- The analysis of the load-deflection curves reveals the contribution of the fibres to control the deflection and to increase the slopes of the curve or the stiffness of the element, which is noticeable at all stages. Furthermore, the energy absorption increment relative to the control beams doubles when the fibre content doubles.
- The constitutive models based on the beam test, in general, reproduce satisfactorily the flexural behaviour of the RC-SFRC beams. However, the approach proposed in the DBV is conservative in the prediction of the flexural response of the beams for large deflections, underestimating the load value in such case by approximately 19%. This difference may be attributed to the use of a coefficient that takes into account the scatter of the flexural tests, penalizing the post-cracking response for high coefficients of variation.
- The model proposed by the RILEM overestimates the flexural behaviour of the RC-SFRC beams for small deflections, reaching values approximately 45% higher than the experimental data. In fact, such outcome was already reported in the literature and new parameters were proposed to define the σ - ε diagram.
- The models proposed by the CNR-DT 204, the EHE-08 and the MC2010 overestimate the response of the beams for small deflections (around 30%). As the deflection increases, the differences with the experimental data become smaller. In general, these models provide satisfactory estimation of the response.

SFRC slabs

- The response of the full-scale SFRC slabs reveals the capacity of the steel fibres as the only reinforcement to resist stresses and provide ductility for the load levels reached during the experimental program.
- The flexural response of the slabs is different according to their geometry. The slabs S (0.2 x 1.5 x 3.0 m) exhibit the highest load values. The average maximum load of slabs S is 7.0% and 16.3% higher than that of slabs M and L, respectively. These minor differences indicate that the residual strength and the ductility provided by the fibres allow the bigger slabs to reach load levels close to the smaller ones.
- A common crack pattern is identified in all slabs. In general, it consists of four main cracks that develop from the centre to the edges where the supports were located. In the case of the bigger slabs, which reached large deflections, secondary cracks are also detected.
- The energy absorption capacity studied in terms of the area enclosed by the load-deflection curve is remarkably higher for slabs L than the estimated for slabs M and S. In fact, the absorbed energy for a rotation angle of 0.01 rad in slab L is 43.5% and 80.9% higher than the estimated for slabs M and S, respectively. This behaviour reveals a significant stress redistribution capacity of the larger slabs (particularly slab L), whereas slabs S present a limited redistribution capacity. In fact, the behaviour of slabs S is strongly affected by their geometry, working almost exclusively in the shortest direction.
- The study of the fibre orientation in the slabs indicates that in radial flows or extensional flows, the fibres tend to rotate and align perpendicular to the flow as they advance from where the concrete is poured to the edges of the formwork. This is more noticeable as the fibres are subjected to the concrete flow for a longer period.
- A fibre orientation pattern was proposed based on the fibre orientation observed in the slabs. This pattern suggests the division of a random slab in three main zones of orientation. The central zone presents a similar percentage of fibres aligned along X and Y axes, whereas the external zone is characterized by a significant difference in the alignment of fibres along both axes due to the flow and the wall effects. The transition zone marks the change between the other two.
- The multidirectional method used to determine the contribution of the fibres in the post-cracking response of the material reveals that, in general, when a high percentage of fibres are aligned along the testing direction, low values of residual

load are obtained. These results might have been affected by differences in the fibre content and the presence of cracks in the specimens extracted from the slabs.

- The numerical simulation shows that the constitutive models in the RILEM and the EHE-08 are not suitable to predict the flexural response of the SFRC slabs, leading to a significant overestimation of the experimental data. In fact, the predicted maximum loads were approximately 60% higher for slabs M and L and 90% higher for slab S than the value registered during the tests.
- The parametric study conducted with the trilinear constitutive diagram (defined by the parameters σ_1 , σ_2 , σ_3 , ε_1 , ε_2 and ε_3) shows that the stress σ_2 is the parameter with the biggest influence over the structural response of the slabs (notice that σ_1 , ε_1 and ε_3 are kept constant in the study). Such parameter influences particularly the maximum load and the energy absorption capacity. The stress σ_3 and the strain ε_2 lead to minor changes in the response of the slabs if compared to σ_2 .
- A numerical fit of the parameters of a trilinear constitutive model was performed for the slabs S, M and L in order to obtain a response that approaches the experimental results. In this procedure, it was detected that one of the characteristics of the P - δ curves most difficult to reproduce accurately was the slope at the final stretch of the curve. Furthermore, the stress values obtained in the analysis for the σ - ε diagrams are considerable smaller than the ones proposed by the EHE-08 and the RILEM. Depending on the size of the slab, reductions between 40%-60% in the value of σ_2 proposed by the EHE-08 are required to fit the experimental results.
- The comparison of the σ - ε diagrams proposed with the numerical fit for each type of slab allowed identifying a fibre network effect, characterized by the increment in the stress bearing capacity in the sectional level as the width increases. In fact, the value of the stress σ_2 for slabs M and L was 17.1% and 42.1% higher than that of slab S. This result may be attributed to a favourable fibre orientation regarding the cracking planes in bigger slabs. Such phenomenon is quantified for the cases studied by means of a fibre network effect factor that presents higher values as the width to length ratio increases.
- A simple method based on geometry factors that take into account the fibre network effect and, indirectly, the internal hyperstaticity of the structure provided by the fibres was proposed to obtain suitable σ - ε diagrams for the design of SFRC slabs.

Predicting the tensile behaviour of SFRC

- An analytical formulation was proposed to estimate σ - ε constitutive model for FRC based on the results of the Barcelona test. The formulation proposed was

simplified in the form of a multilinear σ - ε model in which the values of strain are predefined. This simplified version of the model enables an easy implementation in the current design tools.

- The new constitutive model (BCN model) was validated by comparing experimental data with the numerical simulation of the Barcelona test. Despite some differences, the model yields results with a tendency and absolute values similar to those from the experimental test, although overestimating the post-cracking response. Considering the particularities in the post-cracking behaviour of FRC and the difficulty to simulate the Barcelona test in a finite element model, the results indicate that the simplified model is capable of predicting the FRC tensile response.
- The comparison of the BCN model with the constitutive models in European codes and guidelines based on beam tests revealed that, in average, the former remains between the DBV and the RILEM.

Long-term behaviour of SFRC

- The crack width due to creep rate decreases progressively reaching very low values after 100 days of sustained load (around 0.001 mm/day).
- The creep coefficient exhibited by the SFRC of the beams under climate-controlled conditions stabilized after 5 months, reaching values around 1.0 and 1.2 for the beams with smaller values of pre-cracking width. For the beams pre-cracked up to higher crack widths, the creep coefficient of the SFRC was close to 1.4. Nevertheless, these values should be taken with caution given the reduced number of tests conducted in the study.
- The SFRC beams exposed to ambient conditions exhibited, in general, higher values of crack width due to creep and creep coefficient than the beams under climate-controlled conditions. The reason for that are the changes in relative humidity and temperature conditions observed in the former. Furthermore, the differences in the behaviour of the beams exposed to ambient conditions were greater than the observed among the beams in the climate-controlled room.
- The current formulations in the EHE-08 and the MC2010 to assess the evolution of the creep coefficient underestimate the long-term flexural behaviour measured for the SFRC (even though the EHE-08 provides a prediction close to some of the experimental curves). This may be attributed to the fact that these models are calibrated with creep tests in compression for plain concrete.
- The simplified two-element viscoelastic model proposed represents satisfactorily the experimental response of the beams tested.

9.3. FUTURE PERSPECTIVES

Despite the contributions reported in the previous section, further research on the topics covered in this doctoral are required. For that reason, several suggestions for future research and experimental programs are proposed below.

RC-SFRC beams

The study conducted shows the use of combined reinforcements of rebars and steel fibres as a reinforcing solution for concrete. In this regard, it might be interesting to analyse whether a minimum traditional reinforcement might be used to compensate unfavourable or non-uniform fibre distributions.

Furthermore, it would be interesting to extend the study of the influence of the addition of fibres to the concrete-rebar bond. Even though the contribution of fibres is already considered in formulations to predict the crack spacing, further research on how to introduce the advantages provided by the fibres in the design should be conducted.

SFRC slabs

The study concerning the influence of the dimensions in the flexural performance and fibre orientation of full-scale SFRC slabs was limited in terms of the width of the slab as well as the type and the content of fibres. Hence, in order to generalize the expressions proposed for the fibre network effect and the geometry factors, more experimental studies should be performed. Additionally, the influence of other parameters in the fibre network effect should be analysed in order to comprehend the phenomenon fully.

The use of constitutive models based on beam test was proved to be unsuitable for the design of SFRC slabs. Studies on other structural applications might be interesting to define the scope in which the beam test is suitable for the design. Moreover, a discussion on the approach to compensate the low representativeness of the test should be contemplated. Should an approach based on the specification of tailored tests configurations for each structural application be considered. Should these differences be compensated by the use of coefficients (geometry factors, orientation factors, among others) taking into account the own characteristics of each structural application?

Predicting the tensile behaviour of SFRC

The new constitutive model proposed is based on the Barcelona test, whose failure mechanism is characterized by the formation of a conical wedge that slides into the specimen. In the proposal, a kinetic friction coefficient is assumed based on the values of the static friction coefficient suggested by the Model Code 2010. In this regard, further research should be conducted in order to determine reliable values of the kinetic friction coefficient for concrete and fibre reinforced concrete.

Furthermore, the constitutive model proposed should be validated for other types of FRC such as high-performance FRC (HPFRC) and other types of fibres different from steel and plastic macro-fibres. Likewise, beyond the validation of the model at a small scale (by modelling the Barcelona test), its adequacy to design real scale applications of FRC should be verified.

Long-term behaviour of SFRC

Regarding the long-term behaviour, the influence of other parameters should be studied in addition to the pre-cracking width and the load level (the type of fibre, the fibre content, and the age of concrete at the time of pre-cracking among many others). Some of these parameters are analysed in studies that are currently under development. Nevertheless, these parameters should also be studied in other type of fibre cementitious composites such as HPFRC or HyFRC. Moreover, experimental programs involving longer tests in terms of time and the test of real-scale elements should be considered.

REFERENCES

Acker, P. and Ulm, F.-J. Creep and shrinkage of concrete: physical origins and practical measurements. *Nuclear Engineering and Design*, 2001, vol. 203, no. 2-3, p. 143-158.

AENOR. UNE 83316:1996. Ensayos de hormigón. Determinación del módulo de elasticidad en compresión., Asociación Española de Normalización y Certificación, Madrid, 1996.

AENOR. UNE 83-510 Hormigones con fibras. Determinación del índice de tenacidad y resistencia a primera fisura, Asociación Española de Normalización y Certificación Madrid, 2004a.

AENOR. UNE 83507:2004. Hormigones con fibras. Rotura por compresión., Asociación Española de Normalización y Certificación, Madrid, 2004b.

AENOR. UNE-EN 1337-3:2005 Apoyos estructurales. Parte 3: Apoyos elastoméricos, Certificación. 2005.

AENOR. UNE 83515:2010. Hormigones con fibras. Determinación de la resistencia a fisuración, tenacidad y resistencia residual a tracción. Método Barcelona. , Asociación Española de Normalización y Certificación Madrid, 2010.

AENOR. UNE-EN 12350-8:2011 Ensayos de hormigón fresco. Parte 8: Hormigón autocompactante. Ensayo de escurrimiento, Certificación. Madrid, 2011.

Altun, F., Haktanir, T. and Ari, K. Experimental investigation of steel fiber reinforced concrete box beams under bending. *Materials and Structures*, 2006, vol. 39, no. 4, p. 491-499.

Arango, S. *Fluencia a flexión del hormigón reforzado con fibras de acero (SFRC) en estado fisurado*. Doctoral Thesis, Universidad Politécnica de Valencia, Valencia, 2010.

Arango, S.E., Serna, P., Martí-Vargas, J.R. and García-Taengua, E. A Test Method to Characterize Flexural Creep Behaviour of Pre-cracked FRC Specimens. *Experimental Mechanics*, 2012/10/01 2012, vol. 52, no. 8, p. 1067-1078.

ASM-International *Metals Handbook Volume 1: Properties and Selection: Irons, Steels and High Performance Alloys*. Edition ed.: ASM International, 1990. 1063 p. ISBN 978-0-87170-377-4.

ASTM. ASTM C1018-89. Standard test method for flexural toughness and first-crack strength of fiber-reinforced concrete (using beam with third-point loading). ASTM International, West Conshohocken, 1991.

ASTM. ASTM C1399/C1399M-10:Standard test method for obtaining average residual-strength of fiber-reinforced concrete. In.: American Society for Testing Materials, 2010a, ASTM. C1550-10a. Standard Test Method for Flexural Toughness of Fiber Reinforced Concrete (Using Centrally Loaded Round Panel). Standard. West Conshohocken 2010b.

Barnett, S., Lataste, J.-F., Parry, T., Millard, S. and Soutsos, M. Assessment of fibre orientation in ultra high performance fibre reinforced concrete and its effect on flexural strength. *Materials and Structures*, 2010, vol. 43, no. 7, p. 1009-1023.

Barragán, B. and Zerbino, R.L. Creep behaviour of cracked steel fibre reinforced concrete beams. In *Proceedings of the 7th RILEM Symposium on Fibre Reinforced Concrete: Design and Applications (BEFIB 2008)*, Chennai, India, 2008, Gettu Ed., 577-586.

Barragán, B.E. *Failure and toughness of steel fiber reinforced concrete under tension and Shear*. Doctoral Thesis, Universitat Politècnica de Catalunya, Barcelona 2002.

Barros, J.A.O. and Cruz, J.S. Fracture Energy of Steel Fiber-Reinforced Concrete. *Mechanics of Advanced Materials and Structures*, 2001, vol. 8, no. 1, p. 29-45.

Barros, J.A.O., Cunha, V., Ribeiro, A. and Antunes, J. Post-cracking behaviour of steel fibre reinforced concrete. *Materials and Structures*, 2005, vol. 38, no. 1, p. 47-56.

Barros, J.A.O. and Figueiras, J.A. Flexural Behavior of SFRC: Testing and Modeling. *Journal of Materials in Civil Engineering*, 1999, vol. 11, no. 4, p. 331-339.

Bast, T., Eder, A. and Kusterle, W., Fachhochschule Regensburg, Fakultät Bauingenieurwesen. Untersuchungen zum Langzeitverhalten von Faserbetonen unter Biegezugbeanspruchung - ein Zwischenbericht. 2007. Regensburg, Kriechversuche an Kunststoffmakrofaserbetonen.

Bažant, Z. and Oh, B. Deformation of Progressively Cracking Reinforced Concrete Beams. *ACI Journal*, 1984, vol. 81, no. 3, p. 268-278.

Bažant, Z.P. *Mathematical model of creep and shrinkage of concrete*. Edition ed.: John Wiley & Sons Ltd, 1988.

Bažant, Z.P. Prediction of concrete creep and shrinkage: past, present and future. *Nuclear Engineering and Design*, 2001, vol. 203, no. 1, p. 27-38.

Bažant, Z.P. and Baweja, S. Creep and shrinkage prediction model for analysis and design of concrete structures— model B3, in collaboration with the RILEM Committee TC107-GCS, (RILEM Recommendation). *Materials and Structures*, 1995/07/01 1995, vol. 28, no. 6, p. 357-365.

Bažant, Z.P., Hauggaard, B., Baweja, S. and Ulm, F.-J. Microprestress-solidification theory for aging and drying creep of concrete. *Journal of Engineering Mechanics*, 1997, vol. 123, no. 11, p. 1188-1194.

Bažant, Z.P. and Osman, E. Double power law for basic creep for concrete. *Materials and Structures*, 1976, vol. 9, no. 49, p. 3-11.

Bažant, Z.P. and Prasannan, S. Solidification theory for concrete creep: I. formulation, and II. verification and application. *Journal of Engineering Mechanics*, 1989, vol. 115, no. 8, p. 1691-1725.

Bencardino, F., Rizzuti, L., Spadea, G. and Swamy, R.N. Stress-Strain Behavior of Steel Fiber-Reinforced Concrete in Compression. *Journal of Materials in Civil Engineering*, 2008, vol. 20, no. 3, p. 255-263.

Bernard, E.S. Influence of Fiber Type on Creep Deformation of Cracked Fiber-Reinforced Shotcrete Panels. *ACI Materials Journal*, 2010, vol. 107, no. 5, p. 474-480.

Bischoff, P.H. Tension stiffening and cracking of steel fiber-reinforced concrete. *Journal of Materials in Civil Engineering*, 2003, vol. 15, no. 2, p. 175-182.

Blanco, A., Pujadas, P., Cavalaro, S., de la Fuente, A. and Aguado, A. Métodos recientes para caracterizar el hormigón reforzado con fibras. In *Proceedings of the 55th Congreso Brasileiro do Concreto (55CBC)*, Maceió, 2012. ISSN 2175-8182.

Blanco, A., Pujadas, P., de la Fuente, A., Cavalaro, S. and Aguado, A. Application of constitutive models in European codes to RC-FRC. *Construction and Building Materials*, 2013, vol. 40, p. 246-259.

Bortolotti, L. Double-Punch Test for Tensile and Compressive Strengths in Concrete. *ACI Materials Journal*, 1988, vol. 85, no. 1, p. 26-32.

Boulekbache, B., Hamrat, M., Chemrouk, M. and Amziane, S. Flowability of fibre-reinforced concrete and its effect on the mechanical properties of the material. *Construction and Building Materials*, 2010, vol. 24, no. 9, p. 1664-1671.

Brite-Euram project BRPR-CT98-0813. Test and Design Methods for Steel Fibre Reinforced Concrete, ISBN 90-5682-358-2, 2002

Buratti, N. and Mazzotti, C. Effects of different types and dosages of fibres on the long-term behaviour of fibre-reinforced self-compacting concrete. In *Proceedings of the 8th RILEM Symposium on Fibre Reinforced Concrete: Challenges and opportunities (BEFIB 2012)*, Guimarães, Portugal, September 2012 2012, Barros Ed.

Buratti, N., Mazzotti, C. and Savoia, M. Post-cracking behaviour of steel and macro-synthetic fibre-reinforced concretes. *Construction and Building Materials*, 2011, vol. 25, no. 5, p. 2713-2722.

Burguers, R., Walraven, J.C., Plizzari, G.A. and Tiberti, G. Structural Behavior of SFRC Tunnel Segments during TBM Operations. In *Proceedings of the Underground Space - the 4th Dimension of Metropolises: World Tunnel Congress 2007 and 33rd ITA/AITES Annual General Assembly*, Prague, Czech Republic, 2007, Barták., Hrdina., Romancov.Zlámal. Eds. Taylor & Francis Group, 1461-1467.

Carmona, S., Aguado, A. and Molins, C. Generalization of the Barcelona test for the toughness control of FRC. *Materials and Structures*, 2012, vol. 45, no. 7, p. 1053-1069.

Cavalero, S. *Aspectos tecnológicos de túneles construidos con tuneladora y dovelas prefabricadas de hormigón*. Doctoral Thesis, Universitat Politècnica de Catalunya, Barcelona, 2009.

CEB-FIP. CEB-FIP Model Code 1990: Design code, Précontrainte. Thomas Telford, Lausanne, 1993.

CEN. ENV 1992-1-1 Eurocode 2: Design of Concrete Structures - Part 1: General rules and rules for buildings, European Committee for Standardization, Brussels, 1992.

CEN. EN 14651:2005 Test method for metallic fibered concrete - Measuring the flexural tensile strength (limit of proportionality (LOP), residual), European Committee for Standardization, Brussels, 2005.

CEN. UNE-EN 12390-3:2009 Testing hardened concrete - Part 3: Compressive strength of test specimens, European Committee for Standardization, Brussels, 2009.

Cervenka, V. Simulating a response. *Concrete Engineering International*, 2000, vol. 4, no. 4, p. 45-49.

CNR. CNR-DT 204 /2006 Guide for the Design and Construction of Fiber-Reinforced Concrete Structures, Italian National Research Council, Rome, 2006.

Cochrane, J.T. *Flexural creep behaviour of fibre reinforced concrete under high temperatures*. Master Thesis, Dalhousie University, Halifax, 2003.

CPH. Instrucción del Hormigón Estructural EHE-08, Ministerio de Fomento, Madrid, 2008.

Chanvillard, G. and Roque, O. Behaviour of fibre reinforced concrete cracked section under sustained load. In *Proceedings of the 3rd International workshop on High Performance Fibre Reinforced Cement Composites (HPFRCC 3)*, Mainz, Germany, 1999, ReinhardtNaaman Eds., 239-250.

Chao, S.-H., Karki, N.B., Cho, J.-S. and Waweru, R.N. Use of double punch test to evaluate the mechanical performance of fiber reinforced concrete. In *Proceedings of the 6th International Workshop on High Performance Fiber Reinforced Cement Composites (HPFRCC 6)*, Ann Arbor, Michigan, June 20-22 2011, Parra-Montesinos, ReinhardtNaaman Eds., 26-35.

- Chen, W.F. Double punch test for tensile strength of concrete. *ACI Materials Journal*, 1970, vol. 67, no. 2, p. 993-995.
- Chen, W.F. and Yuan, R.L. Tensile strength of concrete: double punch test *Journal of Structural Divisions*, 1980, vol. 106, no. 8, p. 1673-1693.
- Chiaia, B., Fantilli, A. and Vallini, P. Evaluation of crack width in FRC structures and application to tunnel linings. *Materials and Structures*, 2009a, vol. 42, no. 3, p. 339-351.
- Chiaia, B., Fantilli, A.P. and Vallini, P. Combining fiber-reinforced concrete with traditional reinforcement in tunnel linings. *Engineering Structures*, 2009b, vol. 31, no. 7, p. 1600-1606.
- DBV. Grundlagen zur Bemessung von Industrielufböden aus Stahlfaserbeton, Deutschen Betons-Vereins, Berlin, 1991, p. 2572-2578.
- DBV. Bemessungsgrundlagen für Stahlfaserbetons in tunnelbau, Deutschen Beton-Vereins, Berlin, 1992a.
- DBV. Technologie des Stahlfaser-betons und Stahlfaserspritzbetons, Deutschen Beton-Vereins, Berlin, 1992b, p. 3-8.
- DBV. Guide to Good Practice "Steel Fibre Concrete", German Society for Concrete and Construction Technology, Berlin, 2001.
- de la Fuente, A., Escariz, R.C., de Figueiredo, A.D., Molins, C. and Aguado, A. A new design method for steel fibre reinforced concrete pipes. *Construction and Building Materials*, 2012a, vol. 30, no. 0, p. 547-555.
- de la Fuente, A., Pujadas, P., Blanco, A. and Aguado, A. Experiences in Barcelona with the use of fibres in segmental linings. *Tunnelling and Underground Space Technology*, 2012b, vol. 27, no. 1, p. 60-71.
- Destrée, X. and Mandl, J. Steel fibre only reinforced concrete in free suspended elevated slabs: Case studies, design assisted by testing route, comparison to the latest SFRC standard documents. In *Proceedings of the fib Symposium "Tailor Made Concrete Structures"*, Amsterdam, 2008, WalravenStoelhost Eds. Taylor & Francis Group.
- di Prisco, M., Ferrara, L. and Caverzan, A. Self-compacting fibre reinforced concrete: is the material really isotropic? In *Proceedings of the 3^o Congreso Iberoamericano sobre hormigón autocompactante: avances y oportunidades (HAC2012)*, Madrid, España, December 2012 2012, PaciosSerna Eds., 17-31.
- di Prisco, M., Lamperti, M.G.L. and Lapolla, S. On Double Edge Wedge Splitting Test. In *Proceedings of the Fracture Mechanics of Concrete and Concrete Structures (FraMCoS 7)*, Jeju, Korea, May 2010 2010, Oh Ed., 1533-1540.
- di Prisco, M., Plizzari, G. and Vandewalle, L. Fibre reinforced concrete: new design perspectives. *Materials and Structures*, 2009, vol. 42, no. 9, p. 1261-1281.
- DIN. DIN1048-2. Testing concrete; testing of hardened concrete (specimens taken in situ) e.V., Berlin, 1991.

Dozio, D. *SFRC structures: Identification of the uniaxial tension characteristic constitutive law*. Doctoral Thesis, Politecnico di Milano, Milan, 2008.

Dupont, D. *Modelling and experimental validation of the constitutive law (σ - ϵ) and cracking behaviour of steel fibre reinforced concrete*. Doctoral Thesis, Katholieke Universiteit Leuven, Leuven, 2003.

Dupont, D. and Vandewalle, L. Comparison between the round plate test and the Rilem 3-point bending test. In *Proceedings of the 6th International RILEM Symposium on Fibre Reinforced Concretes (BEFIB 2004)*, Varenna, Italy, September 20-22 2004, di Prisco, FelicettiPlizzari Eds.

Dupont, D. and Vandewalle, L. Distribution of steel fibres in rectangular sections. *Cement and Concrete Composites*, 2005, vol. 27, no. 3, p. 391-398.

Edgington, J. and Hannant, D. Steel fibre reinforced concrete. The effect on fibre orientation of compaction by vibration. *Materials and Structures*, 1972, vol. 5, no. 1, p. 41-44.

EFNARC. European Specification for Sprayed Concrete, Industry. 1996.

Fernández Ruiz, M. *Evaluación no lineal de los efectos estructurales producidos por las deformaciones diferidas del hormigón y el acero*. Doctoral Thesis, Universidad Politécnica de Madrid, Madrid, 2003.

Fernández Ruiz, M., Muttoni, A. and Gambarova, P.G. Relationship between Nonlinear Creep and Cracking of Concrete under Uniaxial Compression. *Journal of Advanced Concrete Technology*, 2007, vol. 5, no. 3, p. 1-11.

Ferrara, L. High performance fiber reinforced self-compacting concrete (HPFR-SCC): a "smart material" for high end engineering applications. In *Proceedings of the 3^o Congreso Iberoamericano sobre hormigón autocompactante: avances y oportunidades (HAC2012)*, Madrid, España, December 2012 2012, PaciosSerna Eds., 325-334.

Ferrara, L., Ozyurt, N. and di Prisco, M. High mechanical performance of fibre reinforced cementitious composites: the role of "casting-flow induced" fibre orientation. *Materials and Structures*, 2011, vol. 44, no. 1, p. 109-128.

Ferrara, L., Park, Y.-D. and Shah, S.P. Correlation among Fresh State Behavior, Fiber Dispersion, and Toughness Properties of SFRCs. *Journal of Materials in Civil Engineering*, 2008, vol. 20, no. 7, p. 493-501.

Ferretti, D. and Bažant, Z.P. Stability of ancient masonry towers: Stress redistribution due to drying, carbonation, and creep. *Cement and Concrete Research*, 2006, vol. 36, p. 1389-1398.

fib. Model Code 2010, International Federation for Structural Concrete, Lausanne, 2010.

Figueiredo, A. Evaluation of the test method for crushing strength of steel fibre reinforced concrete pipes. In *Proceedings of the 7th RILEM Symposium on Fibre Reinforced Concrete: Design and Applications (BEFIB 2008)*, Chennai, India, 2008, Gettu Ed., 989-1000.

- Findley, W.N., Lai, J.S.Y. and Onaran, K. *Creep and Relaxation of Non-Linear Vico-Elastic Materials*. Edition ed. New York: North Holland Publishing 1976.
- Gettu, R., Gardner, D., Saldívar, H. and Barragán, B. Study of the distribution and orientation of fibers in SFRC specimens. *Materials and Structures*, 2005, vol. 38, no. 1, p. 31-37.
- Gopalaratnan, V.S., Shah, S. P., Batson, G. B., Criswell, M. E., Ramakrishnan, V., Wecharatona, M. Fracture Toughness of Fiber Reinforced Concrete. *ACI Materials Journal*, 1991, vol. 88, no. 4, p. 339-353.
- Granju, J.-L., *et al.* Delayed behaviour of cracked SFRC beams. In *Proceedings of the Fifth International RILEM Symposium on Fibre-Reinforced Concrete (BEFIB 200)*, Lyon, France, 2000, RossiChanvillard Eds., 511-520.
- Grünewald, S. *Performance-based design of self-compacting fibre reinforced concrete*. Doctoral Thesis, Delft University of Technology, Delft, 2004.
- Grünewald, S., Laranjeira, F., Walraven, J., Aguado, A. and Molins, C. Improved tensile performance with fiber reinforced self-compacting concrete. In *Proceedings of the 6th International Workshop on High Performance Fiber Reinforced Cement Composites (HPFRCC 6)*, Ann Arbor, Michigan, June 20-22 2011, Parra-Montesinos, ReinhardtNaaman Eds.
- Guàrdia, J. *Characterització del comportament a tracció de formigó d'alta treballabilitat reforçat amb fibres d'acer mitjançant l'assaig Barcelona*. Bachelor Thesis, Universitat Politècnica de Catalunya, Barcelona, 2008.
- Hillerborg, A., Modéer, M. and Petersson, P.E. Analysis of crack formation and crack growth in concrete by means of fracture mechanics and finite elements. *Cement and Concrete Research*, 1976, vol. 6, no. 6, p. 773-781.
- Hoy, C.W. *Mixing and mix proportioning of fibre reinforced concrete*. Doctoral Thesis, University of the West of Scotland, Paisley, 1998.
- IBN. NBN B 15-238 Essais des bétons renforcés de fibres - Essai de flexion sur éprouvettes prismatiques, Institut Belge de Normalisation Brussels, 1992.
- Johansen, K.W. *Yield line formulae for slabs*. Edition ed. London: Cement and Concrete Association, 1962.
- JSCE-SF4 Method of test for flexural strength and flexural toughness of steel fiber reinforced concrete. *Concrete library of JSCE*, 1984, vol. 3, p. 58-61.
- Juan García, P. *Evaluación no destructiva de estructuras de obra civil mediante métodos electromagnéticos*. Doctoral Thesis, Universitat Politècnica de Catalunya, Barcelona, 2011.
- Kameswara Rao, C.V.S. Effectiveness of random fibres in composites. *Cement and Concrete Research*, 1979, vol. 9, no. 6, p. 685-693.

- Kang, S.-T. and Kim, J.-K. The relation between fiber orientation and tensile behavior in an Ultra High Performance Fiber Reinforced Cementitious Composites (UHPFRCC). *Cement and Concrete Research*, 2011, vol. 41, no. 10, p. 1001-1014.
- Kang, S.-T. and Kim, J.-K. Investigation on the flexural behavior of UHPCC considering the effect of fiber orientation distribution. *Construction and Building Materials*, 2012, vol. 28, no. 1, p. 57-65.
- Kanstad, T. and Zirgulis, G. Long-time creep testing of pre-cracked fibre reinforced concrete beams. In *Proceedings of the 8th RILEM Symposium on Fibre Reinforced Concrete: Challenges and opportunities (BEFIB 2012)*, Guimarães, Portugal, September 2012 2012, Barros Ed.
- Kooiman, A. *Modelling Steel Fibre Reinforced Concrete for Structural Design*. Doctoral Thesis, Delft University of Technology, Delft, 2000.
- Krenchel, H. Fibre spacing and specific fibre surface In Neville A. *Fibre Reinforced cement and concrete*. UK: The Construction Press, 1975, p. 69-79.
- Kurtz, S. and Balaguru, P. Postcrack creep of polymeric fiber-reinforced concrete in flexure. *Cement and Concrete Research*, 2000, vol. 30, no. 2, p. 183-190.
- Kusterle, W. Viscous material behaviour of solids-creep of polymere fibre. In *Proceedings of the 5th Central European Congress on Concrete Engineering (CCC 5)*, Baden, Austria, 2009.
- Lappa, L. *High strength fibre reinforced concrete: static and fatigue behavior in bending*. Doctoral Thesis, Delft University of Technology, Delft, 2007.
- Laranjeira, F. *Design-oriented constitutive model for steel fiber reinforced concrete*. Doctoral Thesis, Universitat Politècnica de Catalunya, Barcelona, 2010.
- Laranjeira, F., Aguado, A. and Molins, C. Predicting the pullout response of inclined straight steel fibers. *Materials and Structures*, 2010/07/01 2010, vol. 43, no. 6, p. 875-895.
- Laranjeira, F., Grünewald, S., Walraven, J., Blom, C., Molins, C. and Aguado, A. Characterization of the orientation profile of steel fiber reinforced concrete. *Materials and Structures*, 2011, vol. 44, no. 6, p. 1093-1111.
- Lataste, J.F., Behloul, M. and Breysse, D. Characterisation of fibres distribution in a steel fibre reinforced concrete with electrical resistivity measurements. *NDT & E International*, 2008, vol. 41, no. 8, p. 638-647.
- Lawler, J.S., Zampini, D. and Shah, S.P. Microfiber and Macrofiber Hybrid Fiber-Reinforced Concrete. *Journal of Materials in Civil Engineering*, 2005, vol. 17, no. 5, p. 595-604.
- Lee, S.L., Mansur, M.A., Tan, K.H. and Kasiraju, K. Crack Control in Beams Using Deformed Wire Fabric. *Journal of Structural Engineering*, 1989, vol. 115, no. 10, p. 2645-2660.
- Li, V.C. Large volume, high-performance applications of fibers in civil engineering. *Journal of Applied Polymer Science*, 2002, vol. 83, no. 3, p. 660-686.

- MacKay, J. *Behaviour of steel and synthetic fibre reinforced concrete under flexural creep loading*. Master Thesis, Dalhousie University, Halifax, 2002.
- MacKay, J. and Trottier, J.-F. Post-crack creep behaviour of steel and synthetic FRC under flexural loading. In Bernard. *Shotcrete: More Engineering Developments*. London: Talyor & Francis Group, 2004.
- Mangat, P.S. and Azari, M.M. Compression creep behaviour of steel fibre reinforced cement composites. *Materials and Structures*, 1986/09/01 1986, vol. 19, no. 5, p. 361-370.
- Mangat, P.S. and Motamedi Azari, M. A theory for the creep of steel fibre reinforced cement matrices under compression. *Journal of Materials Science*, 1985/03/01 1985, vol. 20, no. 3, p. 1119-1133.
- Marí, A.R. Numerical simulation of the segmental construction of three dimensional concrete frames. *Engineering Structures*, 2000, vol. 22, no. 6, p. 585-596.
- Markovic, I. *High-Performance Hybrid-Fiber Reinforced Concrete: Development and Utilisation*. Doctoral Thesis, Delft University of Technology, Delft, 2006.
- Marti, P. Size Effect in Double-Punch Tests on Concrete Cylinders. *ACI Materials Journal*, 1989, vol. 86, no. 6, p. 597-601.
- Martinie, L., Rossi, P. and Roussel, N. Rheology of fiber reinforced cementitious materials: classification and prediction. *Cement and Concrete Research*, 2010, vol. 40, no. 2, p. 226-234.
- Martinie, L. and Roussel, N. Simple tools for fiber orientation prediction in industrial practice. *Cement and Concrete Research*, 2011, vol. 41, no. 10, p. 993-1000.
- Maya, L.F., Fernández Ruiz, M., Muttoni, A. and Foster, S.J. Punching shear strength of steel fibre reinforced concrete slabs. *Engineering Structures*, 2012, vol. 40, no. 0, p. 83-94.
- Mehta, P.K. and Monteiro, P.J.M. *Concrete: Microstructure, Properties and Materials*. Edtion ed.: McGraw-Hill, 2006.
- Mendes, P.J.D., Barros, J., Gonçalves, D.M.F. and Sena-Cruz, J.M. Steel fibre reinforced self-compacting concrete for lightweight and durable pedestrian bridges: creep behaviour. In *Proceedings of the 8th RILEM Symposium on Fibre Reinforced Concrete: Challenges and opportunities (BEFIB 2012)*, Guimarães, Portugal, September 2012 2012, Barros Ed.
- Michels, J., Waldmann, D., Maas, S. and Zürbes, A. Steel fibers as only reinforcement for flat slab construction – Experimental investigation and design. *Construction and Building Materials*, 2012, vol. 26, no. 1, p. 145-155.
- Molins, C., Aguado, A. and Marí, A.R. Quality control test for SFRC to be used in precast segments. *Tunnelling and Underground Space Technology*, 2006, vol. 21, no. 3-4, p. 423-424.

- Molins, C., Aguado, A. and Saludes, S. Double Punch Test to control the energy dissipation in tension of FRC (Barcelona test). *Materials and Structures*, 2009, vol. 42, no. 4, p. 415-425.
- Molins, C., Aguado, A., Saludes, S. and T., G. New test to control tension properties of FRC. In *Proceedings of the ECCOMAS Thematic Conference on Computational Methods in Tunnelling (EURO: TUN2007)*, Vienna, Austria., August 27-29 2007.
- Monsó, A. *Análisis del comportamiento del hormigón reforzado con fibras para el ensayo Barcelona y de flexotracción* Bachelor Thesis, Universitat Politècnica de Catalunya, Barcelona, 2011.
- Nakov, D. and Markovski, G. Time dependant behaviour of SFRC elements under sustained loads. In *Proceedings of the 8th RILEM Symposium on Fibre Reinforced Concrete: Challenges and opportunities (BEFIB 2012)*, Guimarães, Portugal, September 2012 2012, Barros Ed.
- Neville, A. *Properties of concrete*. Edtion ed.: Pearson Educational Limited - Prentice Hall, 2004.
- Neville, A.M., Dilger, W.H. and Brooks, J.J. *Creep of plain and structural concrete*. Edtion ed. London and New York: Construction Press, 1983.
- Ozyurt, N., Mason, T.O. and Shah, S.P. Non-destructive monitoring of fiber orientation using AC-IS: An industrial-scale application. *Cement and Concrete Research*, 2006, vol. 36, no. 9, p. 1653-1660.
- Parmentier, B., De Grove, E., Vandewalle, L. and Van Rickstal, F. Dispersion of the mechanical properties of FRC investigated by different bending tests. In WalravenStoelhost. *fib Symposium "Tailor Made Concrete Structures"*. Amsterdam: Taylor & Francis Group, 2008, p. 507-512
- Plizzari, G.A. and Tiberti, G. Steel fibres as reinforcement for precast tunnel segments. *Tunnelling and Underground Space Technology*, 2006, vol. 21, p. 3-4.
- Pujadas, P., Blanco, A., Cavalaro, S.H.P. and Aguado, A. Método para la caracterización multidireccional del HRF. In *Proceedings of the V Congreso de ACHE* Barcelona, 2011 Asociación Científico-Técnica del Hormigón Estructural (ACHE).
- Pujadas, P., Blanco, A., Cavalaro, S., de la Fuente, A. and Aguado, A. New analytical model to generalize the Barcelona test using axial displacement. *Journal of Civil Engineering and Management*, 2012.
- Pujadas, P. *Caracterización y diseño del hormigón reforzado con fibras plásticas*. Doctoral Thesis, Universitat Politècnica de Catalunya, Barcelona, 2013.
- Robins, P., Austin, S. and Jones, P. Spatial distribution of steel fibres in sprayed and cast concrete. *Magazine of Concrete Research*, 2003, vol. 55, no. 3, p. 225-235.
- Romualdi, J.P. and Mandel, J.A. Tensile strength of concrete affected by uniformly distributed and closely spaced short lengths of wire reinforcement. *ACI Journal*, 1964, vol. 61, no. 6, p. 27-37.

Roqueta, G., Jofre, L., Romeu, J. and Blanch, S. Microwave Time-Domain Reflection Imaging of Steel Fiber Distribution on Reinforced Concrete. *IEEE Transactions on Instrumentation and Measurement*, 2011, vol. 60, no. 12, p. 3913-3922.

Roussel, N. Correlation between Yield Stress and Slump: Comparison between Numerical Simulations and Concrete Rheometers Results. *Materials and Structures*, 2006/05/01 2006, vol. 39, no. 4, p. 501-509.

Roussel, N. Rheology of fresh concrete: from measurements to predictions of casting processes. *Materials and Structures*, 2007, vol. 40, no. 10, p. 1001-1012.

Serna, P., Arango, S., Ribeiro, T., Núñez, A. and Garcia-Taengua, E. Structural cast-in-place SFRC: technology, control criteria and recent applications in Spain. *Materials and Structures*, 2009, vol. 42, no. 9, p. 1233-1246.

Serna, P., Bossio, M.E., Zerbino, R.L. and Martí Vargas, J.R. Fluencia y propiedades residuales de hormigones autocompactantes con fibras expuestos en estado fisurado a diferentes condiciones ambientales. In *Proceedings of the 3^o Congreso Iberoamericano sobre hormigón autocompactante: avances y oportunidades (HAC2012)*, Madrid, España, December 2012 2012, PaciosSerna Eds., 221-230.

Soranakom, C. and Mobasher, B. Flexural design of Fiber-Reinforced Concrete. *ACI Materials Journal*, 2009, vol. 106, no. 5, p. 461-469.

Sorelli, L.G., Meda, A., Plizzari, G.A Steel Fiber Concrete Slabs on Ground: A Structural Matter. *ACI Structural Journal*, 2006, vol. 103, no. 4, p. 551-558.

Soroushian, P. and Lee, C.-D. Distribution and Orientation of Fibers in Steel Fiber Reinforced Concrete. *Materials Journal*, 1990, vol. 87, no. 5, p. 433-499.

Stähli, P. *Ultra-Fluid, Oriented Hybrid-Fibre-Concrete*. Doctoral Thesis, Institute for Building Materials ETH Zürich, Zürich, 2008.

Stähli, P. and van Mier, J.G.M. Manufacturing, fibre anisotropy and fracture of hybrid fibre concrete. *Engineering Fracture Mechanics*, 2007, vol. 74, no. 1-2, p. 223-242.

Stroeven, P. The analysis of fibre distributions in fibre reinforced materials*. *Journal of Microscopy*, 1977, vol. 111, no. 3, p. 283-295.

Stroeven, P. Morphometry of fibre reinforced cementitious materials. *Materials and Structures*, 1979, vol. 12, no. 1, p. 9-20.

Stroeven, P. and Hu, J. Effectiveness Near Boundaries of Fibre Reinforcement in Concrete. *Materials and Structures*, 2006, vol. 39, no. 10, p. 1001-1013.

Swamy, R.N. and Theodorakopoulos, D.D. Flexural creep behaviour of fibre reinforced cement composites. *International Journal of Cement Composites*, 1979, vol. 1, no. 1, p. 37-47.

Tan, K.-H., Paramasivam, P. and Tan, K.-C. Cracking characteristics of reinforced steel fiber concrete beams under short- and long-term loadings. *Advanced Cement Based Materials*, 1995, vol. 2, no. 4, p. 127-137.

Tan, K.H. and Saha, M.K. Ten-Year Study on Steel Fiber-Reinforced Concrete Beams Under Sustained Loads. *ACI Structural Journal*, 2005, vol. 102, no. 3, p. 472-480.

Tlemat, H., Pilakoutas, K. and Neocleous, K. Modelling of SFRC using inverse finite element analysis. *Materials and Structures*, 2006, vol. 39, no. 2, p. 221-233.

Torrents, J., Blanco, A., Pujadas, P., Aguado, A., Juan-García, P. and Sánchez-Moragues, M. Inductive method for assessing the amount and orientation of steel fibers in concrete. *Materials and Structures*, 2012, vol. 45, no. 10, p. 1-16.

Torrents, J.M., Juan-García, P., Patau, O. and Aguado, A. Surveillance of steel fibre reinforced concrete slabs measured with an open-ended coaxial probe. In *Proceedings of the XIX IMEKO World Congress: Fundamental and Applied Metrology*, Lisbon, Portugal, September 2009 2009, 2282-2284.

Torres Llinàs, L. *Modelo numérico y verificación experimental del comportamiento en servicio de estructuras de hormigón*. Doctoral Thesis, Universitat Politècnica de Catalunya, Barcelona, 2001.

Torrijos, M.C., Tobes, J.M., Barragán, B.E. and Zerbino, R.L. Orientation and Distribution of Steel Fibres in Self-Compacting Concrete In *Proceedings of the 7th RILEM Symposium on Fibre Reinforced Concrete: Design and Applications (BEFIB 2008)*, Chennai, India, 2008, Gettu Ed., 729-738.

Toutanji, H. and Bayasi, Z. Effects of Manufacturing Techniques on the Flexural Behavior of Steel Fiber-Reinforced Concrete. *Cement and Concrete Research*, 1998, vol. 28, no. 1, p. 115-124.

Trost, H. Auswirkungen des Superpositionsprinzips auf Kriech und Relaxations Probleme bei Beton und Spannbeton. *Beton und Stahlbetonbau*, 1967, vol. 62, no. 10.

Tschegg, E.K. and Linsbauer, H.N. *Testing procedure for determination of fracture mechanics parameters*. Patentschrift no. A-233/86, 1986.

UNI. 11039. Calcestruzzo rinforzato con fibre d'acciaio; (1a) Parte I: Definizioni, classificazione e designazione; (1b) Parte II: Metodo di prova per la determinazione della resistenza di prima fessurazione e degli indici di duttilità, Unificazione. Roma, 2003.

UNI. 11188. Elementi strutturali in calcestruzzo rinforzato con fibre d'acciaio: progettazione esecuzione e controllo, Unificazione. Roma, 2004.

Van Gysel, A. *Studie van het uittrekgedrag van staalvezels ingebed in een cementgebonden matrix met toepassing op staalvezelbeton onderworpen aan buiging* Doctoral Thesis, Ghent University, Ghent, 2000.

Vandewalle, L. Cracking behaviour of concrete beams reinforced with a combination of ordinary reinforcement and steel fibers. *Materials and Structures*, 2000, vol. 33, no. 3, p. 164-170.

Vandewalle, L. Hybrid Fiber Reinforced Concrete: Measuring, Monitoring and Modeling Concrete Properties. In Konsta-Gdoutos. Springer Netherlands, 2006, p. 77-82.

Vandewalle, L., Heirman, G. and Van Rickstal, F. Fibre orientation in self-compacting fibre reinforced concrete. In *Proceedings of the 7th RILEM Symposium on Fibre Reinforced Concrete: Design and Applications (BEFIB 2008)*, Chennai, India, 2008, Gettu Ed., 719-728.

Vandewalle, L., *et al.* Test and design methods for steel fibre reinforced concrete - σ - ϵ Design Method-Final Recommendation. *Materials and Structures*, 2003, vol. 36, no. 8, p. 560-567.

Vasanelli, E., Micelli, F., Aiello, M.A. and Plizzari, G. Long term behaviour of fiber reinforced concrete beams in bending. In *Proceedings of the 8th RILEM Symposium on Fibre Reinforced Concrete: Challenges and opportunities (BEFIB 2012)*, Guimarães, Portugal, September 2012, Barros Ed.

Walraven, J.C. High performance fiber reinforced concrete: progress in knowledge and design codes. *Materials and Structures*, 2009, vol. 42, no. 9, p. 1247-1260.

Wei, X.X. and Chau, K.T. Finite solid circular cylinders subjected to arbitrary surface load. Part II — Application to double-punch test. *International Journal of Solids and Structures*, 2000, vol. 37, no. 40, p. 5733-5744.

Wille, K. and Parra-Montesinos, G.J. Effect of Beam Size, Casting Method and Support Conditions on Flexural Behavior of Ultra-High-Performance Fiber-Reinforced Concrete. *ACI Materials Journal*, 2012, vol. 109, no. 3, p. 379-388.

ANNEX 1. MULTIDIRECTIONAL TEST

A1.1. INTRODUCTION

In Chapter 5 of this thesis, the assessment of the post-cracking behaviour of the SFRC was performed by means of the multidirectional test, presented by Pujadas *et al.* 2011, on the cubic specimens extracted from the slabs described in Chapter 4. The aim of this test was to evaluate the influence of fibre orientation in the post-cracking response of the material by testing the cubic specimens in different directions. However, before using this test method with the cubic specimens from the slabs, an experimental program was conducted to validate the method.

The validation was performed by means of the inductive method (Torrents *et al.* 2011) which allowed identifying the percentage of fibres aligned in the three main directions of the cubic specimen. The results of the inductive method and the multidirectional test were compared and the suitability of the latter to assess how fibre orientation influences the post-cracking behaviour of SFRC was evaluated. Part of the results in this annex was already presented in Pujadas *et al.* 2011.

A1.2. EXPERIMENTAL CAMPAIGN

A1.2.1. Specimens

Three types of cubic specimens (150 x 150 x 150 mm) were tested in this experimental campaign: cubic specimens casted in cubic moulds (CUB), cubic samples cut from prismatic beams at 150 mm of the edge of the beam (CUT1, see Figure A2.1a) and cubic samples obtained also from prismatic beams by cutting at 75 mm and 225 mm from the edge of the beam (CUT2, see Figure A2.1b). In the latter, the two cuts allowed removing the wall-effect of the side in the edge of the beam. For this study, the z axis corresponds to the casting direction and the x axis, in the case of the cubic samples, corresponds to the larger dimension of the beam.

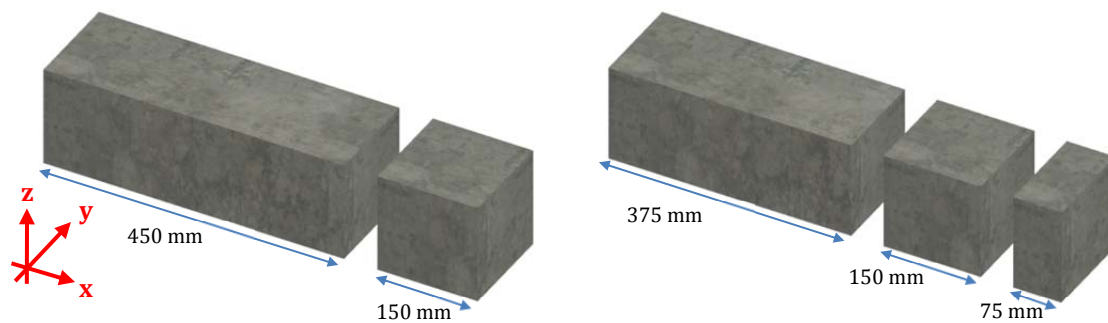


Figure A1.1 Cubic samples obtained from prismatic beam: a) 1 cut; b) 2 cuts.

A1.2.2. Materials and concrete mix

Two concrete mixes defined on the basis of previous experiences were produced (M1 and M2). The concrete was produced at ESCOFET S.A facilities in a 750 litres vertical axis mixer following the same mixing procedure: initially the dried components were mixed during one minute, subsequently the water was added and the paste was mixed during two minutes. Then, the superplasticizer was added and the steel fibres were included. Afterwards, the concrete was mixed for two additional minutes. Considering this, the total time of mixing was around 5-7 minutes. The details of the concrete mix for both series are presented in Table A1.1.


Table A1.1 Concrete mixes.

Materials	Characteristics	Quantities [kg/m ³]	
		M1	M2
Gravel (6/15 mm)	Granite	520	520
Gravel (2.5/6 mm)	Granite	400	400
Sand (0/3 mm)	Granite	500	510
Cement	CEM I 52,5 R	400	350
Filler	Marble dust	260	300
Water		170	178
Superplasticizer	Adva® Flow 400	12	12
Fibres	Steel fibres	40	40

The steel fibres used were of type Dramix® RC80/50BN with circular cross-section and hooked ends. These fibres are made of low carbon steel and are gathered into bundles by water-soluble glue. Further properties are presented in Table A1.2.

Table A1.2 Characteristics of the fibres used (provided by the manufacturer).

Characteristic	Unit	Value
Length (L)	[mm]	50
Diameter (d)	[mm]	0.62
Aspect ratio (L/d)	[-]	83
Tensile strength (f_y)	[MPa]	1270
Modulus of elasticity (E)	[GPa]	210
Number of fibres per kg	[-]	8100



In order to characterize each concrete series, the following specimens were cast: three prismatic beams (150 x 150 x 600 mm) for the flexural strength (EN 14651:2005 (CEN2005)), three cylindrical samples (150 x 300 mm) for the compressive strength (UNE 83507:2004 (AENOR 2004b)) and three cylindrical samples (150 x 300 mm) for the modulus of elasticity (UNE 83316:1996 (AENOR 1996)).

All specimens were vibrated externally by means of a vibrating table at 3000 rpm during 10 seconds approximately. The elements were removed from the moulds within 24 hours of casting and were moist cured under a plastic sheet for approximately one week (see later Table 8.5), after which they were transported from the ESCOFET S.A. facilities to the Laboratory of Structure Technology Luis Agulló at the UPC. Then, the specimens were kept in a curing room at 20 ± 2 Celsius degrees and 95% of relative humidity.

The notation used to refer to the specimens starts with the concrete mix (M1 or M2) and follows with the series to which corresponds (S1 or S2) in case that the specimens were cast in different days. In addition to that, the fibre content was included despite that only one content was used in the study. Therefore, according to that notation the specimens may be referred to as M1/S2/40/CUB or M2/S1/40/CUT2. Table A1.3 indicates the number of specimens tested in each case.

Table A1.3 Notation of each series and number of specimens.

Mix	Specimen	Specimens
M1/S1/40	CUB	6
	CUT1	6
	CUT2	6
M2/S1/40	CUB	6
	CUT1	18
	CUT2	6
M2/S2/40	CUB	6
	CUT1	6
	CUT2	6
M2/S3/40	CUB	6

Table 1.4 shows the average compressive strength (f_{cm}), average modulus of elasticity (E_{cm}), limit of proportionality (f_L) and the residual flexural tensile strengths (f_{R1} , f_{R2} , f_{R3} and f_{R4}) corresponding to CMODs of 0.05 mm, 0.50 mm, 1.50 mm, 2.50 mm and 3.50 mm, respectively.

Table 1.4 Modulus of elasticity, compressive strength and flexural residual strengths at 28 days.

Property		M1/S1/40		M2/S1/40		M2/S2/40		M2/S3/40	
		Average [MPa]	CV [%]	Average [MPa]	CV [%]	Average [MPa]	CV [%]	Average [MPa]	CV [%]
Modulus of elasticity	E_{cm}	24280	1.65	28780	1.52	28640	2.76	32250	3.78
Compressive strength	f_{cm}	37.87	1.07	47.09	1.00	48.92	1.37	47.23	2.09
Residual flexural tensile strengths	f_L	3.73	8.57	5.42	7.05	5.29	2.23	3.76	7.96
	f_{R1}	4.62	12.15	6.25	12.50	6.13	13.71	3.75	22.29
	f_{R2}	5.09	13.77	7.02	12.39	7.04	15.77	4.24	17.91
	f_{R3}	5.10	15.91	7.05	11.59	7.08	15.05	4.30	15.88
	f_{R4}	4.87	14.08	6.62	12.08	6.62	12.08	4.17	15.68

* The results for series M1/S1/40; M2/S3/40 correspond to the testing of 3 beams.

A1.3. RESULTS

A1.3.3. Results for CUB specimens

In this section, the results of the multidirectional method and the inductive method of the CUB specimens are presented from Figure A1.2 to Figure A1.5. The results of the multidirectional method are depicted in terms of load displacement curves taking the cracking as the origin. Two specimens were tested in each direction (X, Y and Z axes). However, less than six specimens might be depicted if the results are not available due to failure in the test equipment. The results of the inductive method are presented in the tables of the aforementioned figures in terms of percentage of fibres aligned along axes Z, X and Y. The shaded results indicate the testing direction of each specimen.

The results of the inductive method reveal a preferential orientation of the fibres in the perpendicular plane to the casting direction (Z axis) since fewer fibres are aligned along with Z axis. Furthermore, the results for X and Y axes show that the percentage of fibres oriented in both directions is very similar (ranging from 35-41%, approximately). This orientation results in higher post-cracking loads for the CUB specimens tested in Z axis and lower loads for X and Y axes. This performance is due to a larger amount of fibres in the perpendicular plane to the Z axis (only the fibres distributed circumferentially in the perpendicular plane to the testing direction contribute in the post-cracking response of the material).

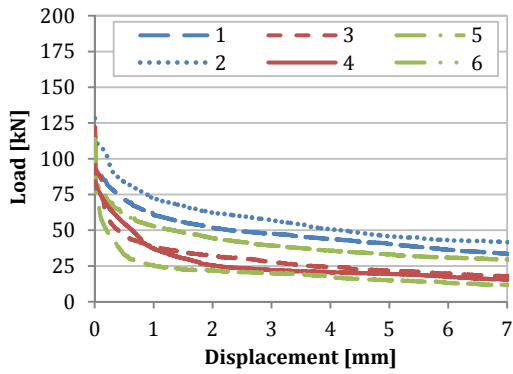


Figure A1.2 Results of series M1/S1/40/CUB.

M1/S1/40/CUB			
Specimen	Z axis	X axis	Y axis
1	20.63%	44.44%	34.92%
2	23.33%	41.67%	35.00%
3	22.08%	38.96%	38.96%
4	19.67%	40.98%	39.34%
5	21.21%	39.39%	39.39%
6	22.06%	36.76%	41.18%

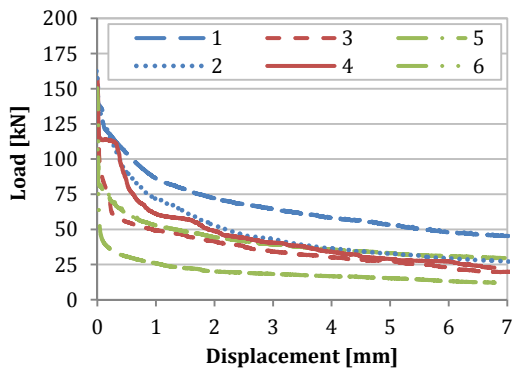


Figure A1.3 Results of series M2/S1/40/CUB.

M2/S1/40/CUB			
Specimen	Z axis	X axis	Y axis
1	23.08%	44.87%	32.05%
2	21.05%	35.53%	43.42%
3	21.92%	36.99%	41.10%
4	26.58%	35.44%	37.97%
5	20.83%	38.89%	40.28%
6	16.44%	42.47%	41.10%

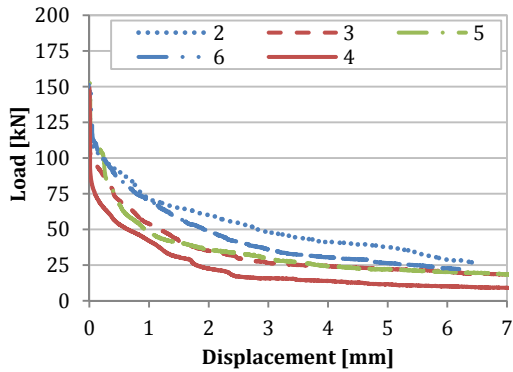


Figure A1.4 Results of series M2/S2/40/CUB.

M2/S2/40/CUB			
Specimen	Z axis	X axis	Y axis
1	22.4%	44.7%	32.9%
2	23.2%	46.3%	30.5%
3	20.5%	35.9%	43.6%
4	19.5%	45.5%	35.1%
5	22.7%	38.6%	38.6%
6	22.4%	44.7%	32.9%

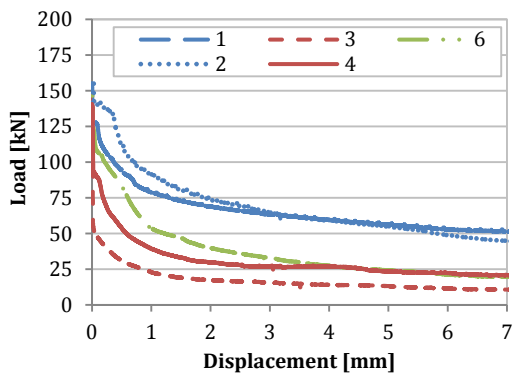


Figure A1.5 Results of series M2/S3/40/CUB.

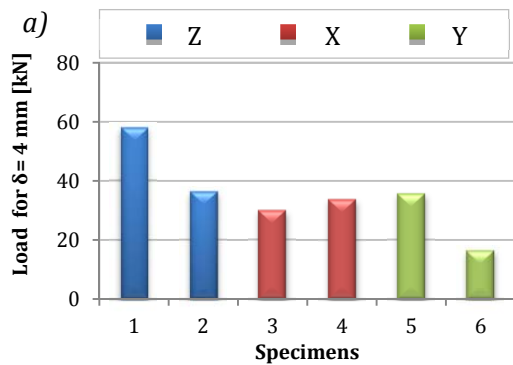
M2/S3/40/CUB			
Specimen	Z axis	X axis	Y axis
1	19.5%	40.2%	40.2%
2	18.2%	36.4%	45.5%
3	17.5%	43.8%	38.8%
4	19.7%	40.8%	39.4%
5	18.9%	41.1%	40.0%
6	21.6%	45.5%	33.0%

A1.3.4. Results for CUT1 and CUT2 specimens

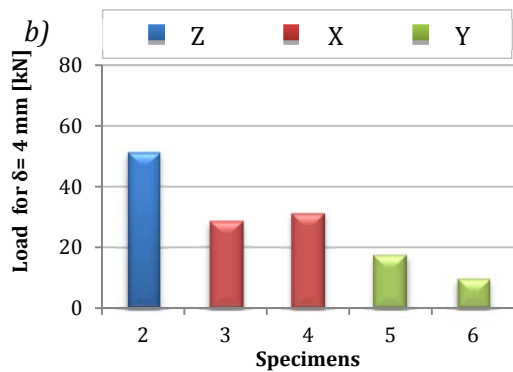
The results of the multidirectional method results for the specimens cut from beams (CUT1 and CUT2) are presented in terms of registered load for a displacement of 4 mm and are depicted in a bar diagram. The orientation results are presented as percentage of fibres aligned along axes Z, X and Y. The testing direction is indicated in the bar diagram and shading the percentage of fibres aligned along the corresponding axis.

Results of M2/S1/40

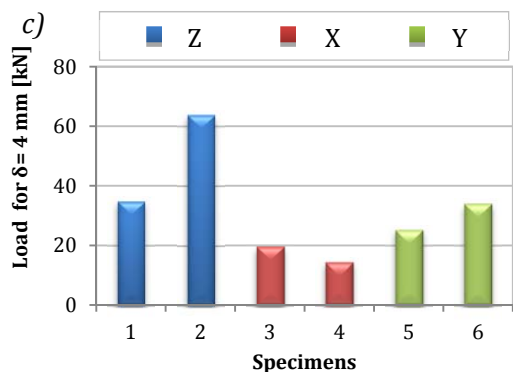
The performance of the CUB specimens has already been described in the previous section and it is characterized by a higher load values when testing in the Z axis and a very similar response when testing in the other two axes (see Figure 1.6a).



M2/S1/40/CUB			
Specimen	Z axis	X axis	Y axis
1	23.08%	44.87%	32.05%
2	21.05%	35.53%	43.42%
3	21.92%	36.99%	41.10%
4	26.58%	35.44%	37.97%
5	20.83%	38.89%	40.28%
6	16.44%	42.47%	41.10%



M2/S1/40/CUT1			
Specimen	Z axis	X axis	Y axis
1	21.6%	39.2%	39.2%
2	22.4%	34.2%	43.4%
3	22.1%	39.7%	38.2%
4	20.8%	41.6%	37.7%
5	17.3%	42.7%	40.0%
6	15.5%	41.7%	42.9%



M2/S1/40/CUT2			
Specimen	Z axis	X axis	Y axis
1	15.3%	54.2%	30.6%
2	17.8%	50.7%	31.5%
3	13.2%	52.6%	34.2%
4	13.0%	54.5%	32.5%
5	15.5%	53.6%	31.0%
6	19.5%	50.6%	29.9%

Figure 1.6 Results of M2/S1/40 for specimens: a) CUB; b) CUT1; c) CUT2.

In the case of the specimens cut from beams there is another preferential orientation: the alignment of fibres along the X axis (along the length of the beam). This phenomenon results in lower values of load in the post-cracking stage when the specimens cut from beams are tested in the X axis if compared to those of the CUB specimens. Such outcome is particularly true for the specimens CUT2 (see Figure 1.6c) since the fibre alignment of fibres along X axis is around 20% higher than along Y axis. Nevertheless, the specimens CUT1 exhibit a different behaviour due to the wall-effect provided by the side of the beam that was not cut (see Figure 1.6b). This local phenomenon distorts the results of the preferential alignment of fibres along X axis by increasing the percentage of fibres along Y axis. Hence, the percentage of both axes is very similar.

After describing the general behaviour observed for each type of specimen taking series M2/S1/40 as an example, the results of the other series are presented and discussed only for the specimens CUT1 and CUT2.

Results for M1/S1/40

The results of series M1/S1/40/CUT1 are representative of the behaviour described previously. From the bar diagram (see Figure A1.7), it may be concluded that in average the load values registered when testing in X axis and Y axis are very similar. Therefore, the alignment of fibres along both axes should be similar even though it is expected that the alignment along X axis remains higher than along Y axis.

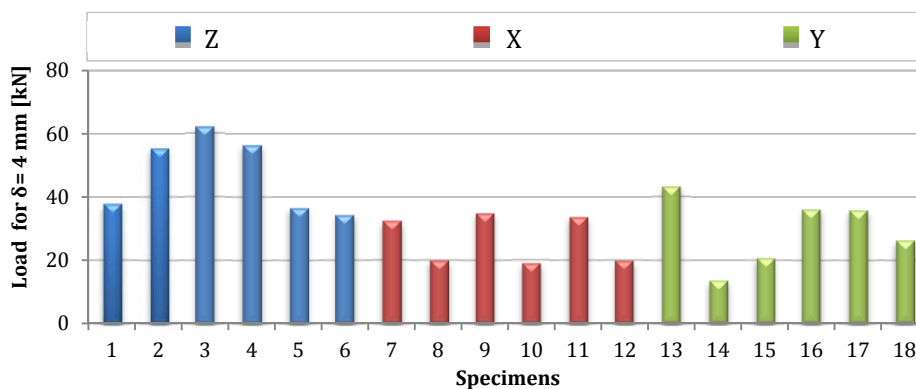


Figure A1.7 Load values for series M1/S1/40/CUT1.

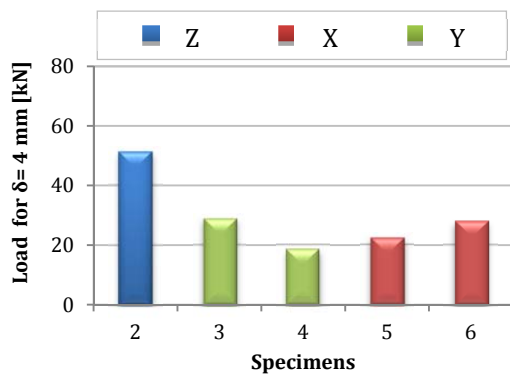
Table A2.5 shows the results of the inductive method. The values indicate that the previous hypothesis regarding the similar percentages of fibre alignment along axes X and Y, except for specimen 6. In such case, the difference between the percentage of fibres aligned along axes X and Y is approximately 20%. This difference is more characteristic of specimens CUT2.

Table A1.5 Percentage of fibres aligned along Z, X and Y axes for specimens in series M1/S1/40/CUT1.

M1/S1/40/CUT1							
Specimen	Z axis	X axis	Y axis	Specimen	Z axis	X axis	Y axis
1	17.74%	45.16%	37.10%	10	23.44%	42.90%	33.65%
2	22.13%	45.87%	32.00%	11	28.55%	35.43%	36.02%
3	25.15%	44.48%	30.37%	12	21.17%	45.13%	33.70%
4	20.82%	48.84%	30.34%	13	19.55%	43.75%	36.70%
5	27.72%	35.96%	36.32%	14	24.35%	40.14%	35.51%
6	19.04%	50.00%	30.96%	15	22.50%	44.46%	33.04%
7	27.14%	37.70%	35.15%	16	22.36%	40.18%	37.45%
8	21.51%	41.67%	36.82%	17	17.74%	45.16%	37.10%
9	25.11%	41.55%	33.33%	18	22.13%	45.87%	32.00%

In the case of specimens CUT2, the preferential alignment of fibres along X axis should be more evident than in the previous case (CUT1 specimens). The results of fibre orientation in series M1/S1/40/CUT2 (see table in

Figure A 1.8) prove this alignment in specimens from 1 to 4. However, it does not occur in specimens 5 and 6. In these two specimens there seems to be a very similar fibre alignment (typical of a CUB specimens for example). For this reason, the values of load for these specimens are similar to those obtained when testing along Y axis.

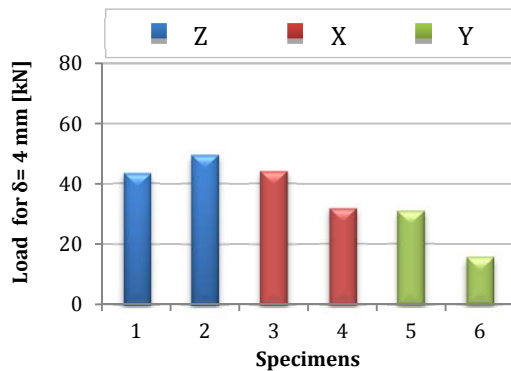


M1/S1/40/CUT2			
Specimen	Z axis	X axis	Y axis
1	16.62%	53.09%	30.29%
2	18.24%	46.35%	35.41%
3	18.71%	53.67%	27.62%
4	18.97%	53.45%	27.59%
5	17.01%	39.97%	43.03%
6	20.22%	39.65%	40.13%

Figure A 1.8 Results of series M1/S1/40/CUT2.

Results for M2/S2/40

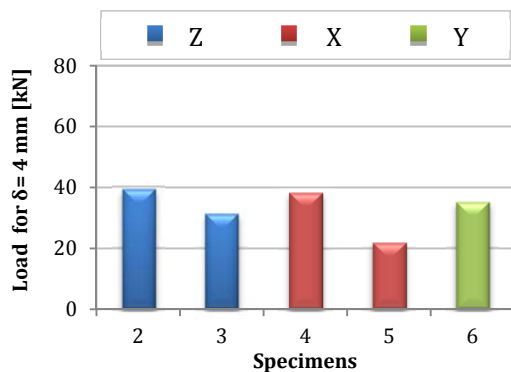
The results of series M2/S2/40/CUT1 regarding the orientation of fibres indicate that the amount of fibres aligned along X and Y axes are very similar (see Figure A1.9). The load values in the bar diagram indicate a preferential orientation of fibres in the casting direction since they are higher for the specimens tested in Z axis; whereas for specimens tested in X and Y axes show, in average, a similar response. These results are in accordance with the results of the inductive method presented in the table in Figure A1.9. The preferential orientation along X axis is, in this case, distorted by the wall-effect in CUT1 specimens.



M2/S2/40/CUT1			
Specimen	Z axis	X axis	Y axis
1	21.6%	39.2%	39.2%
2	22.4%	34.2%	43.4%
3	22.1%	39.7%	38.2%
4	20.8%	41.6%	37.7%
5	17.3%	42.7%	40.0%
6	15.5%	41.7%	42.9%

Figure A1.9 Results of series M2/S2/40/CUT1.

In the case of CUT2 specimens, the inductive methods results show the alignment of the fibres along X axis with a difference with respect to Y axis of around 20%. However, the results in Figure A1.10 regarding the residual load do not reflex this orientation. In order to determine the reason for these results, the real fibre content in the specimens is assessed. It should be noted the difference between nominal or theoretical dosage (40 kg/m^3) and the real content of fibres that can end up in the cubic mould. The fibre content for each specimen can be found in the table in Figure A1.10. The values of fibre content indicate that specimen 4 has 50.4 kg/m^3 of fibre which could be the reason for the high value of residual load, despite the alignment of fibres in the testing direction.



M2/S2/40/CUT2				
Specimen	Z axis	X axis	Y axis	kg/m^3
1	22.9%	47.0%	30.1%	51.6
2	19.7%	52.6%	27.6%	47.3
3	20.8%	48.1%	31.2%	47.9
4	21.0%	55.6%	23.5%	50.4
5	24.4%	52.3%	23.3%	53.5
6	20.3%	56.8%	23.0%	46.0

Figure A1.10 Results of series M2/S2/40/CUT2.

A1.4. CONCLUDING REMARKS

The results of the experimental program herein presented indicate that the multidirectional method shows the influence of fibre orientation in the post-cracking behaviour of SFRC. Preferential orientations due to the geometry of the specimen and the walls of the moulds are detected with this method. Thus, the combination of the multidirectional method and the inductive method is a suitable solution to be applied on the cubic specimens extracted from the SFRC slabs in order to study the influence of fibre orientation and distribution in the structural response of the slabs.

APPENDIX 1. NEOPRENE COMPRESSION TEST

The neoprene used in the tests described in Chapter 4 was tested according to the standard UNE-EN1337-3 (AENOR 2005). The main results from the test are presented in this appendix.

Table AP1.1 includes the main characteristics of the compression test on a neoprene sample (200 x 200 x 20 mm) as well as the compressive modulus (E_{cs}) obtained from the test. The figure in Table AP1.1 shows the test setup, in which the displacement was measured by 3 LVDT transducers located vertically.

Table AP1.1 Main results of the neoprene compression test (UNE-EN1337-3) and test setup.

Characteristics	Unit	Values
Dimensions of the specimen	[mm]	200 x 200 x 20
1/3 Pmax	Load (P)	[kN] 48.0
	Stress (σ_c)	[MPa] 1.2
	Strain (ϵ)	[%] 2.3
Load level Pmax	Load (P)	[kN] 144.0
	Stress (σ_c)	[MPa] 3.6
	Strain (ϵ)	[%] 9.1
Compressive modulus (E_{cs})	[MPa]	35.0



Figure AP1.1a presents the displacement registered by each of the LVDT transducers. Likewise, Figure AP1.1b shows the load-average displacement from the compression test.

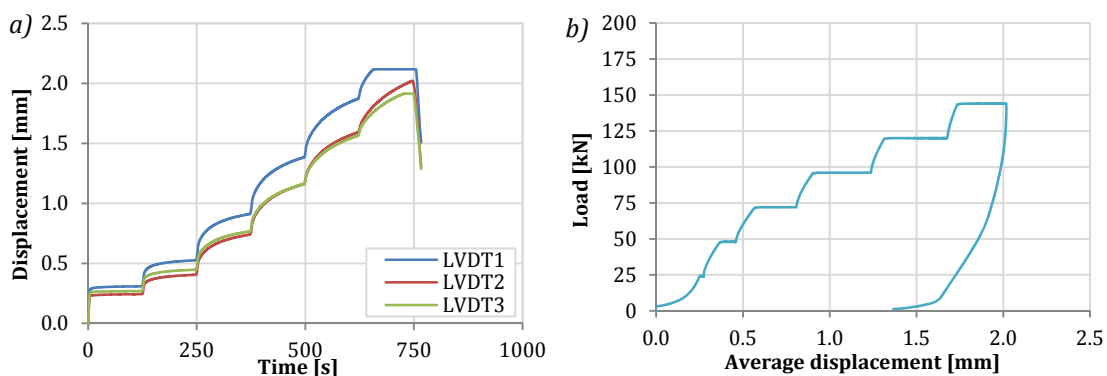


Figure AP1.1a) Compression test setup and b) displacement measured by the LVDT transducers.

According to the results obtained from the compression test on a neoprene sample, the compressive modulus used in Chapter 6 for the numerical simulation of the slab tests described in Chapter 4 is 35.0 MPa.

PUBLICATIONS

The publications developed during the PhD research period are presented subsequently:

Blanco, A., Pujadas, P., de la Fuente, A., Cavalaro, S. and Aguado, A. Application of constitutive models in European codes to RC-FRC. *Construction and Building Materials*, 2013, vol. 40, p. 246-259.

Pujadas, P., Blanco, A., Cavalaro, S., de la Fuente, A. and Aguado, A. New analytical model to generalize the Barcelona test using axial displacement. *Journal of Civil Engineering and Management*, 2013. 10.3846/13923730.2012.756425

Pujadas, P., Blanco, A., Fuente, A. and Aguado, A. Cracking behavior of FRC slabs with traditional reinforcement. *Materials and Structures*, 2012, vol. 45, no. 5, p. 707-725.

Torrents, J., Blanco, A., Pujadas, P., Aguado, A., Juan-García, P. and Sánchez-Moragues, M. Inductive method for assessing the amount and orientation of steel fibers in concrete. *Materials and Structures*, 2012, vol. 45, no. 10, p. 1-16.

de la Fuente, A., Pujadas, P., Blanco, A. and Aguado, A. Experiences in Barcelona with the use of fibres in segmental linings. *Tunnelling and Underground Space Technology*, 2012, vol. 27, no. 1, p. 60-71.

Blanco, A., Pujadas, P., Cavalaro, S., de la Fuente, A. and Aguado, A. Métodos recientes para caracterizar el hormigón reforzado con fibras. In *Proceedings of the 55^o Congreso Brasileiro do Concreto (55CBC)*, Maceió, 2012. ISSN 2175-8182.

Pujadas, P., Blanco, A., Cavalaro, S., de la Fuente, A. and Aguado, A. Análisis comparativo de los modelos constitutivos del hormigón reforzado con fibras. In *Proceedings of the 55^o Congreso Brasileiro do Concreto (55CBC)*, Maceió, 2012. ISSN 2175-8182.

Blanco, A., Pujadas, P., Cavalaro, S. and Aguado, A. Método inductivo para la evaluación de cuantía y orientación de fibras de acero en hormigón. In *Proceedings of the V Congreso de ACHE*, Barcelona, 2011 Asociación Científico-Técnica del Hormigón Estructural (ACHE).

Pujadas, P., Blanco, A., Cavalaro, S.H.P. and Aguado, A. Método para la caracterización multidireccional del HRF. In *Proceedings of the V Congreso de ACHE*, Barcelona, 2011 Asociación Científico-Técnica del Hormigón Estructural (ACHE).

)